Monte-Carlo Simulation of Diffusion as an Aid to Interpreting Quasi-elastic Neutron Scattering from Lattice Gas Systems with Diffusion on Multiple Time-Scales

Jamie Swales

A thesis presented for the degree of

Doctor of Philosophy

School of Science, Engineering and Environment

UNIVERSITY OF SALFORD

May 2022

Contents

List of Figures

xiii

xiv

xv

xix

Acknowledgements

I would like to begin with thanking my supervisor Dr. Dan Bull for the guidance and help given throughout the the research and completion of this PhD, for his availability and support during long periods of working from home due to university closures where face to face meetings were not possible to get to the completion of this work, as well as invaluable expertise and knowledge in the field of inelastic neutron scattering and patience for my attempts to understand the experimental side of the work with no prior experience of such. It was also a privilege to be able to continue and develop further work carried out by my supervisor Dan and his previous student Simon Steel. I would also like to thank my second supervisor Prof. Ian Morrison for the advice on the use of CASTEP for ab-initio calculations and his efforts to maintain the physics department's high performance computing cluster on top of his head of department duties.

I am also incredibly grateful for the opportunity provided by Prof. Nigel Mellors without whom this PhD wouldn't have been possible, allowing me to continue the work I enjoyed during my Masters research with Dan.

I would also like to thank the staff of physics department especially Richard, Bruce and Stuart for the advice and coffee over the years as well as everyone in the PhD office and previous students who made it an enjoyable and friendly place to work.

Finally, thank you to my family for supporting me throughout this time and especially during my write up period with a makeshift office on the dining room table due to the Covid-19 pandemic. To all my friends both in the university and out especially Dan and Nafsika, also my work colleagues at Boulder UK for letting me work on my PhD whilst also working, thank you.

Abstract

Pd and Pd-Ag have recently found application in hydrogen processing technologies, both in terms of purification membranes and isotope-separation systems. Direct measurement of the diffusion processes in these systems is provided by quasi-elastic neutron scattering (QENS); the timescales that can be observed are dependent on the energy range and resolution of the instrumentation. Historical QENS measurements of PdH have been interpreted in terms of single process involving nearest-neighbour jumps between octahedral sites in the fcc lattice. The observation of an additional QENS component arising from motion on significantly more rapid timescale has recently been reported (Steel, 2018), whereby a localised-type motion between tetrahedral and octahedral sites has been suggested.

The work presented in this thesis involves the calculation of pair correlation functions $G(\mathbf{r}, t)$ from Monte Carlo simulations of diffusion in lattice gas systems. Fourier transforming $G(\mathbf{r}, t)$ in both time and space yields a scatting function $S(\mathbf{Q}, \omega)$, comparable to that which would be obtained from QENS measurements from diffusion. $S(\mathbf{Q}, \omega)$ comprises, in general, a number of Lorentzian functions whose widths are related to decay-constants of exponential functions in the intermediate scattering function, $I(\mathbf{Q}, t)$. The separation of components in $I(\mathbf{Q}, t)$ offers a route to interpreting diffusive motions on different time-scales.

In PdH, only jumps between octahedral and tetrahedral sites are allowed in the Monte Carlo simulations, with the relevant interstitial site energies and barrier heights for diffusion being included in the model. It is shown that $I(\mathbf{Q}, t)$ can be interpreted in terms of two decaying exponential functions.

The decay constant, $f(\mathbf{Q})$, from the more slowly decaying exponential component has the form of the Chudley-Elliott model, an analytical expression based on a differential equation describing long-range diffusive motion via a series of uncorrelated jumps. These jumps in the Chudley-Elliott model are interpreted as translational motion via octahedral sites, but given that these jumps are excluded within in the simulation, the actual jump path could instead be interpreted by jumps via a neighbouring tetrahedral site, referred to here as a Octahedral-Tetrahedral-Octahedral (O-T-O) jump mechanism. A more rapid process is suggested to be due to jumps between Octahedral and tetrahedral sites, where there is a much smaller residence time in the tetrahedral sites. Its form as a function of concentration and temperature are discussed in terms of previous experimental spectra.

Whilst the main focus of the work is to examine the effect of jump diffusion processes on the QENS signal from hydrogen in PdH, diffusion of hydrogen in the C15 Laves phase alloy ZrV_2 was also examined in some detail. The rationale here is that this is a system where long-range translational diffusion and localised diffusion have been shown to coexist, and acts as a good test for the techniques developed and presented in this work.

The PdH_x system has important practical applications in the filtering and recycling of the exhaust gasses produced in fusion reactions, which is implemented using an alloy of palladium and silver (PdAg) in particle beds an example of which can be seen in the exhaust processing system in the tritium recovery plant of ITER (Glugla et al., 2006b) in which tritiated waste products are passed through palladium-sliver permiators in multiple stages lowering the tritium content.

Chapter 1

Introduction

1.1 Background

Since its discovery in 1805 (Wollaston, 1805) palladium has been the subject of a wide variety of research and applications. Recently interest has been stimulated by palladium hydride's mechanical properties; unlike most metallic hydrides, it retains its bulk morphology upon repeated absorption and desorption, making it ideal for membranes and particle beds for hydrogen purification (Bernardo et al., 2020; Botter et al., 1988; Fukada et al., 1995; Hatlevik et al., 2010; Yun and Ted Oyama, 2011). In addition, it can be used in isotope separation applications, where the risk of the dispersion of fine powders containing tritium should be avoided. This is a pivotal application in conducting sustained nuclear fusion where exhaust gas recovery systems play a key role (Glugla et al., 2006a,b).

Whilst the palladium hydride system has been extensively researched, being a relatively simple system, since its discovery in 1866 (Graham, 1866), more is still being discovered about the behavior of hydrogen diffusion in this material. In particular, motion of hydrogen taking place on a more

rapid timescale than has previously been observed has been reported by two research groups (Kofu et al., 2016; Steel, 2018).

The diffusion of hydrogen in palladium is generally interpreted as occurring via jumps between neighbouring octahedral interstitial sites. One interpretation of the two timescales is due to two activation energies, where one corresponds to jumps from the ground state, and the other to jumps from the first excited state (Kofu et al., 2016) and more recently in 2020 (Kofu and Yamamuro, 2020). Indeed, the occupation of hydrogen in the 1st excited state has been suggested on the basis of Franck-Condon states, which appear as a shoulder on the standard inelastic neutron scattering data (Kemali et al., 2000) (Krimmel et al., 1994). Here the Franck-Condon state is as a result of a local lattice distortion casued by the presences of hydrogen, minimising the total energy, refereed to as 'self trapping'. This allows for a transition between the states in the fixed ground sate, a Franck-Condon transition, the energy of which can be different to that of a transition to an excited state. This Franck-Condon transition however has not yet been proven and is still under debate. A second hypothesis, from our research group (Steel, 2018), is that the more rapid process is, in fact, due to localised hopping motion between octahedral and neighbouring tetrahedral sites.

It is this latter hypothesis that is the motivation for the present work. Here, Monte-Carlo simulations of hydrogen diffusion in PdH_x and the subsequent calculation of the QENS broadening are presented. Another system of interest here is the C15 Laves-Phase system used here as a prototype system where it is known that hydrogen performs both translational and localised motion in ZrV_2H_x (Schönfeld et al., 1989), and TaV_2H_x (Skripov et al., 1996). This behaviour is attributed to the geometric structure of the intersitital sites, which form inter-connecting hexagons. Here the two types

4

of motion can be easily separated and the effect of site blocking can be seen which has been hypothesised to occur at higher hydrogen concentrations in palladium.

1.2　Metallic-Hydrides

Metal-hydrides are formed when hydrogen readily reacts with a metal to form a compound that is solid at ambient conditions. These fall into a range of categories, ionic hydrides, covalent hydrides, complex hydrides and metallic hydrides. Complex hydrides typically contain covalently bonded hydrogen complexes, such as NH_2 and AlH_4, which are ionically bonded to metal ions. Metallic hydrides, which are of principle interest in this work, typically comprising transition metal elements, contain hydrogen atoms interstitially as bare protons, with their corresponding electrons contributing to the conduction band of the metal.

Metallic hydrides are able to store hydrogen in the bulk of the material via gaseous molecular hydrogen being split at the surface of the material (Broom, 2011), allowing the atomic hydrogen to diffuse via available interstitial sites throughout the material. The occupation of these vacant spaces in the material is dependent on the concentration and temperature of the system. At low concentration the occupation is random, forming a lattice gas, usually referred to as the α phase. At higher concentrations, an ordered hydride phase is observed, labelled the β phase (Fukai, 2005). The ordering of the interstitial atoms is driven by a long-range elastic interaction, but is also dependent on a short range repulsive potential between protons. This repulsive interaction arises from the Coulombic potential, which is heavily screened by the conduction electron in the material. At lower temperatures,

concentration dependent phase transitions in the underlying host lattice are often observed. A number of metal hydrides are of interest for hydrogen storage due to their ability for rapid reversible sorption of hydrogen and the capability to absorb hydrogen at near room temperatures and atmospheric pressure. The most widely encountered example is LaNi$_5$ and its derivatives.

The thermodynamics of hydrogen in metals is most often depicted by pressure-composition isotherms, an example of which is shown in Fig. 1.1, accompanied by an Arrhenius plot from which the gradient is related to the enthaply and entropy of hydride formation.
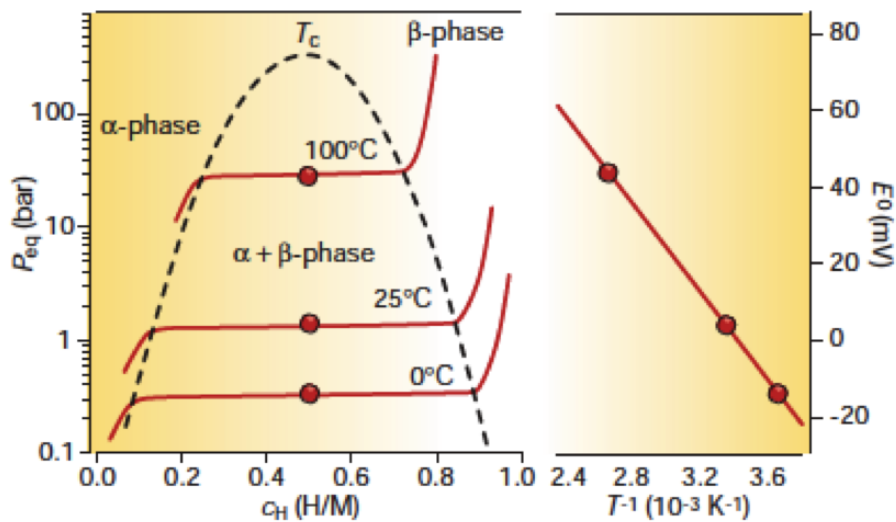
Figure 1.1: Pressure-composition isotherm and Arrhenius plot of LaNi$_5$.(Schlapbach and Züttel, 2011)

During the low-concentration α-phase, gaseous hydrogen is randomly distributed among the host metal's interstitial sites. As the concentration of hydrogen within the host metal increases, H-H pair interactions play a more important role, leading to the formation of an ordered β-phase. The $\alpha + \beta$ phase is seen as a plateau in Fig. 1.1, the length of which determines how

much H can be stored reversibly with small pressure variations. Above a critical temperature T_c only a single phase of hydrogen exists for the whole concentration range resulting in no $\alpha + \beta$ phase being present. The thermodynamic properties of metallic hayrides can be tailored by forming inter-metallic compounds such as $LaNi_5$, which was one of the first compounds allowing for hydrogen absorption and desorption at ambient temperatures and pressures as a result of the combination of stable and unstable hydride forming elements; La and Ni, respectively. (Van Vucht et al., 1970). Lanthanum requires high temperatures in order to reach a reasonable desorption pressure of 2 bar, whereas when combined with nickle forming $LaNi_5$ this plateau pressure for desorption is reached at 20°C compared to that of 1300°C of lanthanum (Dornheim, 2011).

1.2.1 Hydrogen diffusion in Palladium

In the following years after its discovery it was seen that palladium possesses the property of absorbing many times its volume of hydrogen "1 vol. palladium held 526 vol. Hydrogen" (Graham, 1866) at a maximum temperature of 245°C. Further temperature reduction to a range of $90 - 97$°C was shown to yield a greater absorption of hydrogen, "1 vol. palladium held 643.3 vol. Hydrogen". Unlike other metals this absorption process does not cause a change in the bulk morphology. Palladium has become a popular material to work with for use in isotope separation beds and the study of the behaviour of hydrogen and its isotopes within a metal due partly to its very simple structure.

Palladium hydride has been extensively researched in the past via different experimental techniques, indicating that the occupancy of hydrogen in octahedral sites (O-sites), for example from neutron diffraction experiments

7

β-phase PdH (Worsham Jr et al., 1957). Although contrasting claims of tetrahedral occupation have been suggested by some (Davis, 1954) and most recently by Kofu et al (2016), who speculated tetrahedeal occupation in nano particles of palladium hydride at layers close to the surface of the particle. Here, the tetrahedral sites can be occupied due to them becoming stabilised however not as stable as the octahedral sites producing a metastable state. There have been a number of comprehensive literature reviews on the subject of hydrogen in palladium such as Flanagan and Oates (1991), Wicke et al wicke1978hydrogen and F.A Lewis's Book 'The Palladium Hydrogen System'(1967; 1982; 1996).

Initial measurements of the diffusion of hydrogen in palladium were carried out in 1966 by Skold and Nelin (1966) with Quasi Elastic Neutron Scattering (QENS) on $\alpha-$ phase palladium hydride. Fig. 1.2 shows the results of these measurements, where the half widths half maximums of lorentizians resulting from QENS broadening of the elastic delta function (Fig 1.4) are plotted, with curves predicted by an octahedral jump model.
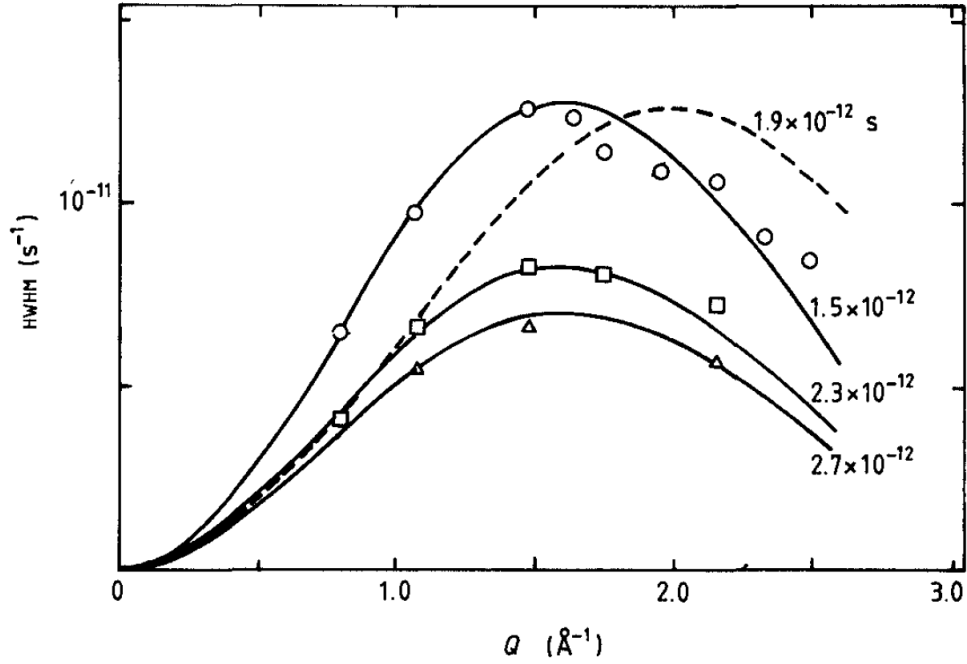
Figure 1.2: Observed widths from QENS data presented by Skold and Nelin (1966) for hydrogen in palladium, where the solid lines are from an octahedral jump model and the dashed line from a tetrahedral jump model

This stimulated further investigations in the behavior of hydrogen. Beg and Ross (1970) shortly after produced work on the $\beta-$ pahse palladium hydride. Recent developments have caused a resurgence in the research of the PdH system due to the hypothesis of the existence of multiple types of motion being undertaken by absorbed hydrogen atoms in the palladium lattice. Work produced by Kofu et al. (2020; 2016) regarding both hydrogen dynamics in bulk of palladium has suggested that the motion taking place on a more rapid time scale is a result of the hydrogen atom making a jump from the first excited state via the octahedral-tetrahedral-octahedsral (O-T-O) jump path to a nearest neighbour vacant octahedral site's first excited state, shown schematically in Fig. 1.3.

9
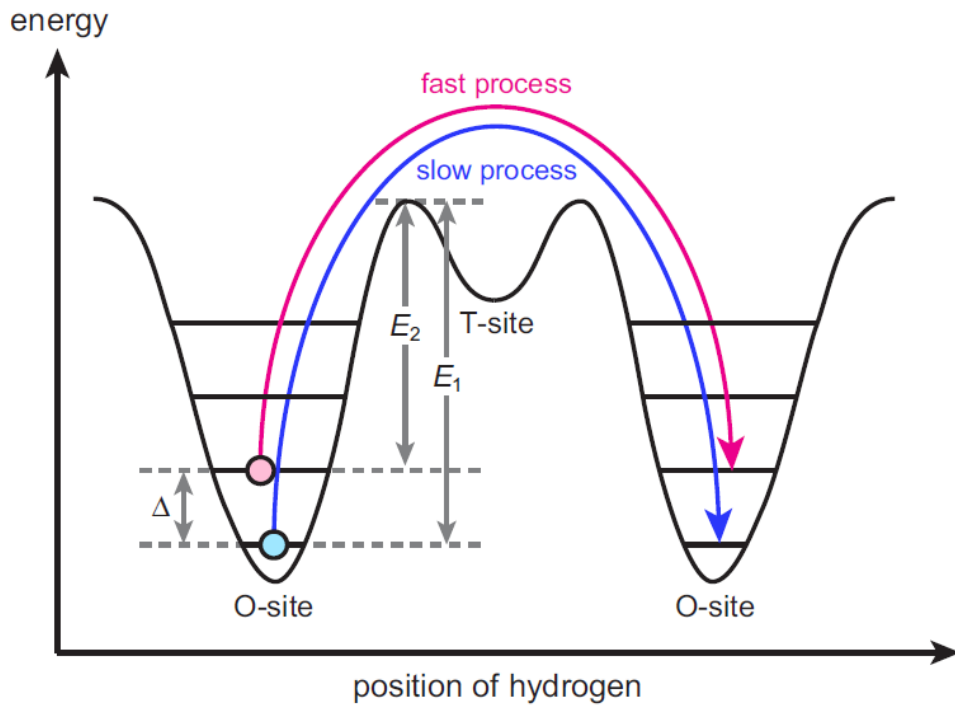
Figure 1.3: A schematic representation of the two suggested diffusion processes by Kofu *et al* (2016)

Steel (2018) reported results from QENS in PdH, both powdered and foil samples. There was some evidence of a broad Lorentzian component in the QENS data, although the experiments were inconclusive. This is attributed to the fact that a broad Lorentzian component could appear as a flat background if the energy window is not sufficiently large. This effect is illustrated schematically in Figs. 1.4 and 1.5, which show the same scattering functions but over two energy transfer windows. In both figures, the blue dotted line would originate from motion on a more rapid timescale than from the dashed red line. In 1.4, the blue dashed line clearly has a Lorentzian form, whereas in Fig. 1.5, it could be mistaken as a flat background contribution. Fig. 1.6 shows the jump mechanism in which a diffusing hydrogen moves between octahedral sites via a tetrahedral site along a direction of (1,1,1). This pathway

is easier the hydrogen atom as the potential barrier and therefore activation energy is much lower than that between neighbouring octahedral sites along the vector (1,1,0).
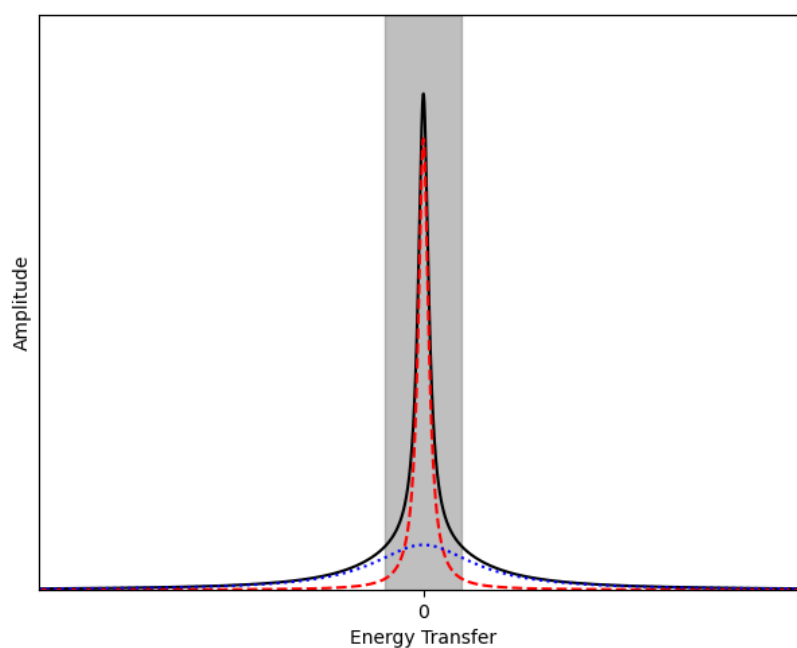
Figure 1.4: Schematic representation of a quasi-elastic scattering arising from motion on two distinct time-scales measured at fixed momentum transfer. The solid line is a sum of the two Lorentzians, broad (dot) and narrow (dash). The shaded area represents a smaller energy transfer window, related to Fig. 1.5.
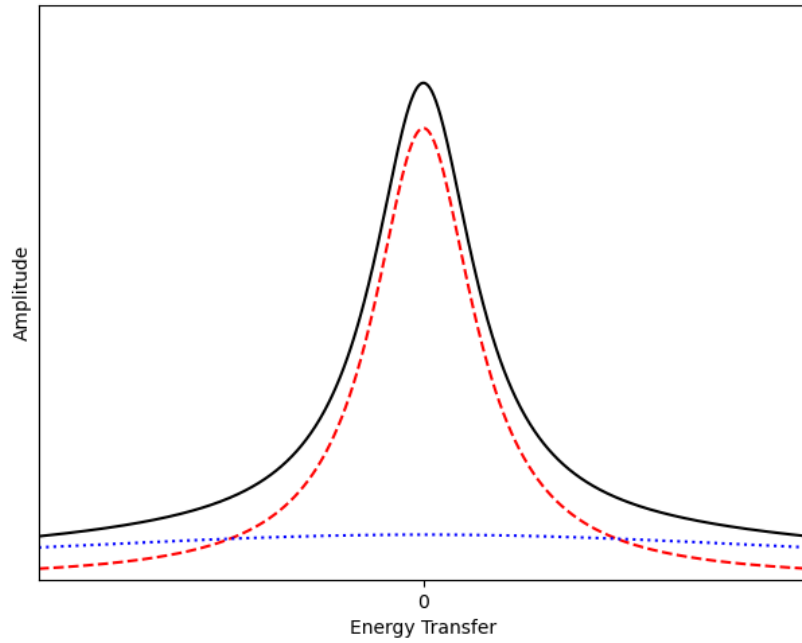
Figure 1.5: Schematic representation of a quasi-elastic scattering arising from motion on two distinct time-scales measured at fixed momentum transfer. The solid line is a sum of the two Lorentzians, broad (dot) and narrow (dash). The energy transfer range corresponds to the shaded area of Fig.1.4. Here, the broader Loerntzian component (dot) could be mistaken from a flat background contribution
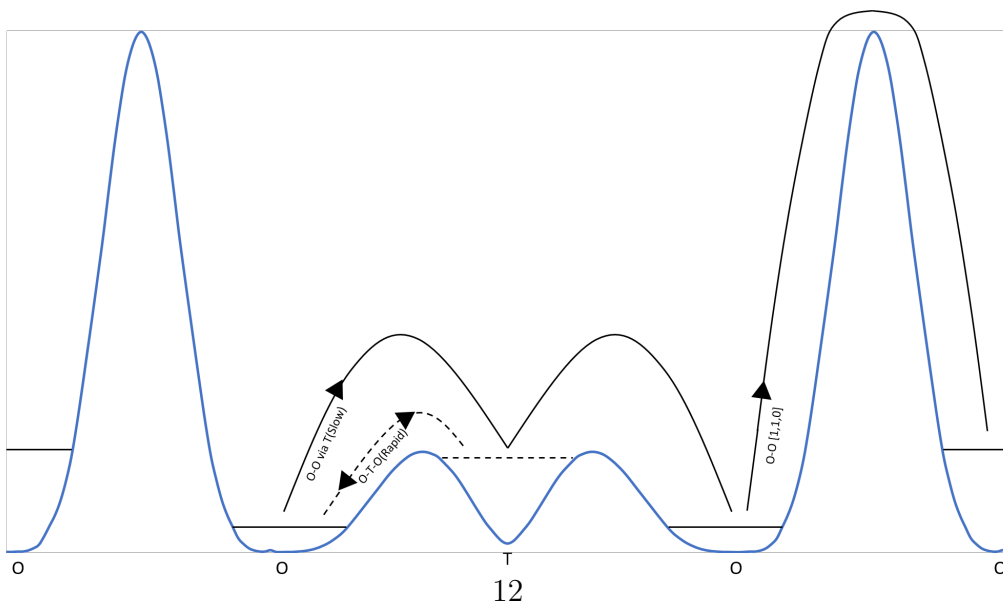
Figure 1.6: Representation of proposed possible jump paths (Steel, 2018). where jumps are shown from the ground sate for both the octerhedral and tetrahedral sites, the dashed line represents the proposed localised motion.

Being the subject of many neutron scattering experiments, the octahedral to octahedral jump that is consistently seen in results can be well represented by the Chudley-Elliott model for octahedral to octahedral jumps on a face-centred cubic lattice (Chudley and Elliott, 1961) as such much has already been learned about the nature of this jump. One of the pieces of information gained from this is the diffusion coefficient D_0, reported as $D = 6.1 \times 10^{-3} \exp(-(5990 \text{cal.}/\text{mol})/\text{RT}) \text{cm}^2 \text{sec}^{-1}$ (Simons and Flanagan, 1965), where $5990 cal/mol$ is the activation energy. A variety of other methods exist for finding the diffusion coefficients, for example Nuclear Magnetic Resonance on both α and β phase palladium and Palladium-silver alloys (Cornell and Seymour, 1975)(Davis et al., 1976) and Molecular dynamics (MD) calculations using the Embedded Atom Model (EAM) (Li and Wahnström, 1992).

Here however, the interest of this work is on a larger time scale, with a greater focus on the transitional probabilities of the diffusion of hydrogen atoms, rather than the specifics of the jump mechanisms themselves, for which molecular dynamics (MD) simulations are more suited. The Monte-Carlo simulations are motivated by examining the possibility of the presence of the rapid localised motion suggested in the experimental data (Steel, 2018) and how this could be affected by the concentration of the system; it is believed that at higher concentrations the localised motion would become more pronounced due to site blocking of the octahedral sites.

With the increase in computing power using Monte-Carlo (MC) simulations and ab-initio calculations has become increasingly common, with the aim of the latter determining properties such as lattice constants and zero-point energies of interstitial sites by using Density Functional theory. Work produced by C. Elsasser, et al (1991) using pseudopotentials to calculate the total energies for hydrogen in palladium gave a picture of the single crys-

tal diffusion paths possible, along with the energies of the tetrahedral sites relative to the octahedral sites and as a result the barrier height energies, Fig. 1.7. Recent work by Hajime Kimizuka *et al* (2018) with palladium hydride where site energies and barrier height energies were presented and Erich Wimmer *et al* (2008) with hydrogen isotopes in nickel used transition state theory in order to locate the saddle point between interstitial sites which all lie along a minimum energy pathway (MEP). The energy of these saddle points determines how easily an atom in a interstitial site can jump to a vacant site on the opposite side of the saddle point. Data for the barrier heights calculated with this method is used in the Monte-Carlo calculations to calculate the probability of atoms being able to jump between available sites. However the finer details of these calculations will not be tackled in this piece of work.
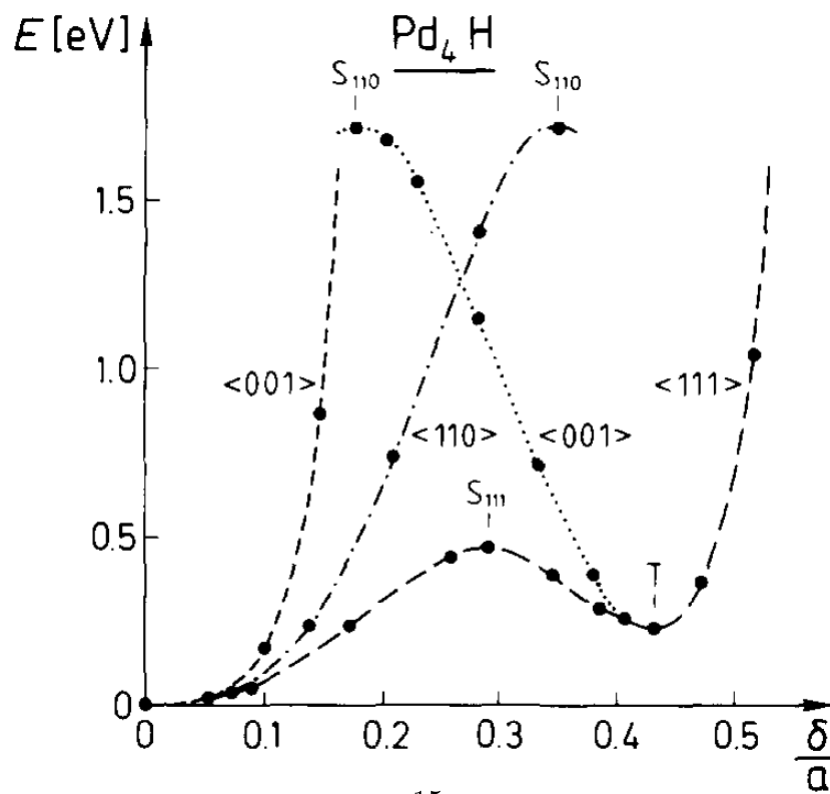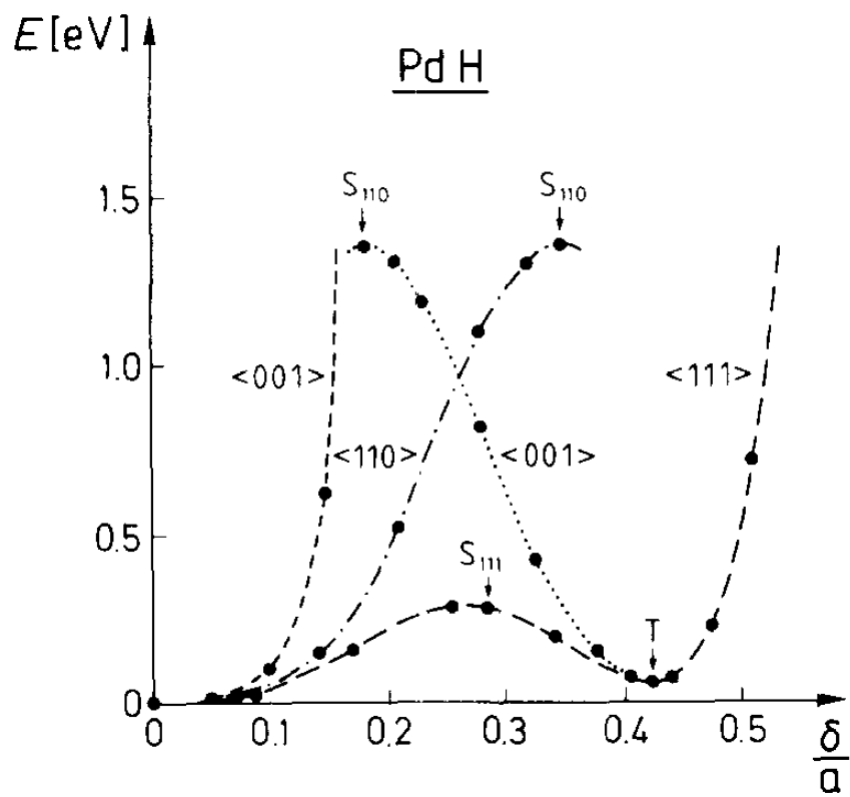
Figure 1.7: Energy displacement curves showing the saddle points between Octahedral and Tetrahedral sites for PdH and Pd_4H (Elsässer et al., 1991)

1.3 Research Aims and Objectives

The main aim of the current work is to apply an existing frame-work for calculating neutron scattering functions via Monte-Carlo simulation (Bull and Ross, 1999a, 2001) to diffusion among the octahedral and tetrahedral sites in a face-centered cubic host lattice. One of the particular issues is the comparison of simulated data with experimental data, which is generally obtained for polycrystalline samples. In this case, directionally averaged scattering functions are required.

The research objectives are:

1. Development of code to calculate the static scattering function, $S(\mathbf{Q})$ and the intermediate dynamic scattering function, $I(\mathbf{Q}, t)$, via Fourier transform of the real-space pair-correlation functions obtained from Monte-Carlo simulation, produced using the pre-existing code named GRT (Bull, 2001; Bull et al., 2003), described in Section 3.2;

2. Development of the methodology for producing and interpreting spherically averaged scattering functions

3. Examine the case of localised motion in the C15 system ZrV_2H

4. Hypothesis testing of two-timescale diffusion models of Kofu et al. kofu2016hydrogen and Steel SteelSA2018Sotp using extreme cases for jump-rates;

5. Use of input parameters for interstitial site energies and diffusion barriers from Density Functional Theory (DFT) work;

1.4   Thesis Synopsis

Chapter 2: Diffusion in a Lattice Gas. An overview of the nature of neutron scattering with a focus on quasi-elastic neutron scattering from a lattice gas and corresponding analytical models is given.

Chapter 3: Monte-Carlo Simulations of a Lattice Gas. Details the Monte-Carlo methods applied to diffusion in a lattice gas are given, along with a description of the programme 'GRT' and a guide to its operation. Post-processing of the output of GRT is described, including the format of the pair-correlation functions produced by the GRT programme and how they are interpreted using a suite of developed python scripts to arrive at the widths of $S(\mathbf{Q}, \omega)$

Chapter 4: The C15 Laves-phase System (ZrV_2H_x). Details on the structure and characteristics of the intermetallic compound ZrV_2H_x are presented, followed by a series of results obtained from Monte-Carlo calculations of the self pair correlation functions, demonstrating the presence of motion on multiple time scales.

Chapter 5: The Palladium Hydride System (PdH_x). As an extension from the data in Chapter 5, the details of the palladium hydride system are outlined along with its structural characteristics, followed by significant results suggesting that the motion of diffusing hydrogen can be interpreted on two different time scales; rapid and slow types of motion in both the polycrystaline and single crystal cases.

Chapter 6: Concluding Remarks and Further Work. The key results found in the presented work for both PdH_x and ZrV_2H_x are reviewd and outlined, with comparisons to previously reported results and possible future extensions to further describe each system.

Chapter 2

Diffusion in a Lattice Gas

The work presented in this thesis concerns Monte Carlo simulation of diffusion in lattice gas systems. This chapter starts with an overview of diffusion (Section 2.1) followed by a discussion of its interpretation in terms of time-dependent pair correlation functions, $G(\mathbf{r},t)$, and subsequent production of scattering functions by Fourier transform (Section 2.2). In later chapters, these scattering functions are interpreted in terms of equivalent results that would be obtained from quasielastic neutron scattering (QENS) experiments; Section 2.3 contains a description of neutron scattering to a level of detail that is necessary to understand the interpretation of the simulation data, a more detailed approach can be found in G.L. Squires book (1996 - 1978) . Finally, Section 2.4 discusses various analytical models for interpreting QENS in terms of quantites that can be compared to results obtained from the Monte-Carlo simulations.

2.1 Particle diffusion

In a lattice gas model, a diffusing species moves between spatially well-defined positions. In a metallic hydride, the host lattice defines a potential through which the diffusing species moves through via a series of jumps between interstitial sites. Here, there are a number of possible diffusion mechanisms, from quantum effects such as tunneling and phonon assisted tunneling in the low temperature range to thermally activated diffusion at higher temperatures. If the motion is thermally activated, the temperature dependence of the diffusion rate can be described by an Arrhenius law,

$$D(T) = D_0 \exp\left(\frac{-E_a}{k_B T}\right). \tag{2.1}$$

There are essentially two ways of describing particle diffusion: chemical diffusion and tracer diffusion.

Following Fick (1855), chemical diffusion, relies on a concentration gradient, ∇c, and works by describing the local fluctuation in particle density from an average value, whereby the flux of particles passing through an area per second, $\mathbf{J}$, is proportional to the concentration gradient, being related by the chemical diffusion coefficient, D_{chem},

$$\mathbf{J} = -D_{chem}\nabla c. \tag{2.2}$$

Tracer diffusion, or self-diffusion, (Einstein, 1905; Langevin, 1908; Smoluchowski, 1906) is where distinguishable particles are tagged and their displacement is measured from their origin. Self-diffusion describes the mean squared displacement of such particles, and can be quantified via the probability of finding a particle within a small volume element $d\mathbf{r}$ at a point in space and time, $P(\mathbf{r}, t)$. The time evolution of the probability is then

described by the following differential equation, (Squires, 1996 - 1978)

$$\frac{\partial P(\mathbf{r}, t)}{\partial t} = D_t \nabla^2 P(\mathbf{r}, t).$$ (2.3)

Here, D_t is the tracer diffusion coefficient. For the initial condition $P(\mathbf{r}, 0) = \delta(\mathbf{r})$, which is a delta function at the origin at t=0, the solution takes the form of a Gaussian with a width related to the mean squared displacement,

$$\left\langle \mathbf{r}^2(t) \right\rangle = 6D_t t.$$ (2.4)

2.1.1 Random Walk

The process of particle diffusion can be described by means of a random walk process (Markov, 1912), whereby the probability of a particular sequence of N uncorrelated events moving the system from configuration x_n to x_{n+1}, e.g. particle jumps in a stochastic process, is given by,

$$P_N(x_1, x_2, ..., x_N) = P_1(x_1)P_1(x_2)...P_1(x_N).$$ (2.5)

The idea of a random walk can be used to produce a Markovian chain that describes the evolution of the spatial probability distribution. In a Markovian process, the probability of a transition from state x to a new state x' is considered. In relation to diffusion, the states x' are determined by the set of allowed jumps.

$$P_N(x_1, x_2, ..., x_N) = P_1(x_1)T(x_1 \rightarrow x_2)T(x_2 \rightarrow x_3)...T(x_{N-1} \rightarrow x_N).$$ (2.6)

When time is taken into consideration, the probability of configuration becomes $P(x,t)$, so for a continuous time scale we arrive at a differential equation for the rate of change of the probability.

$$\frac{\partial P(x,t)}{\partial t} = \Sigma_{x'}T(x \to x')P(x,t) + \Sigma_{x}T(x' \to x)P(x',t). \qquad (2.7)$$

Note that, in a steady state, the rate-of-change of P(x,t) is zero, and so,

$$T(x \to x')P(x,t) = T(x' \to x)P(x',t). \qquad (2.8)$$

As an example, Gissler and Rother (1970) considered $P(\mathbf{r},t)$ for a single particle as an infinite series of n displacements, which is the self correlation function $G_s(\mathbf{r},t)$.

$$G_s(\mathbf{r},t) = \sum_{n=1}^{\infty} P_n(\mathbf{r})T_n(t). \qquad (2.9)$$

The time dependent component $T_n(t)$, which is the probability of the nth jump occurring at a time t, is determined here by a Poisson distribution,

$$T_n(t) = \frac{(\lambda t)^n}{N!} \exp(-\lambda t). \qquad (2.10)$$

Here, λ is equal to the inverse of the jump rate, τ. In order to compare with scattering experiments, it is necessary to take the Fourier transform over both time and space to give a scattering function, $S(\mathbf{Q},\omega)$, via an intermediate scattering function.

$$I_S(\mathbf{Q},t) = \exp{-[1 - (F(\mathbf{Q}))t/\tau]} \qquad (2.11)$$

Here, following the convention in neutron scattering, we define $\mathbf{Q} = \mathbf{k}' - \mathbf{k}$, which is commonly referred to as the momentum transfer. The solution to

21

Eqn. 2.9 from a spatial and temporal Fourier transform yields a Lorentzian with a width $[1 - f(Q)]/\tau$.

$$S(\mathbf{Q}, \omega) = \frac{1}{\pi} \frac{(1 - F(\mathbf{Q}))\tau}{[(1 - F(\mathbf{Q}))]^2 + \tau^2 \omega^2}. \tag{2.12}$$

In the next section, time-dependent pair correlation functions, G($\mathbf{r}$,t) and the corresponding scattering functions, $S(\mathbf{Q}, \omega)$ will be considered in detail. The subsequent section discusses the relation of $S(\mathbf{Q}, \omega)$ to neutron scattering.

2.2   Pair-Correlation Functions

Whilst the main focus of the work presented here concerns time-dependent pair distribution functions, a useful starting point is to consider static pair correlation functions, which are related directly to structure factors obtained from diffraction measurements.

2.2.1   The Static Pair Correlation Function

The static pair correlation, $g(\mathbf{r})$, defines the probability of finding a particle at position $\mathbf{r}$ relative to a particle at the origin,

$$g(\mathbf{r}) = \frac{1}{N} \sum_i^N \sum_{j \neq i}^N \langle \delta(\mathbf{r} - \mathbf{R}_{ij}) \rangle. \tag{2.13}$$

$$g(\mathbf{r}) = \frac{1}{N} \sum_i^N \sum_{j \neq i}^N \langle \delta(\mathbf{r} - \mathbf{R}_i + \mathbf{R}_j) \rangle. \tag{2.14}$$

Here, summations run over atoms in a particular configuration, whilst the triangular brackets indicate a thermal average over configuration space.

It is often convenient to take the spherical average of Eqn. (2.14), giving a radial distribution function, as commonly used in relation to liquid and amorphous materials. Fig. 2.1 shows a schematic of the radial distribution function from an ideal gas and a solid. For an ideal gas, where there is very little spatial order, beyond a certain radius the pair correlation function will be constant value. Conversely, for a crystalline lattice where atoms have well defined positions and spacing, the pair correlation function comprises sharp peaks corresponding to the correlation in position between pairs of atoms.
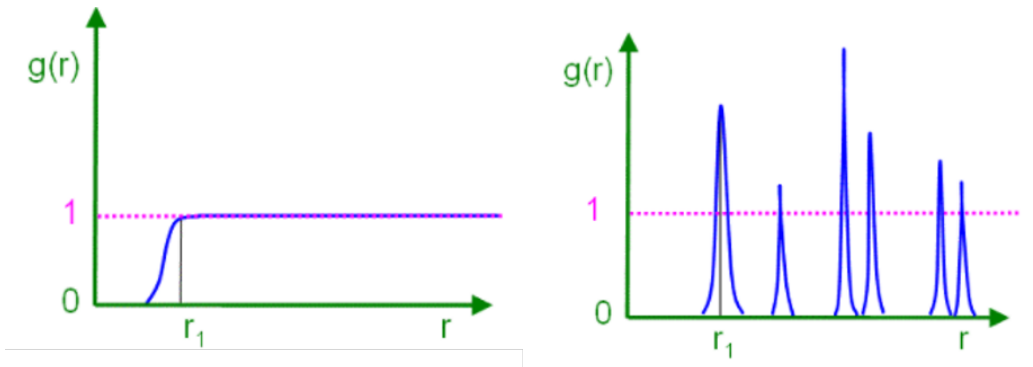
Figure 2.1: Schematic representation of pair correlation function (radial distribution function) for an ideal gas and an ordered solid. The latter is shown convoluted with an experimental resolution function. (Liao, 2006)

In an ordered solid, $g(\mathbf{r})$ has sharp peaks at radial distances from the origin correlating with the nearest neighbours to the atom positioned at the origin. The formation of a pair correlation function for a square lattice is shown in Fig. 2.2. A r increases, peaks are associated with subsequent sets of nearest neighbours, with the intensity relative to the number of nearest neighbour atoms. The difference in intensity can be seen clearly between the 3rd and 4th nearest neighbour atoms, having 4 and 8 respectively.
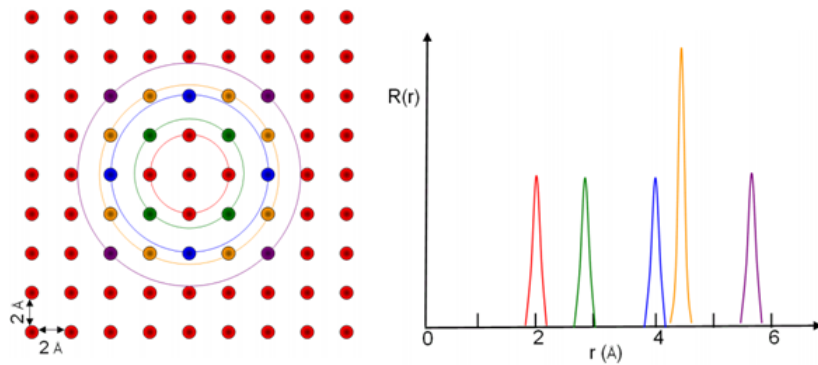
Figure 2.2: Formation of the radial distribution function from successive neighbour shells in a square lattice. (Liao, 2006)

In Fig. 2.3, pair correlation functions are shown for a periodic lattice and for an amorphous structure, where there is only short-range order present. In a lattice gas, there is typically a superposition of short-range ordering on top of an ordered lattice, shown schematically in Fig.2.4.
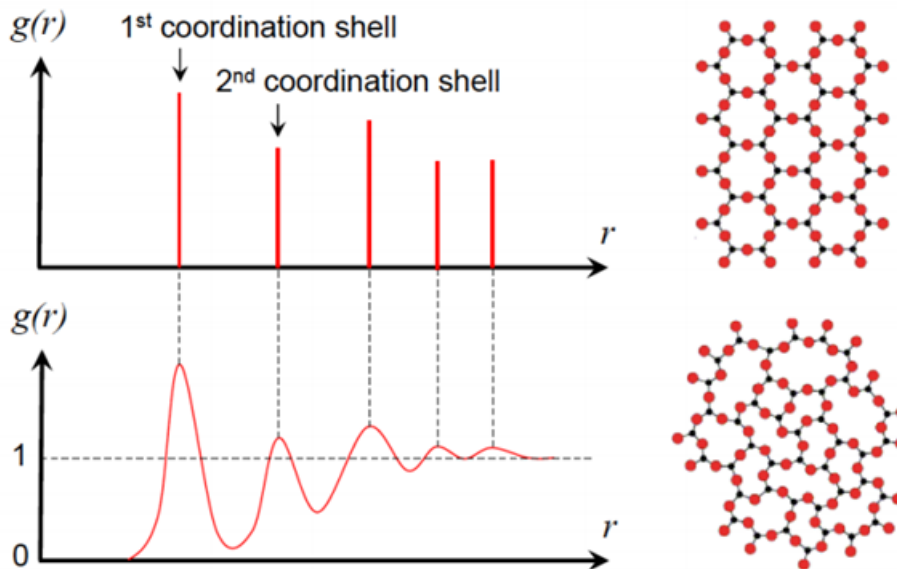
Figure 2.3: schematic of a radial pair correlation function for an ordered structure and an amorphous structure. (Hu, 2015)

24

(a) Non-interacting lattice gas

(b) Lattice gas with inter-particle interactions
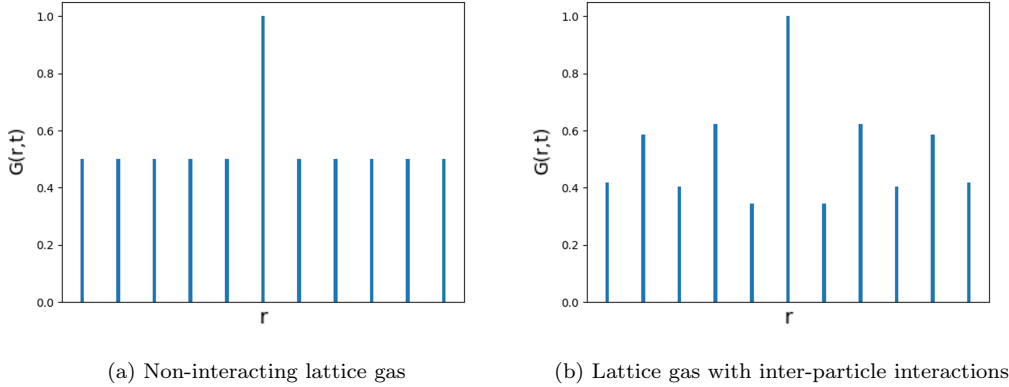
Figure 2.4: Schematic of the pair correlation function in a particular direction from a lattice gas. Note that the value at the origin has been included here, which is unity, by definition.

The Fourier transform of the pair correlation function yields the structure factor $S(\mathbf{Q})$. In terms of a lattice gas, one is generally concerned with the deviation from the average concentration, so the structure factor is evaluated as

$$S(\mathbf{Q}) = 1 + A \sum_{i,j \neq i} [g(\mathbf{r}_{i,j}) - c] \exp\left[i\mathbf{Q} \cdot \mathbf{r}_{i,j}\right]. \qquad (2.15)$$

2.2.2 Time Dependent Pair Correlation Functions

In the classical regime, the time dependent pair correlation function, $G(\mathbf{r}, t)$, often simply referred to as the pair correlation function, is as a natural extension of the static pair correlation function g($\mathbf{r}$) (Van Hove, 1954). Here the spatial correlation of a given particle with itself becomes important. The *total* pair correlation function is defined as the probability of finding a particle at position $\mathbf{r}$ at time, t from an origin that was populated by any particle at $t = 0$. Equation 2.14 then becomes,

$$G(\mathbf{r}, t) = \frac{1}{N} \sum_{i=1}^{N} \sum_{j=1}^{N} \langle \delta(\mathbf{r} - \mathbf{R}_i(0) + \mathbf{R}_j(t)) \rangle. \tag{2.16}$$

The *total* pair correlation function can be separated into a 'self' and a 'distinct' part,

$$G(\mathbf{r}, t) = G_S(\mathbf{r}, t) + G_D(\mathbf{r}, t), \tag{2.17}$$

such that

$$G(\mathbf{r}, t) = \frac{1}{N} \left[\sum_{i=1}^{N} \langle \delta(\mathbf{r} - \mathbf{R}_i(0) + \mathbf{R}_i(t)) \rangle + \sum_{i \neq j}^{N} \langle \delta(\mathbf{r} - \mathbf{R}_i(0) + \mathbf{R}_j(t)) \rangle \right].$$
$$\tag{2.18}$$

The *self* correlation function represents the probability of finding particle i at t given it was at the origin at $t = 0$. The *distinct* correlation function is then the probability of finding a different particle j at t to that of particle i that was at the origin at $t = 0$. Note that, at $t = 0$ the distinct pair correlation function reduces to the static pair correlation function $g(\mathbf{r})$.

As will be discussed in the next section, the correlation functions of interest when comparing with quasi-elastic neutron scattering measurements are the self correlation function, $G_s(\mathbf{r}, t)$ and the total correlation function, $G(\mathbf{r}, t)$. The typical evolution of these two functions for a lattice gas on non-interacting particles are shown in Fig. 2.5. For the self correlation function, there is a delta function at the origin at zero time, which spreads out with time. For the total correlation function, there is also a contribution equal to the average concentration of the lattice gas, c, at every non-zero value of r. The delta function at the origin at t=0 spreads out with time, such that the evolution of $G(\mathbf{r}, t)$ as $t >> 0$ is towards the average concentration, c.

26
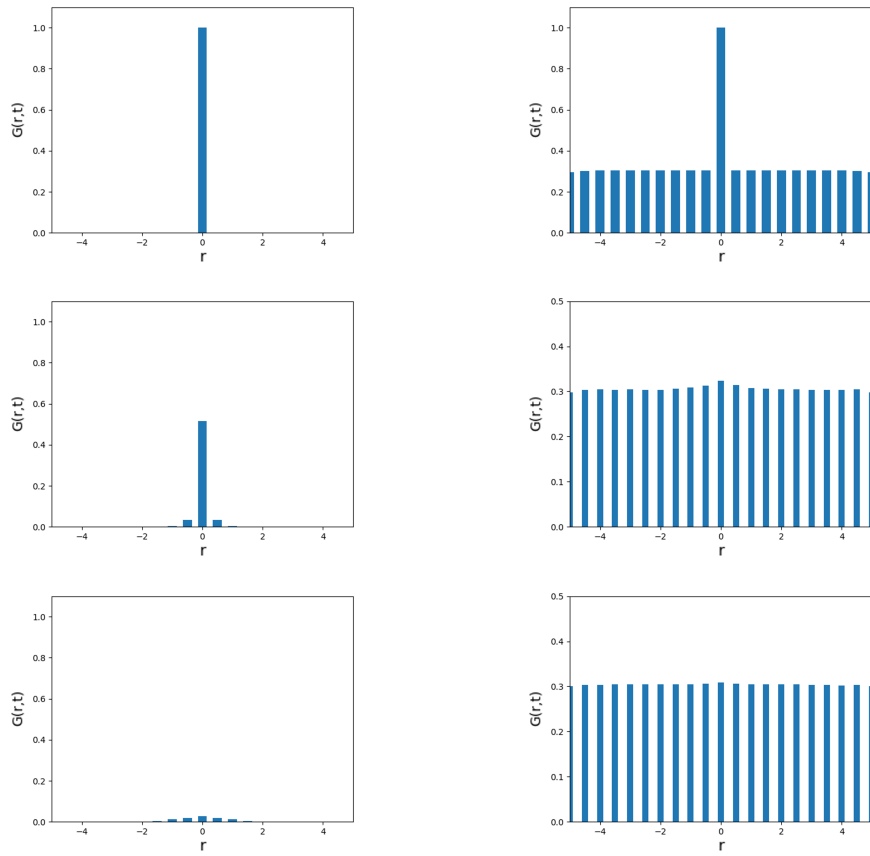
Figure 2.5: Schematic of a Self pair correlation function (left hand column) and the total pair correlation function (right hand column) at t = 0, t >0 and t >>0

By analogy with Eqn. (2.15), a scattering function, $S(\mathbf{Q}, \omega)$, can be defined that is the spatial and temporal Fourier transform of the time-dependent pair correlation function $G(\mathbf{r}, t)$.

$$S(\mathbf{Q}, \omega) = A \int_{-\infty}^{\infty} \int_{\mathbf{r}} G(\mathbf{r}, t) \exp\left[i(\mathbf{Q} \cdot \mathbf{r} - \omega t)\right] d\mathbf{r} dt. \qquad (2.19)$$

It is convenient to define an intermediate scattering function, I($\mathbf{Q}$,t). This can be obtained either from G($\mathbf{r}$,t) or $S(\mathbf{Q}, \omega)$, respectively:

$$I(\mathbf{Q}, t) = A \int_{\mathbf{r}} G(\mathbf{r}, t) e^{i\mathbf{Q} \cdot \mathbf{r}} d\mathbf{r}, \qquad (2.20)$$

$$I(\mathbf{Q}, t) = A \int_{-\infty}^{\infty} S(\mathbf{Q}, \omega) e^{-i\omega t} dt. \qquad (2.21)$$

In general, for particle diffusion, the intermediate scattering function is in the form of an exponential decay, with the corresponding scattering function $S(\mathbf{Q}, \omega)$ in the form of a Lorentzian. The decay constant for the exponential in $I(\mathbf{Q}, t)$ is directly related to the Lorentzian width. This provides a useful point for comparison between Monte-Carlo data and QENS data. It is worth considering here that a rapidly decaying exponential term, i.e. over a short time scale, corresponds to a broad Lorentzian component, i.e. a large frequency or energy. The relationship between the various functions is shown schematically in Fig. 2.6.
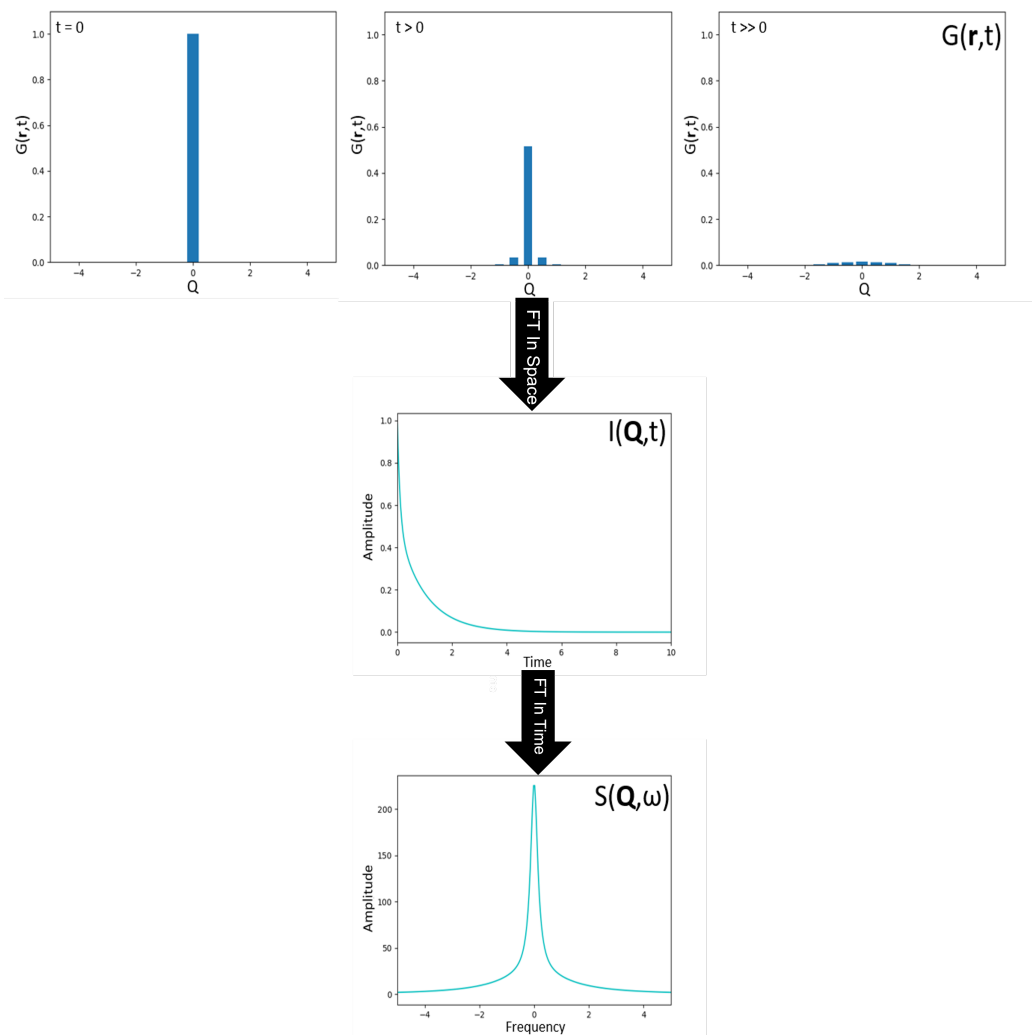
Figure 2.6: Schematic representation of the Fourier transform from interme-
diate scattering function to the scattering function, $S(\mathbf{Q}), \omega)$, beginning at
$G(\mathbf{r}, t)$.

2.3 Neutron Scattering

Neutrons are an ideal probe of dynamics in condensed matter, owing to them having a wavelength comparable to atomic spacing and energies of the order of atomic and molecular excitation. A moderator at T = 300 K produces thermal neutrons with average energies $k_B T = 0.025$ eV, corresponding to a wavelength $\lambda = 1.78$ Å. This offers the possibility of examining spatial and temporal characteristics simultaneously enabling, for example, measurement of the spatial dependence of diffusion dynamics and of phonon dispersion. Neutrons incident on a scattering system will have a wave vector $\mathbf{k}$ and energy E. A scattered neutron can experience a change in both momentum and energy, resulting in a detected wave vector $\mathbf{k}'$ and an energy of E'. It then becomes convenient to define the change in wave vector, commonly known as the momentum transfer, as $\mathbf{Q} = \mathbf{k}' - \mathbf{k}$ and the energy transfer as $\Delta E = E' - E$.
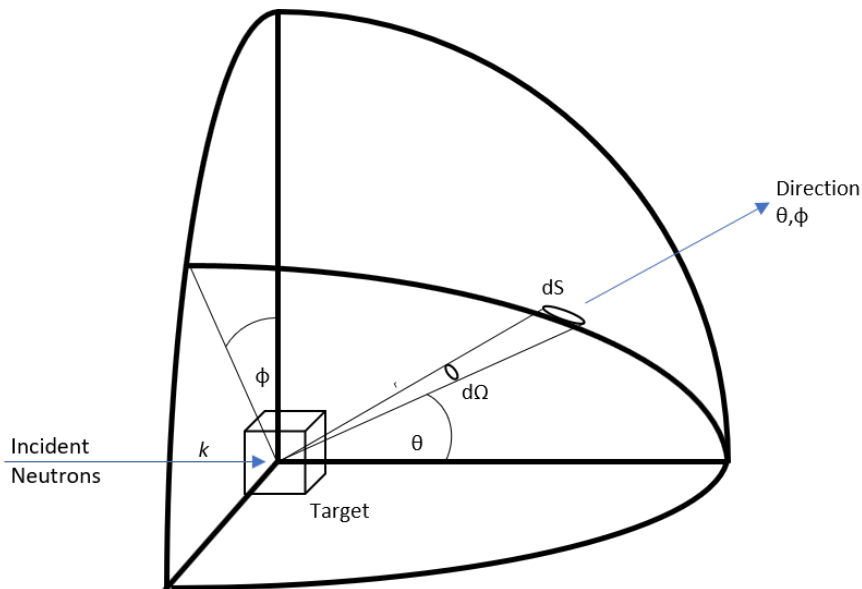
Figure 2.7: Geometry of a neutron scattering measurement

2.3.1 Scattering Cross Sections and Scattering Lengths

The probability of a neutron interacting with a nucleus can be expressed in terms of a cross-section, which can be thought of as an effective area presented to the neutron, usually expressed in barns, 10^{-28} m^2. The total cross-section is a sum of the absorption cross-section and the scattering cross-section. In this discussion, only the latter will be considered.

The scattering cross section is defined as the rate of reaction per nuclei in a unit of incident neutron flux, Φ

$$\sigma = \frac{[\text{Total number of neutrons scattered per unit time}]}{\Phi}. \qquad (2.22)$$

The differential scattering cross-section measures the angular dependence of scattered neutrons, giving a measure of the number of neutrons scattered by the system per second into a small solid angle, $d\theta$ in a given direction

$$\frac{d\sigma}{d\Omega} = \frac{[\text{Number of neutrons scattered per unit time into } d\Omega \text{ in direction } \theta, \phi]}{\Phi d\Omega}. \qquad (2.23)$$

The double differential cross section extends the differential cross section to measure the a final neutron energy between that of its original plus a small amount of energy gain or loss divided by the incident neutron flux.

$$\frac{d^2\sigma}{d\Omega dE'} = \frac{\left[\begin{array}{l}\text{Number of neutrons scattered per unit time into } d\Omega \text{ in} \\ \text{direction } \theta, \phi \text{ with final energy between } E' \text{ and } E' + dE'\end{array}\right]}{\Phi d\Omega dE'} \qquad (2.24)$$

31

The three cross-sections are related by integration:

$$\frac{d\sigma}{d\Omega} = \int_0^\infty \left(\frac{d^2\sigma}{d\Omega dE'}\right) dE' \tag{2.25}$$

$$\sigma = \int_{all\ directions} \left(\frac{d\sigma}{d\Omega}\right) d\Omega \tag{2.26}$$

A neutron will interact with a nucleus via both nuclear and magnetic forces. The latter is not considered in this work, whilst the former has a very short range compared to the typical neutron wavelength. The important consequence of this difference in length scales, some five orders of magnitude, means that the scattering can be considered as isotropic and can be characterised by a single parameter, b, the scattering length. The scattering length is, in general, complex, with the imaginary part corresponding to adsorption and the real part to scattering. The real part can be positive or negative, depending on the attractive or repulsive nature of the interaction.
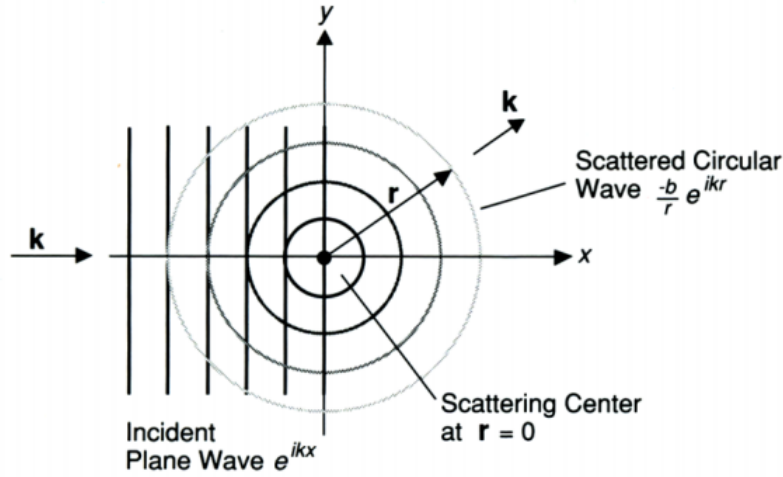
Figure 2.8: Incident plane wave scattering isotropically from a scattering center (Pynn, 2009)

32

If the nucleus is at a position $\mathbf{R}_i$ and the neutron at $\mathbf{r}$, the Fermi pseudopotential is defined

$$V(r) = \frac{2\pi\hbar^2}{m} b_i \delta(\mathbf{r} - \mathbf{R}_i). \tag{2.27}$$

Far from the nucleus, the Fermi pseudopotential causes the same scattering as the actual interaction.

Unlike X-rays, which scatter from the electrons in atoms, neutrons interact with the nucleus, meaning that different isotopes and nuclear spin states can have different scattering lengths. The interaction depends not only on the nature of the nucleus, but also on the total spin state of the nucleus-neutron system.

The average over all the isotopes and spin states is called the coherent scattering length,

$$b_i^{coh} = \langle b_i \rangle. \tag{2.28}$$

The incoherent scattering length is defined as the root mean square deviation of b_i from the average value,

$$b_i^{inc} = \left[\langle b_i^2 \rangle - \langle b_i \rangle^2 \right]^{1/2} \tag{2.29}$$

The bound cross sections are then defined as

$$\sigma_{coh} = 4\pi \langle b \rangle^2, \tag{2.30}$$

and

$$\sigma_{inc} = 4\pi \left[\langle b_i^2 \rangle - \langle b_i \rangle^2 \right]. \tag{2.31}$$

33

The coherent scattering is just the average value, and gives information about the correlation between different atoms. It is the coherent cross section that is used to describe interference effects such as diffraction. The incoherent scattering is that due to the randomness of the system and has no equivalence in X-ray scattering. It only shows interference effects between the same atom at different times. The scattering from different atoms has random phases and cancels out.

Mainly in this work the scattering nuclei of interest are hydrogen, which have a significantly larger incoherent scattering cross section than its corresponding coherent cross section. Furthermore, it is generally significantly larger than the cross sections of other elements. This means that neutron scattering is an ideal tool to observe the motion of hydrogen in a scattering system.

Nucleus	σ_{inc}	σ_{coh}
H	80.2	1.8
D	2.0	5.6
Pd	0.093	4.39
V	0.018	5.08
Zr	0.02	6.44

Table 2.1: Coherent and incoherent scattering cross sections for the elements of interest in this work

Deuterium's (D) cross sections are also shown in Table 2.1. D has has uses in structural studies, due to the fact that hydrogen has a particularly large incoherent scattering cross section, and thus produces a background that makes analysis difficult.

2.3.2 Elastic Scattering

If there is no energy transferred between a neutron and the scattering system the resulting scattering is known as elastic. For neutrons, which have energies similar to atomic and molecular transitions, elastic scattering is often approximated by effectively integrating over all energies for a given angle, as per Eqn. (2.25). If the scattering system is an ordered structure, elastic scattering would result in a strong, well defined Bragg peaks.

In order to describe the scattering process, it is necessary to consider the initial, k and final, k', states of the neutron. Here, if both the incident and the scattered neutrons can be considered as plane waves, the differential cross section is the absolute square of the Fourier transform of the potential. For a single nucleus, this gives

$$\frac{d\sigma}{d\Omega} = \left(\frac{m}{2\pi\hbar^2}\right)^2 |\langle \mathbf{k}'|V|\mathbf{k}\rangle|^2 = \left(\frac{m}{2\pi\hbar^2}\right)^2 \left|\int V(\mathbf{r})e^{i\mathbf{Q}\cdot\mathbf{r}}dr\right|^2. \qquad (2.32)$$

For a collection of nuclei, and inserting the Fermi pseudopotential,

$$\frac{d\sigma}{d\Omega} = \sum_{i,j} b_i b_j e^{i(\mathbf{Q}\cdot(\mathbf{R}_i - \mathbf{R}_j))}. \qquad (2.33)$$

Under the assumption that there is no coupling between the scattering length of each nucleus and its position, the average can be performed independently of the spin states and on the nuclear locations, and we can seperate into coherent and incoherent terms

$$\frac{d\sigma}{d\Omega} = \frac{N}{4\pi} \left[\sigma_{inc} + \sigma_{coh} \sum_{i,j} e^{i(\mathbf{Q}\cdot(\mathbf{R}_i - \mathbf{R}_j))} \right]. \qquad (2.34)$$

The coherent cross section is then related to $S(\mathbf{Q})$.

$$\left(\frac{\partial \sigma}{\partial \Omega}\right)_{coh} = \frac{\sigma_{coh}}{4\pi} N S(\mathbf{Q}).$$ (2.35)

2.3.3 Inelastic Scattering

Inelastic neutron scattering (INS) can occur from a range of processes across several orders of magnitude in energy, as shown schematically in Fig. 2.9.
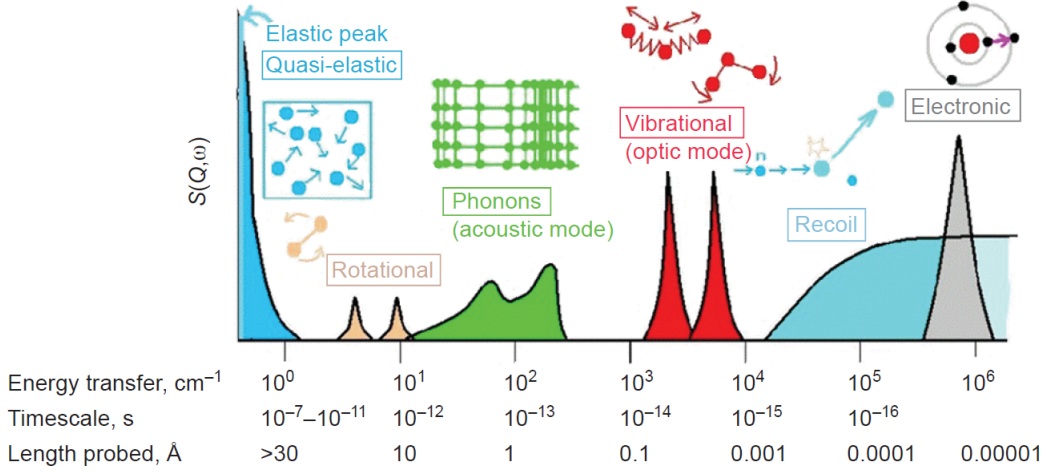
Figure 2.9: The types of scattering associated with Inelastic neutron scattering with their respective time and energy ranges (Parker and Collier, 2016)

INS from molecular vibrartions, both optical and acoustic, occurs when 'thermal neutrons', typically in the energy range of 10-100 meV, are used (Giustino, 2014). Here, quanta of energy are transferred between the incident neutron and system; the scattered neutron will have either a gain or loss in energy. This type of scattering is used to for vibrational spectroscopy.

The double differential cross section, by analogy with Eqn. (2.32), can be written (Van Hove, 1954).

36

$$\frac{\partial^2 \sigma}{\partial \Omega \partial \omega} = \frac{k'}{k} \frac{1}{2\pi} \sum_i \sum_j \int_{-\infty}^{\infty} \langle b_i b_j \exp\left(i\mathbf{Q} \cdot \mathbf{R}_i(t)\right)$$

$$\exp\left(-i\mathbf{Q} \cdot \mathbf{R}_j(0)\right)\rangle \exp\left(-i\omega t\right) dt \quad (2.36)$$

A derivation is not given here, but a good account is given by Bée (1988). Again, assuming no coupling between scattering length and position, the expression can be broken down into a coherent and an incoherent part

$$\frac{\partial^2 \sigma}{\partial \Omega \partial \omega} = \left(\frac{\partial^2 \sigma}{\partial \Omega \partial \omega}\right)_{coh} + \left(\frac{\partial^2 \sigma}{\partial \Omega \partial \omega}\right)_{inc}. \quad (2.37)$$

In the case of a single isotope, the double differential cross section can be written

$$\frac{\partial^2 \sigma}{\partial \Omega \partial \omega} = \frac{1}{4\pi N} \frac{k'}{k} \left[\sigma_{coh} S(\mathbf{Q}, \omega) + \sigma_{inc} S(\mathbf{Q}, \omega)\right]. \quad (2.38)$$

The scattering functions are the temporal Fourier transforms,

$$S(\mathbf{Q}, \omega) = \frac{1}{2\pi} \int_{-\infty}^{\infty} I(\mathbf{Q}, t) \exp(-i\omega t) dt, \quad (2.39)$$

and

$$S_{inc}(\mathbf{Q}, \omega) = \frac{1}{2\pi} \int_{-\infty}^{\infty} I_{inc}(\mathbf{Q}, t) \exp(-i\omega t) dt. \quad (2.40)$$

The corresponding intermediate scattering functions are

$$I(\mathbf{Q}, t) = \frac{1}{N} \sum_i \sum_j \langle \exp\left(i\mathbf{Q} \cdot \mathbf{R}_i(t)\right) \exp\left(-i\mathbf{Q} \cdot \mathbf{R}_j(0)\right)\rangle, \quad (2.41)$$

and

$$I_{inc}(\mathbf{Q}, t) = \frac{1}{N} \sum_i \langle \exp\left(i\mathbf{Q} \cdot \mathbf{R}_i(t)\right) \exp\left(-i\mathbf{Q} \cdot \mathbf{R}_i(0)\right) \rangle . \qquad (2.42)$$

Finally, we can take a further Fourier transform in space, to give the time dependent pair correlation functions

$$G(\mathbf{r}, t) = \frac{1}{(2\pi)^3} \int I(\mathbf{Q}, t) \exp(-i\mathbf{Q} \cdot \mathbf{r}) d\mathbf{Q} \qquad (2.43)$$

$$G(\mathbf{r}, t) = \frac{1}{N} \sum_i \sum_j \int \langle \delta\left(\mathbf{r}' - \mathbf{R}_i(0)\right) \delta(\mathbf{r}' + \mathbf{r} - \mathbf{R}_j(t)) \rangle \, d\mathbf{r}' \qquad (2.44)$$

$$G_S(\mathbf{r}, t) = \frac{1}{(2\pi)^3} \int I_{inc}(\mathbf{Q}, t) \exp(-i\mathbf{Q} \cdot \mathbf{r}) d\mathbf{Q} \qquad (2.45)$$

$$G_S(\mathbf{r}, t) = \frac{1}{N} \sum_i \int \langle \delta\left(\mathbf{r}' - \mathbf{R}_i(0)\right) \delta(\mathbf{r}' + \mathbf{r} - \mathbf{R}_i(t)) \rangle \, d\mathbf{r}' \qquad (2.46)$$

The expression given here for the pair correlation functions involve positional operators, which in general do not commute, except for $t = 0$. However, under the assumption that we can treat the system classically, the expressions in Eqn. 2.18 are recovered.

Both the *total* and *self* correlations functions considered in the previous section can be related to two forms of scattering function produced from QENS, the *coherent* scattering function and *incoherent* scattering function respectively.

When considering the total pair correlation function $G(\mathbf{r}, t)$ the Fourier transform in both space and time yields the coherent scattering function,

$$S_{coh}(\mathbf{Q}, \omega) = A \int_{-\infty}^{\infty} \int_{\mathbf{r}} G(\mathbf{r}, t) e^{i(\mathbf{Q} \cdot \mathbf{r} - \omega t)} d\mathbf{r} dt. \qquad (2.47)$$

On the other hand the *self* correlation function $G_s(\mathbf{r}, t)$ is related to the *incoherent* scattering function,

$$S_{inc}(\mathbf{Q}, \omega) = A \int_{-\infty}^{\infty} \int_{\mathbf{r}} G_s(\mathbf{r}, t) e^{i(\mathbf{Q} \cdot \mathbf{r} - \omega t)} d\mathbf{r} dt. \qquad (2.48)$$

2.3.4   Quasi-Elastic Neutron scattering

Quasi elastic neutron scattering originates from interactions with particles diffusing over a time scale of about 10^{-10} to $10^{-12} s$. This corresponds to energy transfer ranges in the range $\pm 2 meV$, producing a broadening of the elastic line.

Fig. 2.10 is a (highly) schematic representation of scattering from different processes in a simple interstitial metallic hydride, such as PdH_x. In a real system, the features would be convolved with the instrumental resolution. The top figure is over the larger energy-transfer range, where optical vibrational peaks can be seen at $\pm 58 meV$. At lower energy transfers, an intensity arriving from the acoustic phonon modes of the host lattice is shown. This will typically be much weaker than the signal from the hydrogen. Finally, one can see the elastic peak at zero energy transfer. Quasi-elastic broadening is also shown in red, but is barely discernible from the elastic peak. The bottom plot in Fig. 2.10 is zoomed-in, and clearly quasi-elastically broadened signal, which is Lorentzian in form.
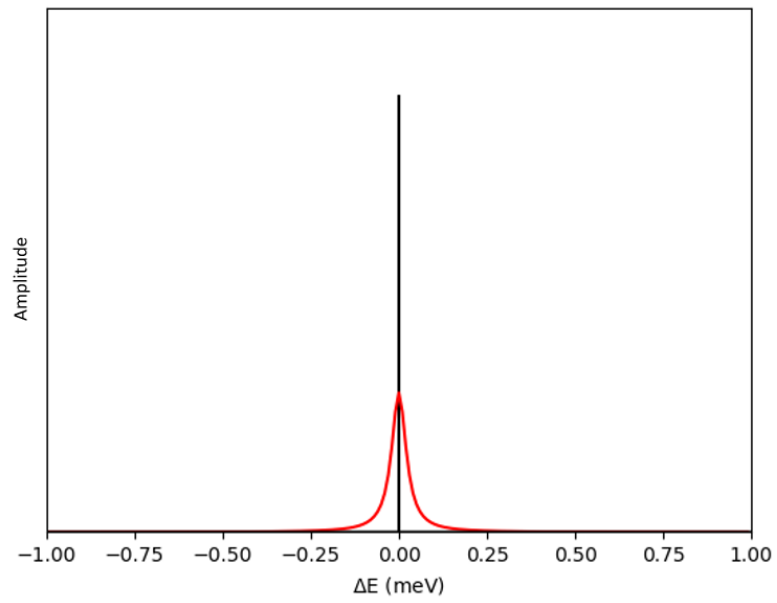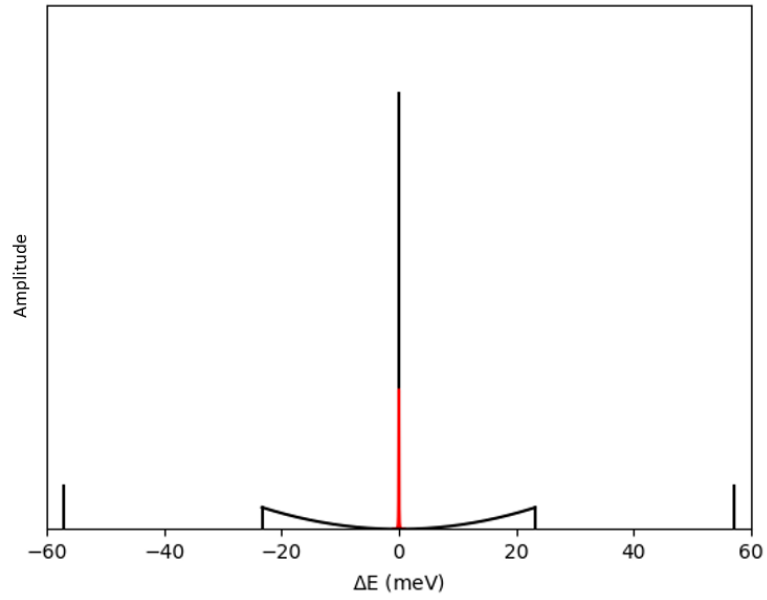
Figure 2.10: Schematic of neutron scattering from an interstitial metallic hydride. Energy values are representative of PdH_x

When the motion of particles is unrestricted and purely long range i.e. the absence of trapping sites, such as in hydrogen in metals, only the quasi-elastic broadening will be observable with no elastic peak from hydrogen. However, if this motion is spatially confined by geometry, i.e. by site blocking effects or for hydrogen rotation in a molecular complex, the resulting scattering function will be a combination of the elastic δ-function and the quasi-elastic components. The scattering functions and corresponding intermediate scattering functions arising from translational and from localised diffusion are shown schematically in Fig. 2.11.
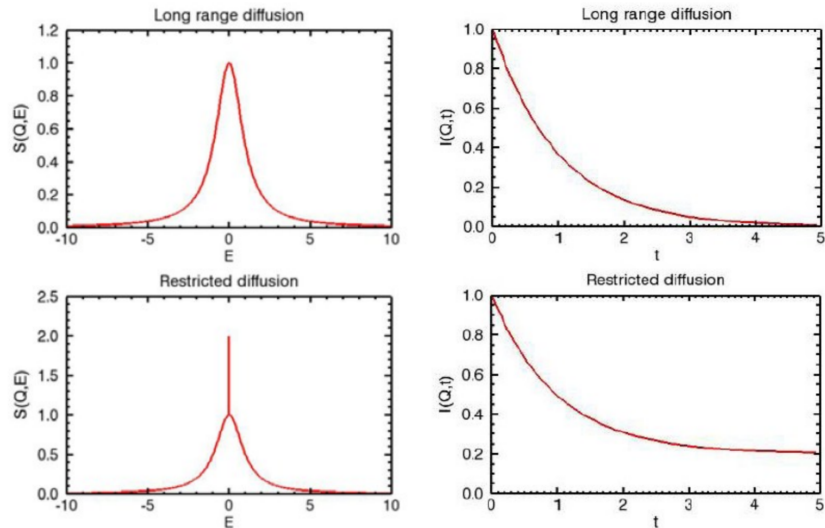
Figure 2.11: Schematic of the long range and restricted diffusion scattering functions with the intermediate function, from a Fourier transform in time. (Demmel, 2013)

QENS is sensitive to the instrumental energy resolution, related to the time scale in which the motion is taking place by the Heisenberg uncertainty principle. As a result, the slower the motion of diffusing atoms, the higher a resolution is required. If motion occurs within the available energy-transfer window, typically $10^{-3} - 10^{-8}$ m^{-1}, the δ-function (elastic peak) will become

quasi-elastically broadened. This would correspond to particle motion on a time scale between $10^{-8} - 10^{-13}$ seconds.

2.4 Analytical Models for QENS

The first analytical model of QENS was given by Chudley and Elliott (1961), which relates to self diffusion in the low concentration limit. This was generalised to non-Bravais lattices by Rowe et al. (1972). Ross and Wilson (1978) considered the expression for the coherent scattering function from collective diffusion, the main result being that the quasi-elastic broadening, $f(\mathbf{Q})$ is independent of concentration. Sinhar and Ross (1988) extended this to include the effects of inter-particle interactions in the mean-field limit using linear response theory. Barnes (1973) provided a generalised model describing the case of a particles diffusing amongst sites on a circle, producing a corresponding spatially bound scattering function including both a quasielastic and an elastic contribution.

2.4.1 QENS from Translational Diffusion

An expression for the time evolution of the probability of site occupancy was presented by Chudley and Elliott via a differential equation. If the diffusion occurs on a Bravais lattice, the rate of change of occupational probability, $P(\mathbf{r}, t)$, between site $\mathbf{r}$ and the neighbour site $\mathbf{r} + \mathbf{l}$ can be written

$$\frac{\partial P(\mathbf{r}, t)}{\partial t} = \frac{1}{n\tau} \Sigma_l \left[P(\mathbf{r} + \mathbf{l}, t) - P(\mathbf{r}, t) \right], \qquad (2.49)$$

where τ is the mean residency time, which is assumed the same for all sites, and the summation is over the set of vectors linking a site to its nearest

neighbours. In the model, the initial condition is such that $P(\mathbf{r}, 0)$ is a δ-function at $\mathbf{r} = 0$

$$P(\mathbf{r}, 0) = \delta(\mathbf{r}). \tag{2.50}$$

Note that, in this case, $P(\mathbf{r}, t)$ is equivalent to the self pair-correlation function $G_s(\mathbf{r}, t)$.

Solution of Eqn. (2.49) is best approached by Fourier transform. This can be performed in two steps, firstly to obtain the intermediate scattering function,

$$I_{inc}(\mathbf{Q}, t) = \int_{\mathbf{r}} G_s(\mathbf{r}, t) e^{i\mathbf{Q}\cdot\mathbf{r}} d\mathbf{r}, \tag{2.51}$$

which when applied to Eqn. (2.49) gives

$$\frac{\partial I_{inc}(\mathbf{Q}, t)}{\partial t} = \frac{1}{n\tau} \sum_l \left[e^{-i\mathbf{Q}\cdot\mathbf{l}} I_{inc}(\mathbf{Q} + \mathbf{l}, t) - I_{inc}(\mathbf{Q}, t) \right]. \tag{2.52}$$

The solution is

$$I_{inc}(\mathbf{Q}, t) = e^{-f(\mathbf{Q})t}, \tag{2.53}$$

where $f(\mathbf{Q})$ is the decay constant.

$$f(\mathbf{Q}) = \frac{1}{n\tau} \Sigma_l \left(1 - e^{-i\mathbf{Q}\cdot\mathbf{l}} \right). \tag{2.54}$$

A further Fourier transform in time yields the scattering function, which has the form of a Lorentzian with a half width half maximum (HWHM) that is given by the decay constant in Eqn. (2.54).

$$S_{inc}(\mathbf{Q}, \omega) = \frac{1}{\pi} \frac{f(\mathbf{Q})}{f^2(\mathbf{Q}) + \omega^2} \tag{2.55}$$

Eqn. 2.55 is equivalent to Eqn. 2.12 with $f(\mathbf{Q}) = [\mathbf{1} - \mathbf{F}(\mathbf{Q})]/\tau$.

For jump diffusion on an fcc lattice, the expression for $f(\mathbf{Q})$ becomes (Appendix C):

$$f(\mathbf{Q}) = 1 - \frac{1}{3}(\cos(\pi Q_x)\cos(\pi Q_y)$$
$$+ \cos(\pi Q_x)\cos(\pi Q_z)$$
$$+ \cos(\pi Q_y)\cos(\pi Q_x)) \quad (2.56)$$

Where,

$$\mathbf{Q} = \frac{2\pi}{a}(Q_x, Q_y, Q_z) \quad (2.57)$$

For the most part, however, samples used in scattering experiments are not single crystals, but are in fact polycrystalline. The scattering arrising from a polycrystalline sample can be represented by taking the spherical average of $f(\mathbf{Q})$ from Eqn. 2.55.

$$f(Q) = \frac{1}{4\pi\tau} \int_0^{2\pi} \int_0^{\pi} [1 - \exp(-i\mathbf{Q} \cdot l)] \sin\theta d\theta d\phi, \quad (2.58)$$

with the solution,

$$f(Q) = \frac{1}{\tau}\left[1 - \frac{\sin(Ql)}{Ql}\right]. \quad (2.59)$$

Eqn. 2.56 is plotted in Fig. 2.12 in various high symmetry directions, along with the corresponding spherical averaged version.

44
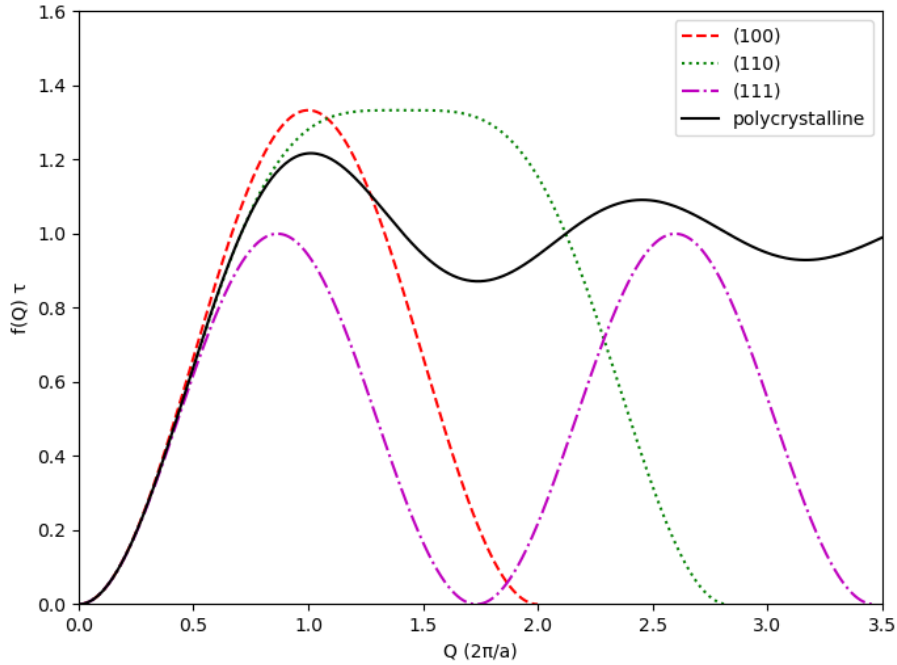
Figure 2.12: f($\mathbf{Q}$) for nearest neighbour jumps on an fcc lattice along three high symmetry paths compared with the Chudley and Elliot model and the spherically averaged (polycrystalline) version

Fig. 2.12 shows $f(\mathbf{Q})$ for nearest neighbour jumps on an fcc lattice along three directions in reciprocal space for a single crystal Eqn. (2.56) and for the spherically averaged case. Eqn. (2.59). It is important to note that Eqns. (2.54) and (2.59) are only valid in the limit of zero particle concentration. At finite concentrations, $f(\mathbf{Q})$ will be reduced by a factor of $(1 - c)$ due to site-blocking of neighbouring sites; this factor is the probability of a given neighbouring site being vacant. In addition to this there is a correlation effect due to the probability of a particle performing a jump back to the same site that it just left, known as the tracer correlation function, $f_t(c)$.

45

2.4.2 QENS from Spatially Restricted Diffusion

Spatially restricted motion can be present in systems where the number of available sites to diffuse over is reduced to a finite amount via either the presence of trapping sites or concentration related site blocking for example.

A case of this can be seen in C15 Laves phase systems such as ZrV_2, which shall be detailed in a proceeding chapter. A diffusing species i.e. Hydrogen can perform a combination of translational (long-range) and spatially restricted (short-range) motion due to variations in barrier heights along its diffusion path (Skripov et al., 1996).

If the diffusion occurring is indeed spatially restricted, this will result in an elastic contribution to the incoherent scattering function $S_{inc}(\mathbf{Q}, \omega)$. Barnes (1973) gave a formalisation of this spatially restricted motion with the circular random walk model describing the probability of finding a particle at a site after n steps on a circle of N sites around which the particle is allowed to preform a random walk.

$$S_{inc}(Q, \omega) = A_0(Q)\delta(\omega) + \sum_{l=1}^{N} A_l(Q)\frac{1}{\pi}\frac{\tau_l}{1 + \omega^2\tau_l^2} \tag{2.60}$$

For the case of two sites, this reduces to

$$S_{inc}(Q, \omega) = A_0(Q)\delta(\omega) + A_1(Q)\frac{1}{\pi}\frac{\tau}{1 + \omega^2\tau^2} \tag{2.61}$$

with

$$A_0 = \frac{1}{2}\left[1 + j_0(2Qd)\right] \tag{2.62}$$

$$A_1 = \frac{1}{2}\left[1 - j_0(2Qd)\right] \tag{2.63}$$

Here, $j_0(x)$ is a spherical Bessel function of zero order and d is the jump distance between the two sites. $A_0(Q)$ and $A_1(Q)$ represent the elastic and quasi-elastic amplitudes, respectively. Note that the quasi-elastic broadening is independent of Q, even though its amplitude depends on Q.

For 4 sites and above, there is more than one Lorentzian contribution. Whilst each of these components is independent of Q, the amplitudes are Q dependent, and so the effective width of the composite quasi-elastic scattering function shows a Q dependence at higher values of Q, but tends to a constant, non-zero value at low Q. This contrasts with long-range diffusion, for which the Q dependent with goes to zero at low Q. Fig. 2.13 shows the quasi-elastic widths for jumps amongst N sites.
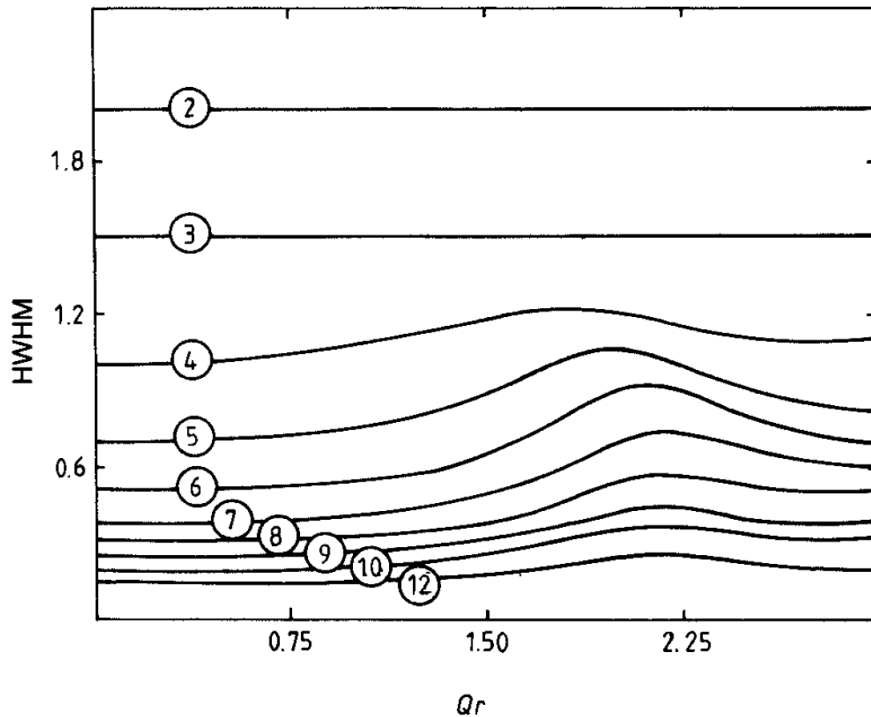
Figure 2.13: Quasi-elastic broadening resulting from localised diffusion over a number of restricted sites (Bée, 1988)

Considering the form of the intermediate scattering function, if the particle is allowed to diffuse freely the intermediate scattering function would decay to 0 in the limit of $t = \infty$. However, if there are only a finite number of sites available to the diffusing particle then $I_{inc}(\mathbf{Q}, \infty)$ will be a finite value as a result of the elastic contribution.

The spatially restricted incoherent intermediate scattering function then takes the form,

$$I_{inc}(Q, t) = A_0(Q) + A_1 \sum_{l=1}^{N} A_l(Q) \exp\left(2t/\tau_l\right) \tag{2.64}$$
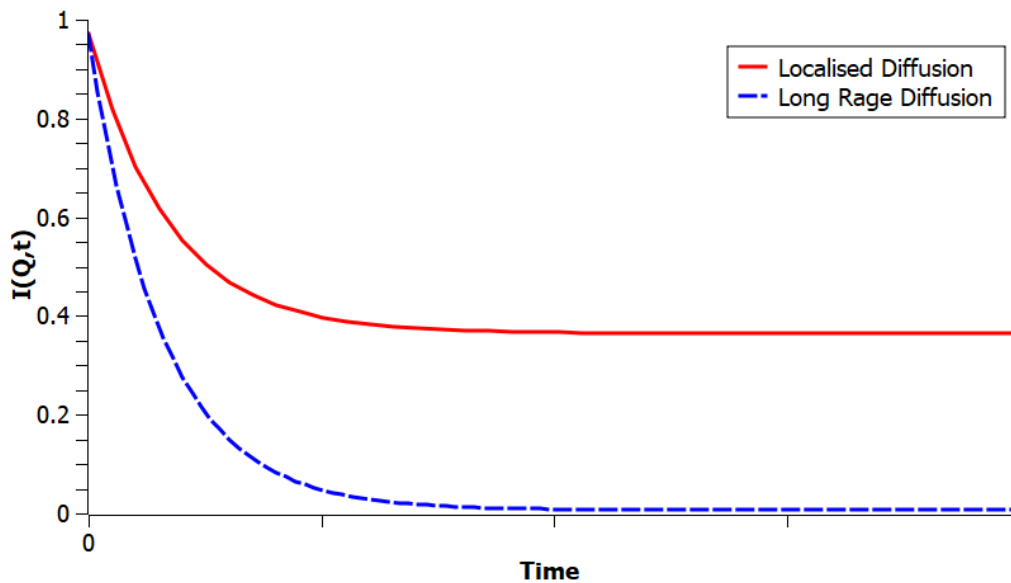
Figure 2.14: Form of the localised and long-ranged intermediate scattering functions

The the term $A_0(\mathbf{Q})$ is the elastic incoherent structure factor (EISF), which can yield information about the nature of the jumps in spatial restricted diffusion via its Q dependence. Fig. 2.15 shows the EISF for jumps among N sites. Of interest in this work is the two-site model, in relation to

PdH$_x$, and the six-site model, in relation to hydrogen diffusion among sites in a hexagon in Laves-phase intermetallic compounds, the EISF of which is

$$EISF = \frac{1}{6}[1 + 2j_0(Qr) + 2j_0(Qr) + 2j_0(Qr\sqrt{3}) + j_0(2Qr)] \qquad (2.65)$$
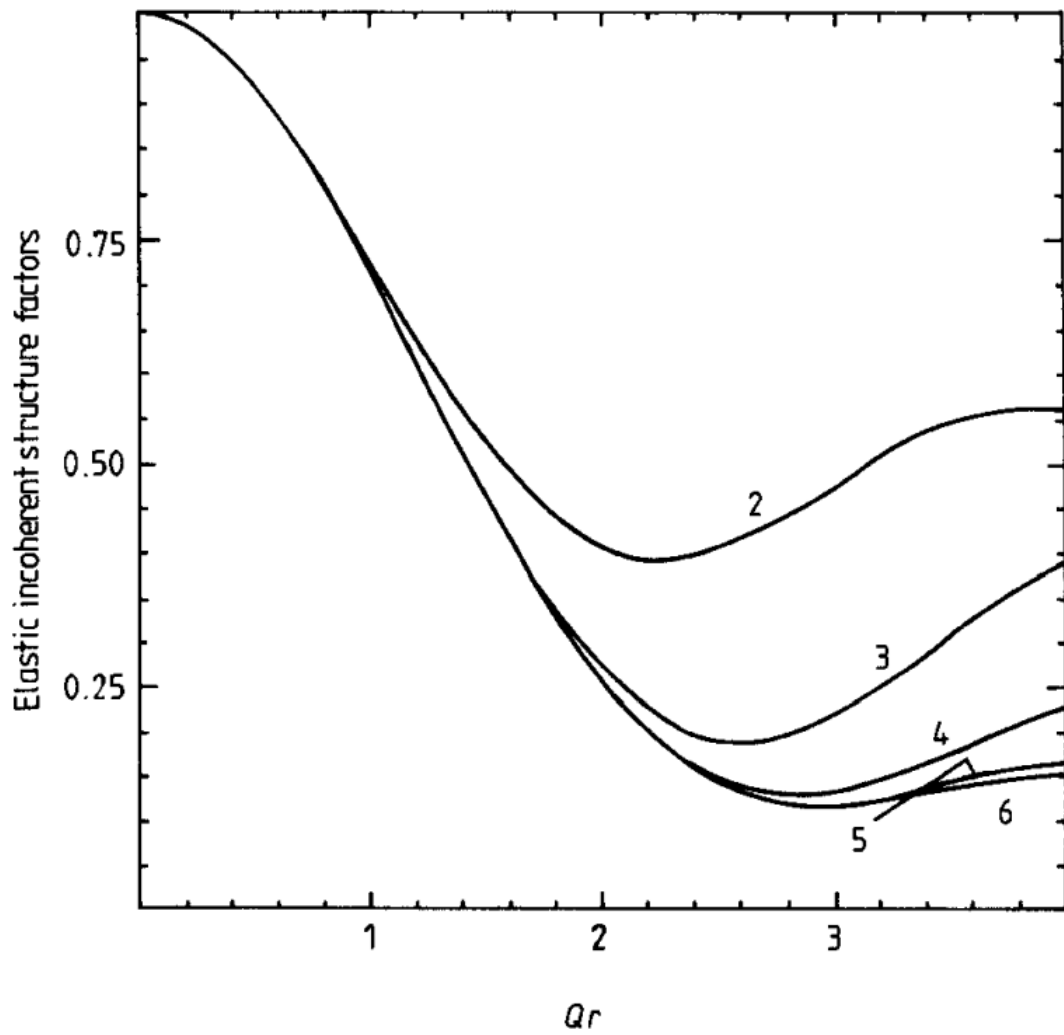
Figure 2.15: EISF for jump models over N sites spaced equally on a circle. (Bée, 1988). The number of sites on each respective circle is given on the the corresponding curve.

Chapter 3

Monte-Carlo Simulation of Diffusion In a Lattice Gas

The idea of the Monte-Carlo simulation was first proposed as a possible statistical approach to solving the problem of neutron diffusion in fissionable material during the Manhattan Project (Metropolis, 1989). In its most general sense, a Monte-Carlo simulation uses computer-generated pseudo-random numbers in order to simulate stochastic processes in physical systems. A particularly powerful application of the Monte-Carlo method provides a means of approaching multi-dimensional integrals that are not practically solvable by conventional methods; this method can be employed to approximate the partition function of multi-particle systems, and hence to calculate thermodynamic observables.

3.1 Performing Monte-Carlo Simulations

In order to produce a pair correlation function for a lattice gas, the system is labelled in terms of occupation numbers,

$$\sigma_\alpha(p) = \begin{cases} 1, & \text{if site p is occupied by a particle of type } \alpha \\ 0, & \text{otherwise.} \end{cases} \tag{3.1}$$

If there is only one type of particle present in the lattice gas, in the present case hydrogen, the subscript α can be dropped. The sum of the occupation numbers over all sites is equal to the number of particles in the system. The concentration of particles, c, is thus

$$c = \frac{1}{N} \sum_p \sigma(p) \tag{3.2}$$

It is often useful to distinguish between different types of site. For example, in the case of hydrogen in palladium, a distinction can be made between the octahedral sites and the tetrahedral sites. In addition, one might wish to distinguish between different geometrically nonequivalent sites, for example in PdH there is an O site and two T sites per primitive cell in the Fm3m space group. Here, the index β is used to label different site types, or sub lattices.

It is useful to define the fraction of particles on each sublattice

$$f_\beta = \frac{n_{atoms,\beta}}{n_{atoms}}, \tag{3.3}$$

as well as the concentration of site type β,

$$c_\beta = \frac{f_\beta c}{f_{sites,\beta}}. \tag{3.4}$$

Here the term $f_{sites,\beta}$ represents the fraction of the total sites that are of the same type, β.

3.1.1 The Metropolis Algorithm

For the canonical ensemble (fixed N, V and T), the general idea behind the Monte-Carlo method in statistical mechanics is that partition functions, and hence observable thermodynamic quantities, are estimated by sampling a representative set of configurations, rather than explicitly performing integration. The obvious approach to doing this would be to generate multiple configurations at random along with their associated Boltzmann weights, $e^{-E/k_B T}$, in an attempt to approximate the desired observable quantity. This algorithm, however, can be very inefficient, as it includes numerous configurations that have a very low statistical weight. A more efficient way, known as importance sampling, is to generate random configurations according to the probability distribution $Ae^{-E/k_B T}$ itself and assign an even weighting to each. The practical implementation of this approach has become known as the Metropolis Algorithm (Metropolis et al., 1953):

1. An atom is selected at random;

2. A vacant target site is chosen at random from an allowed subset of sites;

3. The transition probability associated with moving the atom is calculated, $T(x \rightarrow x') = min\{1, e^{-\Delta E/k_B T}\}$;

4. The trial configuration is accepted if a random number selected in the range $\{0, 1\}$ is less than the calculated transitional probability.

3.1.2 Ballistic and Jump Diffusion

In terms of the selection of a vacant site, there are two principle methods:

1. Ballistic Diffusion: A particle can move to any vacant site in that lattice even if this jump is unphysical in its nature, this is only of interest if we wish to generate a set of successive un-correlated configurations of a system with a minimum of pair exchanges.

2. Jump Diffusion: The purpose of jump diffusion is to actually simulate a physically meaningful diffusion process. Here the selection of allowed sites are smaller and normally corresponds to allowed diffusion paths, made up by nearest neighbour sites, giving a physical meaning to the system being simulated.

3.1.3 Monte-Carlo Cycles: Attempted and Successful Jumps

A unit often used in Monte Carlo simulations is the Monte Carlo Cycle (MCC), in which the number of generated configurations is counted relative to the number of atoms. Here, successive configurations can either be defined in terms of attempted or successful transitions, depending on the type of system being simulated:

If diffusion is being simulated, then attempted transitions (particle jumps) are used. If a particle tries to jump but is unable to do so successfully due to either site blocking effects or the jump probabilities, the original configuration

is counted as a step in the MCC. In other words, the MCC is defined as when each particle has attempted to jump once. Thus, over many MCC's, on average, each atom will have attempted to jump once. This allows a link to timescales in real systems, whereby the MCC can be mapped onto attempt frequencies, which is essentially the pre-exponential factor in an Arrhenius expression for the temperature dependent jump rate.

If one is only interested in the thermodynamic properties, then successful jumps are more appropriate. Here, a new configuration is only counted if the particle has moved from its origin sites from the previous configuration. For successful jumps, the MCC is not associated with a real timescale. In this scheme, the MCC is defined such that the number of new configurations per cycle is equal to the number of atoms.

3.1.4 Populating the Lattice and Reaching Equilibrium

Generally, at the beginning of a Monte-Carlo simulation, a number of cycles are performed in order to reach an equilibrium state, or a steady-state; this is especially important if the lattice is populated at random initially. This is referred to in this work as the 'burn-in' period. Here, care needs to be taken. A particular case in hand is when jump diffusion occurs over barriers. An example used in this work is H diffusion in Pd, where there a different transition probability from T to O sites than for O to T sites. Fig. 3.1 shows the effects of the various combinations of jump / ballistic diffusion and attempted / successful jumps, starting from random occupancy.

54
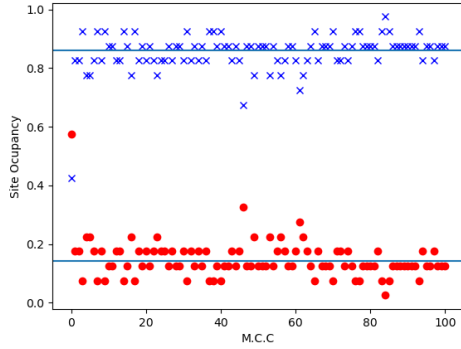
(a) Jump Diffusion Successful Jumps
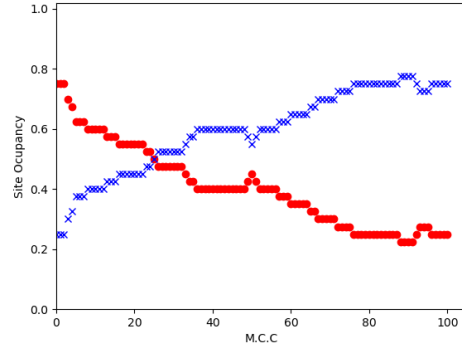
(b) Jump Diffusion Attempted Jumps
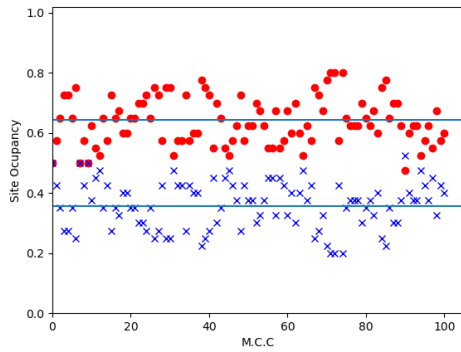
(c) Ballistic Successful Jumps
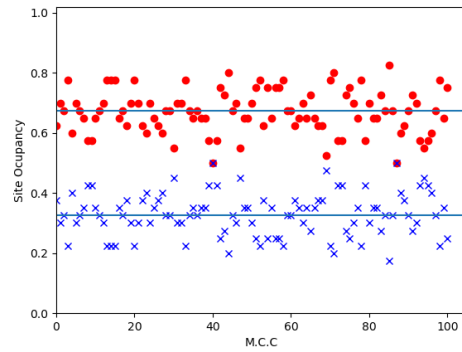
(d) Ballistic Attempted Jumps

Figure 3.1: Occupation of Octahedral and Tetrahedral sites in an face centered cubic lattice for the Jump and Ballistic diffusion

The solid lines in each plot of Fig. 3.1 show the average occupation for each of the two sites between 20 and 100 Monte-Carlo cycles (per atom) to be executed in the static Canonical Ensemble simulation after the lattice has been filled, used for the simulation to be in a steady state before the main simulation is carried out. The method of jump diffusion where a particle movement is only counted if the jump is successful can be seen to give the best approximation of equilibrium site occupation after a 100 cycle 'burn in' time.

3.2 The GRT Code

Pre-existing code for the extraction of pair-correlation functions from Metropolis Monte-Carlo simulations of particle diffusion in lattice gas systems (Bull, 2001) has been used and extended in this work. In section 3.2.1 the working of the code, at the time of writing, is described. In section 3.2.2, details are given of the various extensions to the code made by the present author.

3.2.1 Description of the Code

The name GRT is intended to represent the function G(r,t), being inspired by the QENS data analysis software SQW formerly in use at the Institute Laue Langevin neutron facility in Grenoble, France. The GRT code was extended from the DEVIL code, originally developed at Harwell, UK, to perform static relaxation of crystals containing defects (Thetford, 1989). The GRT code is used to preform simulations of dynamic and static processes in a lattice gas system, resulting in the calculation of correlation functions for a given system of interacting particles. The main function of this code is represented schematically in Fig. 3.2.

The code has been further extended in this work to allow for the calculations of the pair correlation functions by considering the allowed jump paths used with either jump probabilities specified or probabilities determined by the barrier heights between sites.
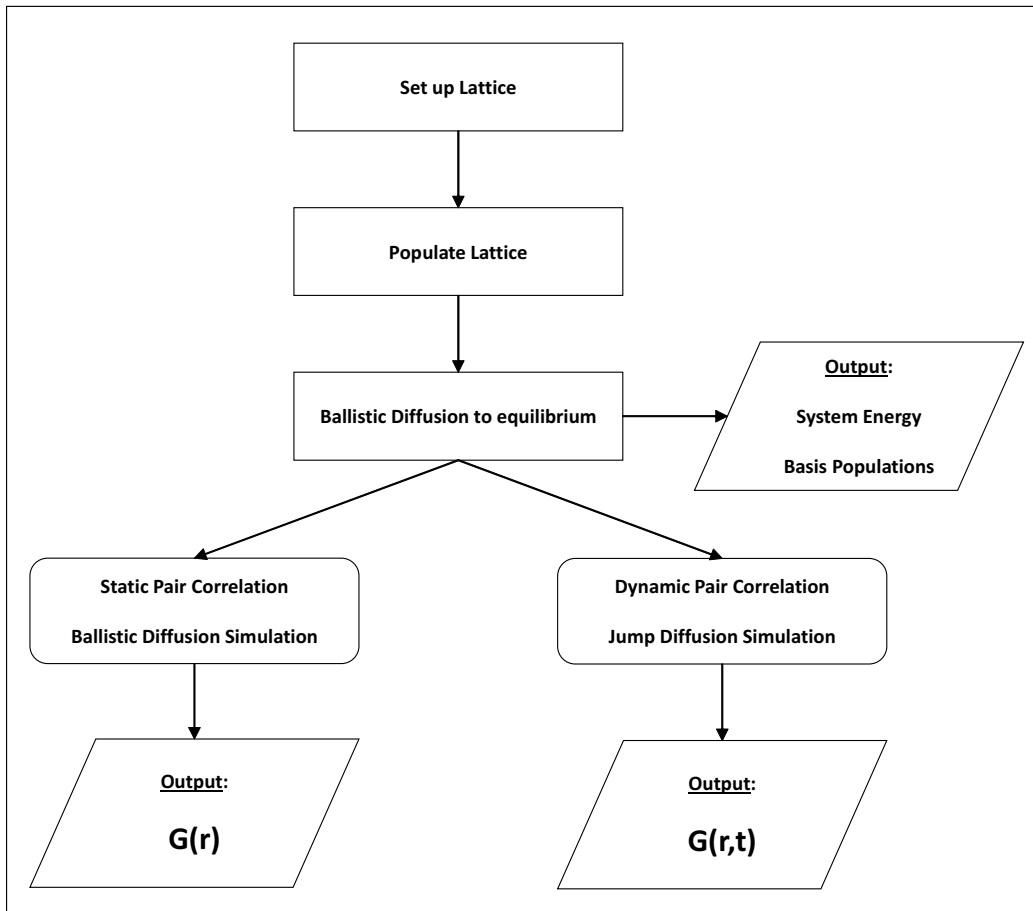
Figure 3.2: Diagram showing the basic function of the GRT-program

The structure of the code can be broken down into three main sections. Firstly, the positions of the lattice sites, jump vectors and the vectors for the pair-correlation function are determined, including the effects of periodic boundary conditions. Secondly, the lattice is populated to the required concentration, and burn-in simulation is performed to take the system to equilibrium. Finally, the main simulation is run, either to calculate the static or dynamic pair correlation function. All the parameters for each of these processes are passed to the code via an input file. A more detailed description of each step in the code will be given below with the relative part of the input

file used.

Setting Up a Lattice

```
XLAT(1,1), XLAT(2,1), XLAT(3,1)
XLAT(1,2), XLAT(2,2), XLAT(3,2)
XLAT(1,3), XLAT(2,3), XLAT(3,3)
NBAS
     XBAS(1), YBAS(1), ZBAS(1), LBAS(1)
     ⋮
     XBAS(NBAS), YBAS(NBAS), ZBAS(NBAS), LBAS(NBAS)

XMI(1,1), XMI(2,1), XMI(3,1)
XMI(1,2), XMI(2,2), XMI(3,2)
XMI(1,3), XMI(2,3), XMI(3,3)
NFX, NFY, NFZ
```

Figure 3.3: Section of the input file to the FORTRAN code GRT that deals with setting up the lattice

The first part of program (actually the last part of the input file) relates to setting up the lattice, the structure of which is shown in Fig. 3.3. The first three lines, XLAT(I,J), are the lattice vectors defining the unit cell. This is followed by the number of basis sites, NBAS, and a list of the relative positions in the unit cell, XBAS, YBAS and ZBAS, and an integer denoting the type of site, LBAS. The next three lines, XMI(I,J), are the lattice block axes. The final values, NFX etc., represent the size of the lattice in terms of the number of unit cells; negative values result in periodic boundary conditions in that particular direction.

Populating the Lattice and Reaching Equilibrium

The part of the input file relating to populating the lattice and performing the burn-in simulation is shown in Fig. 3.5. The first three lines are: the name of the output file, the lattice parameter in Å and the temperature in K. This is followed by details of the number of site types and their respective energies. The inter-particle interactions are handled either by a stepped potential chosen by the key word 'SHELLS' or a Thomas-Fermi screened Coulombic interaction.

The next set of parameters deal with populating the lattice, either via a previous configuration (FILLPREV), a random configuration of atoms up to the required concentration 'c' (FILLRAN), or using a grand canonical ensemble with a specified chemical potential and number of attempted particle exchanges (FILLGCE). The latter option is generally used for simulating pressure-composition absorption isotherms, where an external gas-pressure can be related to the chemical potential. This option is not used in this work.

The next step is to calculate the average configurational energy of the system and the site occupancy fractions - both the fraction of atoms in each crystallographic basis and the fraction of atoms on each site type, according to Eqns. 3.3 and 3.4. This process is carried out by selecting 'CE' in the input file and the results are written to a dedicated output file. The original method was to use ballistic diffusion and successful jumps. However, it was necessary in the present work to have the flexibility to change this to allow jump diffusion. At the time of writing, this was hard coded into the GRT program, but will be incorporated into the input file in due course.

```
outfile [string]
apar [float]
temp [float]

nsite [int]
     siten(1) [float]
     ⋮
     siten(nsite) [float]


inttype [string: SHELLS, TFERM]

<IF SHELLS>
     nshells [int]
          rshell(1) [float], v(1) [float]
          ⋮
          rshell(nshells) [float], v(nshells) [float]
<IF TFERM>
     rscreen [float], cutoff [float]

fill [string: FILLPREV, FILLRAN, FILLGCE]
<IF FILLPREV>
     enin [float]
<IF FILLRAN>
     c [float]
<IF FILLGCE>
     gcedump [string]
     chempot [float]
     nswap [int]

cesim [string: CE, NOCE]
<IF CE>
     inconf [int]
     enfile [string]

cdump [string: DUMP, NODUMP]
<IF DUMP>
     confout [string]
```

Figure 3.4: Section of the input file to the FORTRAN code GRT that deals with populating the lattice and running an initial simulation to approach equilibrium

Simulation of Diffusion

```
grtsim [string: GRT, NOGRT]
<IF GRT>
      datfile [string]
      datatype [string: FORMAT, NO FORMAT]
      radgr [float]
      maxsamp [int]
      timerat [float]
      istat [string: STATIC, DYNAMIC]
      njt [int]
          jump1(1) [int], jump2(1) [int], r_min(1) [float], r_max(1) [float],
              r_tor(1) [float], r_en(1) [float]
          ⋮
          jump1(njt) [int], jump2(njt) [int], r_min(njt) [float], r_max(njt) [float],
              r_tor(njt) [float], r_en(njt) [float]

      ntmax [int]
      inc [string: TOTAL, SELF]
```

Figure 3.5: Section of the input file to the FORTRAN code GRT that deals running the main simulation

The main process of the program is the calculation of a pair correlation function, which is only performed with the flag 'GRT'; using 'NOGRT' will skip the pair correlation calculation and the program will end and write an output file. When 'GRT' is selected a 'STATIC' or 'DYNAMIC' simulation can be performed, the type of simulation selected depends on the type of diffusion process used;

1. The flag 'STATIC' invokes ballistic diffusion. Here, the transition probability between configurations is determined by the respective difference in energies, which includes the interstitial site energy and the interaction with neighbouring particles. A Monte-Carlo cycle (MCC) is defined in terms of successful jumps.

2. The flag 'DYNAMIC' invokes jump diffusion, over the defined subset of sites. During this, one Monte-Carlo cycle (MCC) is defined in terms of attempted jumps. The number of time samples to be calculated and the time sample frequency, in units of MCC is specified. The number of allowed jump types is given by *njt*. Each jump type is specified by giving the origin basis type, the target basis type, a pair of values bracketing the jump length. The last two values allow the user to either explicitly give the jump probability (a value for *r_tor* is given and *r_en* is set to zero), or to specify an activation energy for diffusion (*r_en* is assigned a value and *r_tor* is set to one). For the latter option, the jump probability will have a temperature dependence based on a Boltzmann factor.

The last key part of the main simulation is whether the 'TOTAL' or 'SELF' correlation functions are calculated. The generated output file contains the jump vectors and their associated pair correlation functions required for further analysis.

3.2.2 Extensions to the Code in this Work

To utilise the pre-existing code for the purposes of this work, some modifications and extensions were needed to simulate the desired characteristics of the specific systems considered here.

1. To change calls to the random number generator; the original code used routines from the NAG library, which were not open source. Here, the FORTRAN 90 function, RANDOM_NUMBER(), is used to produce pseudo-random numbers. These are used both for selecting atoms and vacant sites for determining the transition probabilities in the Metropo-

lis algorithm in addition to determining whether a particular transition is accepted.

2. Extending the processes by which the burn-in simulation can be performed. Originally, this could be done via ballistic diffusion only; this was extended to allow jump diffusion and also to specify whether successful or attempted jumps were used, via the flags 'jtype' and 'jdiff' in Fig. 3.4.

3. Extending the definitions of the site occupancies to be calculated during the burn in process, as per Eqns. (3.3) and (3.4). Due to the code being used with multiple site types it was necessary to determine if the system was in equilibrium prior to the main calculation of the pair correlation function being simulated. This meant that the fraction of particles on each site type could be seen and was a good indicator of the Monte-Carlo calculation working correctly.

4. Allowing for specific jump probabilities between different site types. This was necessary to module the jump diffusion between different site types in palladium hydride. Here, either the explicit jump probabilities or the barrier heights can be are specified, as described in the previous section and shown in Fig. 3.5.

3.3 Interpretation of the Output of the GRT Code

The output file from GRT contains values for the pair-correlation function, either static or dynamic. A suite of post-processing python scripts have been developed by the author in order to produce respective scattering functions, either $S(\mathbf{Q})$, or the intermediate scattering function $I(\mathbf{Q}, t)$. In addition, code has been developed to determine the directional averages of these quantities for comparison with experimental data on polycrystalline samples.

Once values for $I(\mathbf{Q}, t)$ have been obtained, rather than performing the temporal Fourier transform to give $S(\mathbf{Q}, \omega)$ numerically, analytical functions, specifically a sum of decaying exponentals, were fitted to $I(\mathbf{Q}, t)$ in order to determine values for the decay constants, $f(\mathbf{Q})$ (Bull and Ross, 1999b). The justification for this approach is that experimental QENS data are generally interpreted by fitting a sum of Lorentzian functions and extracting the corresponding widths, which are directly related to the decay constants. In addition, the sampling frequency used when calculating $I(\mathbf{Q}, t)$ is a limiting factor in determining the range over which $S(\mathbf{Q}, \omega)$ can be calculated. Fig. 3.6 shows the generic form of $f(\mathbf{Q})$ obtained either from $I(\mathbf{Q}, t)$ via simulation or from $S(\mathbf{Q}, \omega)$ measured experimentally.
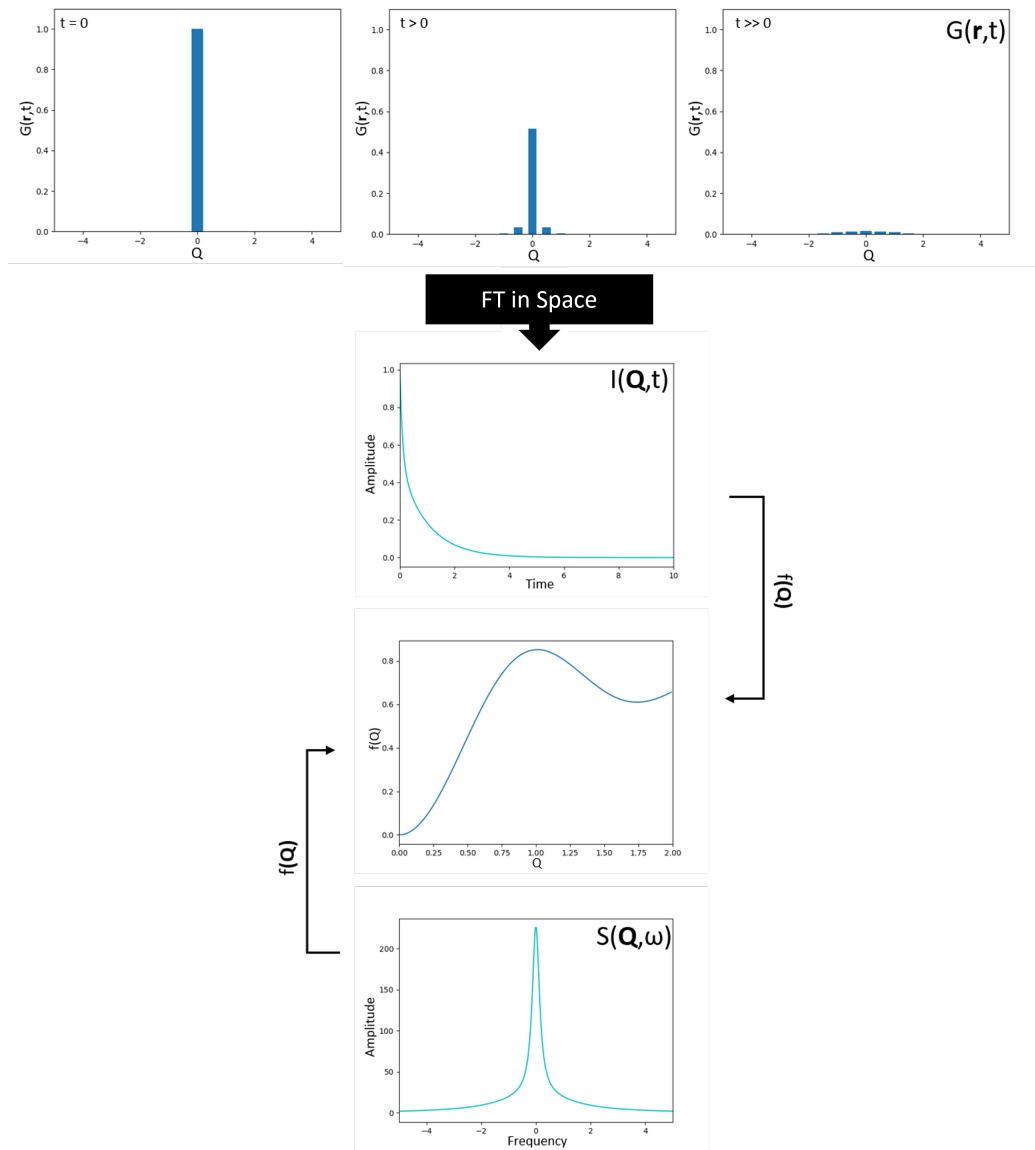
Figure 3.6: Schematic representation of the process used to arrive at the half widths half maxima (HWHM) from Monte-carlo simulations of G(**r**,t).

3.3.1 Calculation of the Intermediate Scattering Function

In general, the intermediate scattering function is obtained from a spatial Fourier transform of the time-dependent pair-correlation function. As the system considered is a lattice gas, the Fourier transform can be performed as a summation over a discrete set of vectors. Considering firstly the Fourier transform of the self-correlation function, $G_S(\mathbf{r}, t)$, the corresponding incoherent intermediate scattering function, $I_{inc}(\mathbf{Q}, t)$ can be obtained via:

$$I_{inc}(\mathbf{Q,t}) = \sum_{\mathbf{r}} G_s(\mathbf{r}, t) \exp(i\mathbf{Q} \cdot \mathbf{r}) \tag{3.5}$$

Equivalently, the coherent intermediate scattering function, $I_{coh}(\mathbf{Q}, t)$ can be obtained from the total pair correlation function, $G(\mathbf{r}, t)$, although here a value related to the concentration should be subtracted. This represents the contribution from the underlying host lattice. In practice, this value can be determined by taking the average of $G(\mathbf{r} \neq 0, 0)$, the pair correlation function excluding the value at the origin at t = 0. This ensures that $G(\mathbf{r}, t)$ tends to zero at large distance. If this were not the case, then a truncation error would arise; the Fourier transform would effectively be a convolution with a step-function, producing spurious components in the Fourier transform at low Q, varying as a sinc function centred on Q=0.

$$I(\mathbf{Q}, t) = \sum_{\mathbf{r}} (G(\mathbf{r}, t) - G_0) \exp(i\mathbf{Q} \cdot \mathbf{r}), \tag{3.6}$$

where G_0 is

$$G_0 = \frac{1}{N} \sum_{\mathbf{r} \neq 0} G(\mathbf{r}, t = 0). \tag{3.7}$$

However, $G_s(\mathbf{r}, t)$ can only be evaluated properly if it is calculated over a finite region of real-space. If the pair-correlation function is not calculated sufficiently far enough out in real space then the summation over r would not be exact. This volume of space of radius r_{max} is examined up to a given maximum in the unit of time (M.C.C) t_{max}, this is the maximum time up to which $I_{inc}(\mathbf{Q}, t)$ can be calculated. At this point, $G(\mathbf{r}, t)$ should have decayed sufficiently to zero for the system in question. The values for the radius and time must be selected carefully as to ensure that all the data available for the system is captured fully. Due to this now being carried out within a sphere of a given radius the $\mathbf{r}$ from Eqn. (3.5) becomes a sub-set of real space vectors within the sphere.

The effect that the maximum radius of the sphere effects the intermediate scattering function can be seen in Fig. (3.7) where $I_{inc}(\mathbf{Q}, t)$ is calculated at a Q-vector of $(0, 0, 0)$ with different values of r_{max} in a Face-Cantered Cubic lattice with the lattice size being 20x20x20 unit cells.

67
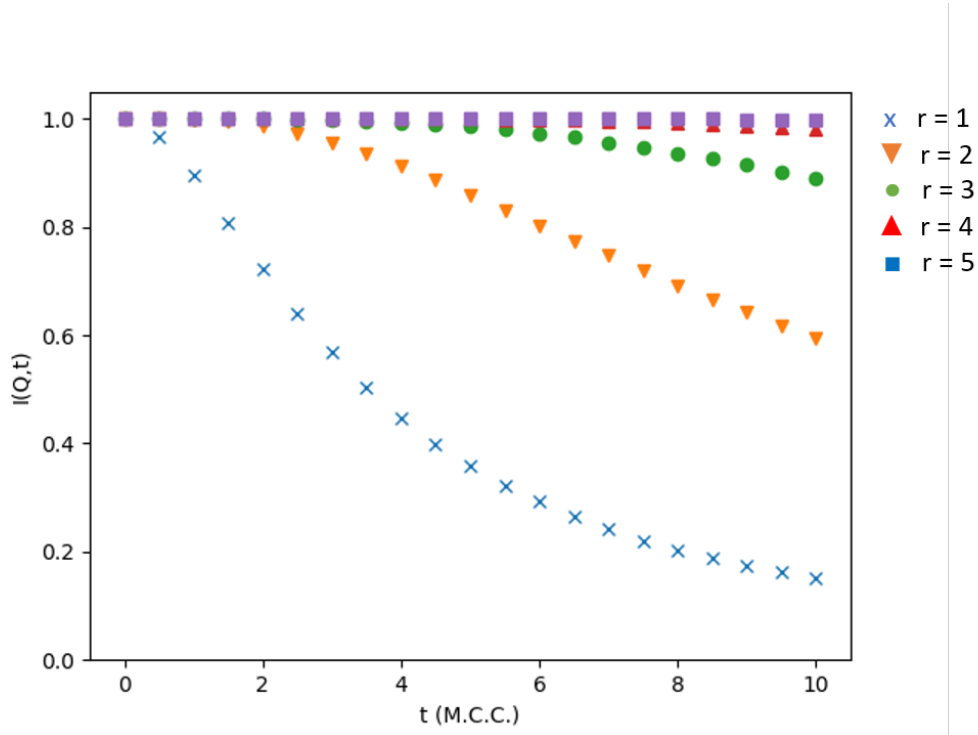
Figure 3.7: Incoherent intermediate scattering function at Q=0 from a Fourier transform of $G_s(\mathbf{r}, t)$ for an fcc lattice at C=0.1 at different radii of real-space spheres, r=1,2,3,4,5.

A test for convergence is that $I(\mathbf{Q} = 0, t)$ should be equal to 1 for all times. When the radius is set to small values of r_{max} such as 1 (represented by the blue x) it can be seen that $I_{inc}(\mathbf{Q} = 0, t)$ decays rapidly towards zero. This decay is due to the fact that a particle initially at the origin has a probability of diffusing outside the sphere in real space that is being sampled within the limit of t_{max}. As r_{max} is increased the decay becomes much slower until effectively a flat line is seen within the allowed time frame. For this system an $r_{max} = 5$ is ideal for the evaluation of the $I_{inc}(\mathbf{Q}, t)$. This however will very for concentration as site blocking effects can occur causing the scattering function to decay much slower. Proceeding from here with a suitable volume of real-space being sampled the $I_{inc}(\mathbf{Q}, t)$ can now

be calculated at a given Q-vector for example in the $(1,1,1)$ high symmetry direction of a FCC lattice, Fig. 3.8
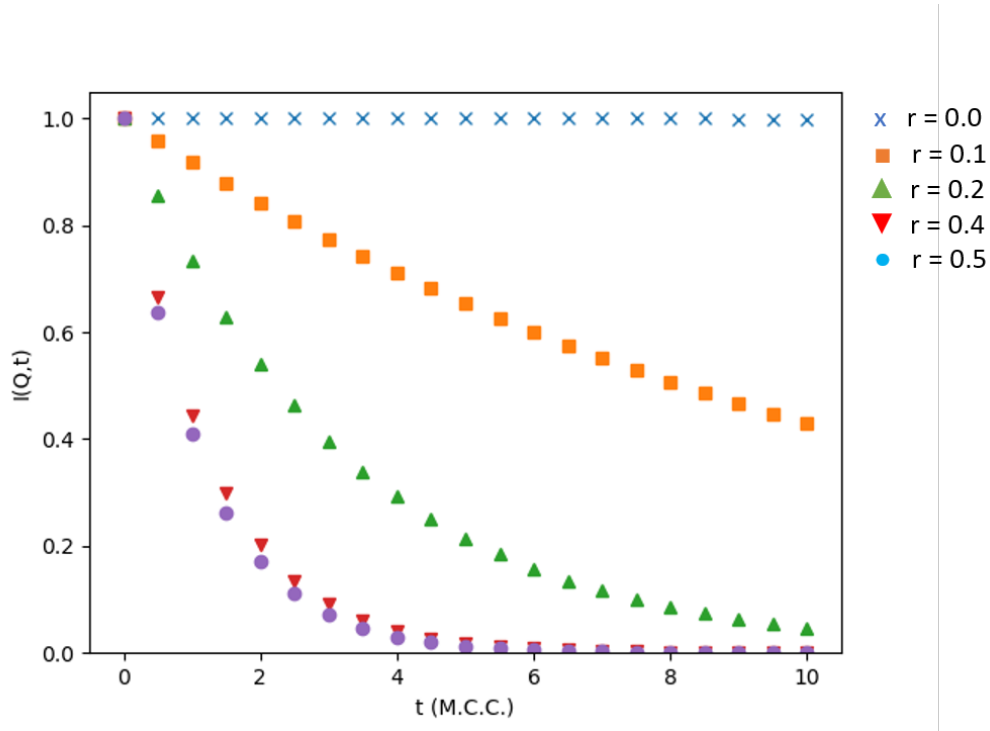
Figure 3.8: $I_{inc}(\mathbf{Q}, t)$ for a range of Q-values in the $(1,1,1)$ for an fcc lattice. $(Q_x, Q_y, Q_z) = 0.0, 0.1, 0.2, 0.4$ and 0.5.

When a system involving a number of non-geometrically equivalent sub-lattices, GRT produces a set of $G(\mathbf{r}, t)$ values for each sub-lattice. Here, an intermediate scattering function is associated with each sub-lattice, β, creating a set of partial $I_\beta(\mathbf{Q}, t)$, where the full $I(\mathbf{Q}, t)$ is the sum over the sub-lattices. It is therefore possible to see the contributions of each site type to the overall intermediate scattering function.
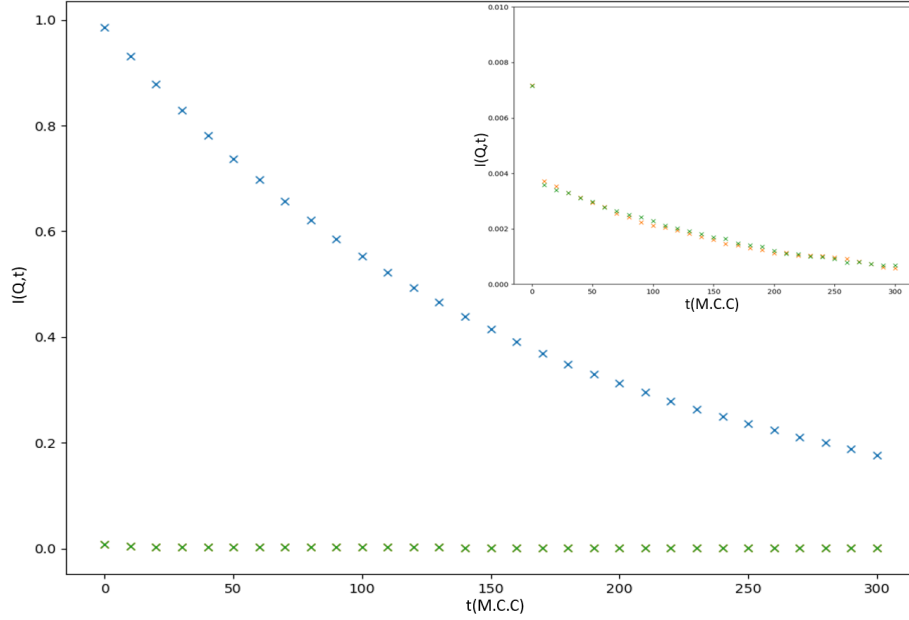
Figure 3.9: Intermediate scattering functions calculated from for a fcc with a 3 sub-lattices from a octahedral site and two tetrahedral sites.

The Fourier transform of $G_s(\mathbf{r}, t)$ decays more rapidly as Q moves away from a reciprocal lattice point up to a maximum about which it is symmetrical or the Brillouin zone boundary, in the case of the $(1, 1, 1)$ direction the reciprocal lattice points are located at are $Q = (0, 0, 0)$ and $(1, 1, 1)$. The accuracy of the $I_{inc}(\mathbf{Q}, t)$ and the exponential fits to the data can also be effected by the thermal average of the correlation function this is formed by a number of samples of the function and the result is the average over these samples. The $I_{inc}(\mathbf{Q}, t)$'s in Fig. 3.8 are averaged over 500 samples. In figure(3.10) a comparison for sampling rates is shown.
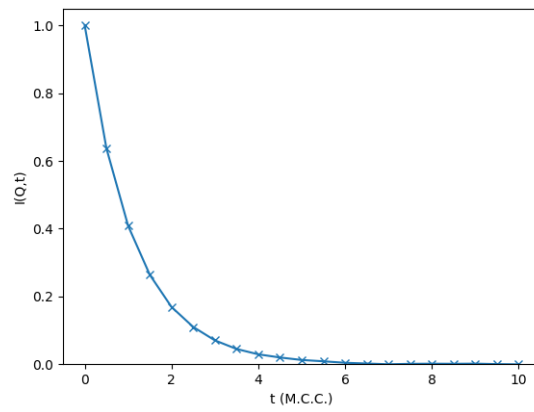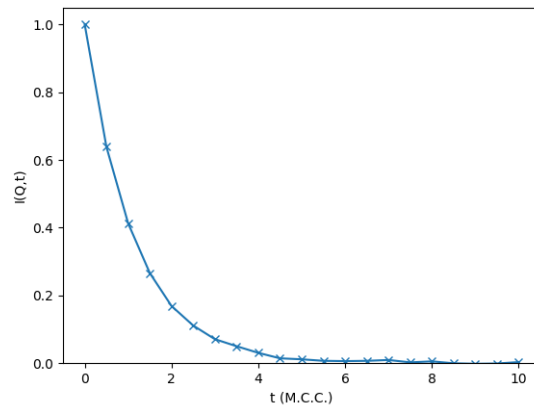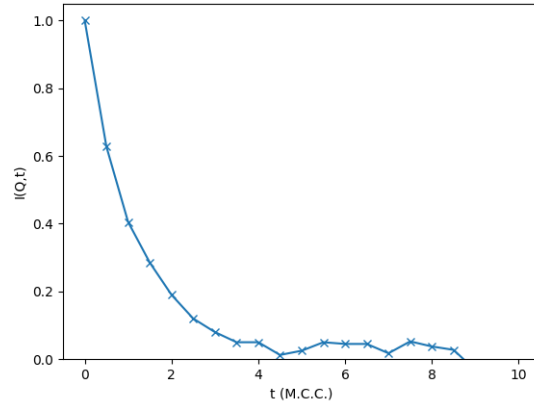
Figure 3.10: Sample rates of 1 (top), 50 (middle) and 500 (bottom) for a Q-vector in an fcc lattice

71

3.3.2 Calculation of f(Q)

Single Crystal

Beginning with the intermediate scattering function, where the pair correlation function undergoes a partial Fourier transform, as outlined in a previous chapter. This can either be done by means of a total $I(\mathbf{Q}, t)$ where this is a sum over the sub-lattices in the system. At this point, one could, in principle, perform a subsequent Fourier transform to obtain the scattering function. As discussed previously, this requires $G(\mathbf{r}, t)$ to be calculated at many different times. Instead, the intermediate scattering function is fitted by an analytical function. In particular, as sum of decaying exponentials can be used, from which $f(\mathbf{Q})$ can be extracted directly. This is done, in practice by fitting a weighted sum of exponentials to the data sets for each Q,

$$I(\mathbf{Q}, t) = \sum_{\beta} A_{\beta}(Q) \exp(-f_{\beta}(Q)t) \tag{3.8}$$

These exponential fits are shown in Fig. 3.11, where a single exponential if fitted to the intermediate scattering function at specific Q points,(Q_x, Q_y, Q_z).
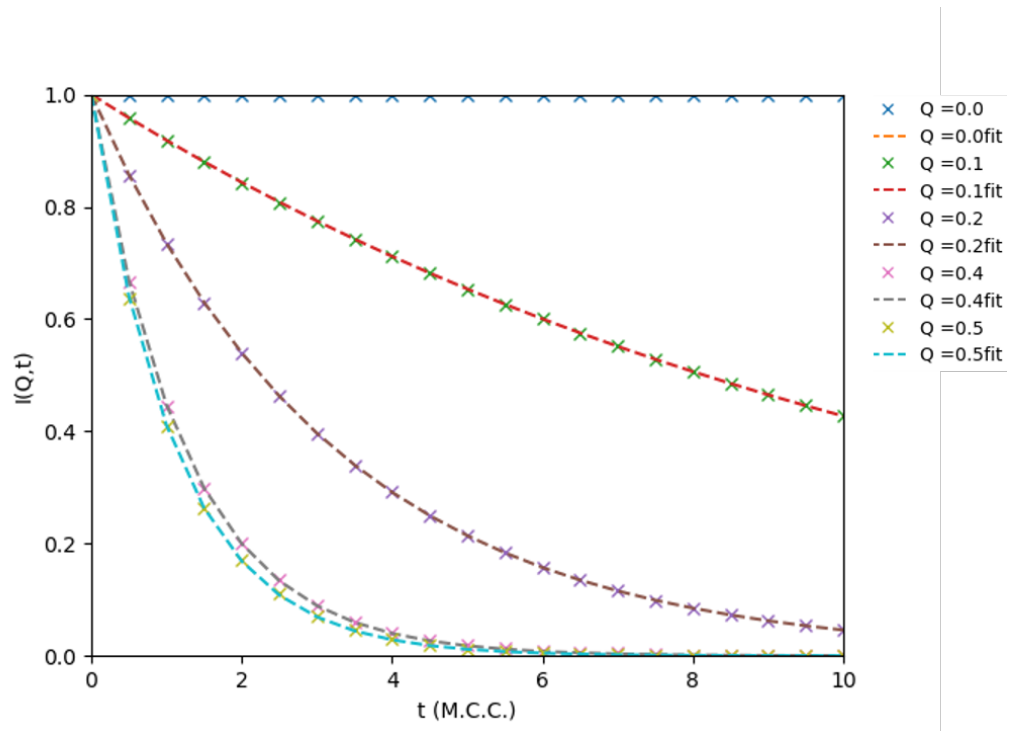
Figure 3.11: $I(\mathbf{Q}, t)$'s calculated at $(Q_x, Q_y, Q_z) = 0.0, 0.1, 0.2, 0.4$ and 0.5 (x) with a single exponential fitted $(--)$.

The decay constants $f(\mathbf{Q})$, from each of the fits at $\mathbf{Q}$ vectors along the $(1, 1, 1)$ direction are plotted and compared to the Chudley-Elliott model in Fig.3.12.
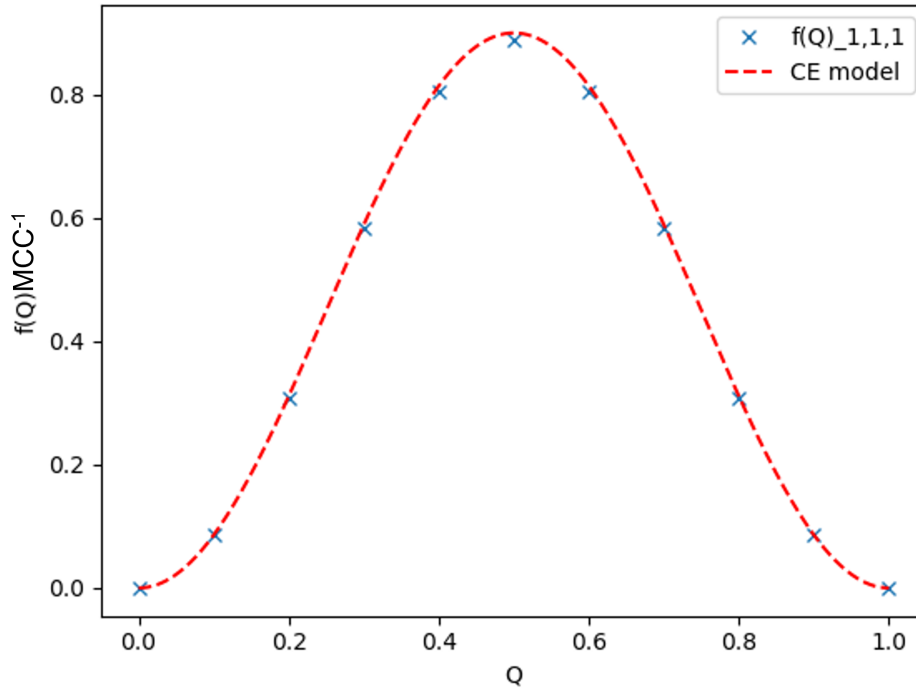
Figure 3.12: Fit of the Chudley-Elliott model to fitted HWHMs of the intermediate scattering functions.

There is a slight deviation of the fitted $f(Q)$s towards the peak from the curve created by Chudley-Elliott (CE) model (Fig.3.12). This is most likely due to the tracer correlation factor. But at Q values close to the reciprocal lattice points the CE model and the fitted values are seen to be equivalent.

Polycrystalline

In quasi-elastic neutron scattering experiments often a powder sample is used. As a result it is more relevant to calculate the polycrystaline form of the scattering function. To do this from a Monte-Carlo calculated $G(\mathbf{r}, t)$ the directionally averaged intermediate scattering function is needed, where the $I(\mathbf{Q}, t)$ is calculated at different points throughout the sphere of radius r.

The most straightforward way of doing this is using an inbuilt function, such as dblequad in python. However, this can become very computationally inefficient. For example, the spherical average of $f(Q)$ from the Chudley-Elliot model calculated via dblequad is shown in Fig. 3.13, along with the cumulative time taken to calculate each width at Q Fig. 3.14.
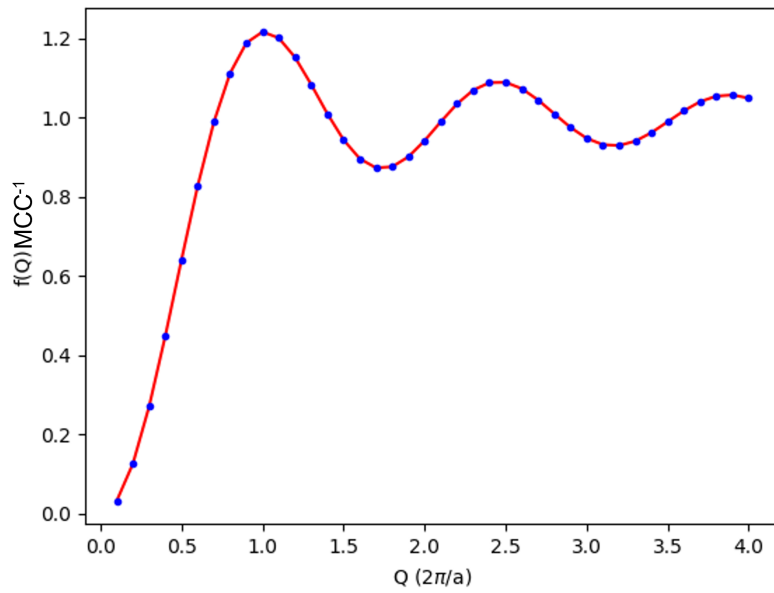
Figure 3.13: spherical average of $f(Q)$ from the Chudley-Elliott model calculated via dblequad.
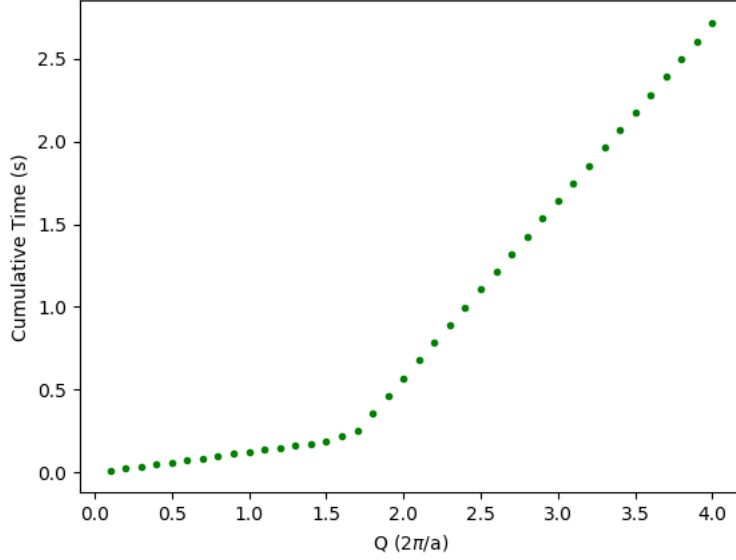
Figure 3.14: Cumulative time for the calculation of $f(Q)$ using the dblequad method with respect to the magnitude of Q used.

An alternative method is to use Lebedev quadrature (Lebedev, 1975), implemented in the quadpy package (pyp).

$$I[f] = 4\pi \sum_{i=1}^{N} w_i f(\theta_i, \phi_i), \qquad (3.9)$$

Fitting a single exponential to the directionally averaged forms of I(Q,t) will only accurately reproduce the form of the polycrystalline CE model at low values of Q as the Fourier transform is less sensitive to individual jump steps at low Q. At larger values, fitting a single exponential becomes a poor approximation for the polycrystalline causing a divergence from the the analytical form, Fig.3.15, here the fitted vales of the decay constants $f(Q)$ themselves need to be directionally averaged.
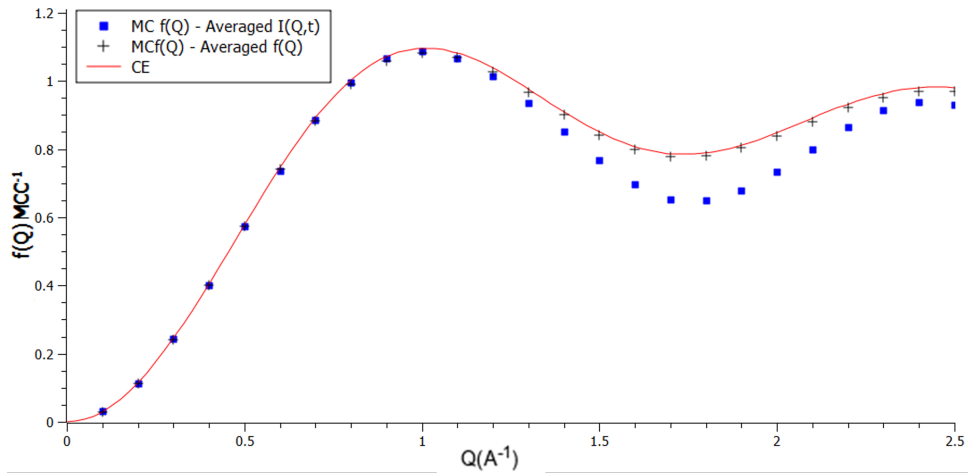
Figure 3.15: Comparison between the Chudley-Elliott model and the widths gained directionally averaged $I(\mathbf{Q}), t)$ and directionally averaged widths f(Q).

An issue with Lebedev quadrature is ensuring a sufficiently high order is used, which has been achieved here by convergence testing, illustrated in figure 3.16. It should be noted that higher orders can become rather computationally expensive which is why convergence testing can be beneficial. Another advantage of using this package is that for each order of quadrature used the Q-vectors used to calculate $I(\mathbf{Q}, t)$ are predetermined for each magnitude of Q used. Therefore, it makes it ideal for comparing results and in the event of multiple time scales, ensuring that the points used are the same between runs.
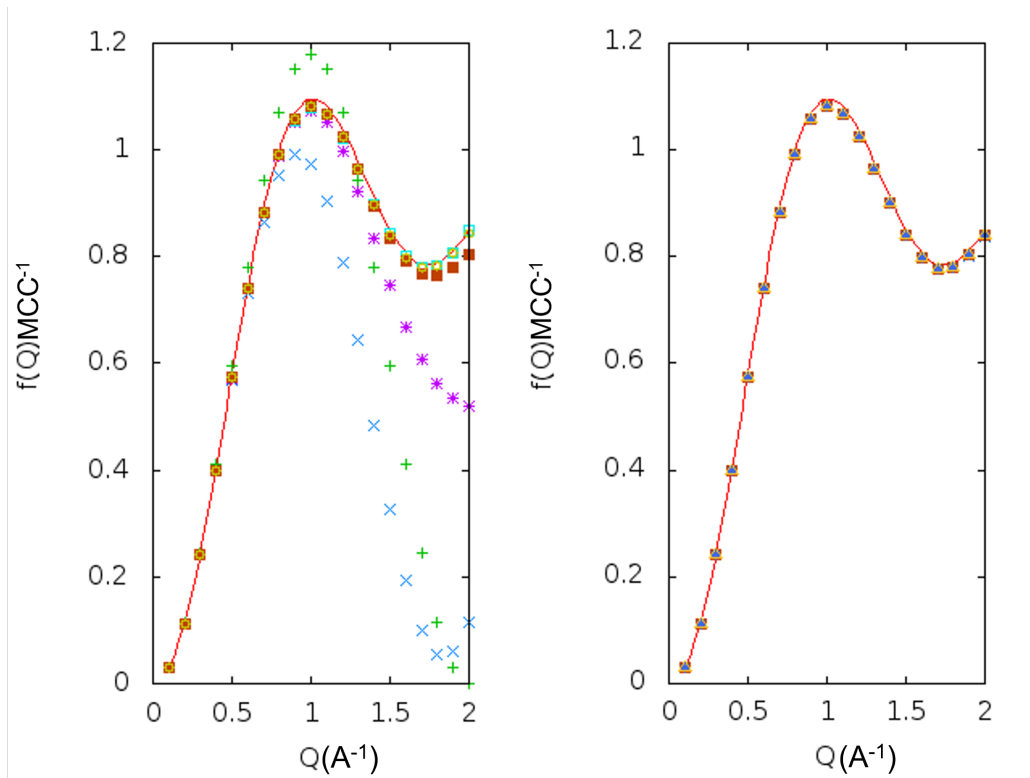
Figure 3.16: f(Q) calculated for a polycrystalline FCC lattice from fitting a single exponential to I(Q,t) against the Chudley-Elliott model. Where the data points are for each increasing Lebadev order. The left hand side panel shows orders 3(+), 5(×), 7(*), 9(solid □) and 11(□). The right hand side shows orders 13 and above which show good agreement to the Chudley-Elliott model.

3.4 Pairing experiment with simulation

Experimental measurements of the quasi-elastic broadening from neutron scattering are represented as Lorentzians which have an associated half width half maximum (HWHM), Γ.

$$\Gamma(Q) = \frac{1}{\tau}\left(1 - \frac{\sin(Ql)}{Ql}\right) \tag{3.10}$$

The widths from the experimental readings can be compared to those extracted from the simulated pair correlations functions $G(\mathbf{r}, t)$, as the intermediate scattering function is,

$$I(\mathbf{Q}, t) = e^{-f(\mathbf{Q})t}, \tag{3.11}$$

where f($\mathbf{Q}$) is equivalent to Γ. From these widths for given $\mathbf{Q}$ values. These widths in both cases can be used to determine jump length, l, and the mean residency time, τ. This is achieved by fitting Eqn.(3.10) to a set of HWHM's from either the Lorentz component of QENS spectra or widths calculated from Eqn.(3.11). Quasi-elastic neutron scattering from a target results in a continuous spread of energy best represented as a lorentzian whose half width half maximum at a selected $\mathbf{Q}$ vector,

$$\hbar\mathbf{Q} = (\mathbf{k}' - \mathbf{k}) \tag{3.12}$$

In simulation these Q values are defined in terms of a position vector (r_x, r_y, r_z), in the polycrystaline case (powder sample). These are sampled from a sphere of radius, r and on the single crystal (foil) these are sampled points along a high symmetry direction such as face-centred cubic's' $(h/2, h/2, h/2)$.

3.4.1 Multiple Time-scales

With the GRT-program, measuring the desired contributions to the broadening is done by allowing specific jumps to occur. Mainly the octahedral to octahedral and the tetrahedral to octahedral jumps. It is now possible within the GRT-program to "turn off" the long range motion of the hydrogen to examine solely the short range component by specifying the jump probabilities between the sites.

In neutron scattering experiments the observable time scales are dictated by the accessible range of energy available ΔE done by selecting the incident wavelength of neutrons. For localised motion, the change in energy needs to be sufficiently broad enough to mask the long range motion arising from translational diffusion. The simulated pair correlation functions are presented in terms of change in time, Δt, where t is defined in terms of Monte-Carlo cycles (section 3.1.3). Selecting the range of Δt has the same effect on the pair correlation function as selecting the energy range dose for the scattering function. If this time range is sufficiently short the long range type motion will be missed out in the spatial transform to $I(\mathbf{Q}, t)$ leaving only the short ranged localised type motion observable if present, with a longer change in time required to examine the long range diffuse motion.

Given that energy is given by $E = \hbar\omega$ where ω has the unit of inverse time (t^{-1}) which can be equivalent to an inverse Monte-Carlo cycle (MCC^{-1}). So the selection of the number of Monte-Carlo cycles sampled over gives access to different ranges of the intermediate scattering function, demonstrated in Fig.3.17, from a rapidly decaying exponential expected from short range type motion to a more slowly decaying exponential or a combination of both.
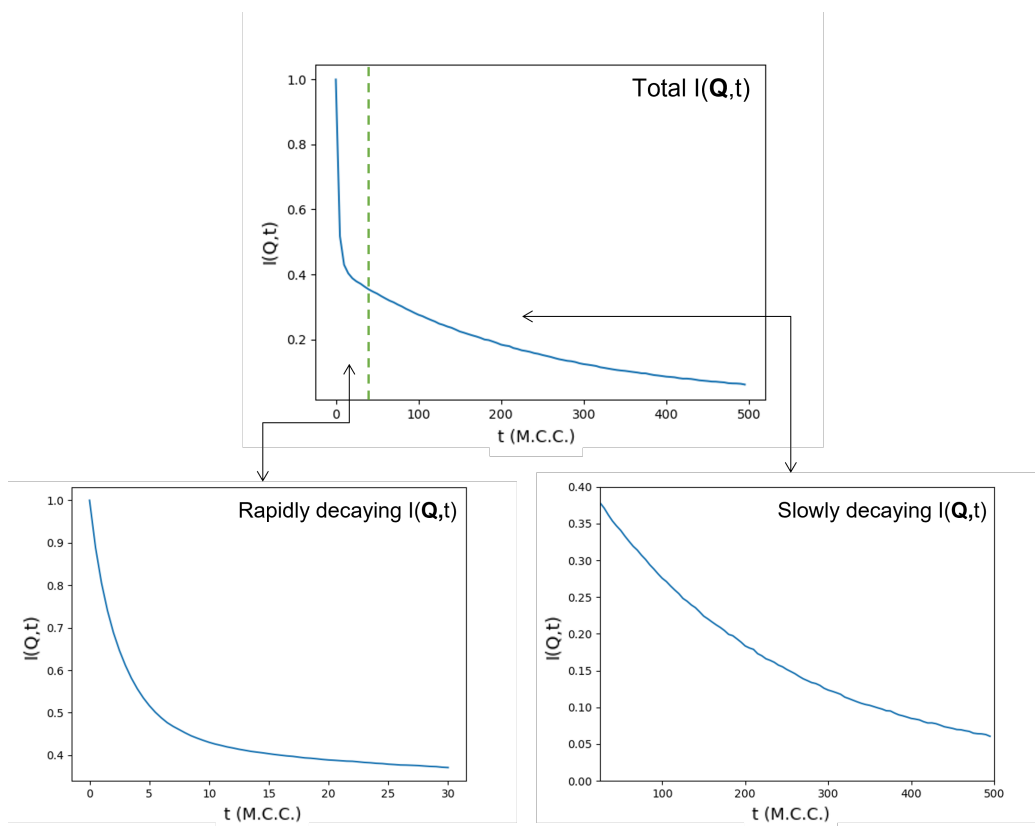
Figure 3.17: Representation of the two time scale components masked within the total intermediate scattering function.

Chapter 4

Monte-Carlo Simulations of Hydrogen Diffusion in a C15 Laves Phase System

4.1 Introduction

The motivation for the work in this thesis is the experimental observation of hydrogen diffusion on two distinct time-scales in palladium hydride. One hypothesis is that this is due to a long-range translational component coupled with a localised, spatially restricted, motion on a more rapid timescale (Kofu and Yamamuro, 2020; Kofu et al., 2016; Steel, 2018). Such motion is observed in C15 Laves-phases hydrides, cubic AB_2 compounds such as TaV_2 (Skripov et al., 1996) and ZrV_2 (Schönfeld et al., 1989). Interstitial sites available to hydrogen include a network of interconnected hexagons, where localised motion around particular hexagons is coupled with motion between the hexagons. A particularly intriguing feature is the apparent change in the average jump length with temperature (Campbell et al., 1999; Skripov

et al., 1999). Monte Carlo simulations of hydrogen diffusion in these compounds has been reported previously (Bull and Ross, 2001). Here, this work is extended.

4.2 The C15 Laves-phase System

The cubic C15 Laves phase structure belongs to a group of inter-metallic compounds with the space group $Fd3m$ among which is the compound ZrV_2 which is of interest in this body of work due to its ability to hold hydrogen within the host lattice in the α phase across the complete range of concentrations above 340K. Diffusion of hydrogen in this compound and other AB_2 compounds has been previously been studied both experimentally, via quasi-elastic neutron scattering (Schönfeld et al., 1989; Skripov et al., 1996), and with Monte Carlo simulations (Bull and Ross, 1999a; Bull et al., 2003) and Nuclear Magnetic Resonance study on TaV_2H_x (Skripov et al., 1990). More recently it is suggested (Skripov et al., 2000) that rapid jumps are made by hydrogen atoms within hexagons made by neighbouring g-sites.
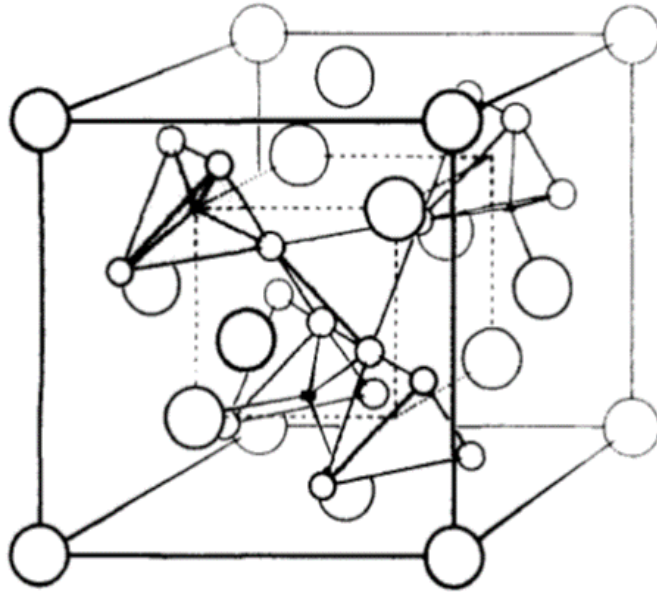
Figure 4.1: A typical C15 unit cell structure (Schönfeld et al., 1989)

There are three types of tetrahedral site available for hydrogen to occupy within the unit cell, which has a hydrogen-free lattice parameter of 7.44Å (Didisheim et al., 1979). In the disordered (α-phase, Fig(4.2)) hydrogen occupation causes no noticeable change to the structure of the compound, but a lattice expansion is observed to 7.44Å at $H_{4.8}$ (Schönfeld et al., 1989). The main sites of interest here is the g sites formed by 2 Zr and 2 V atoms, creating a total of 96 available g-sites. In addition, there are 32 e-sites and 8 b-sites, this possible occupancy of three types of site has also suggested by Hempelmann *et al* (Hempelmann et al., 1989). The ways in which hydrogen is able to diffuse around theses sites are of particular interest along with the effect of possible site blocking due to the hydrogen concentration of the system. Since the C15 laves-phase has can radially dissolve hydrogen in large quantities in a range of ZrV_2 to ZrV_2H_6 without structural change to the host lattice (Didisheim et al., 1980) except a lattice expansion with increasing

84

hydrogen concentration changing the lattice parameter to 7.29 angstroms for $H_{4.8}$ (Schönfeld et al., 1989) making it a very interesting structure for the study of hydrogen sorption. At relatively low hydrogen concentrations $x <$ 1.5 the hydrogen protons occupy the g-site and as hydrogen concentration tends towards a upper limit of $x = 4.8$ the e-sites formed by one Zr atom and three v atoms begin to become occupied (Shaltiel, 1980) and at the high end of the concentration range b site occupation has been inferred from neutron scattering measurements.
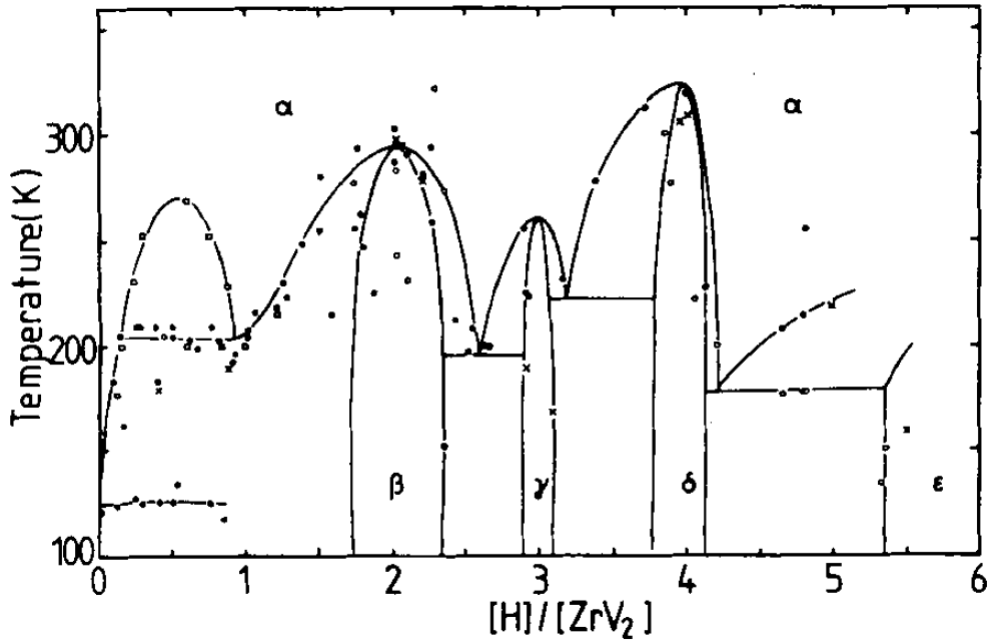
Figure 4.2: ZrV_2H_x Phase diagram produced from a combination of data (Schönfeld et al., 1989)

By considering the pair interactions between neighbouring hydrogen atoms and energies of each of the three site types the occupation as a function of concentration can be better understood, given that theoretically the maximum occupancy is $x = 17$ per formula unit due to 12 g-sites, 4 e-sites and

85

one b-site, however there has only been a maximum occupancy of 6 observed experimentally leading to the conclusion that the H-H pair interactions play a greater role.
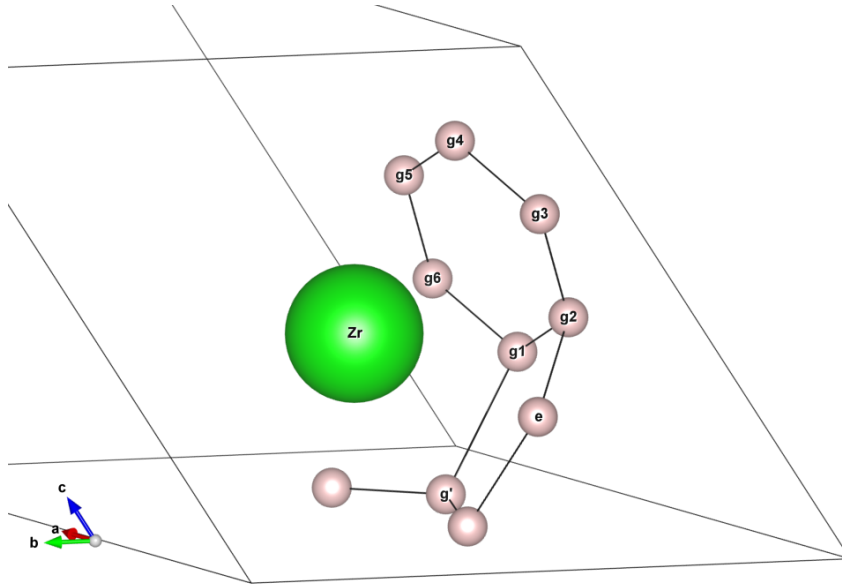
Figure 4.3: Hexagons formed by neighbouring g-sites around a Zr atom (g), g' is the nearest neighbour site on another hexagon and e site is shown.

The g-sites within ZrV_2 form a network of hexagons containing 3 of the same energetically equivalent neighbour sites, two of which are on the same hexagons and one on an adjacent hexagon, Fig.4.3, and although while having the equivalent energy the diffusion barriers between hexagons differ. To help distinguish between theses intra and inter hexagon sites and corresponding jump paths, sites on the same hexagon with be denoted as g-sites and those on an adjacent hexagon denoted as g'-sites as well as having a nearest neighbour e-site which will have three nearest neighbour g-sites. This gives two available jump paths for the hydrogen protons to diffuse via, $g-g$ and $g-g'$. These multiple hexagons formed by the g sites around Zr atoms are shown in a more complete structure in Fig. 4.4. The "ideal" nearest neighbour distances of

a C15 compound for the g and g' sites are given as $r_{g-g} = 0.1531a$ and $r_{g-g'} = 0.1768a$ giving a ratio of 1.225, ZrV_2 is close to this ideal ratio with a value of 1.19 from neutron scattering experiments,(Didisheim et al., 1980; Fischer et al., 1997). Nuclear Magnetic Resonance has also been used as a means of finding the activation energies for these jumps at 0.16ev (Shinar et al., 1984; Skripov et al., 1991).
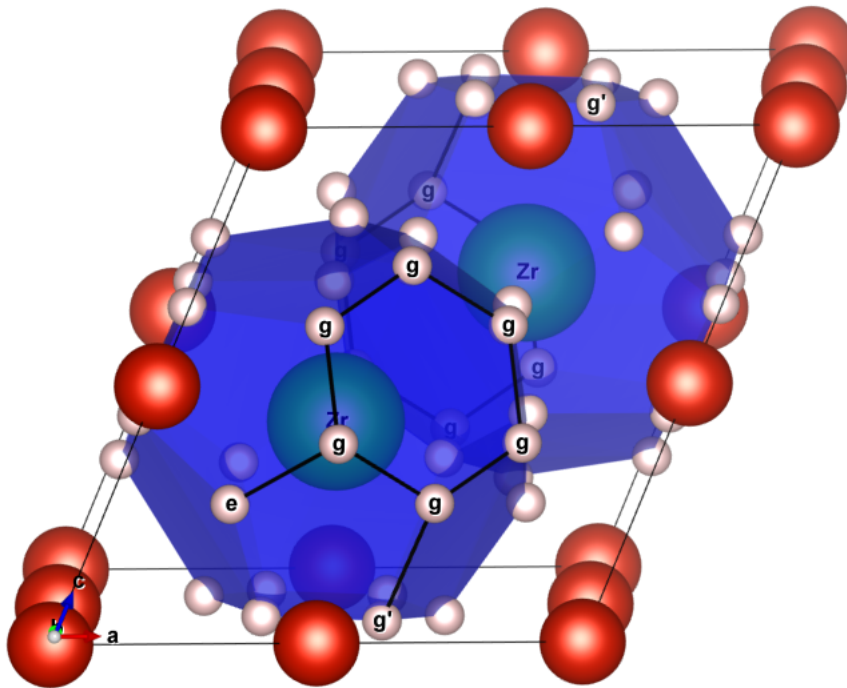
Figure 4.4: A more complete structure of ZrV_2H with the hexagons created by g-sites around a Zr atom.

The hypothesis of two distinct time scales has been suggested by skirpov et al (Skripov et al., 2000) in the C15 compound $HfMo_2$ where the ratio of jump lengths is related to the relative distances between sites on the same and adjacent hexagons, after earlier work on TaV_2H_x displayed proton movements in the form of rapid localised motion with long-range diffusion on a

slower time scale (Skripov et al., 1990, 1996). By the use of both QENS and Monte-Carlo Simulations D.J.Bull (1999a) suggested similler types of motion to those seen by Skripov on ZrV_2 and C.Schonfeld, R.Schatzler and R.Hempelmann in 1989 (Schönfeld et al., 1989) where they presented an example of broad and narrow components of $ZrV_2H_{4.8}$ scattering functions at a temperature of 340K along with the associated weights,
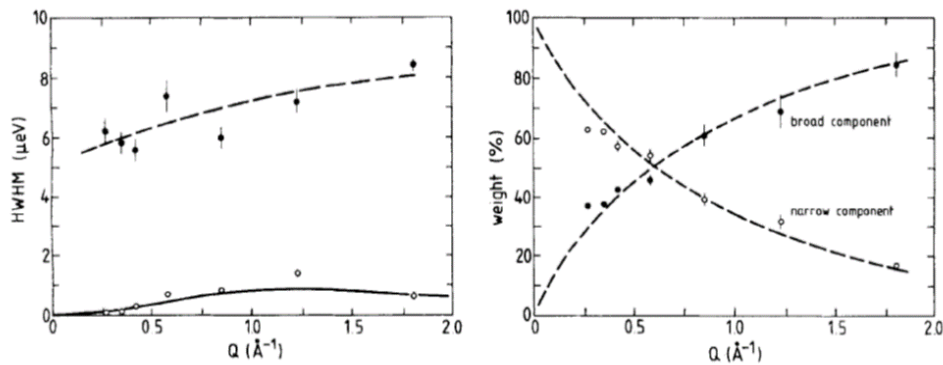
Figure 4.5: first demonstration of the hypothesis of multiple types of motion in ZrV_2H (Schönfeld et al., 1989)

This presence of two distinct jump times is a useful demonstration for the possibility of multiple jump times being present within other hydrides as the hydrogen concentration in the bulk increases. It is expected in QENS results that if scattering from motion occurring on multiple time scales is occurring the scattering will be the combination of two Lorentz components. By selecting a broad resolution function the narrow component associated with the long range type diffusion occurring on the longer time scale can not be resolved, thus the scattering from the localised motion can be isolated and is represented by the sum of an elastic an Lorentzian component (Skripov et al., 1996) Eqn.4.1 where $B + C\omega$ is a small background component,

$$S(\mathbf{Q}, \omega) = A_0(\mathbf{Q})\delta(\omega) + [1 - A_0(\mathbf{Q})]L(\omega) + B + C\omega \qquad (4.1)$$

88

If the widths of the broad loretnzian component display discernible Q dependence at low Q, this can be seen as a quality indicative to localised motion. A good demonstration of this has been presented by Schonfeld et al (Schönfeld et al., 1989), Fig. 4.5, where the the Half Width Half Maximums (HWHM) are shown along with the associated weights for both lorentzian components. Where the widths of the narrow components appear to follow a Chudley-Elliot type behaviour. Whilst the widths from the broad component show no obvious Q dependence, and the weights go to zero at low Q and increase with Q which is another feature associated with localised motion.

4.3 Monte-Carlo Simulations of Incoherent QENS from Hydrogen Diffusion in ZrV_2H_x

4.3.1 Multiple time scales

Evidence of motion occurring on multiple time scales has previously been seen from temperature dependent spin relaxation times of hydrogen from NMR measurements. Which showed a deviation from the Arrhenius-type behaviour of hydrogen. Sets of data given by Bowman R C et al (Bowman Jr et al., 1983) and Skripov A V et al (Stepanov et al., 1989) seem to imply the presence of two types of motion taking place on different frequency scales. Following these results direct evidence of this was presented by Skripov in 1990 where the spin lattice relaxation rates for TaV_2H_x were studied over a range of temperatures and concentrations. An additional low temperature maximum in the spin-lattice relaxation rate was found, indicating the existence of hydrogen undergoing localised motion on a rapid time scale. It was also observed that as the concentration increased the amplitude

of the motion increased along with the decreases of the motion's frequency.

In order to obtain the geometric details of this localised diffusion process, quasielastic neutron scattering needs to be carried out using a high resolution spectrometer. Skripov et al carried out such experiments on $TaV_2H_{0.6}$ and confirmed that the localised motion of hydrogen takes place with a hopping rate in the order of $10^9 s^{-1}$ where the suggested model for this motion was that of a 3 equally spaced sites on a circle of radius 1.1 angstroms with the caveat that six site model for the motion may be appropriate.

The scattering function for a system where two types of motion is occurring is expected to consist of two Lorentzian components attributed to both the localised and long-range diffusive processes respectively. This can be related to the results seen below here in terms of time scales on which the motions are occurring. By selecting a broad resolution function, the narrow Lorentzian component caused by the diffuse process happening on a slower, larger time scale will not be resolved. Meaning that the Lorentz component resolved will be that belonging to the localised motion taking place on a more rapid, much shorter time scale than that of the long-range diffusion.

4.3.2 Choice Of Sampling rates

As neutron scattering experiments are carried out in terms of an energy resolution window in which the scattering function is to be evaluated over, however this is obviously not the case when carrying out Monte-Carlo simulations of the pair correlation functions. In these calculations the choice of energy resolution window can be analogous to the choice of sampling rate used in terms of Monte Carlo Cycles (MCC). In attempt to examine the two-time scales hypothesised in the C15 system two time windows are to be selected such that each has a single exponential component is seen in the intermediate scattering function produced.
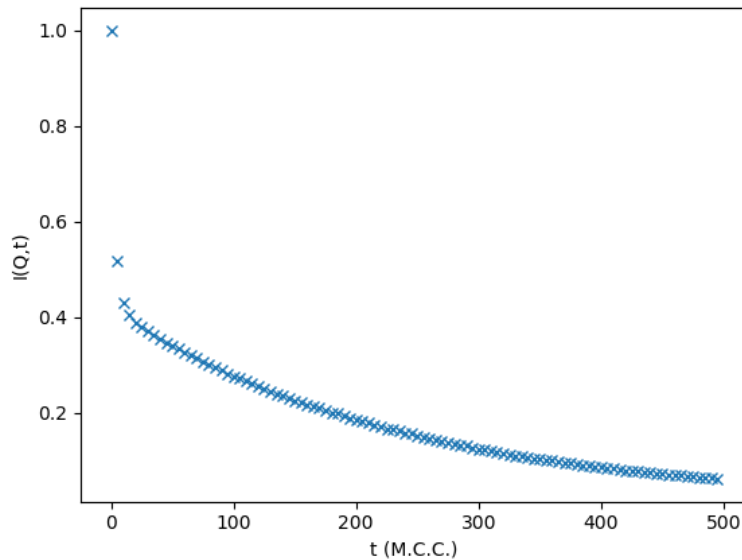
Figure 4.6: $I(Q,t)$ for a large number of M.C.C samples

Fig. 4.6 represents motion on a larger time scale seen by the slow decay towards zero. This however does not appear to be a single exponential due to the very rapid decay between the first two points at which the Monte-Carlo simulations was sampled (a Monte Carlo Cycle). We can confirm

this existence of multiple exponentials by taking the log of the intermediate
scattering function,
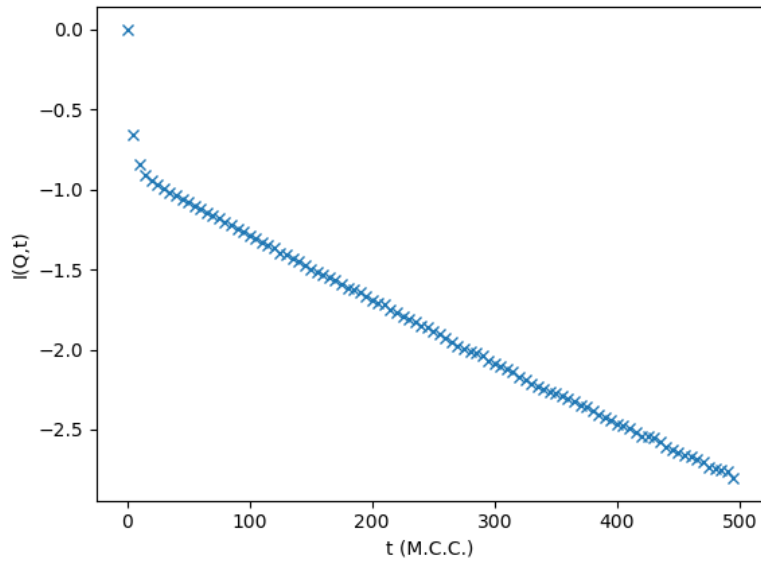
Figure 4.7: The log of $I(Q, t)$ fig.(4.6), showing a non exponential decay
component

The straight line portion of the $ln(I(\mathbf{Q}, t))$, Fig. 4.7 indicates a single
exponential, as can be seen at the lower number of Monte-Carlo cycles this
is not the case, there for a second simulation of the pair correlation function
is carried out within the lower time window.
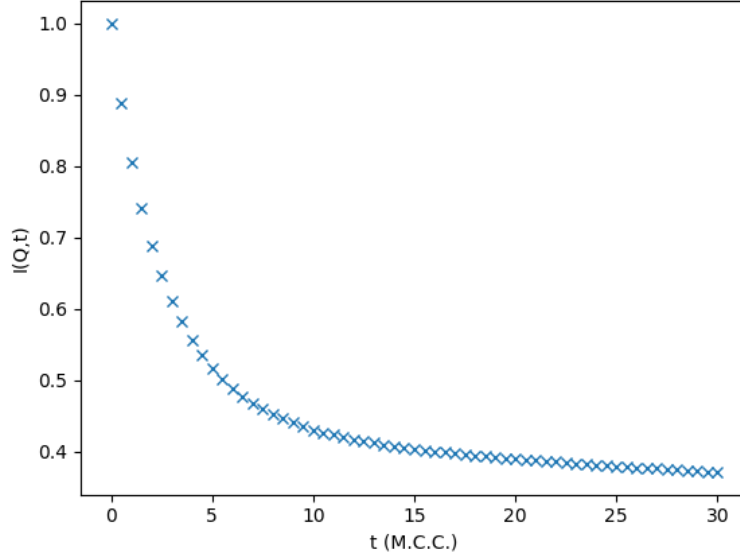
Figure 4.8: $I(Q,t)$ for the range of M.C.C samples that are not logarithmic

There an exponential can be seen. So in order to fully evaluate the Intermediate scattering function for the C15 system two time windows are needed, one for a larger and slow decaying time scale and one for a much shorted and rapidly decaying time scale. This results in the overall fit to the data being a sum of two exponetials;

$$I_{inc}(\mathbf{Q},t) = A_{st}e^{-f(\mathbf{Q}_{st})t} + A_{lt}e^{-f(\mathbf{Q}_{lt})t} \tag{4.2}$$

Taking the $f(Q)$ for each of the respective exponential functions gives the scattering function for the short time scale and the long time scale.

When there is evidence of diffusion taking place on multiple time scales within the system the procedure described in the previous chapter is varied slightly due to the sum of exponentials Eqn. (4.2). It is best to begin with the more slowly decaying time scale, here a number of points are removed from the intermediate scattering functions data, the number of points removed is

93

based on the results from $ln(I(Q,t))$ where the linear set of points represents the long time (LT) single exponential function in Eqn. (4.2). When fitted to the new range of points the fitted variables need to be retained but will also be the weightings and the HWHM's for the diffusion occurring on the longer time scale. Once carried out for a given Q-vector the rapidly decaying (higher sampling frequency) $I(Q,t)$ needs to be evaluated, this set of data replaces the few points removed from the slowly decaying I(Q,t) (lower sampling frequency). Here a double exponential is now fitted to this set of data but only two of the variables in Eqn. (4.2) are allowed to change freely, the values acquired from the previous lower sampling rate fit are used as constants. As a result, the weights and HWHM's extracted from here are those of the shorter time scale diffusion taking place in the system By plotting both the single fit and the double fit onto the same time scale it is possible to see the effect that the double exponential has on the fit of I(Q,t).
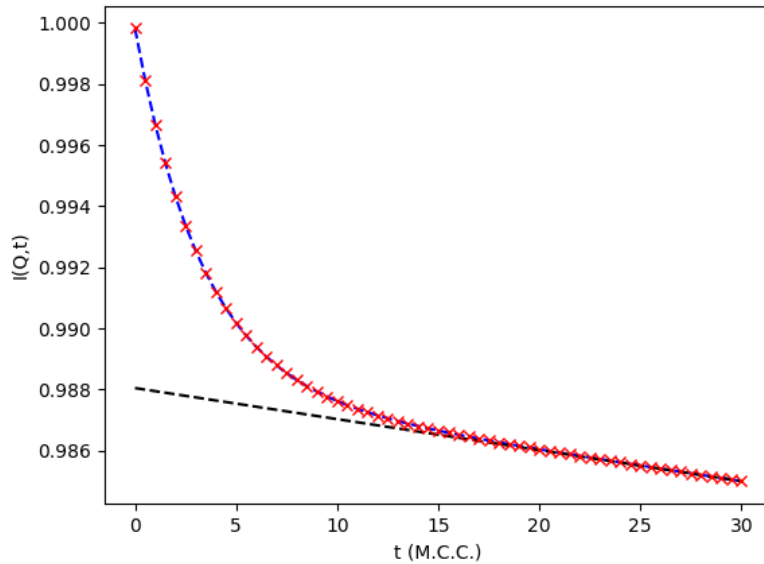
Figure 4.9: The divergence between the single fit (dashed line) and the double exponetial fit and short time scale data

94

The fits here are represented by the black and blue dashed lines along with the points from the short time scale I(Q,t) as red x's. The single exponential it therefore only shows agreement with the data points above 20 M.C.C,s where it begins to diverge off intersecting the y axis at 0.988. Whereas the double exponential fit using the weight and the decay constant of the single exponential fit, shows good agreement over the full range of points, giving support to the hypothesis that there is a double exponential and thus two types of diffuse motion occurring in the C15 system.

4.3.3   Jump ratios

Within the Monte-Carlo's input file is the ability to artificially set the probabilities of a specific jump occurring successfully given the absence of barrier heights and site energies, this is referred to as a jump rate,

$$\frac{\tau_2}{\tau_1} \tag{4.3}$$

where τ_1 is defined as the jump probability among sites in the same hexagon and τ_2 is defined as the jump probability between sites on different hexagons.In more general terms the probabilities of jumps between pairs of the same site types and pairs of different site types.

When run in this state the system is effectively at an infinite temperature and therefore all temperature dependence is removed and no interactions are included in order to determine weather the quasi-elastic scattering function can be interpreted in terms of a long raged and localised types of motion.

Elastic Component

Localised motion can occur in a spatially restricted system such as that found in C15 type structures, where there is the presence of diffusion paths which have different activation energies. Here in the C15 system using Monte-Carlo simulations of the time dependent correlation function $G(\mathbf{r}, t)$ and selecting the correct jump ratio such that $\frac{\tau_2}{\tau_1} = 0$, it is possible to look at this localised motion in the form of an intermediate scattering function that has an elastic contribution.
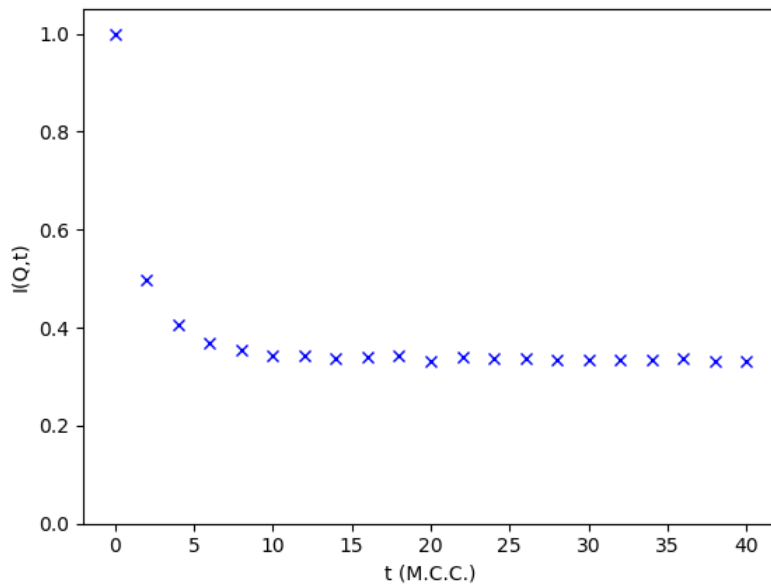
Figure 4.10: Example of the elastic component displayed as an $I(Q, t)$

here we can see that due to the bound nature of the system as a result of the jump ratio the $I(Q, t)$ decays down to a finite value Fig. 4.10, which can be seen at any given Q value with a variation in the value at which the $I(Q, t)$ becomes finite, Fig. 4.11.
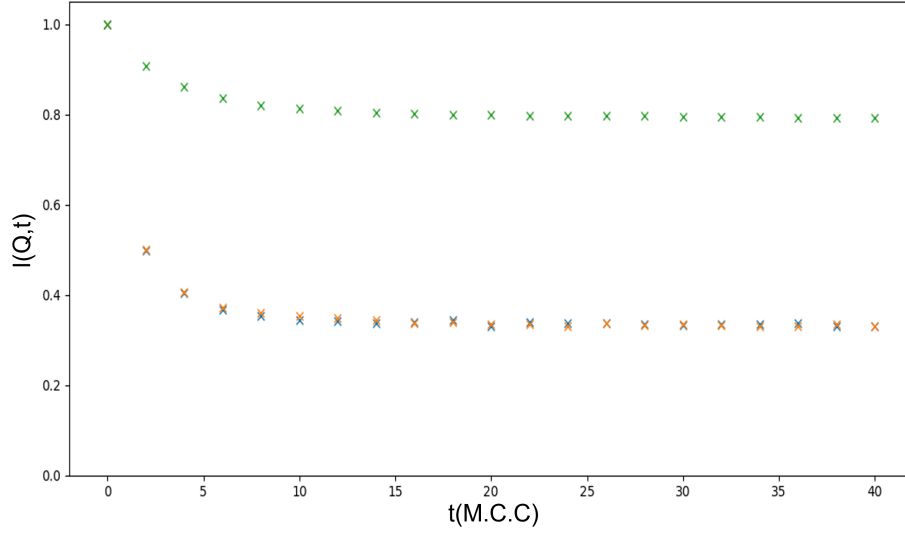
Figure 4.11: The effect of chosen Q value on the elastic component of the intermediate scattering function

The incoherent intermediate scattering function $I(Q, t)$ for spatially restricted motion is given by,

$$I_{inc}(\mathbf{Q}, t) = A_0(\mathbf{Q}) + \sum_{i=1}^{N} A_i(\mathbf{Q}) \exp\left(-t/\tau_i\right) \tag{4.4}$$

When the Q-dependence of the term $A_0(Q)$ is calculated the elastic incoherent structure factor, EISF is produced. Using the Monte-carlo simulated pair correlation functions, the spherically averaged $I_{inc}(\mathbf{Q}, t)$ are calculated to represent a polycrystalline sample, shown in Fig. 4.12.
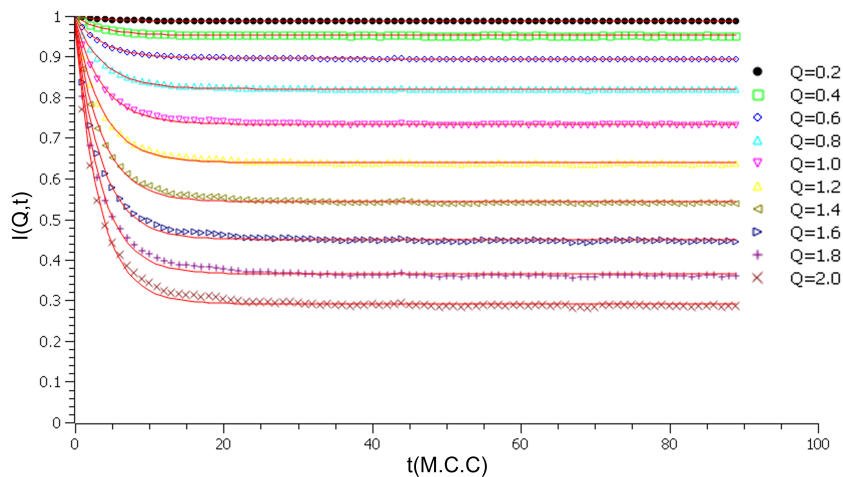
Figure 4.12: Spherically averaged I(Q,t) for a spatially restricted C15 compound containing hydrogen

The solid line on each data set represents the fit of Eqn. 4.4. As demonstrated earlier the I(Q,t)'s decay to a finite value which varies with the Q value used for the radius of sphere over which the I(Q,t) is spherically averaged. From these fits the HWHMs of the incoherent scattering function can be obtained from the exponential term along with the EISF from the first term $A_0(Q)$.
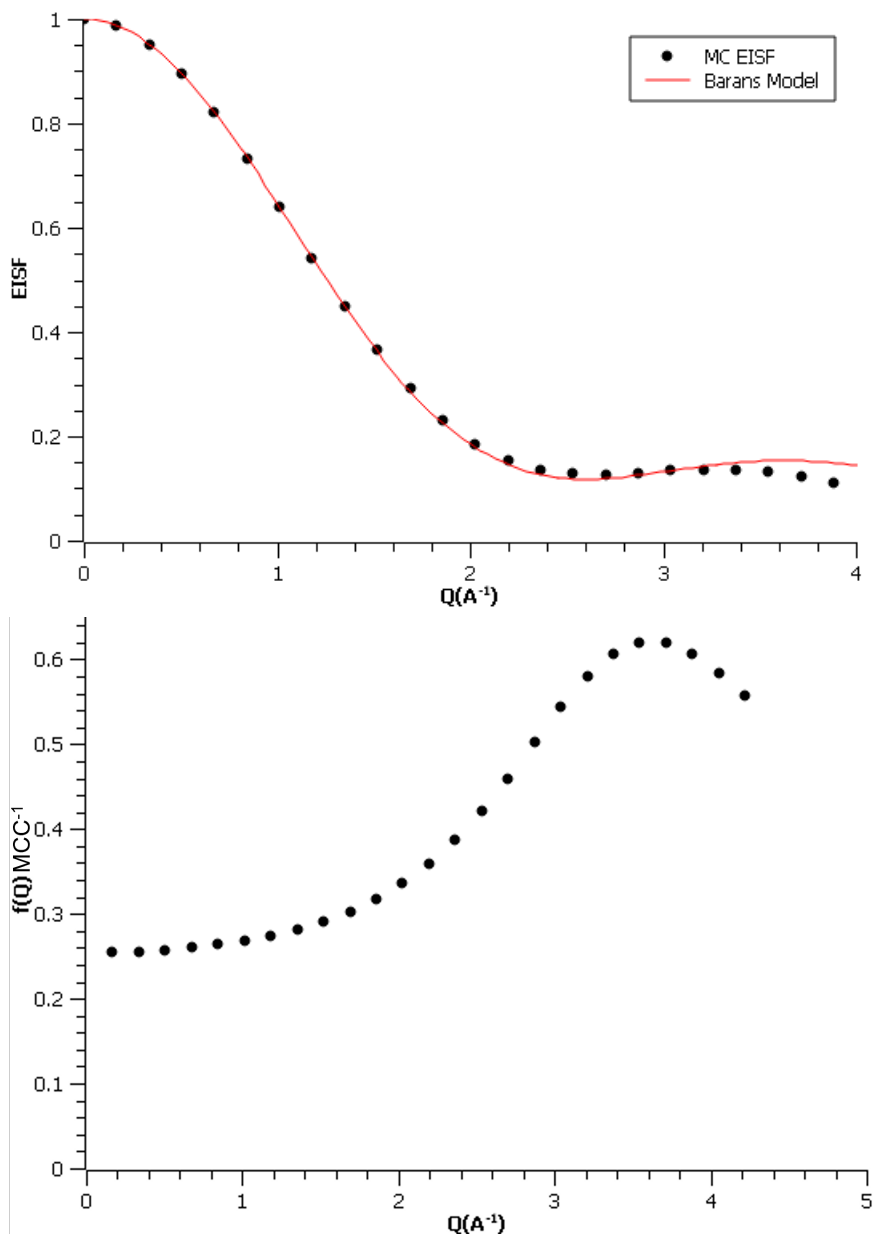
Figure 4.13: The Elastic Incoherent Scattering function and the localised motion as a result of turning off long ranged motion

The EISF gives information on the geometry of the motion taking place in the system, it can be seen that the six-site Barne's model Eqn. 2.65 (Skripov et al., 1996) represented by the solid red line fits the calculated EISF well.

99

As the jump ratio is increased away from zero the elastic component of the intermediate scattering function becomes a combination of the elastic component and the lorentzian as a result the form of I(Q,t) decaying to a finite value is reduced and begins to decay to zero or near zero with time.
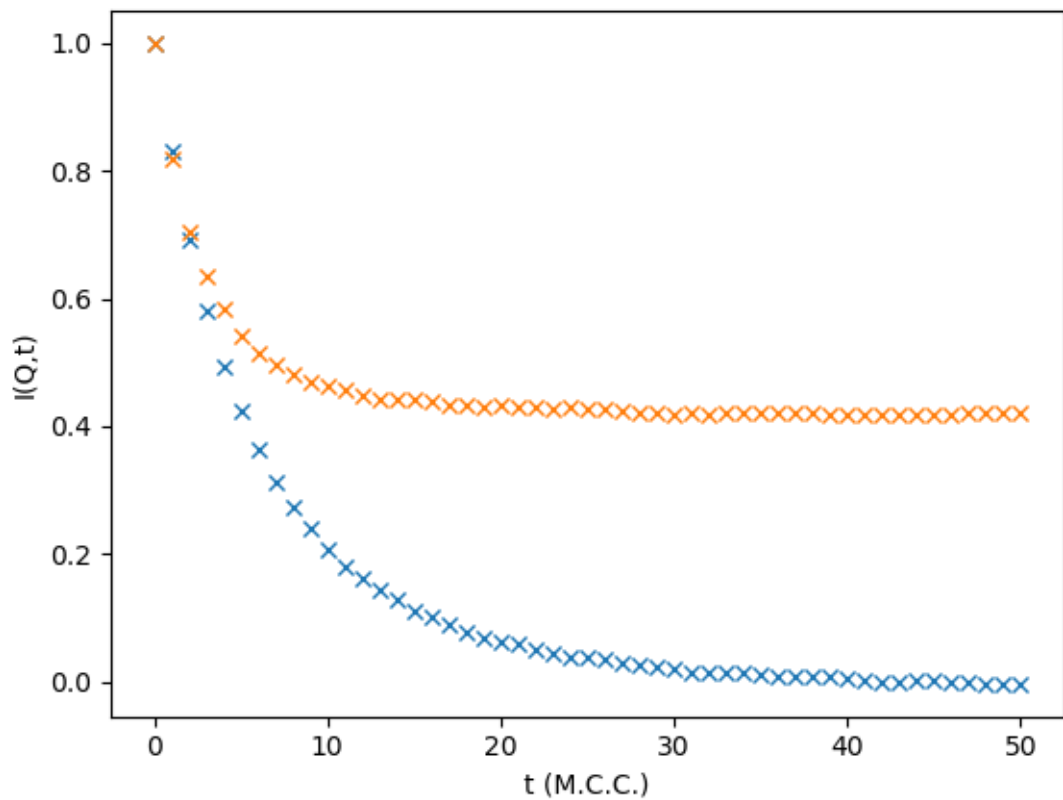
Figure 4.14: Purely localised motion compared to a combination of both localised and long range motion

Fig. 4.14 demonstrates the difference in I(Q,t) when only inter hexagon g-sites are included and when all g-sites are included from inter and intra hexagon jumps.

4.3.4 Equal Jump Probabilities

A logical starting point to determine the nature of the multiple time scales present within the C15 system is to examine the scattering widths when the jump probabilities are equal to each other and therefore the system has a jump ratio of 1. As the jump probabilities are being fixed the system the $G(\mathbf{r}, t)$ is calculated at effectively an infinite temperatures and is not effected by the site energies or the barrier heights.

Polycrystalline

At low Q values the widths calculated from the MC simulations are in agreement with the polycrystalline Chudley-Elliott model however as the Q-value increases past one they begin to diverge. At this point the scattering function becomes more sensitive to the small motions made by diffusing particles which is useful for information regarding localised motion in the system. Another contributing factor to the divergence could be the need for the widths themselves to be directionally averaged rather than just the intermediate scattering functions.
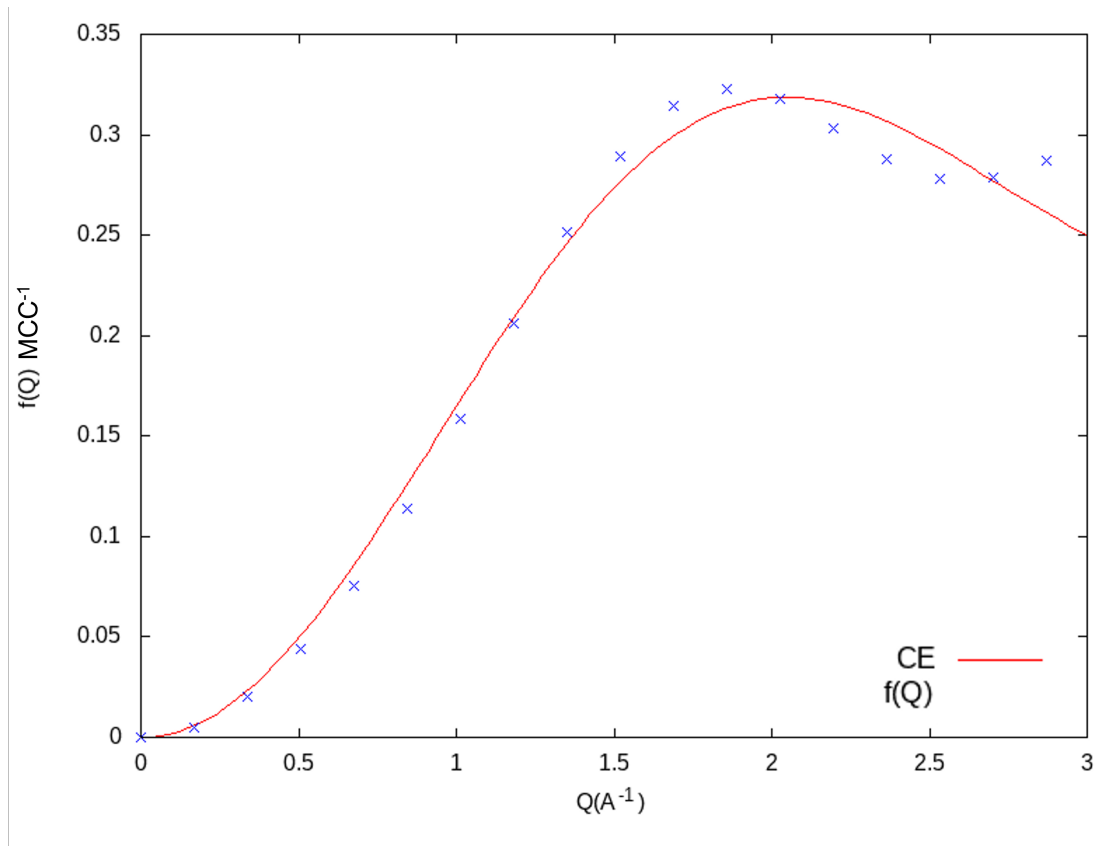
Figure 4.15: Polycrystalline widths $\tau_2/\tau_1 = 1$ and Chudley-Elliott model fit.

The data above shows the HWHMs from the directionally averaged intermediate scattering functions Fig. 4.15 with the solid red line showing the fit of the CE model. A comparison between the directionally averaged widths and intermediate scattering decay constants over a larger range of Q values is shown in Fig. 4.16. Displaying how directionally averaging the decay constants over intermediate scattering functions themselves improves the resulting broadening.
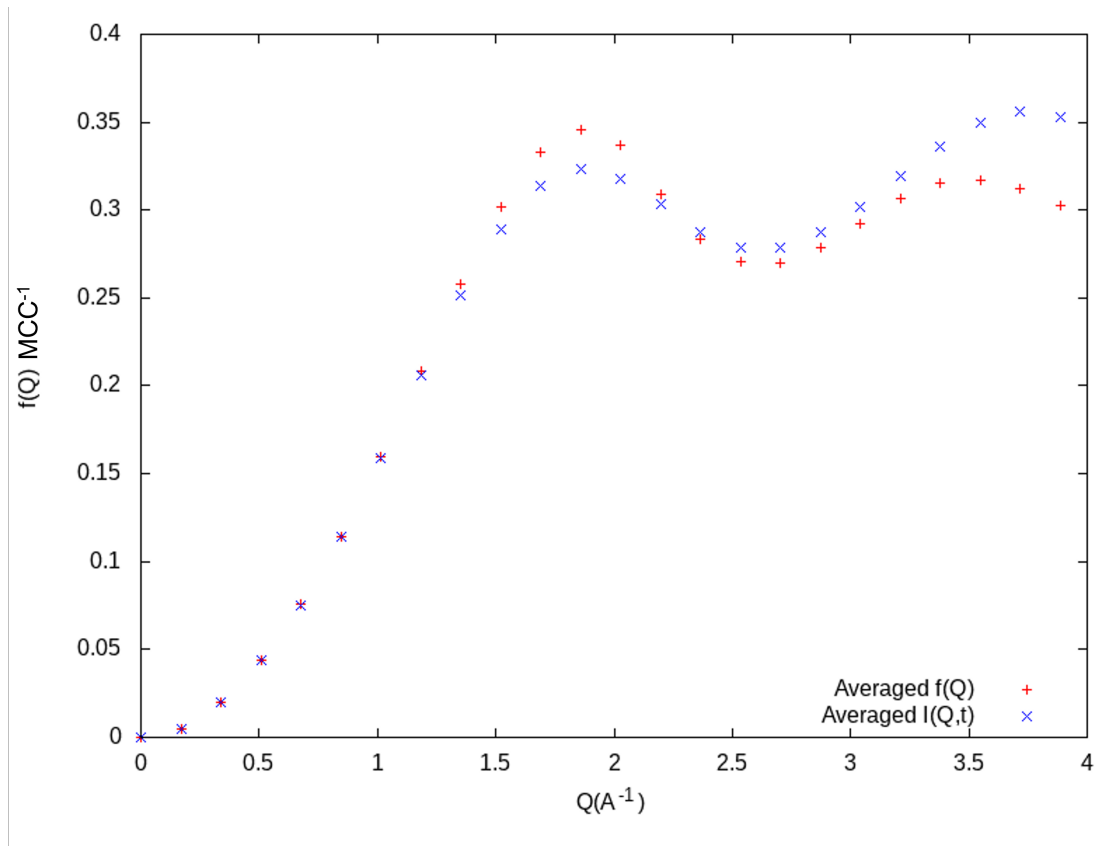
Figure 4.16: Comparison of the averaged decay constants $f(Q))$ and the averaged $I(Q,t)$.

By continuing with the hypothesis that the $I(Q,t)$ is a sum of two exponentials, when the single exponential is fitted to the slowly decaying component at low Q values this is not a good approximation of the process occurring in the system as it diverges from the rapidly decaying time scale $I(\mathbf{Q},t)$. This is demonstrated in Fig. 4.17 at four different Q values. In each case a single exponential is fitted to the data at large times ($t > 4$ MCC), represented by the black dashed line.

A second exponential component is then added to represent the more rapidly decaying component, resulting in a double exponential fit, where the parameters are retained from the single exponential fit represented by the blue dashed lines. This can be seen to give a satisfactory fit to the data.

(a) Q=0.2 $\AA^{-1}$

(b) Q=0.8 $\AA^{-1}$

(c) Q=1.8 $\AA^{-1}$

(d) Q=2.6 $\AA^{-1}$
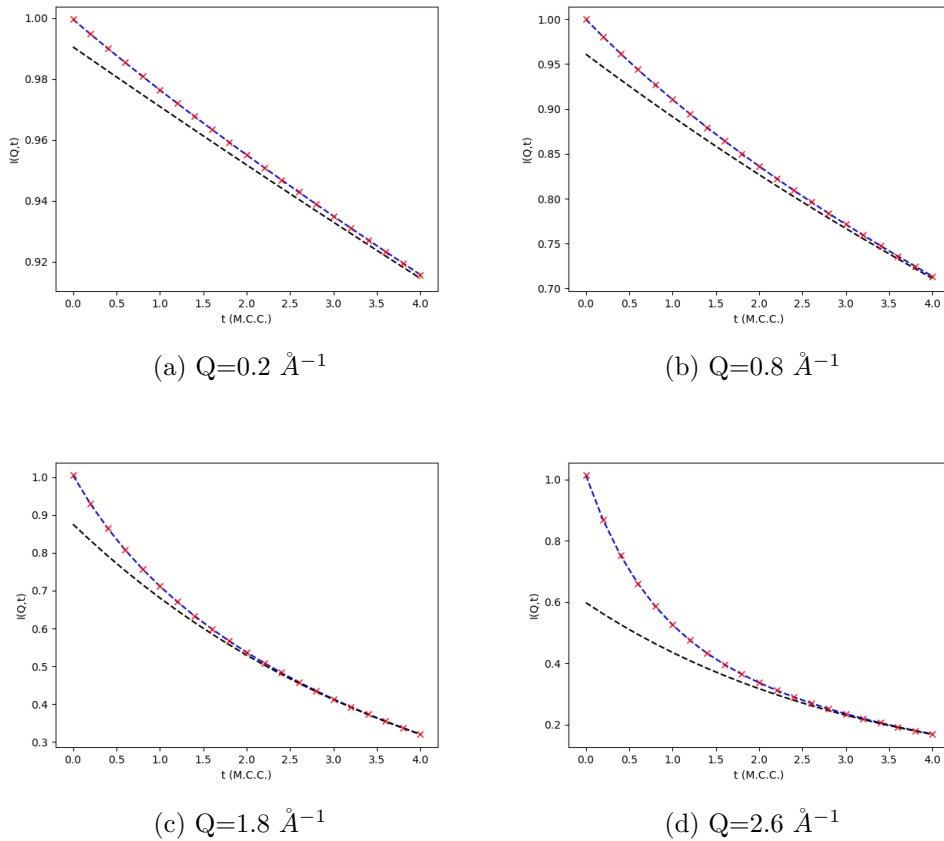
Figure 4.17: $I_{inc}(Q,t)$ at various values of Q. Data points are from the simulations. The black dashed line results from a single fitted exponential at $t > 4$ MCC (not shown here). The blue dashed line represents a double exponential fit, where the parameters from the more slowly decaying component are retained from the single exponential fit (compare with Fig. 4.9).

As the jump ratio here is set to 1.0, it could be expected that there would be no localised diffusion so the broadening would purely follow Chudley-Elliott type behaviour seen in Fig. 4.15. However in this case the diffus-

ing proton is twice as likely to undergo jumps between g sites on the same hexagon as the origin site as there are two neighbouring g sites but only one neighbouring g'-site, rather than move to an adjacent hexagon when a jump is attempted. This suggest that the widths shown in Fig. 4.18 below from the short time scale $I(\mathbf{Q}, t)$ displaying the characteristics of localised motion are influenced by some degree by the geometry of the jump paths in ZrV_2H.
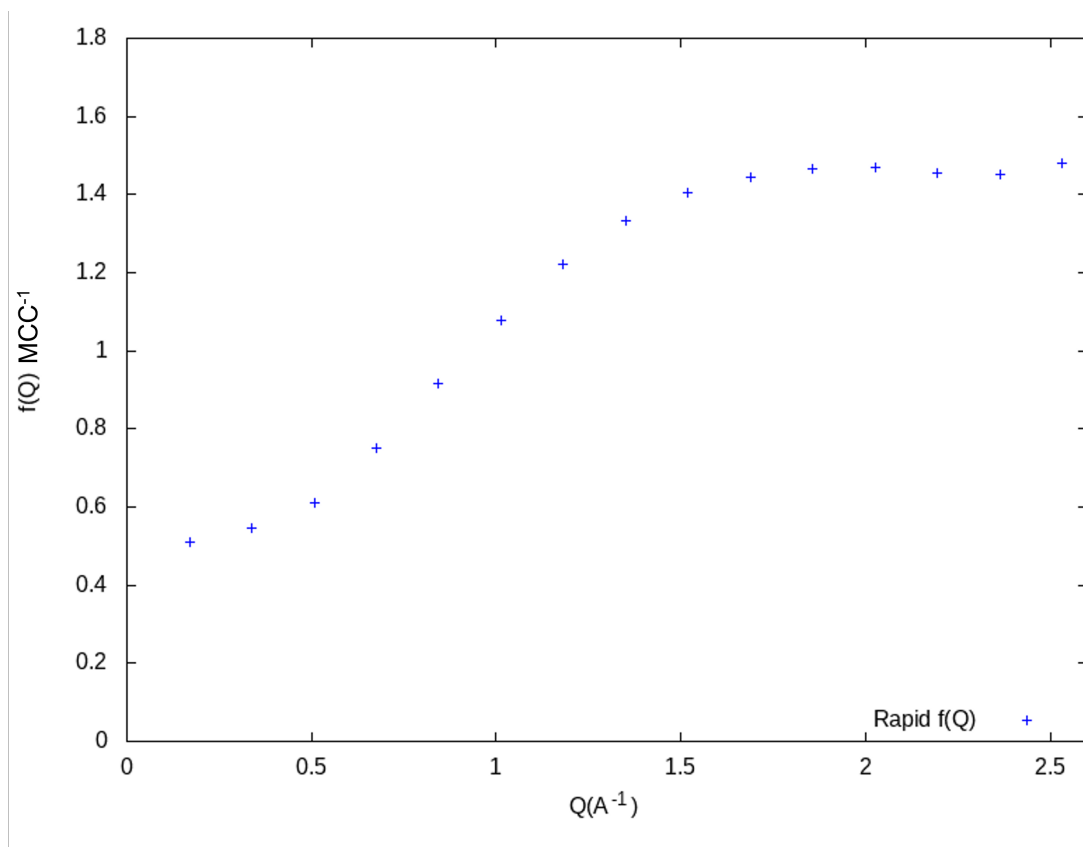
Figure 4.18: Widths from the short time scale component of $I(Q, t)$, for equal jump probabilities.

The weights of both component of the intermediate scattering fiction are also calculated during this process along with the elastic incoherent structure factor, Fig. 4.19 and Fig. 4.20.

105
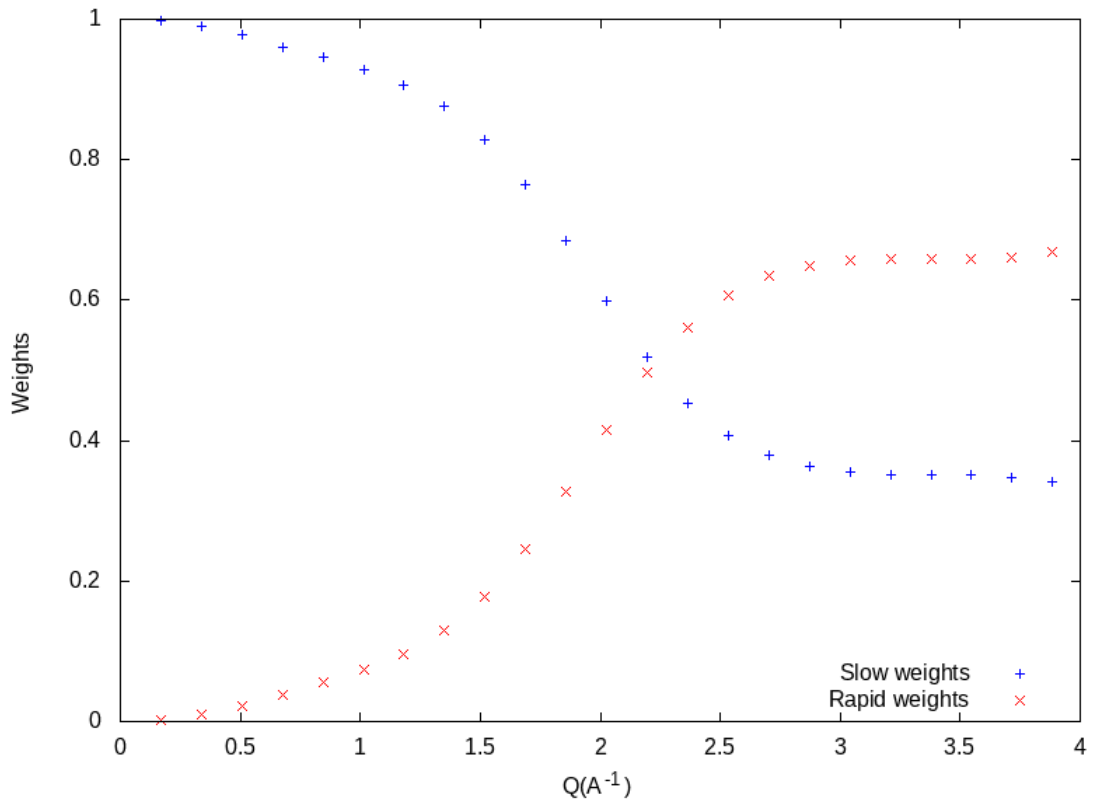
Figure 4.19: Associated widths for both the long and short time scale components of jump ratio = 1 $I(Q,t)$.

Supporting the evidence of localised motion taking place is the weights for the rapid localised motion in Fig. 4.19 they tend towards zero at low Q but increases as Q increases which is indicative to localised motion. The same behaviour is displayed in work by Schonfeld (Schönfeld et al., 1989) in Fig. 4.5. The Elastic incoherent structure factor produced below resembles that modelled by motion between two sites in Fig. 2.15.
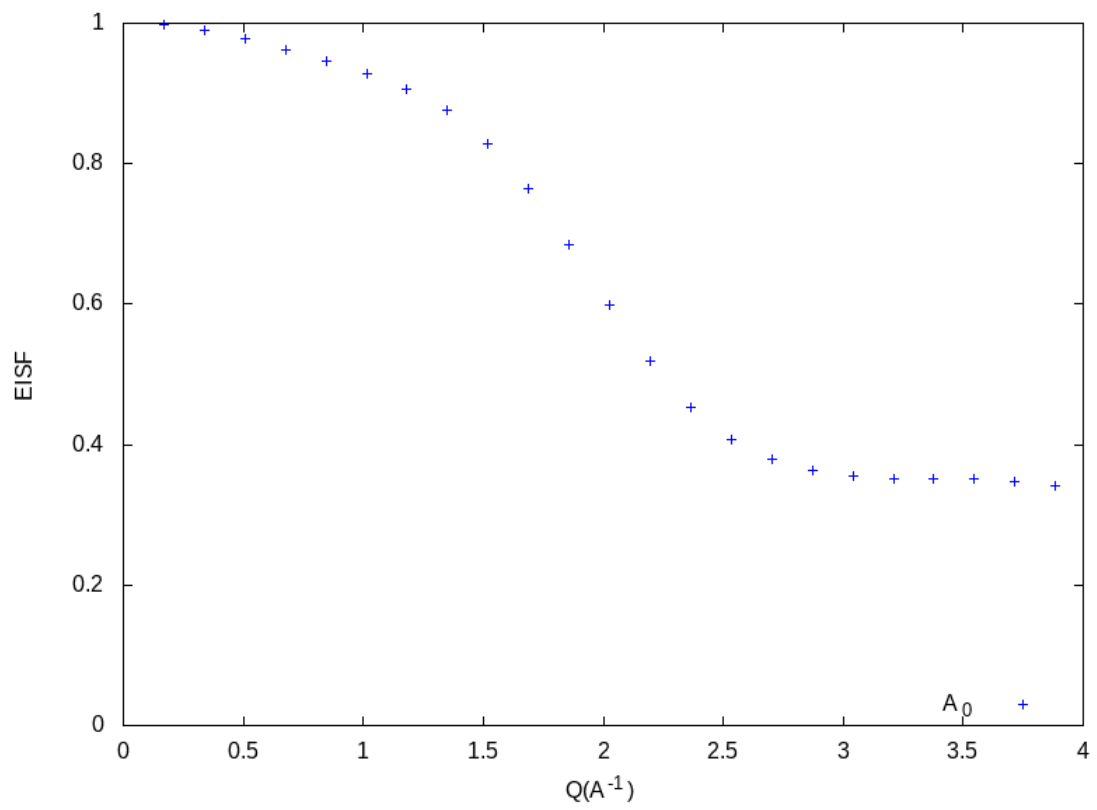
Figure 4.20: The Elastic Incoherent Structure factor for an equal jump ratio.

Single Crystal

The single crystal widths for the long time scale have also been examined to see what behaviour can be seen from given Q vectors through the unit cell; (1,1,1), (1,1,0) and (1,0,0).
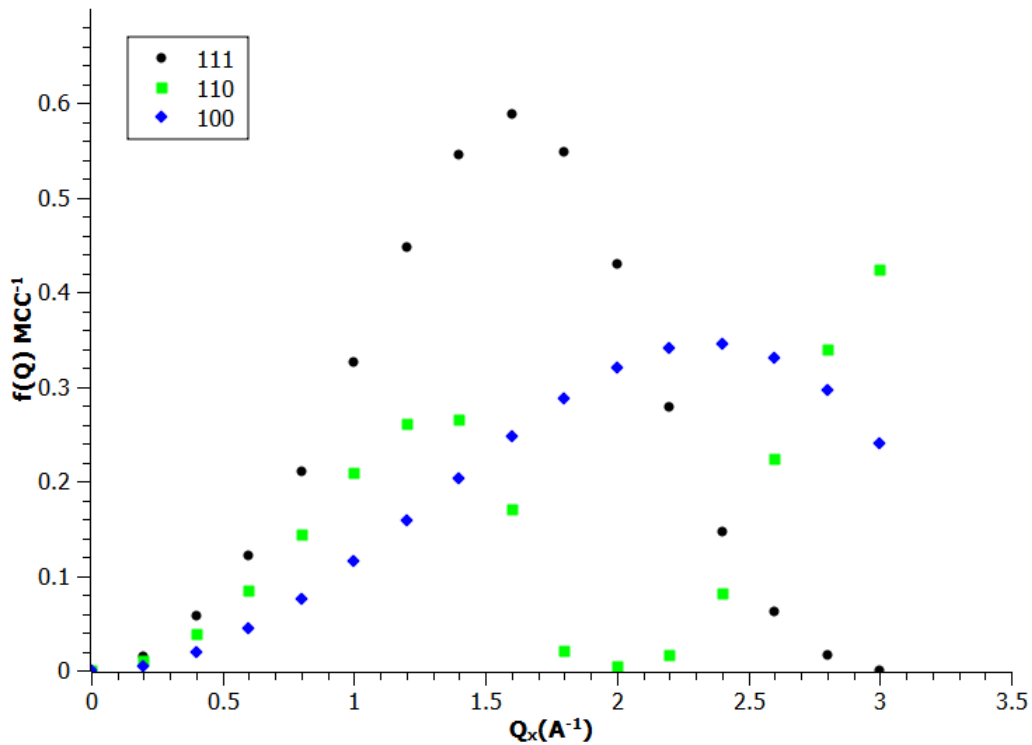
Figure 4.21: Fitted widths along the three Q-vectors (1,1,1), (1,1,0) and (1,0,0) when the jumpratio = 1.

It was expected that Chudley-Elliott type behaviour would be seen similar to that shown in the same directions in a face centered cubic lattice, however this dose not appear to be the case for the (1,1,0),(1,0.0) directions. In the (1,1,1) direction some similarity is shown to predictions from that of the Chudley and Elliott model.

4.4 Forced Jump Probabilities

Following on from the previous section it is now useful to see the effect of exaggerating the jump ratios such that the probabilities of jumps on each time scale occurring are significantly different. By varying the jump ratios from unity to 0.01 the effect of this can be seen in the long time scale polycrystalline directionally averaged widths, Fig. **??**.
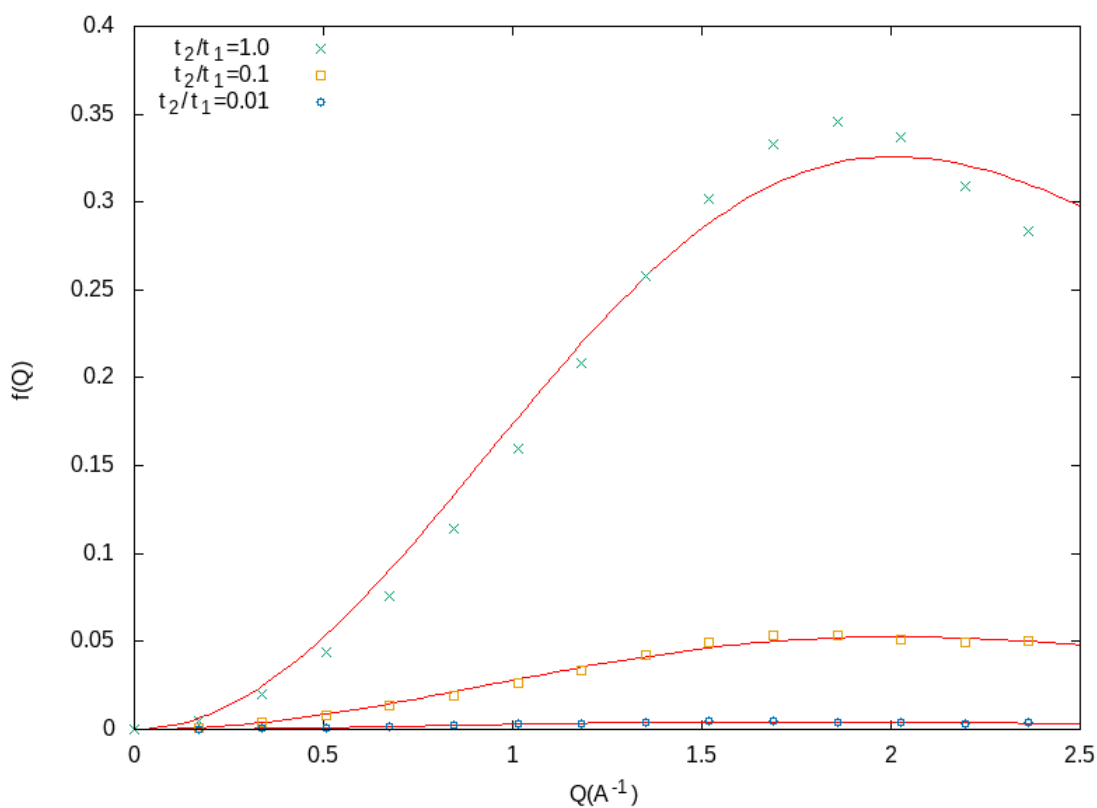
Figure 4.22: Comparison of the polycrystalline broadening when the jump ratios are varied from 1.0 to 0.01, where the lines are the predicted Chudley-Elliott model for each jump ratio

For both the jump ratios 0.1 and 0.01 the polycrystalline widths have been calculated for both the long and short time scales with associated weights. By fitting the polycrystalline form of the Chudley-Elliott model to the scattering

function of the large time scale the jump length l can be extracted for each of the jump ratios, giving 2.232 ± 0.044 Å and 2.661 ± 0.049 Å respectively Fig. 4.23

(a) Jump Ratio = 0.1 widths

(b) Jump Ratio = 0.1 weights

(c) Jump Ratio = 0.01 widths

(d) Jump Ratio = 0.01 weights
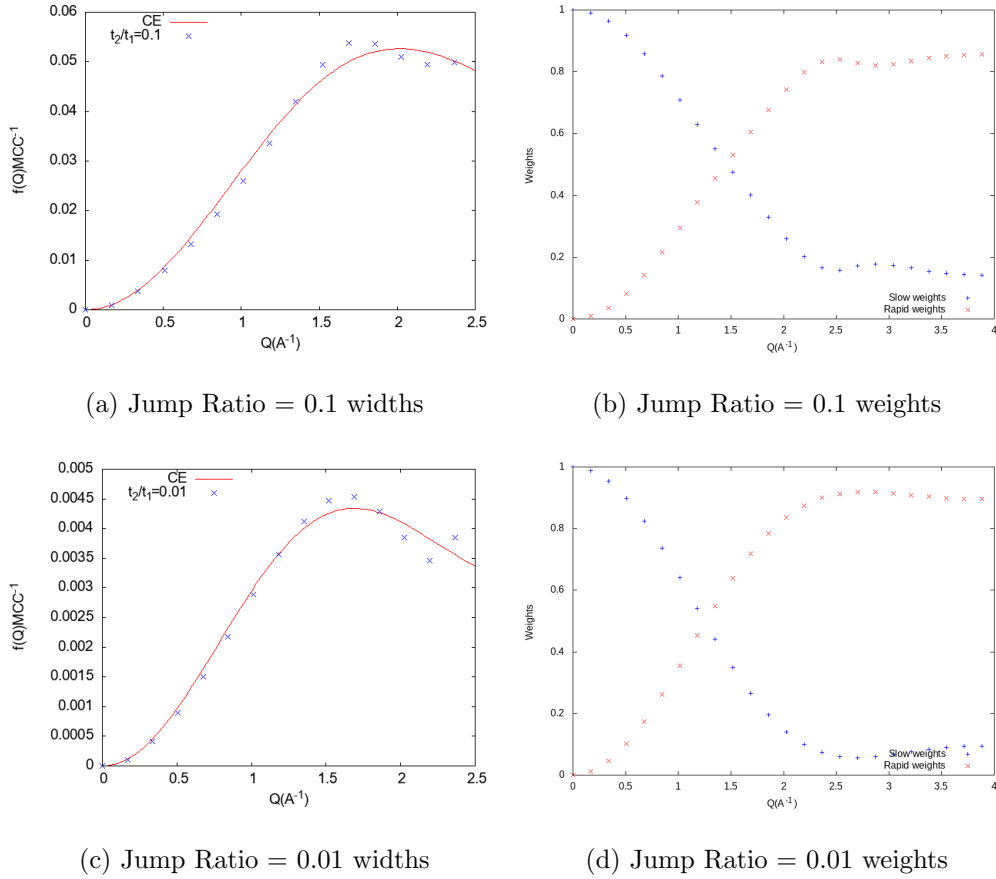
Figure 4.23: Both the polycrystalline broadening and the associated weights for jump ratios 0.1 and 0.01.

Again, a comparison between the methodology of approaching the calculation of the polycrystalline widths has been made as a means of testing the accuracy of each method for moving forward. Fig. 4.24.
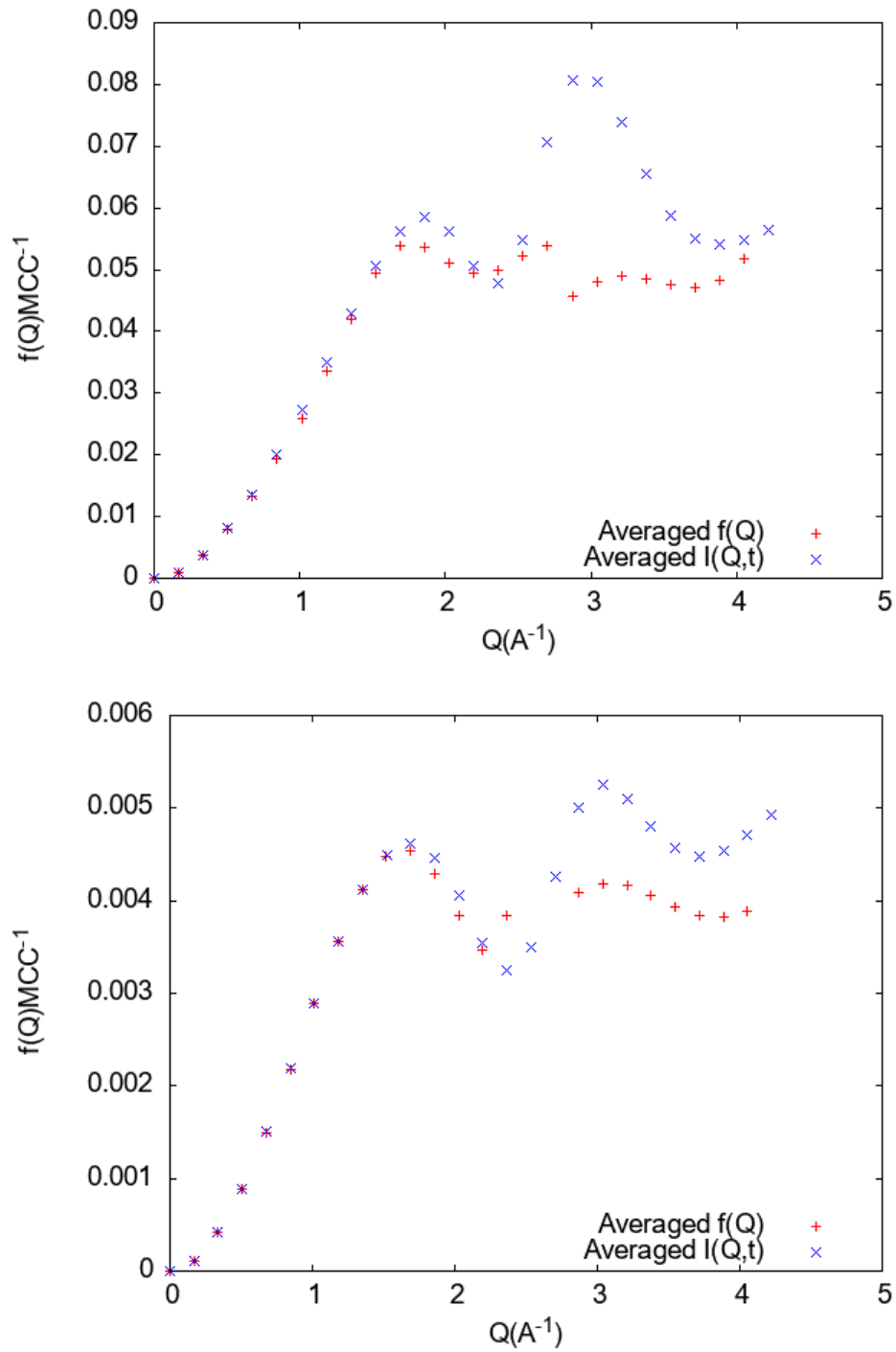
Figure 4.24: Comparison between the averaged decay constants of I(,t) and the decay constants of averaged I(Q,t)'s. 0.1(top), 0.01(bottom).

111

The comparisons between the directionally averaged I(Q,t)s and the directionally averaged f(Q)s in Fig.4.24 shows that the widths calculated a the first peak and at lower Q values are in good agreement. As the Q values increase the directionally averaged I(Q,t)s display an over estimation of the polycrystalline widths, resulting in a second peak of higher intensity, whereas the directionally averaged widths produce data points at higher Q vales to be expected in line with the Chudley-Elliott model for a polycrystalline structure.

The localised component (Fig. 4.25) of the scattering function has been calculated following the same procedure as used when calculating the components for the equal jump rates.
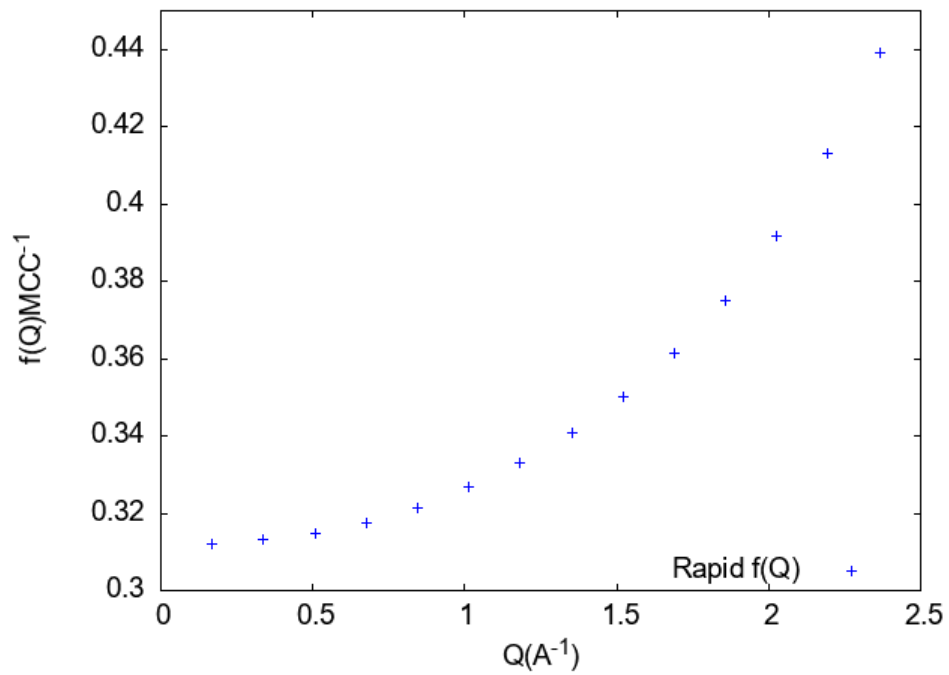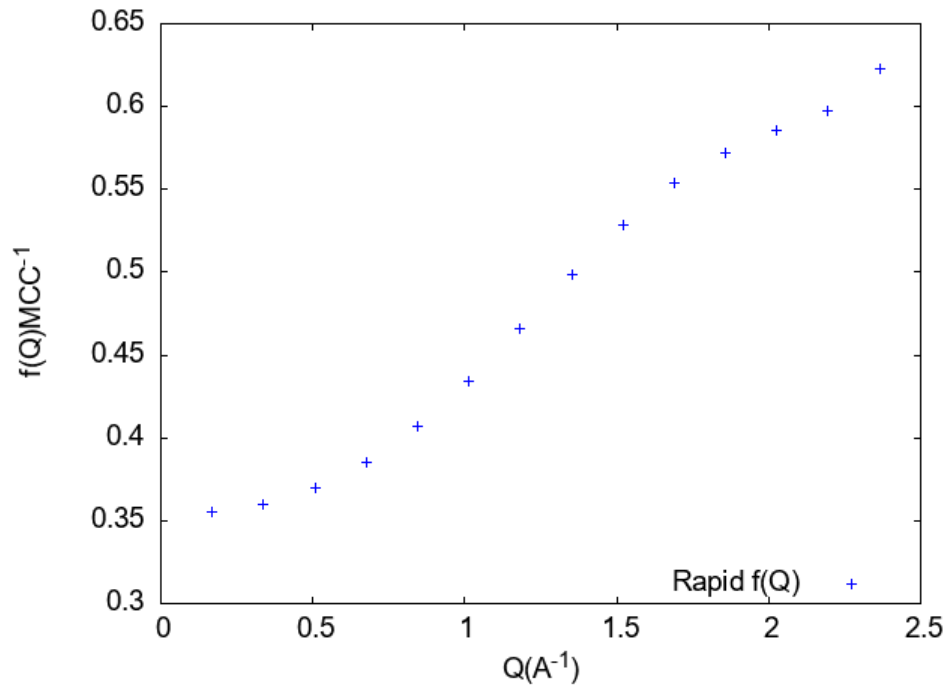
Figure 4.25: The widths extracted from the rapidly decaying exponential on the shorter time scale for both 0.1 (top) and 0.01 (bottom) jump rate ratios.

Here the presence of localised motion is confirmed by the widths tending towards a finite value at low Q values (Fig. 4.25), if there was no localised component to the intermediate scattering function then it would be expected that this would go to zero at low Q values. The elastic incoherent structure factors for each of the jump rate ratios have also been compared.
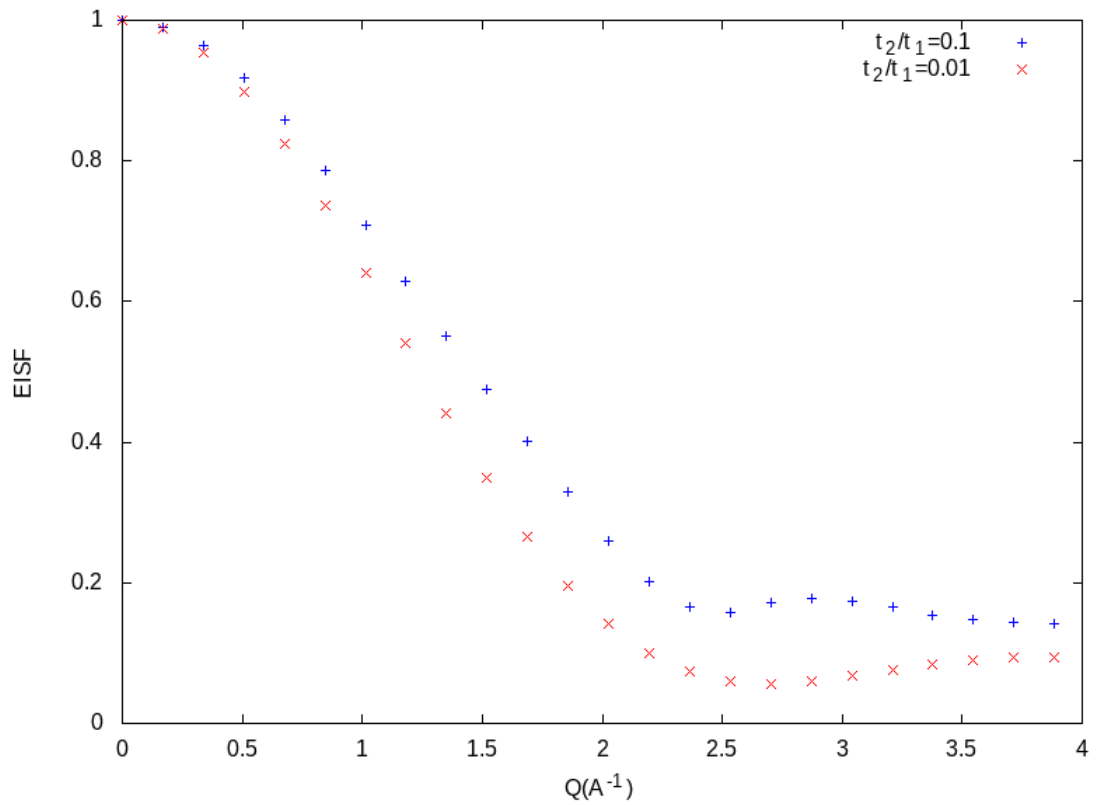
Figure 4.26: Elastic Incoherent Structure factor for both the 0.1 and 0.01 jump ratios.

4.5　Temperature Dependence

In order to investigate the effect of temperature on the Quasi-elastic broadening calculated from Monte-Carlo simulations values for barrier height's in eV were introduced to give a more realistic jump rate ratio. The barrier heights used here have been taken from previous work carried out by Bhatia and Sholl (2005) utilising transition state theory for high and low temperature limits in ZrV_2 given as 0.165eV and 0.063eV. In the Monte-Carlo runs preformed here for varying temperatures, the low temperature value being used for intra-hexagon jump length (g-g) and the high temperature value used for inter-hexagon jump length (g-g') the jump ratio has been set to 1 in the following calculations such that the barrier heights and temperature are the only governing factors in the resulting jumps.

Initially the single crystal case was looked at along three specific Q vectors; (1,1,1), (1,1,0) and (1,0,0). Carried out over a temperature range of 250K-500K with a concentration of 0.0417 and lattice parameter of 7.44 Å.
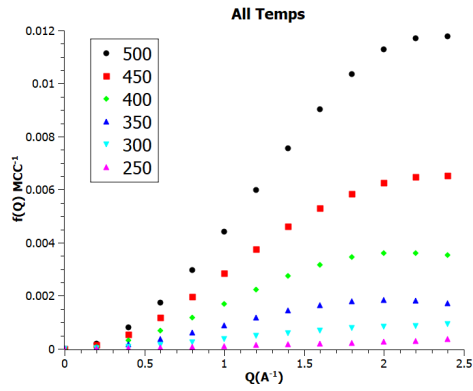
(a) All temperatures along (1,0,0)
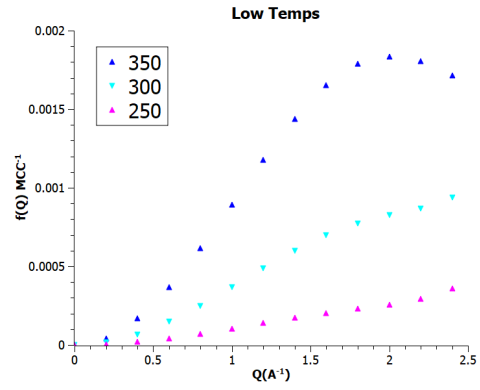
(b) Low temperature range along (1,0,0)
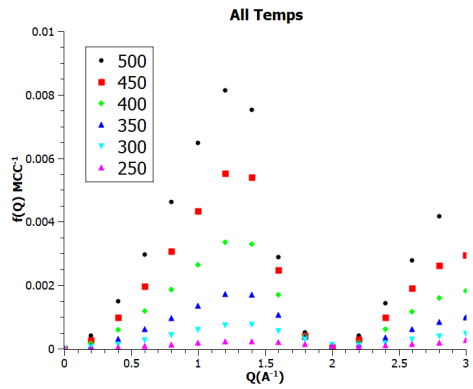
(c) All temperatures along (1,1,0)
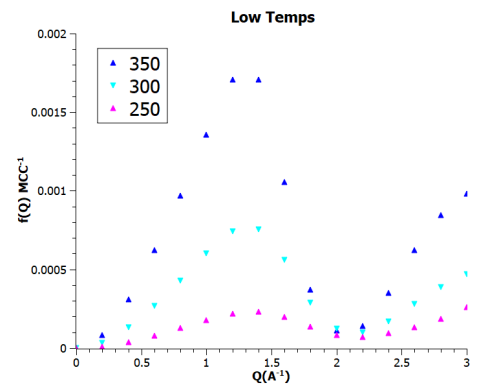
(d) Low temperature range along (1,1,0)
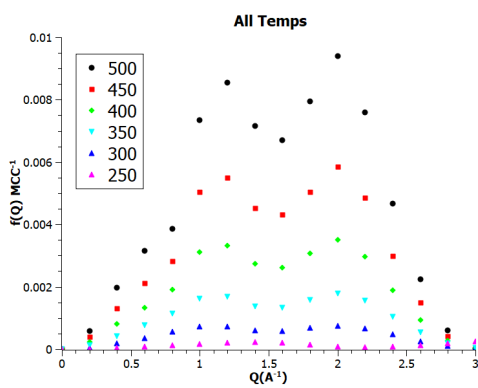
(e) All temperatures along (1,1,1)
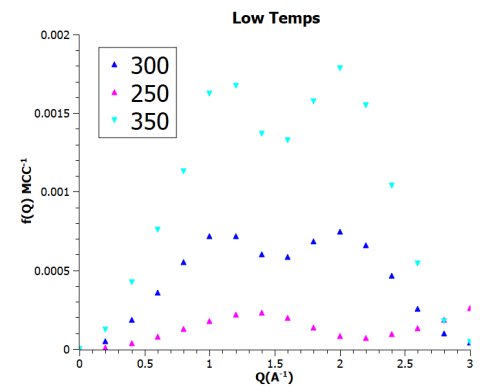
(f) Low temperature range along (1,1,1)

Figure 4.27: Single crystal broadening separated for low and high temperatures along vectors (1,1,1), (1,0,0) and (1,0,0).

116

The widths from the long time scale do not appear to follow Chuddly-Elliot type diffusion, this could be due to the multiple diffusion processes occurring in the C15 system. The double peak seen in the (1,1,1) that appears to be more pronounced at higher temperatures could be a result of thermally activated jumps from both the g-g sites and the g-g' sites.

4.5.1 Polycrystalline

Long time Scale

To gain a more complete picture of the movement of particles in ZrV_2 the polycrystalline case can be examined. This will give a more direct comparison to the results seen from QENS experiments as it is often due to the nature of the samples that the polycrystalline case is investigated. All the parameters are kept the same as for in the single crystal case. Working along the hypothesis that there is two types of motion occurring two time scales for each temperature are evaluated. The importance here is if from this longer time scale, the Chudley-Elliott model for long range diffusion can be extracted.
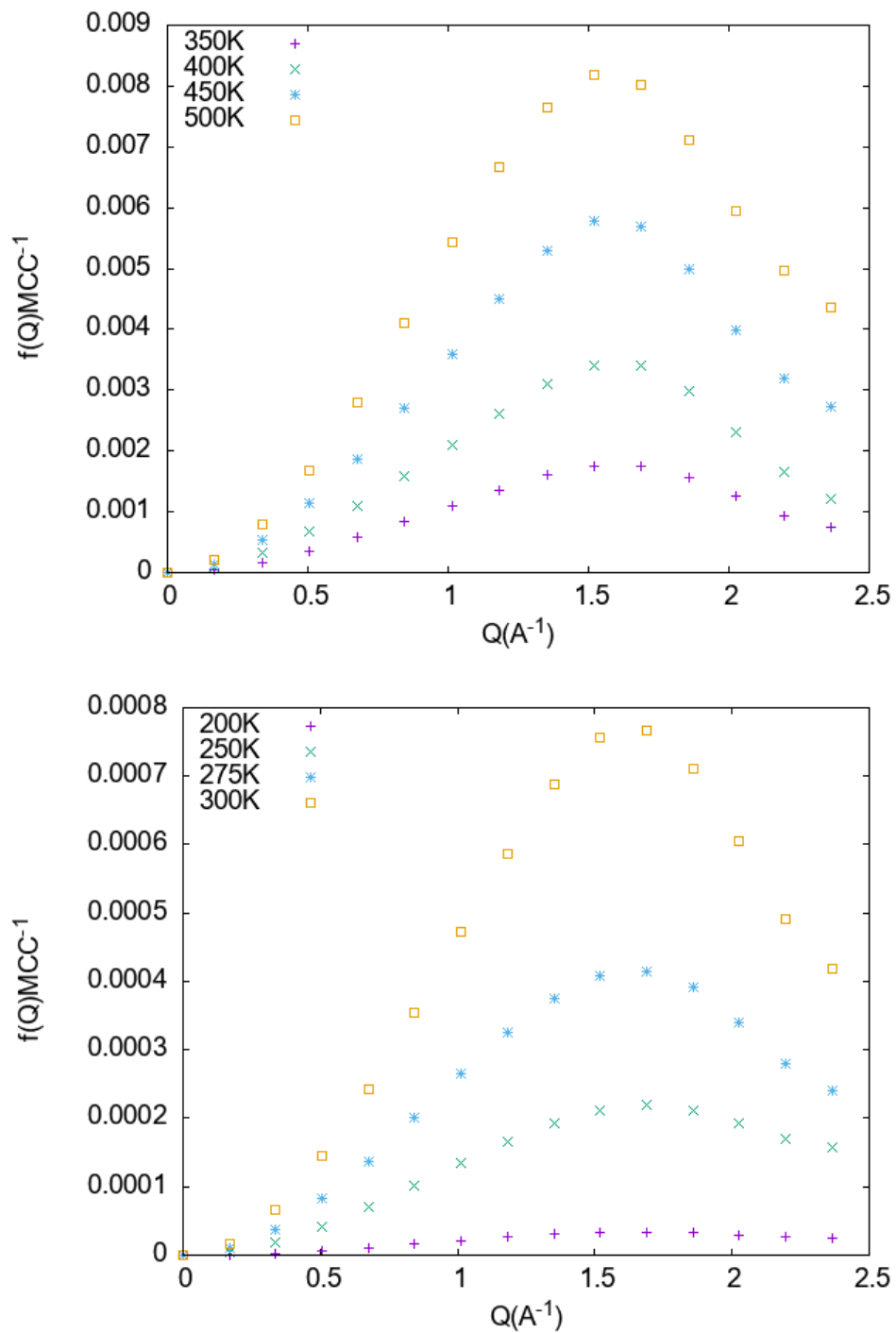
Figure 4.28: Polycrystaline widths $f(Q)$ from a single exponential fit of reduced set of points at high and low temperatures.

118

The polycrystalline HWHMs for multiple temperatures calculated from a single exponential fit Fig.4.28 to the slowly decaying component of the directionally averaged I(Q,t). By fitting the polycrystalline Chudley-Elliott model eqn.4.5 to the long-time scale scattering function the jump lengths (l) can be extracted

$$f(Q) = A \left[1 - \frac{\sin(Ql)}{Ql} \right] \tag{4.5}$$

(a) 200K widths

(b) 300K widths

(c) 400K widths

(d) 500K widths
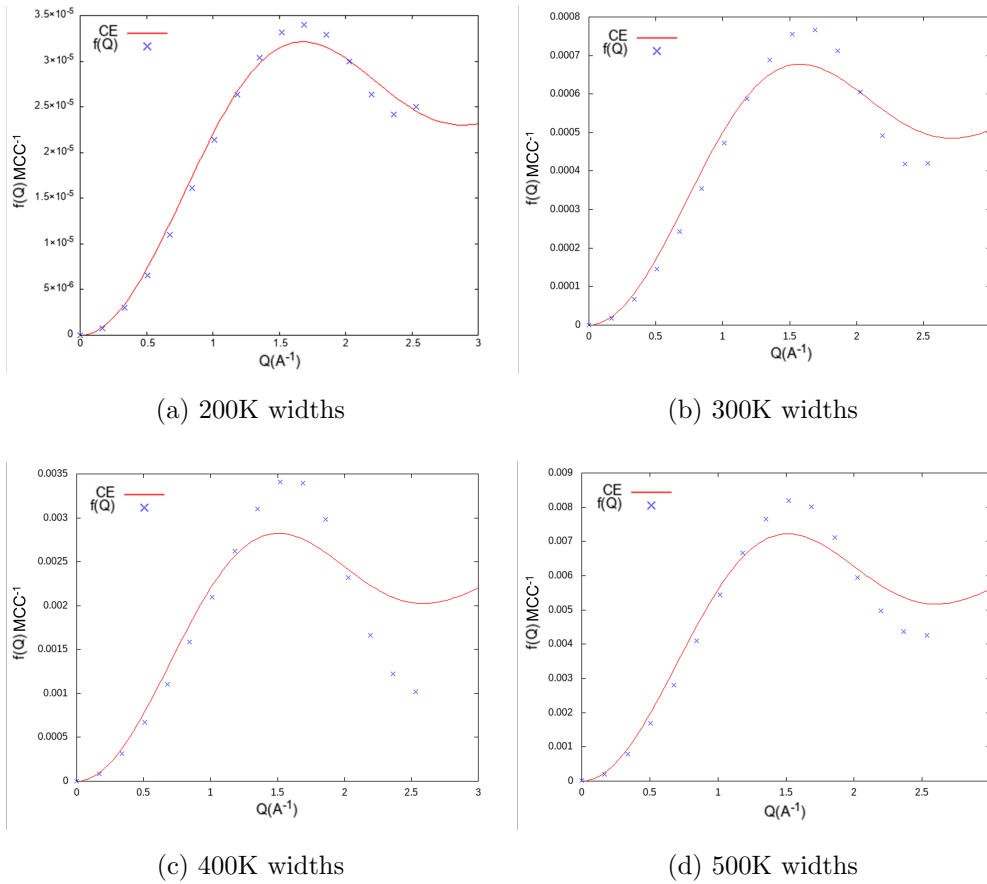
Figure 4.29: Polycrystalline broadening with Chudley Elliott model fits included at 200K, 300K, 400K and 500K.

119

At a lower temperature such as 200K Fig.4.29(a) there is good agreement at low Q-values with the Chudley Elliott model, as the Q increases there is a slight divergence from the Chudley Elliott model, this divergence can also be seen to increases as the temperature increases seen in fig.4.29(b)(c) but still in close agreement at $Q < 1\AA^{-1}$. By fitting the Chudley-Elliott polycrystalline model an estimate of the jump length can be made, due to the large divergence at higher temperatures the errors associated with this fit become significantly larger as seen in Table.4.1. This divergence could be due to the need to directionally average the fitted widths.

Temperature(K)	Amplitude	l($\AA$) (MC)	l($\AA$) (exp)
200	2.6402e-05	2.6766 ± 0.0433	
250	0.0002	2.7237 ± 0.0531	
300	0.0006	2.8477 ± 0.1068	
350	0.0012	2.9739 ± 0.1820	2.6
400	0.0023	3.0010 ± 0.2287	3.0
425	0.0032	2.9005 ± 0.1225	
450	0.0040	2.9661 ± 0.1498	3.4
500	0.0059	2.9685 ± 0.1135	4.3

Table 4.1: Comparison of fitted jump lengths via the Chudley-Elliott model model with amplitudes and experimental jump length values (Bull and Ross, 1999a)

Directionally averaged Widths

Instead of passing the calculated total I(Q,t) from the 24 bases to the Lebedev function the fitted width f(Q) is passed to the Lebedev function for each of the generated Q-vectors. The comparison between both the directionally averaged intermediate scattering functions and the directionally averaged HWHMs can be seen below. A selection of temperatures from the range have been shown (Fig.4.30,4.31,4.32) win which it can be seen that the HWHMs for the directionally averaged widths deviate less from the Chudley-Elliott model.
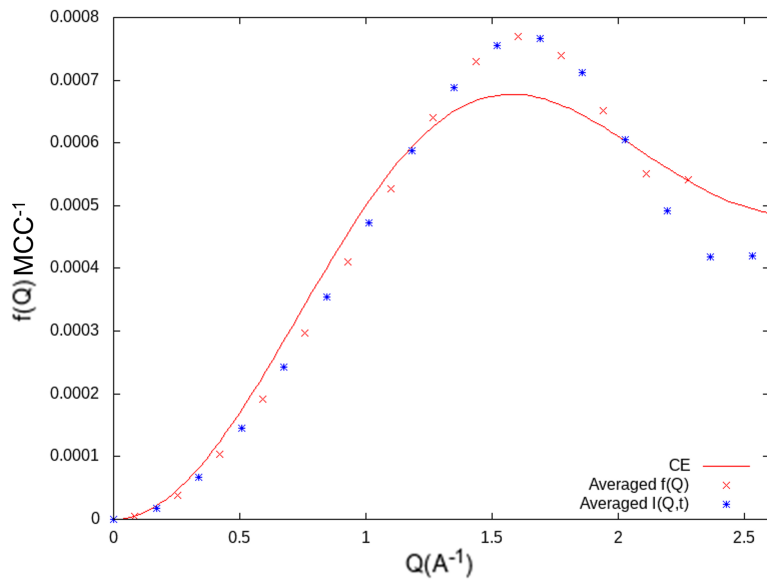
Figure 4.30: Comparison between the directionaly averaged decay constants of I($\mathbf{Q}$,t) and the decay constants of I(Q,t)s at 300K.
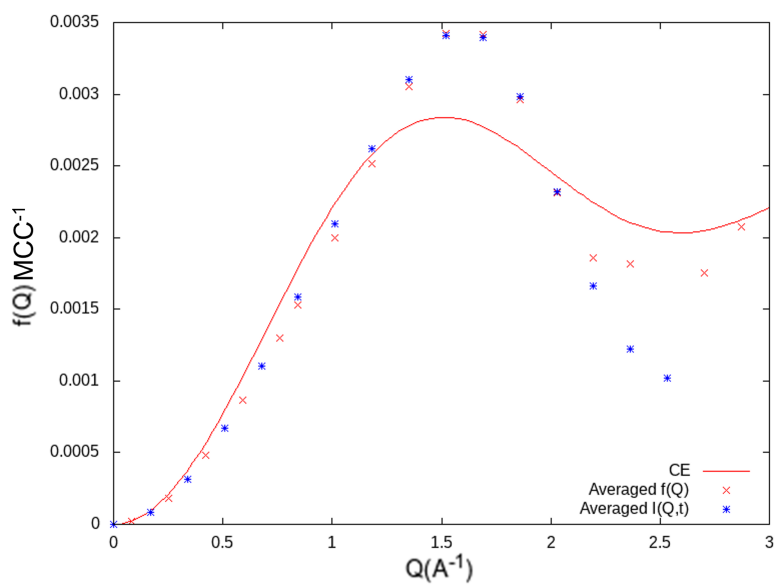
Figure 4.31: Comparison between the directionaly averaged decay constants of I($\mathbf{Q}$,t) and the decay constants of I(Q,t)s at 400K.
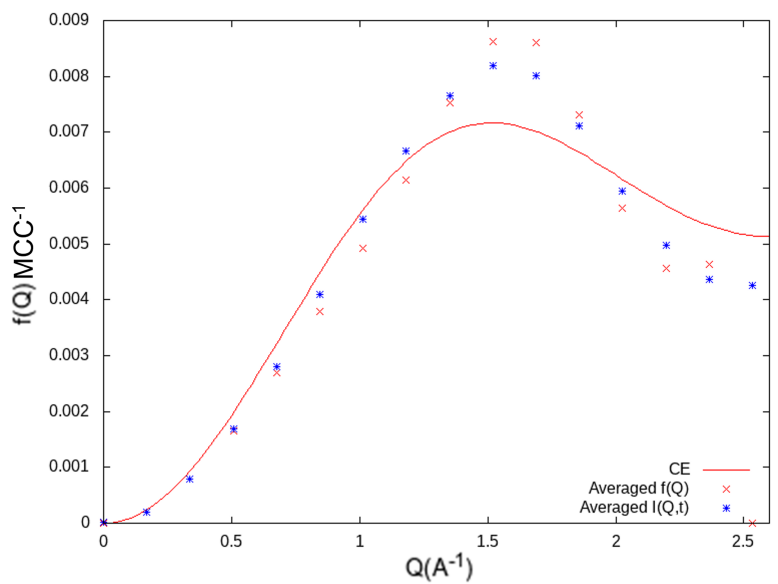
Figure 4.32: Comparison between the directionaly averaged decay constants of I($\mathbf{Q}$,t) and the decay constants of I(Q,t)s at 500K.

Comparing now the estimated jump lengths from the both methods (Table.4.2) at temperatures that showed a large deviation from the Chudley Elliot model, an increase in jump length with temperature can still be seen however the large error in the Chudley Elliot fit still persists all be it slightly smaller, raising doubt if this is indeed the best way to approach extracting the jump length from the Monte-Carlo simulated data.

Temperature(K)	Ave $I(Q,t)$ l(Å)	Error($\pm$Å)	Ave $f(\mathbf{Q})$ l(Å)	Error($\pm$Å)
300	2.848	0.107	2.931	0.098
400	3.001	0.229	2.978	0.105
500	2.969	0.113	2.963	0.108

Table 4.2: Table comparing the fitted jump lengths of the directionally averaged widths and the directionally averaged intermediate scattering functions

An alternative method was derived in order to estimate the jump length from the MC calculated incoherent scattering function. By fitting a 2nd order polynomial to the first peak over the scattering function to determine the turning point of the curve Q_{max}, this can then be related back to the jump length by,

$$l = \frac{3\pi}{2Q_{max}} \tag{4.6}$$

With this method for extracting the jump lengths the non-interacting polycrystalline jump lengths have been calculated, table.4.3 again these are compared to experimental QENS results,

Temperature (K)	Jump length l(Å)	Jump length Exp l(Å)
200	2.81	
250	2.83	
275	2.88	
300	2.92	
350	2.97	2.6
400	2.99	3.0
450	3.00	3.4
500	3.02	4.3

Table 4.3: Directionally averaged $f(\mathbf{Q})$ jump lengths compared to experimentally calculated jump lengths.

Localised Motion

By using the example shown earlier in the chapter where solely localised motion is taking place, it can be seen that the fitted width at small Q does not go to zero as would be expected if there was no localised motion occurring, We can then apply this same reasoning when looking at the HWHM's for the double exponential fit to the rapidly decaying time scale. As $Q \to 0$ the widths tend towards a finite value which can be indicative of localised motion Fig.4.33. The weights for the rapidly decaying component of the intermediate scattering functions decreases with decreasing Q and goes to zero at Q=0.
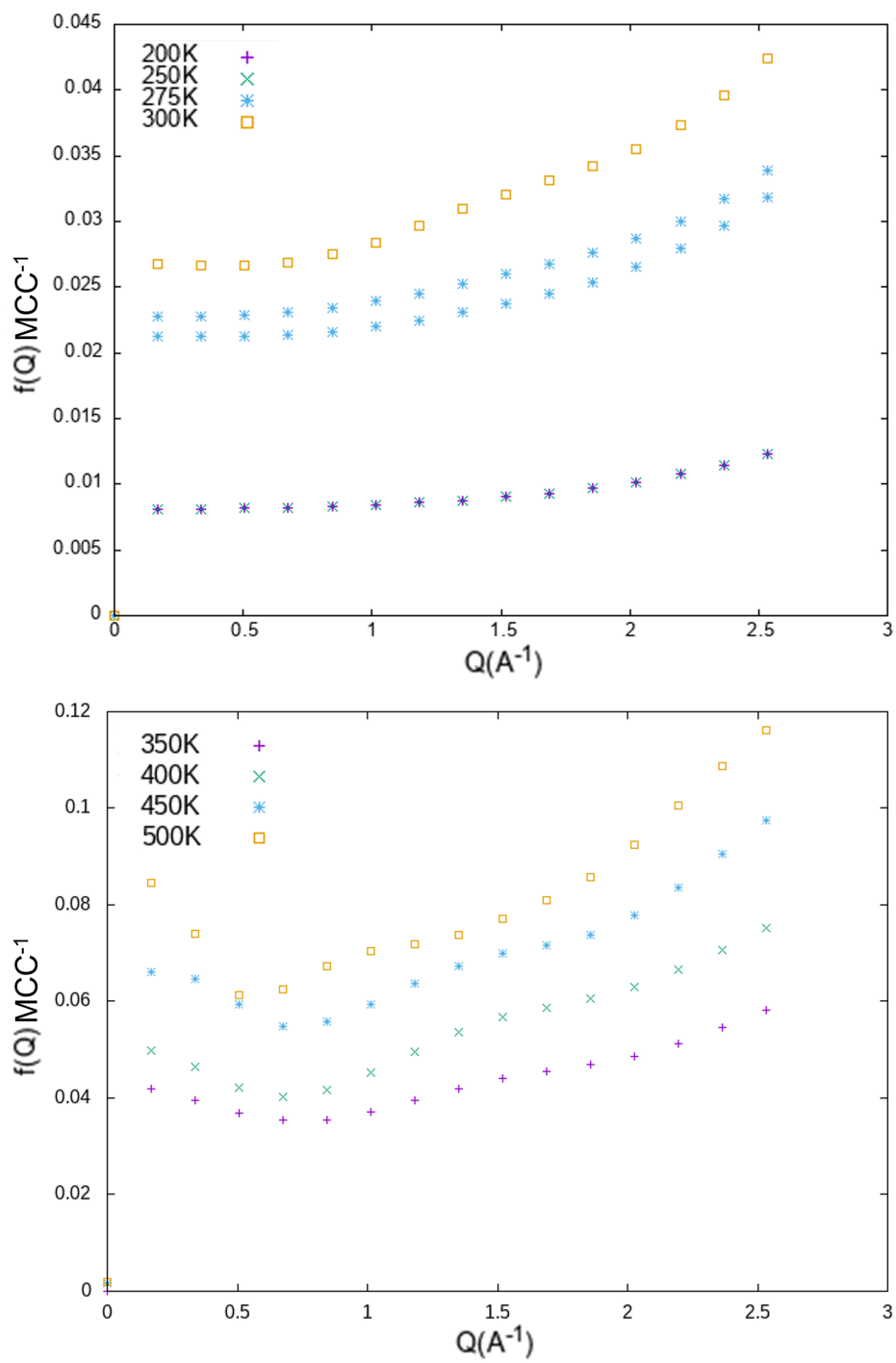
Figure 4.33: Widths from the double exponential fit over a range of temperatures.
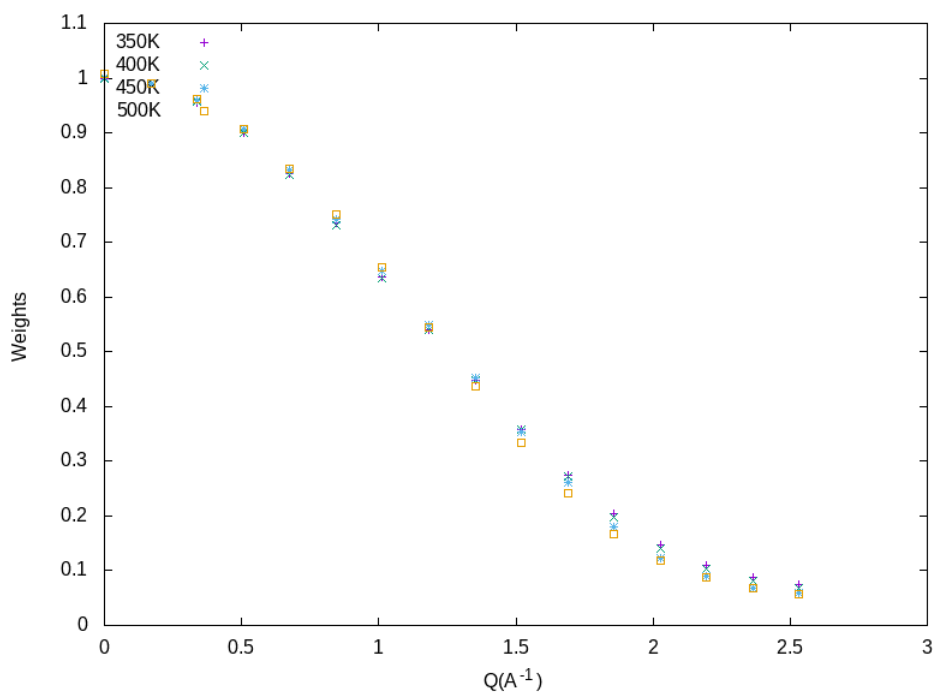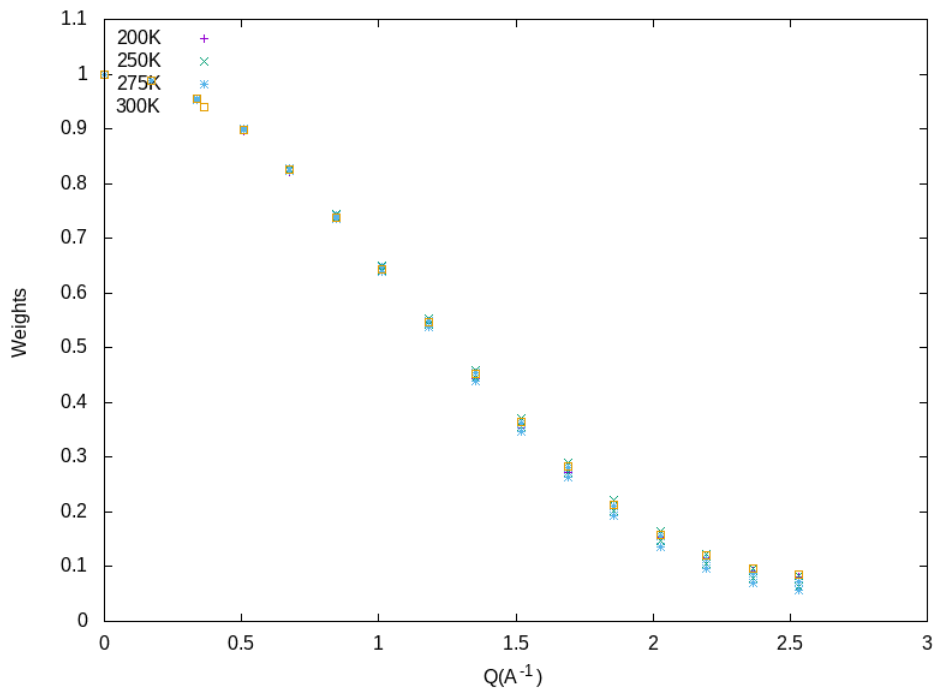
Figure 4.34: Associated weights of the rapid time scale for both low and high temperatures.

The behaviour of the data presented here displays similarities to the behaviour described in data presented by C.Schonfeld, R.Schatzler and R.Hempelmann in 1989 (Schönfeld et al., 1989) from QENS experiments. These results also add credence to experimental QENS results measured on the time-of-fight spectrometer IN5 Fig. 4.35.
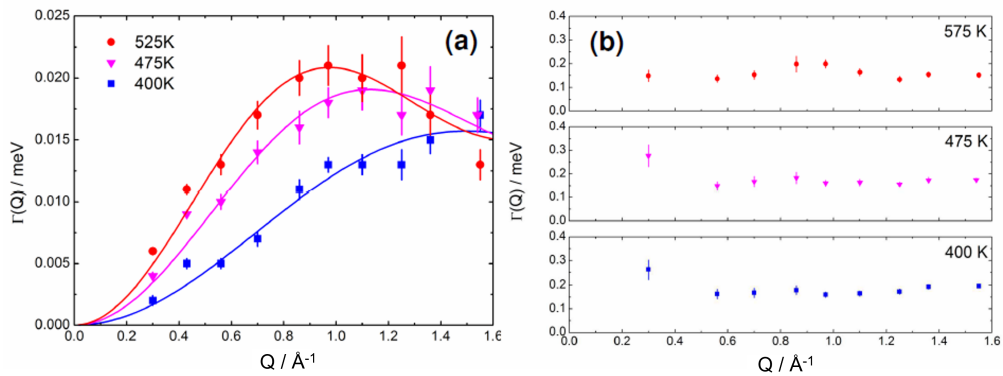
Figure 4.35: Experimental Quasi elastic broadening results from both time scales carried from IN5 spectrometer.

The form of the rapidly decaying component of the MC simulated intermediate scattering functions shows similarities with the form given by the widths of the broad Lorentzian component from QENS. Further information about the motion of the diffusing hydrogen can be gleaned from the EISFs for given temperatures.
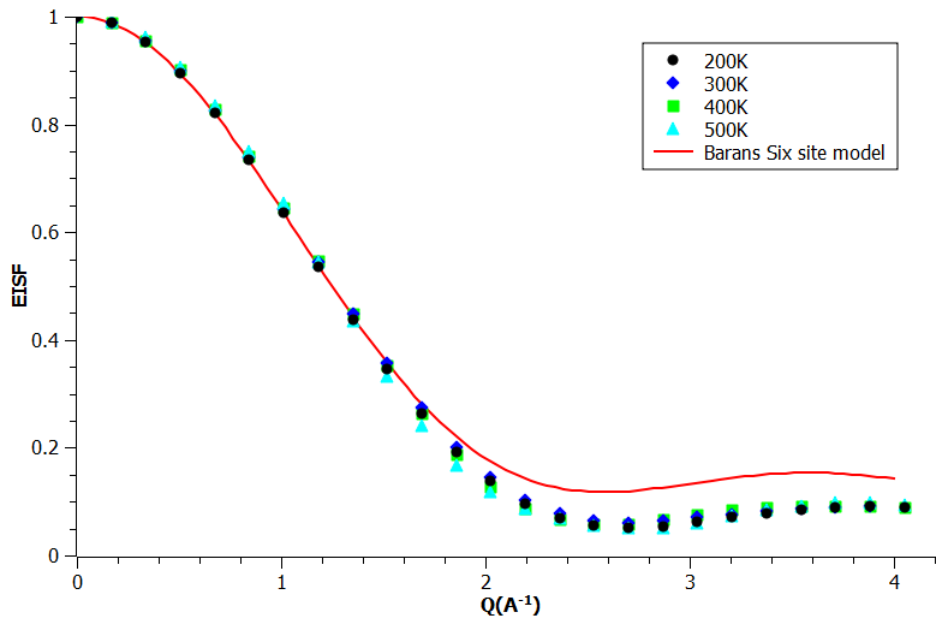
Figure 4.36: Elastic incoherent structure factor for a range of temperatures compared with the six site barans model.

The elastic incoherent structure factors appear to show similarities with six site Barnes model show by the solid red line in Fig. 4.36 with an $l = 0.13906a$ which is the ideal jump length for jumps between g-sites on the same hexagon. The results of the EISF can be seen to suggest that there is indeed localised motion around neighbouring g sites on the same hexagon.

4.5.2 Hydrogen pair interactions

A reasonable next step in building up a more comprehensive picture of the system with the introduction of hydrogen-hydrogen interactions. Lee (1993) obtained parameters for repulsive H-H interaction estimated by calculating hydrogen uptake as a function of chemical potential using the grand canonical ensemble Monte-Carlo simulation, implemented by means of a stepped potentials involving a hard sphere blocking radius of 0.2a and a stepped potential out to a radius of 0.38a, further out the potential drops to zero.

$$
V_{H-H}(r) = \begin{cases} 0.2\text{eV}, & 0.2 < r \leq 0.27a \\ 0.05\text{eV}, & 0.27 < r \leq 0.38a \\ 0\text{eV}, & r > 0.38a \end{cases} \tag{4.7}
$$

Following the same process as the non-interacting polycrystalline case the HWHMs for the rapidly decaying and slowly decaying time scale have been calculated for the same range of temperatures so that the effect of the H-H interactions can be seen.
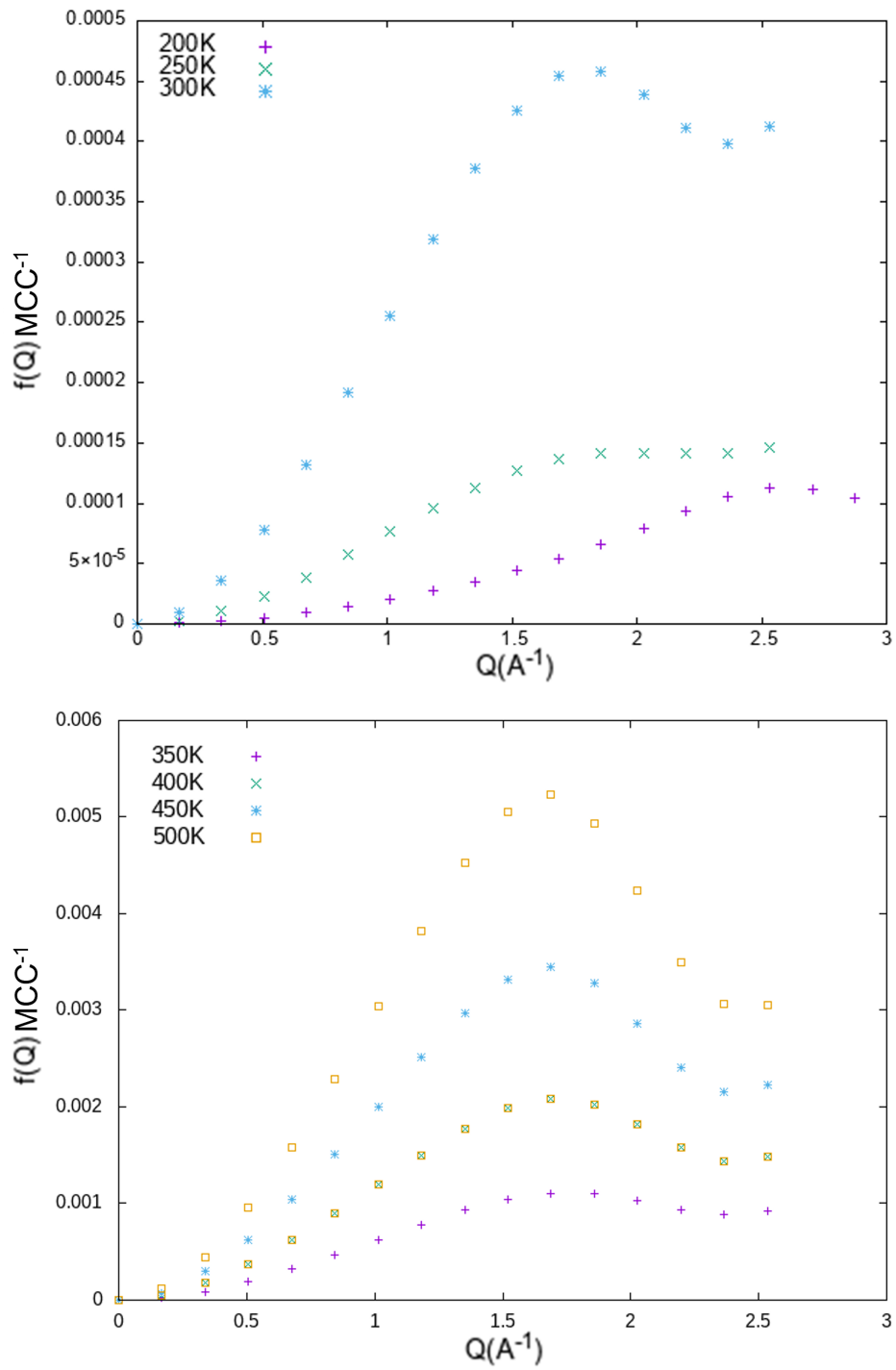
Figure 4.37: Directionally averaged polycrystalline Decay constants f(Q) from a single exponential fit with hydrogen pair interactions included.

130

Following the method used to estimate the jump lengths from the long-time scale in the non-interacting case, the jump lengths can be estimated for the H-H interactions polycrystalline case.

Temperature(K)	Non Interacting l(Å)	Interacting l(Å)
200	2.8127	1.7991
250	2.8339	2.3383
300	2.9226	2.5817
350	2.9766	2.6625
400	2.9923	2.7675
450	3.0026	2.8157
500	3.0206	2.8385

Table 4.4: Comparison of fitted jump lengths from the interacting and non-interacting hydrogen cases.

An effective increase in jump lengths can be seen in both instances, however when interactions are included an overall decrease in the magnitude of the jump length is observed. Although displaying the same trend as the experimental results the magnitude of the jump lengths at higher temperatures deviates from this data.

Localised motion

With the inclusion of Hydrogen pair interactions the widths can be seen to again tend towards a finite value as the value of Q decreases as displayed in the non-interacting case. In the lower temperature range this is more defined further out in Q but at higher temperatures this appears to only be the case at $Q < 1 Å^{-1}$.
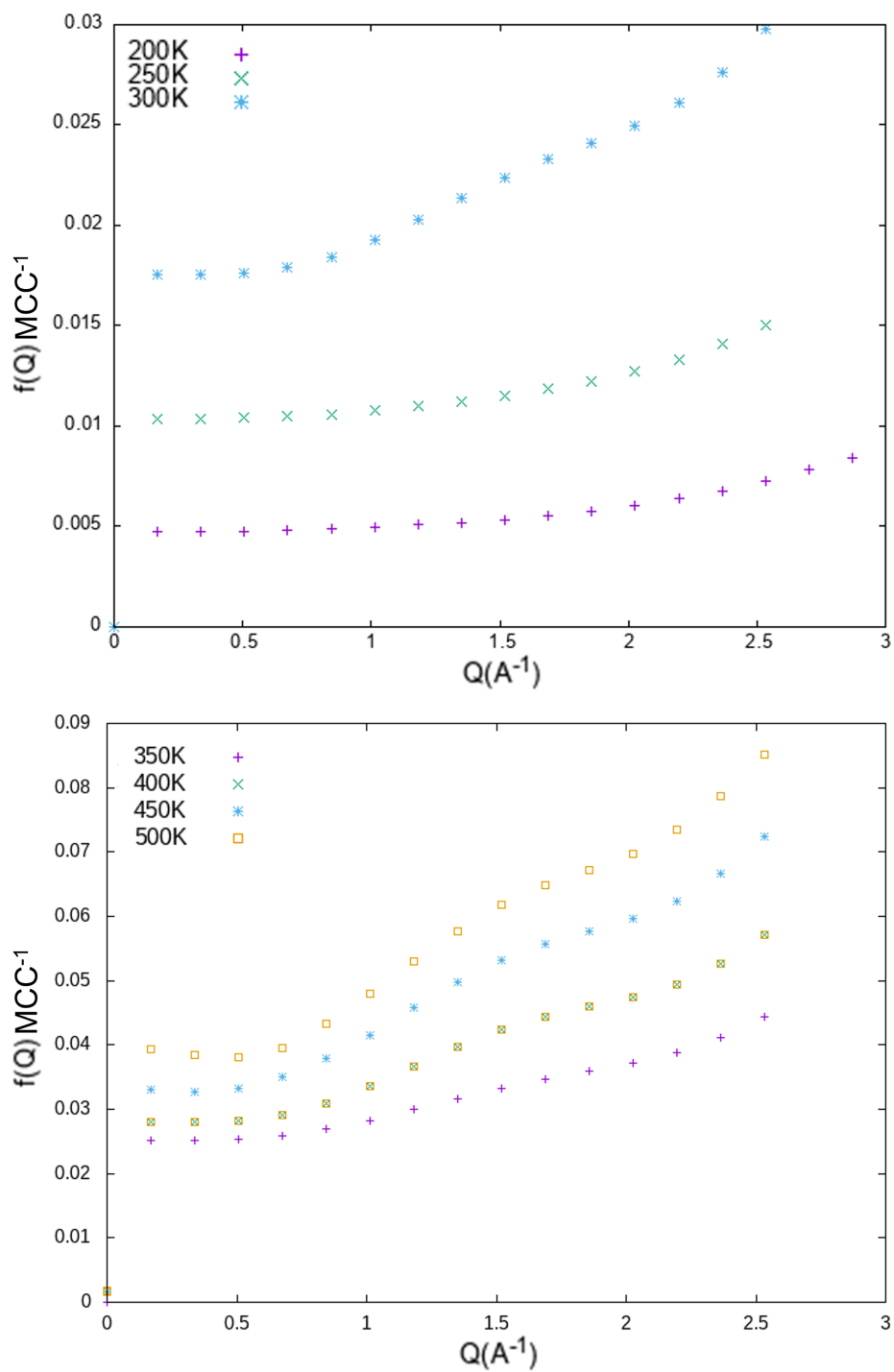
Figure 4.38: Directionally averaged polycrystalline decay constants f(Q) from a double exponential fit with hydrogen pair interactions included in the short time scale.

132

The interactions brings the EISF into good agreement with the six site model for the temperatures used when compared to the non-interacting case where the Barnes model appeared to be an over estimate of the elastic incoherent scattering function.
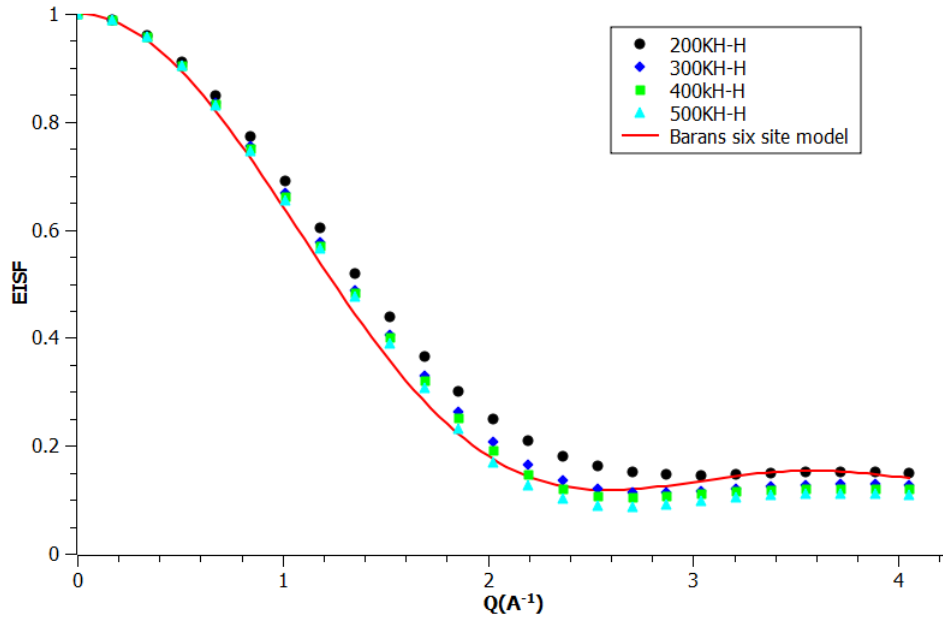
Figure 4.39: Elastic incoherent structure factor for temperatures when hydrogen pair interactions are included, showing agreement with the Barnes six site model.

Looking at a system such as ZrV_2H where localised motion is expected to be seen and has been suggested in previous experimental work stands as a good example of the behaviour of the widths produced from the rapidly decaying component when localised motion is present. Because of this it is helpfully to compare the results from other systems such as the PdH system discussed in the preceding chapter to give an insight into the behaviour of hydrogen among interstial sites where localised motions is hypothesised or believed to not exist from the results of experimental quasie-elastic neutron scattering.

Chapter 5

Monte-Carlo Simulations of Palladium Hydrides

5.1   The Pd-H system

Pd has a face centred cubic crystal structure with two available interstitial sites for hydrogen occupation. The relative geometrical simplicity of the hydride makes it an attractive material for hydrogen studies. One key property is its ability to retain a face-centred cubic (fcc) structure, Fig. 5.2, suffering very little macroscopic deformation after a series of loading and unloading cycles. In other metals and intermetallic compounds, internal stresses on hydrogen loading causes brittle fracture to occur, causing the host lattice to turn into a powder.
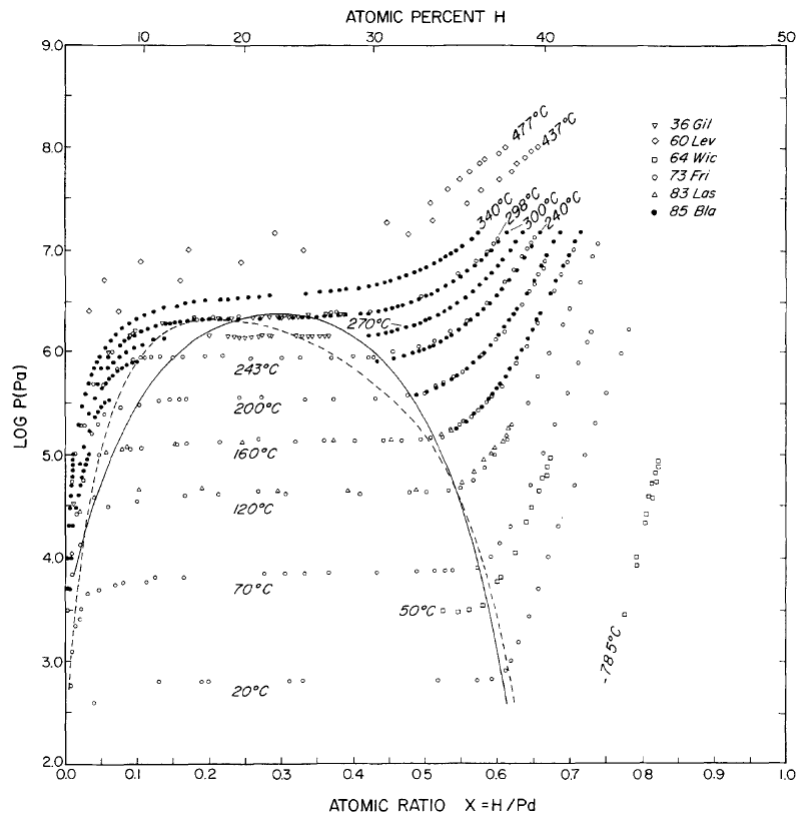
Figure 5.1: Pressure vs composition isotherms for the Pd-H system. Compiled data by (Manchester et al., 1994).

Palladium in its equilibrium state has a lattice constant of 3.88Å with only a very small expansion at low concentrations during the α-phase (the dilute disordered hydrogen phase). According to Density Functional Theory calculations, this increases to 4.07Å for full octahedral-site occupation (Elsässer et al., 1991), as a result of local lattice deformation around occupied octahedral sites in both the α and β (the ordered hydride) phases. A small average expansion of the lattice is attributed to α-phase, whereas as H concentrations increases in the β-phase there is a larger increase in the lattice parameter. Fig 5.1 shows pressure-composition isotherms for the equilibrium thermodynamics of these two phases along with the mixed phases for given

135

temperatures collated from previous works (Manchester et al., 1994). During the absorption of hydrogen into palladium, molecular hydrogen readily dissociates at the palladium's surface. It has been suggested from palladium nano-particles that up to a few layers deep (subsurface) the tetrahedral site can become occupied due to them being stabilised, however the octahedral sites are still energetically favorable. (Akiba et al., 2016).
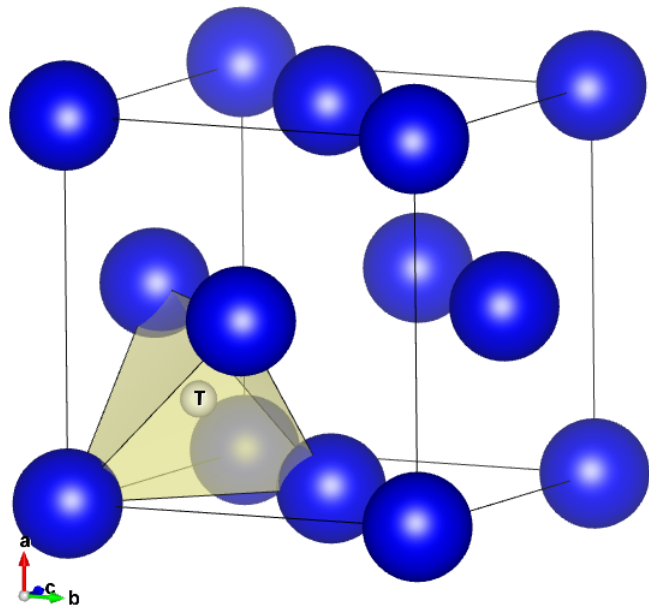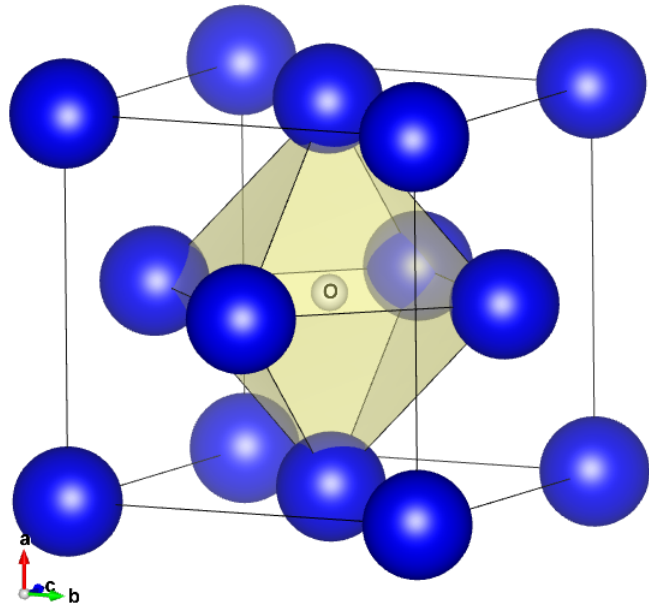
Figure 5.2: The octahedral site highlighted in a palladium fcc lattice with an occupying hydrogen atom.

Hydrogen is widely accepted to occupy octahedral sites in the bulk of Pd in both the α and β phases. The first results published in regrades to the site occupancy in the system were produced from a neutron diffraction (Worsham Jr et al., 1957) on both β-phase Pd-H and β-phase Pd-D. The diffraction patterns were reported to be "representative of the NaCl-type structure, in which the hydrogen and deuterium atoms have entered the octahedral positions about the palladium atoms", shown in Fig. 5.2. Skold and Neil (1966; 1967) reported, on the basis of QENS measurements, a jump length of 2.75Å, which corresponds to the distance between two neighbouring octahedral sites ($\frac{\sqrt{2}a}{2}$) of which each has 4 nearest neighbour sites, with a further 8 nearest neighbour tetrahedral sites at a distance of ($\frac{\sqrt{3}a}{4}$). Inelastic scattering of hydrogen in palladium is indicative of the transition between the ground and excited states in the ocathedral sites (Kemali et al., 2000). Octahedral occupancy is also indicated from density functional theory calcualtions of the ground state energies (Elsässer et al., 1991) and from Molecular Dynamics (MD) simulations (Gillan, 1986; Salomons, 1990). However in recent years there has been suggested that hydrogen atoms can occupy tetrahedral sites (Caputo and Alavi, 2003).

In addition to the site occupancy, the diffusion of protons between sites is of interest, which can be investigated with Quasi-Elastic Neutron Scattering (QENS). The majority of QENS measurements have been interpreted on the basis of jumps between ocatahedral sites (Rowe et al., 1972; Sköld and Nelin, 1966, 1967), although it is known that the barrier height between octahedral sites is too large to allow thermally activated diffusion at room temperature, and it is generally accepted that diffusion occurs via tetrahedral sites. This was discussed originally by Beg and Ross (1970), who tentatively interpreted their data in terms of two activation energies. More recently, clearer evidence

of motion on two time scales has been reported (Kofu et al., 2016; Steel, 2018). Kofu et al (2016) attributed this to jumps from the ground state and the first excited state, citing previous observations of a shoulder in the inelastic neutron scattering data (Kemali et al., 2000), who attributed this to the Franck–Condon process. Steel (2018) has suggested a possible localised-type motion via O-T-O jumps. The residency time for the tetrahedral site is small and therefore it is difficult to see due to the available energy range of most spectrometers, in addition to being a rather small feature in the background noise. The use of Monte-Carlo calculations of a lattice gas have also been carried out as a means of calculation for both the incoherent and coherent scattering functions to evaluate the behavior of hydrogen in metallic and inter-metallic compounds (Barlag et al., 2002) (Bull and Ross, 2001).
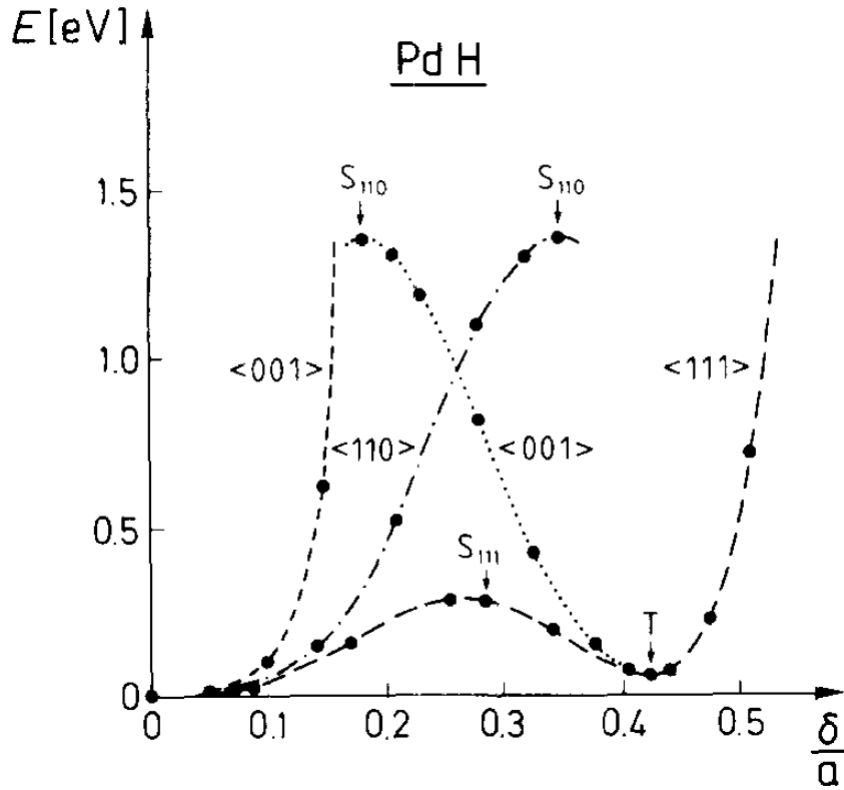
Figure 5.3: PdH_1 potentials between octahedral and tetrahedral sites along high symmetry diffusion paths. (Elsässer et al., 1991).

Diffusion from O sites occurs via tetrahedral sites along paths in the (1,1,1) direction, due to the absence of a tetrahedral site along the remaining two possible diffusion paths (1,1,0) and (1,0,0). Hydrogen occupying an octahedral site has 4 nearest neighbour O sites with the barrier heights, denoted by S_{110}, of 1.4eV in Fig. 5.3, or 8 neighbouring T sites who's barrier height is significantly lower, 200meV, denoted by S_{111}. This lower barrier height means less thermal energy is required for the hydrogen atom to make a jump. In addition, the zero point energy in the tetrahedral site is close to the saddle point energy. Thus, it is likely that the residency time within the tetrahedral site will be short. From each T site there are 4 neighbouring

octahedral sites. This process has not been widely reported experimentally, presumably as its jump-rate would lie outside the energy / frequency window of the spectrometers in the majority of reported measurements.

5.2 Hydrogen Diffusion between Octahedral Sites

Initial Monte Carlo simulations were performed for diffusion amongst octahedral sites in a palladium host lattice. Here, site energies and barrier heights were not included in the model, so that the jump probability to a vacant site is equal to 1. At low hydrogen concentration, this model is equivalent to the Chudley-Elliott model for jumps on an fcc lattice. At higher concentrations, both site blocking and tracer correlation effects should act to reduce the diffusion rate, and hence the values of $f(\mathbf{Q})$. The effects of particle concentration on both incoherent and coherent QENS, arising from the self and total correlation functions, respectively, for the polycrystalline average were examined.
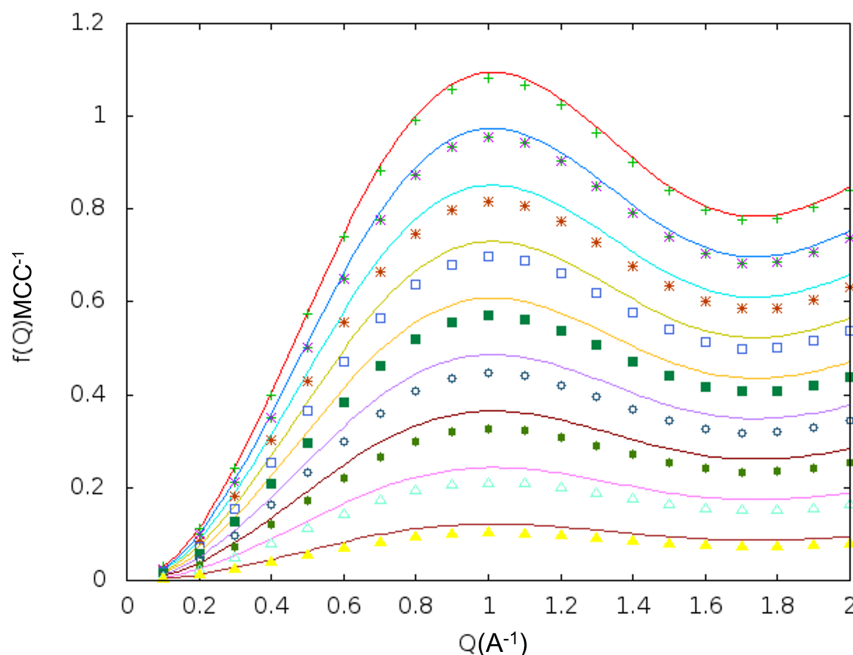
Figure 5.4: Polycrystalline f(Q) obtained from $I_{inc}(\mathbf{Q}, t)$ extracted from Monte-Carlo simulations of particle diffusion on a fcc lattice as a function of concentration from c=0.1 to 0.9 in steps of 0.1. The solid lines are the equivalent expressions from the Chudley-Elliot model multiplied by a factor of (1-c) to account for site-blocking effects.

Fig. 5.4 shows values of $f(Q)$ obtained from Monte-Carlo simulations at different particle concentrations. Also shown are equivalent values from the Chudley-Elliott model, which have been multiplied by a factor of (1-c) to account for concentration-dependent site-blocking effects. This factor accounts for the reduction in jump probability due to neighbouring sites being 'blocked'.

The discrepancy between the curves for each concentration is due to a further factor known as tracer correlation, which is related to the enhanced probability of a particle jumping back to the site it has just vacated when it next attempts to move. Here, we make the assumption that values for $f(\mathbf{Q})$ based on the Chudley-Elliott model including both site-blocking and tracer

correlation effects can be expressed as

$$f(Q) = (1-c)f_t(c)\frac{1}{\tau}\left[1 - \frac{\sin(Ql)}{Ql}\right].$$ (5.1)

This offers a direct way of obtaining values for the tracer-correlation factor from values of $f(Q)$, determined from the difference between the 'site-blocking corrected' Chudley-Elliott model and the corresponding Monte-Carlo values. A comparison of these results with previous work, which determined values for the tracer-correlation factor directly from diffusion rates in Monte-Carlo simulations (Kelly and Sholl, 1987) is shown in the Table 5.1.

c	$(1-c)f_t$	f_t	f(Kelly and Sholl, 1987)
0.1	0.890	0.989	0.986
0.2	0.784	0.980	0.972
0.3	0.671	0.959	0.956
0.4	0.572	0.954	0.938
0.5	0.467	0.934	0.917
0.6	0.365	0.913	0.896
0.7	0.268	0.894	0.870
0.8	0.173	0.864	0.843
0.9	0.084	0.839	0.814

Table 5.1: Comparison of calculated correlation factors to those previously presented by S W Kelly and C A Sholl (Kelly and Sholl, 1987).
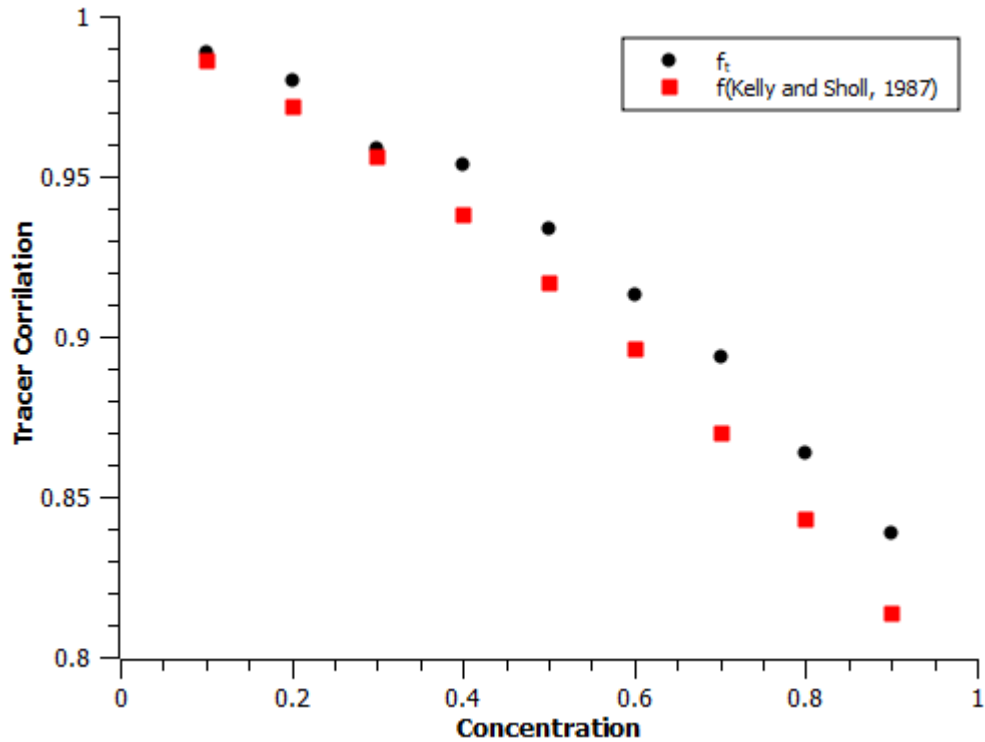
Figure 5.5: Plot of tracer correlation data in Table 5.1

The results presented so far were calculated for the self pair-correlation function, it is also of interest to calculate the broadening for the total pair-correlation function. When dealing with the coherent broadening, both the effect of the site blocking and the tracer correlation factors are not apparent. This is because both these effects are cancelled out on average when the correlation between pairs of diffusing atoms is considered. So when the broadening is calculated for different finite concentrations there is no variation in the amplitude, as is seen in the case of incoherent scattering, Fig. 5.6
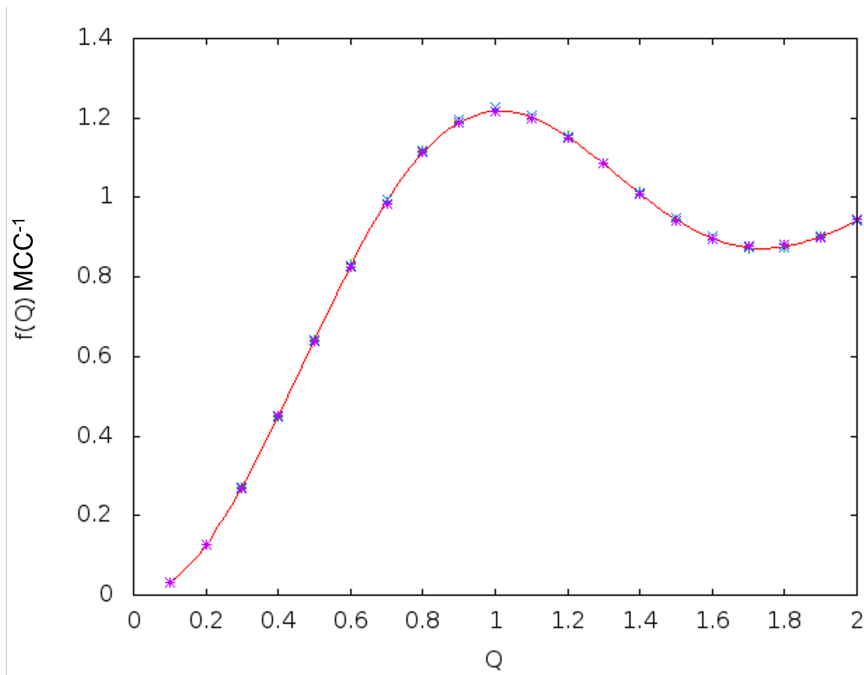
Figure 5.6: Polycrystalline f(Q) obtained from $I_{coh}(\mathbf{Q}, t)$ calculated from $G(\mathbf{r}, t)$ from Monte-Carlo simulations of particle diffusion on a fcc lattice for c=0.1, 0.3, 0.5, 0.7, 0.9. The concentration independence of f(Q) is apparent.

5.3 Hydrogen Diffusion including Tetrahedral Sites

Simulations were performed including both octahedral and tetrahedral sites. The initial objective was to determine whether, only allowing O-T and T-O site jumps, it is possible to recover the form of $f(Q)$ seen experimentally. Initially, rather than explicitly using site energies and barrier heights, the jump probabilities were defined, allowing direct control of the ratio of the jump probabilities / rates. In particular, the limit where the jump rates are significantly different from each other can be investigated.

Initially, the effect of the jump rate ratio on the average site occupancies

was investigated. One would expect the relative occupancy of the octahedral sites to increase as the jump rate from T to O is increased. Filling the lattice at random would give an concentration, c, of 1/3. Calculation of the fraction of atoms distributed over the available O sites during the initial phase of the Monte-Carlo calculations using jump diffusion, shows an increase in O site occupation from the random initial distribution, Fig. 5.7. This effect becomes greater as the relative jump probability from T to O increases.
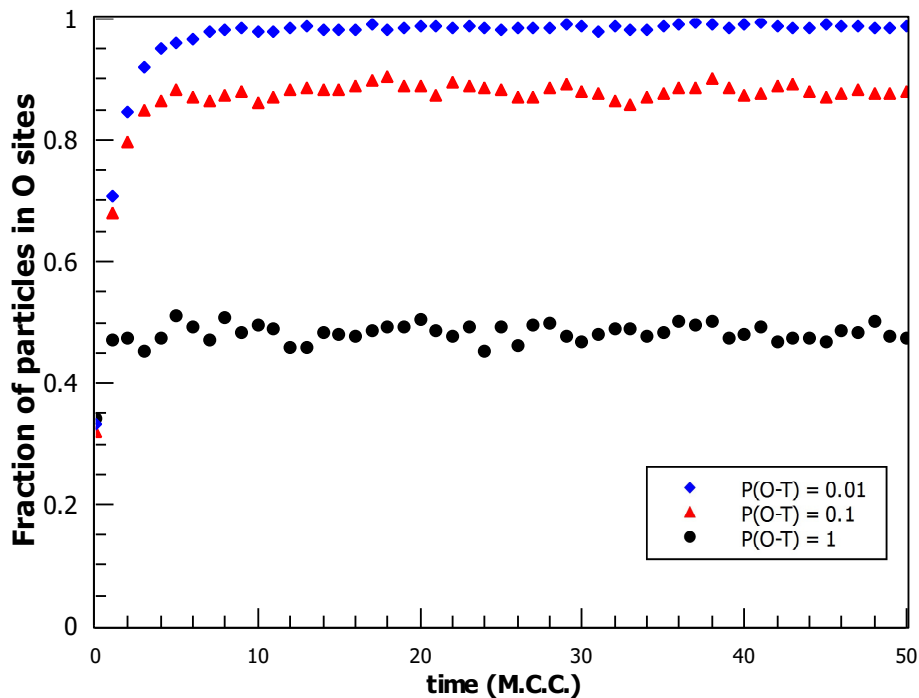
Figure 5.7: Fraction of particles in the O and T sites as a function of time for the O-T site transition probability of 1.0, 0.1 and 0.01

It is, perhaps, worth highlighting the effects of not including a burn-in with jump diffusion. One of the consequences of including the tetrahedral sites is that the 'standard' burn-in method of using ballistic diffusion does not result in a steady state. This is because the site occupancies are determined by the jump probabilities.

146
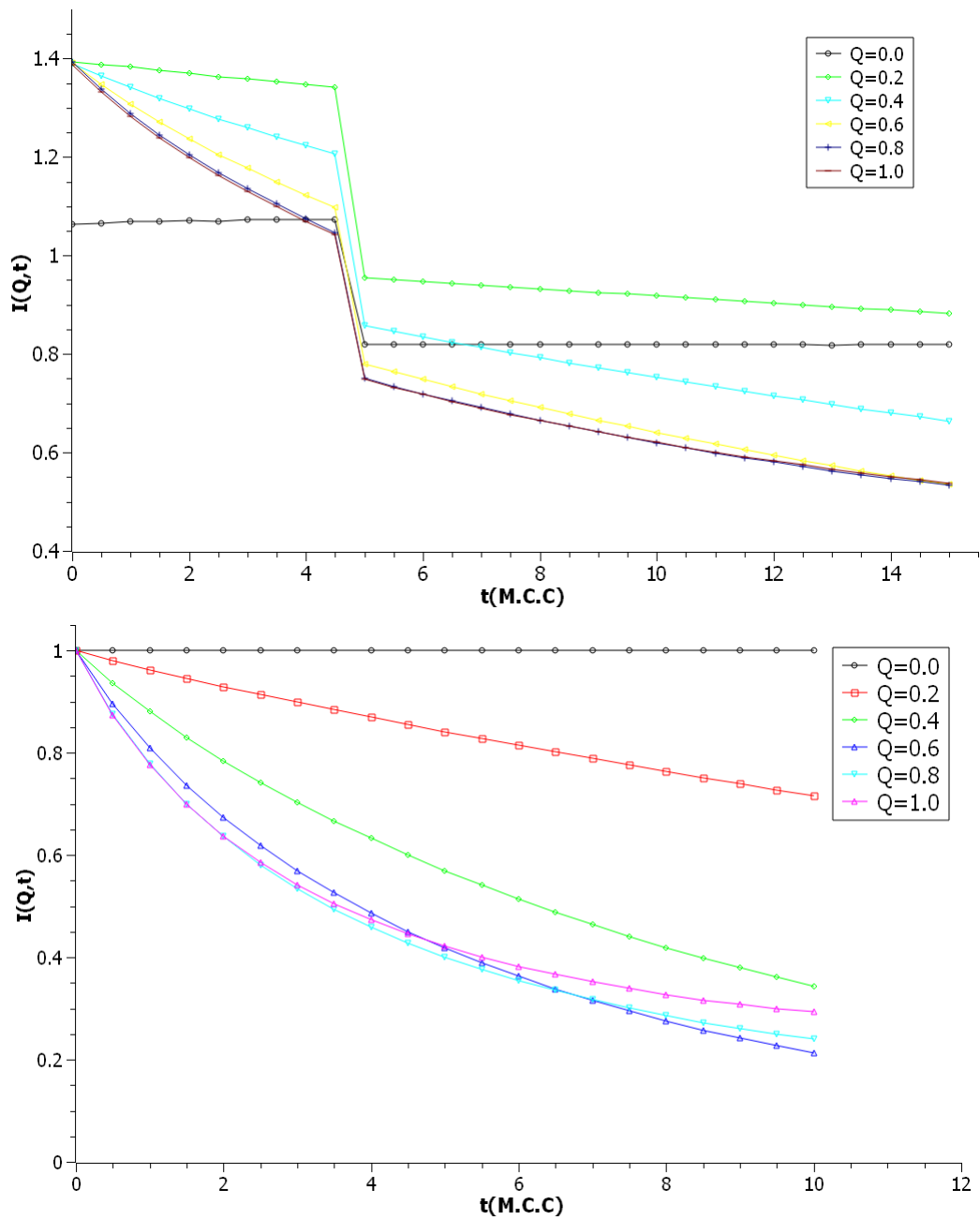
Figure 5.8: Intermediate scattering functions before (top) and after (bottom) equilibrium has been reached using 'Burn-in'.

Equilibrium is approached in the original GRT code using ballistic diffusion with the site energies used to determine the transition probabilities. This means that, where the site energies are equal, the particles will be randomly distributed over all the sites in the lattice, and then when the main simulation commences, it can take several MCC for the O sites to become preferentially occupied due to the jump transition probabilities. The effects of not doing this become evident when the intermediate scattering function is plotted, as shown in Fig. 5.8.

5.3.1 Diffusion in a Single Crystal

With the palladium hydride having some diffusion paths of key interest due to them containing both tetrahedral and octahedral sites, it is first useful to look at these in a single crystal case. Based on the data in Fig. 5.7, the jump ratio was set to $\frac{\tau_T}{\tau_O} = 0.01$. Widths are calculated via fitting a single exponential to the intermediate scattering function, $I(\mathbf{Q}, t)$ at $t > 0$, Fig. 5.9.
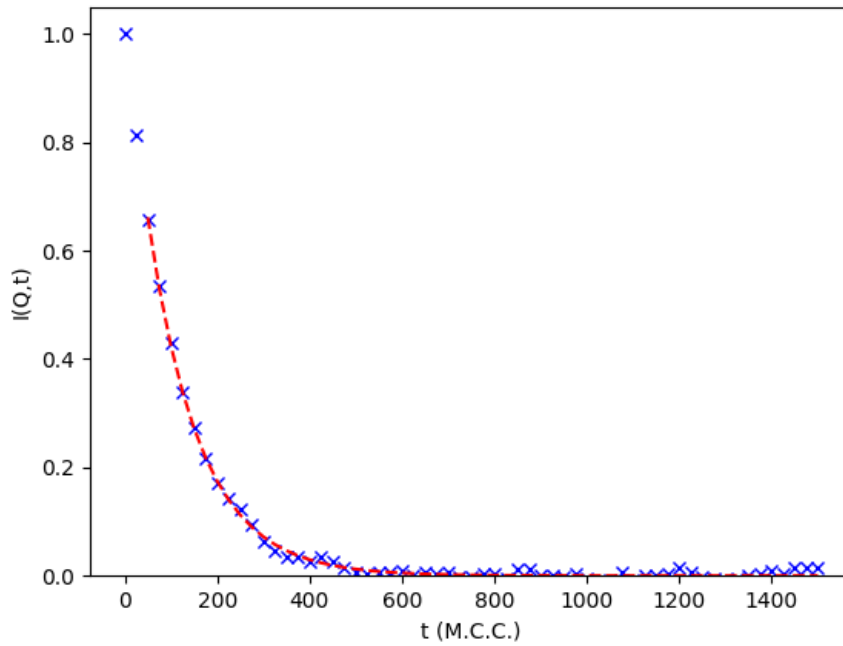
Figure 5.9: Example of an intermediate scattering function in a single crystal PdH sample at $\mathbf{Q}$=(0.8,0.8,0.8) with low t points not included in the fitting. Where the dashed line is the single exponential fit to t > 150M.C.C
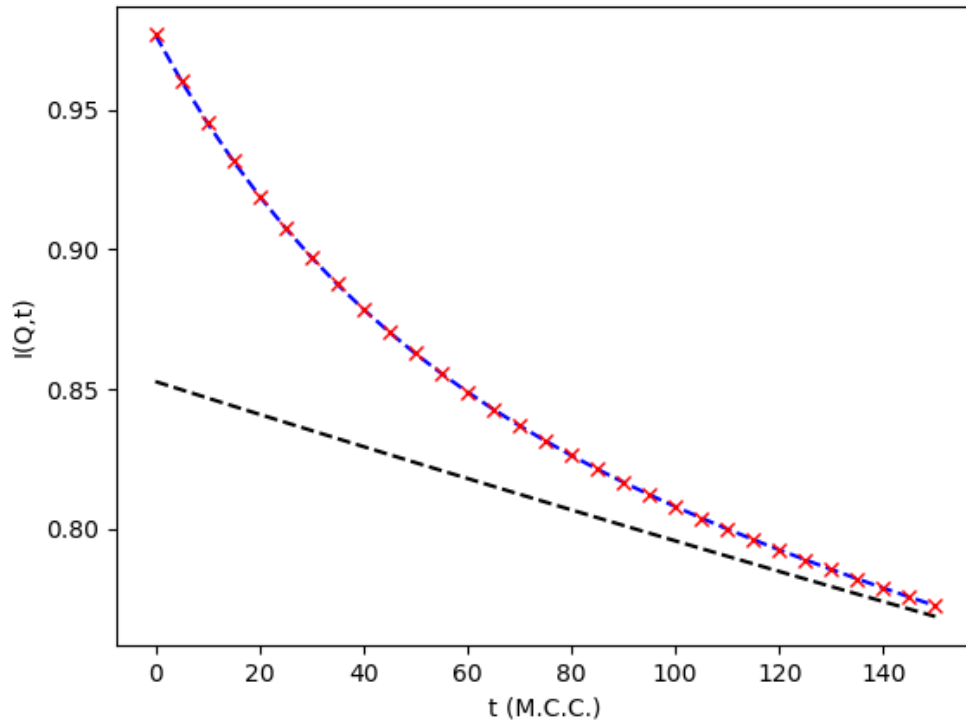
Figure 5.10: The single exponential fit from Fig. 5.9 (black dashed line), when plotted over the low t range (t,150 M.C.C) excluded from the data set of Fig. 5.9, compared with a double-exponential fit (dot-dash). where the parameters of the slowly decaying component is the same as in Fig. 5.9

The dashed line in figure 5.10 represents the single exponential fit from the slowly decaying component of I($\mathbf{Q}$,t) which can be seen to diverge from the fit of the double exponential where one exponential is held constant using the fitted parameters from the single exponential fit in Fig. 5.9.

The results of this fitting processes at Q vectors along high-symmetry directions in reciprocal space is shown in Fig. 5.11.

150
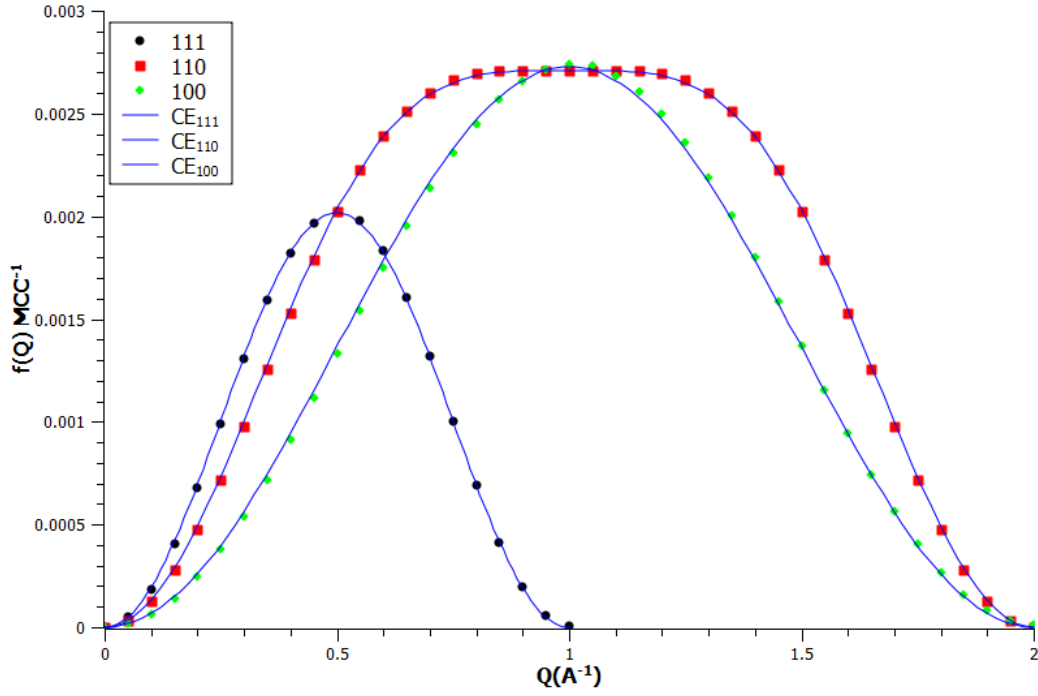
Figure 5.11: f(Q) from the slowly decaying component of I($\mathbf{Q}$,t) fits along the (1,1,1), (1,1,0) and (1,0,0) directions in reciprocal space.

For each of the plots along the three high-symmetry directions, Fig. 5.11, the Chudley Elliott model for an fcc can be fitted; these functions are given below.

$$f_{100}(\mathbf{Q}) = 1 - \frac{1}{3}(2\cos(\pi Q_x) + 1) \qquad (5.2)$$

$$f_{110}(\mathbf{Q}) = 1 - \frac{1}{3}(\cos^2(\pi Q_x) + \cos(\pi Q_x)) \qquad (5.3)$$

$$f_{111}(\mathbf{Q}) = 1 - \cos^2(\pi Q_x) \qquad (5.4)$$

It can be seen that the Chudley Elliott model can be retrieved from the long time scale intermediate scattering function by fitting a single exponen-

tial over an appropriate range. This is an significant result, as it means the intermediate scattering function can be interpreted as a combination of different types of diffusive motion.

The widths of the rapidly decaying component, an example of which is shown in Fig. 5.12, do not follow the form of the CE model, perhaps indicating the presence of localised motion occurring in the PdH system.

[The ratio of T to O sites is 2:1, so an overall concentration c=0.33 over the whole system would give $C_O = 1.0$ if all of the hydrogen atoms were in the O sites.]
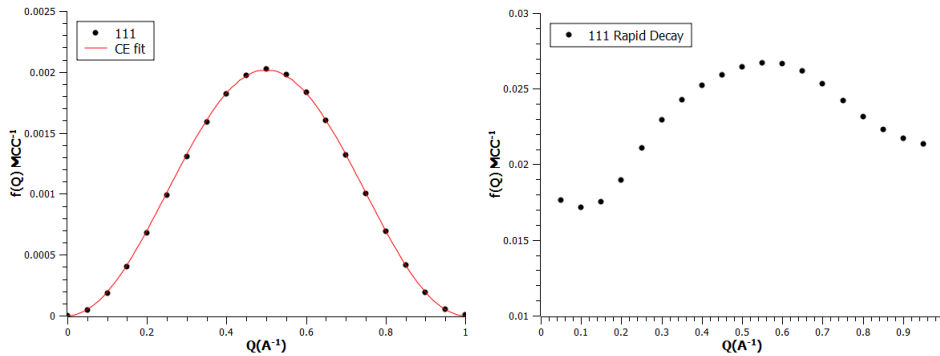
Figure 5.12: Long and short time scales along the (1,1,1) for a single crystal, with Chudley-Elliott fit possible on the longer time scale.

Calculations of the f($\mathbf{Q}$) from the decaying exponential component of a double exponential fit show that they do not go to zero at low Q values. This could be indicative of localised motion, similar to that seen in C15 Laves-phase systems. In addition, f($\mathbf{Q}$) from the rapidly decaying component is significantly larger than for the component attributed here to translational motion.

5.3.2   PolyCrystalline PdH_x

MC simulations of diffution in Pd-H were initially carried out at low concentration, $c = 0.0033$ or $c_0 = 0.01$).
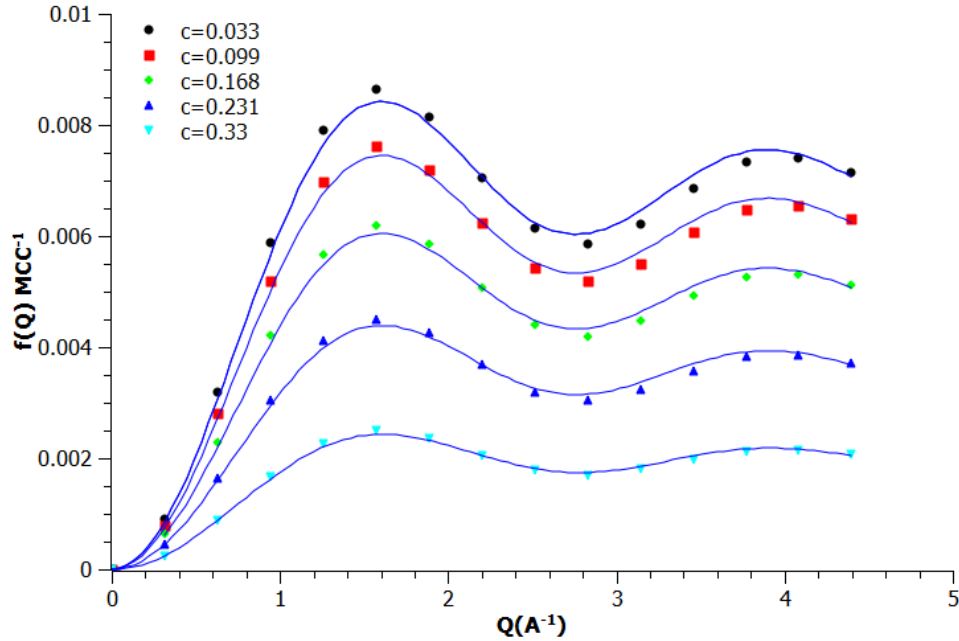
Figure 5.13: Polycrystalline widths of low concentration (C=0.0033) with jump ratio = 0.01 along with the Chudley-Elliott model fit.

Fig. 5.13 shows the spherically-averaged (polycrystalline) broadening from the longer time-scale. Here at low Q the f(Q) show strong agreement with the CE model shown by the solid red line but begins to deviate at the higher Q values. Note that experimental measurements are typically reported up to $2 - 3\text{Å}^{-1}$. The f(Q) from the double exponential fit over the short time scale are shown in Fig. 5.14
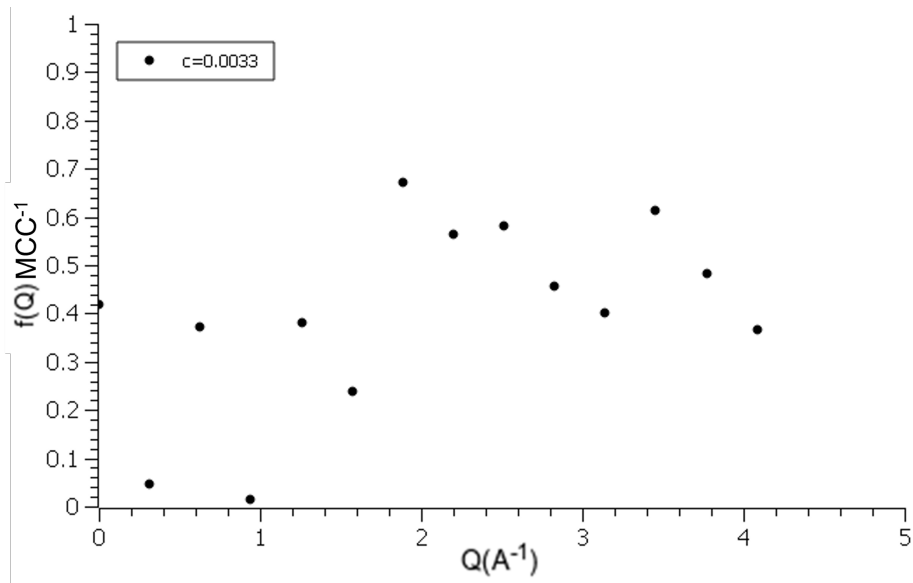
Figure 5.14: Widths extracted from the rapidly decaying exponential component for low concentration (C=0.0033) with jump ratio = 0.01

The next step is to examine f(Q) at higher concentrations, from c = 0.033 up to c = 0.33, which would correspond to all the octahedral sites being fully occupied. The effect of concentration on the localised component of the scattering function can be determined. The widths associated with the slowly decaying exponential behave as expected for the intermediate scattering function, with the increase in concentration demonstrated in Fig. 5.15 along with the widths belonging to the rapidly decaying exponential, Fig. 5.16 .
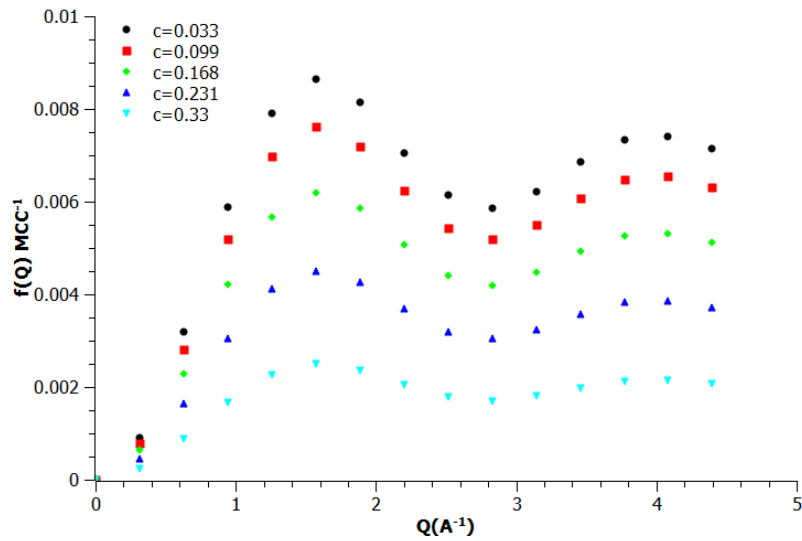
Figure 5.15: f(Q) from the slowly decaying exponential component as a function of concentration, up to the equivalent of full O site occupancy.
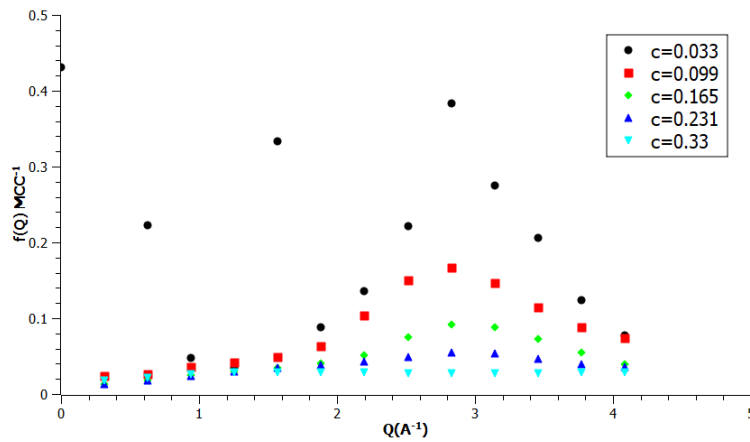
Figure 5.16: f(Q) from the rapidly decaying exponential component as a function of concentration, up to the equivalent of full O site occupancy.

Evidence of localised motion can be seen here in the rapidly decaying component of the intermediate scattering function seen in the spherically averaged values of f(Q). In the long time-scale, where the intermediate scattering function decays much more slowly, the Chudley-Elliot model agrees

well with the calculated values of f(Q) (Fig. 5.17a, 5.17b). However, the important result here is that in the poly crystalline case the CE model for O-O jumps can be extracted from the slowly decaying exponential. There is also some indication of of localised motion in the rapidly decaying component of the double exponential fit, Fig. 5.18a, 5.18b.

(a)   (b)
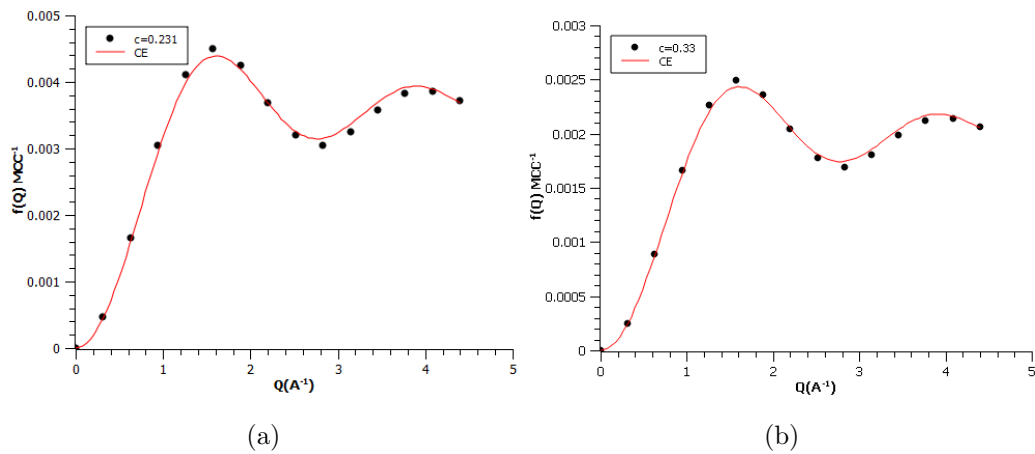
Figure 5.17: Long time scale widths with Chudley-Elliott fits for PdH β-phase c=0.23 and c=0.33

(a)   (b)
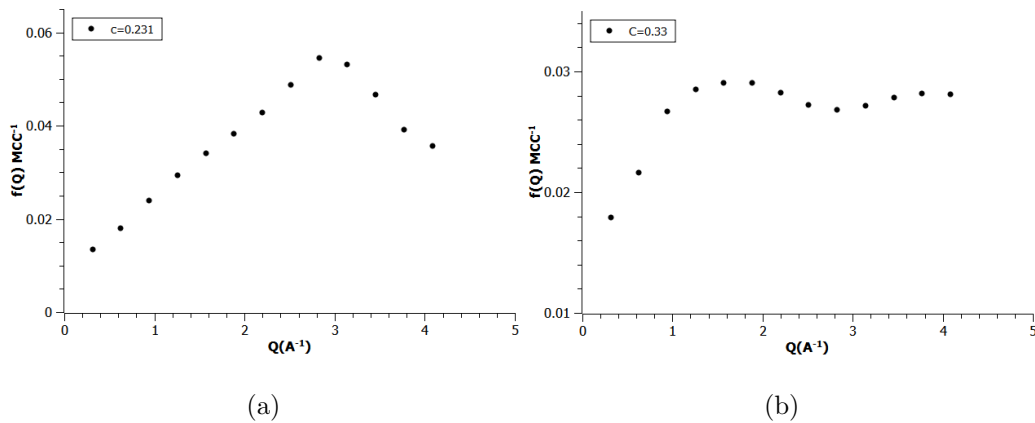
Figure 5.18: Short time scale widths for PdH β-phase c=0.23 and c=0.33

As the concentration of hydrogen on the O sites increases into the region that corresponds to the β-phase, the contribution of site blocking on the localised motion becomes more pronounced. As the concentration of atoms on the O sites increases, the chance of an atom jumping back from a T site to the O site it has just vacated would be expected to increase, resulting in a greater contribution to localised motion. This is, in effect, a sub-lattice dependent tracer correlation effect.

5.3.3 Temperature Dependence

Introducing barrier heights to the calculation of G(r,t) allows for a more realistic idea on the motion of the diffusing hydrogen in the system. By using values for the zero point energy corrected barrier heights of 0.11eV and 0.16eV between tetrahedral and octahedral sites from ab-initio Density Functional Theory (DFT) calculations presented in work by Hajime Kimizuka et al(2016; 2018; 2019). Using these barrier from T-S as 0.11eV and S-O as 0.16eV, where S is the saddle point, to investigate the temperature dependence of the slow and rapidly decaying motions to be examined. The low concentration case and the full octahedral occupation have been calculated over a temperature range 200K-500K for a polycrystalline sample. The long time scale is firstly examined to determine if the Chudley Elliott model of diffusion between octahedral sites is extractable from the intermediate scattering function.

157
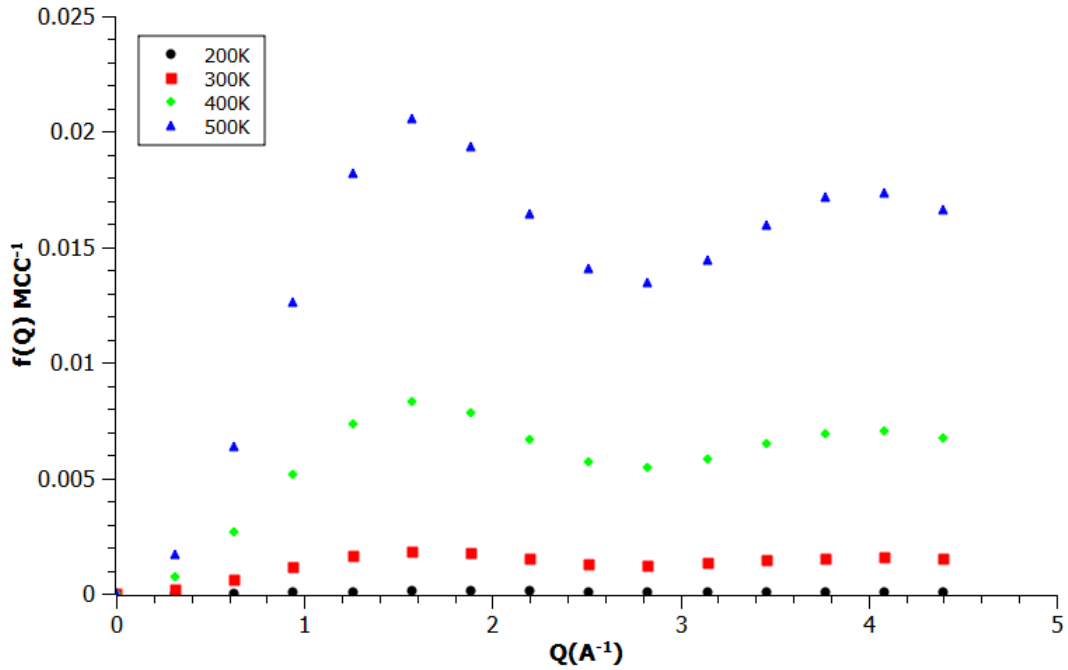
α-phase

Figure 5.19: Polycrystalline f(Q)s from the long time scale over a range of temperature in α-phase (c=0.033).

The amplitude of the widths for each temperature increases as the temperature increases as these are all at the same concentration seen in figure 5.19. By fitting the polycrystalline Chudley-Elliott model to the widths at each temperature the confirmation of the Chudley-Elliott model being extracted from the slowly decaying component of the I(Q,t). There are slight deviations from the Chudley-Elliott model shown by the solid red line in figure 5.20 as the Q values become larger, this could be explainable by the higher Q values being more sensitive to localised motion than lower Q values ($Q < 0.15 Å^{-1}$).

(a) T=200K

(b) T=300K

(c) T=400K

(d) T=500K
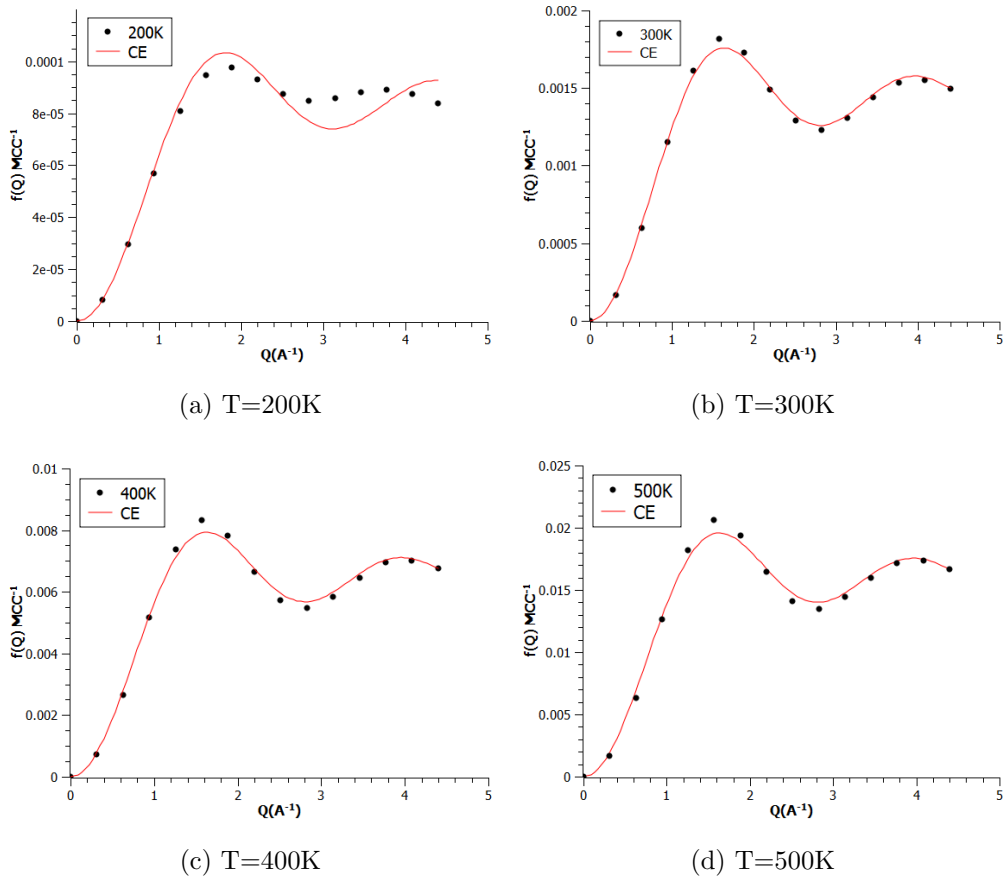
Figure 5.20: Chudley-Elliott fits to each individual broadening from, 200K, 300K, 400K and 500K. C=0.033

Temperature(K)	Amplitude (MCC^{-1})	l(Å) (MC)
200	8.49e-05	2.4783
300	0.001445	2.7491
400	0.006515	2.7548
500	0.016079	2.7492

Table 5.2: Fitted jump lengths from directionally averaged widths via the Chudley-Elliott model with amplitudes when barrier heights are included at C=0.033

159

From these data given in Table. 5.4 a linear behaviour can be seen in the Arrhenius plot in Fig. 6.12b, which mirrors X.W.Zhou et al. (2018) suggesting the presences of just one diffusion barrier in operation at low hydrogen concentrations.

(a)   (b)
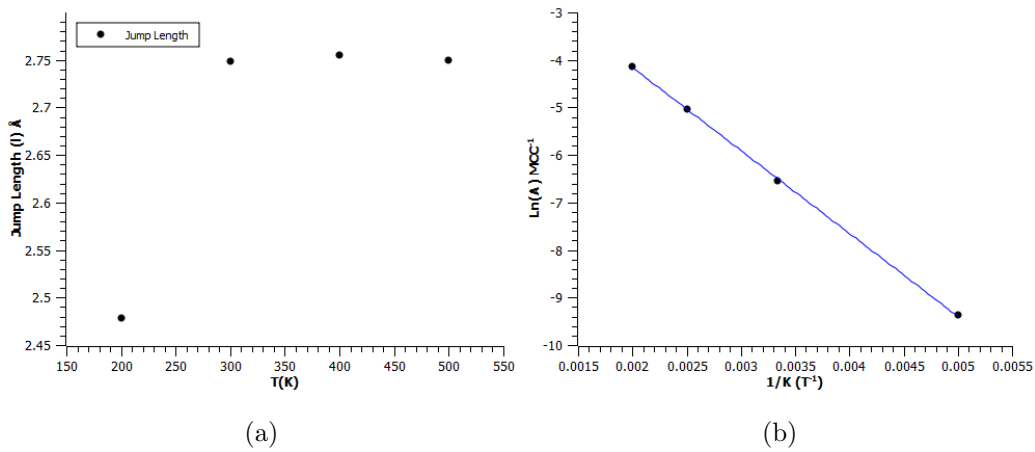
Figure 5.21: Extracted jump lengths from Chudley Elliott fits with an Arrhenius plot at a low hydrogen concentration (C=0.033).

The widths from the rapidly decaying component extracted from the short time scale I(Q,t), Fig. 5.22, show widths that tend towards a finite value at low Q at temperatures below 500K. At 500K the widths decrease to 0 as the Q values tend towards zero. At higher temperatures it could be assumed that there is enough thermal energy available to the occupying hydrogen atom that it is possible to jump from O-O site as a result instead of via a O-T-O jump mechanism. Site blocking should be less of a factor in this instance as C=0.033 resulting in there being a number of vacant octahedral sites.

160
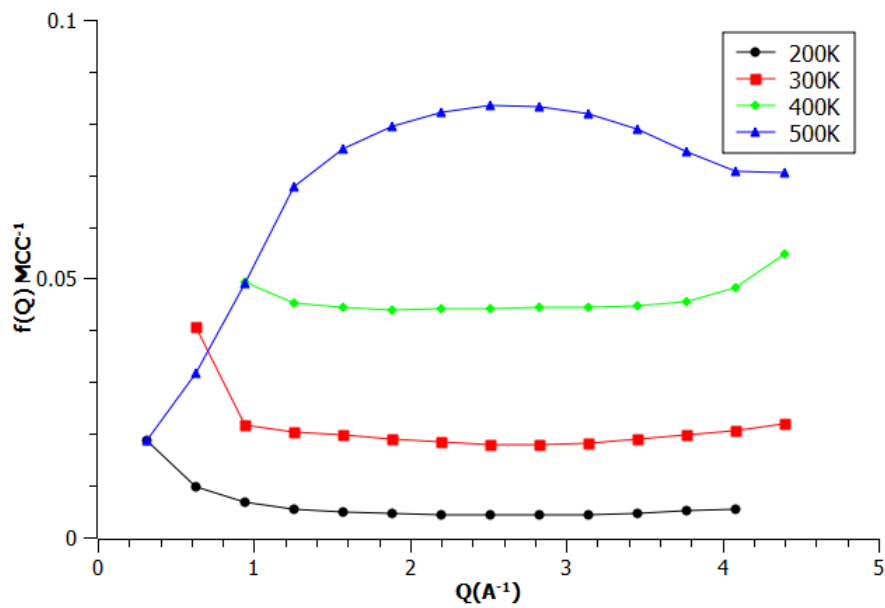
Figure 5.22: Polycrystalline widths from the short time scale over a range of temperature, here a spine has been added to the points for ease of showing the trend of the data sets.

At temperatures below 500K it appears that, from Fig. 5.23 the widths from the short more rapid time scale suggest a second type of motion is occurring within the total time. The form of these widths suggest a localised type of motion as at low Q they do not go to zero.

(a) T=200K
(b) T=300K
(c) T=400K
(d) T=500K
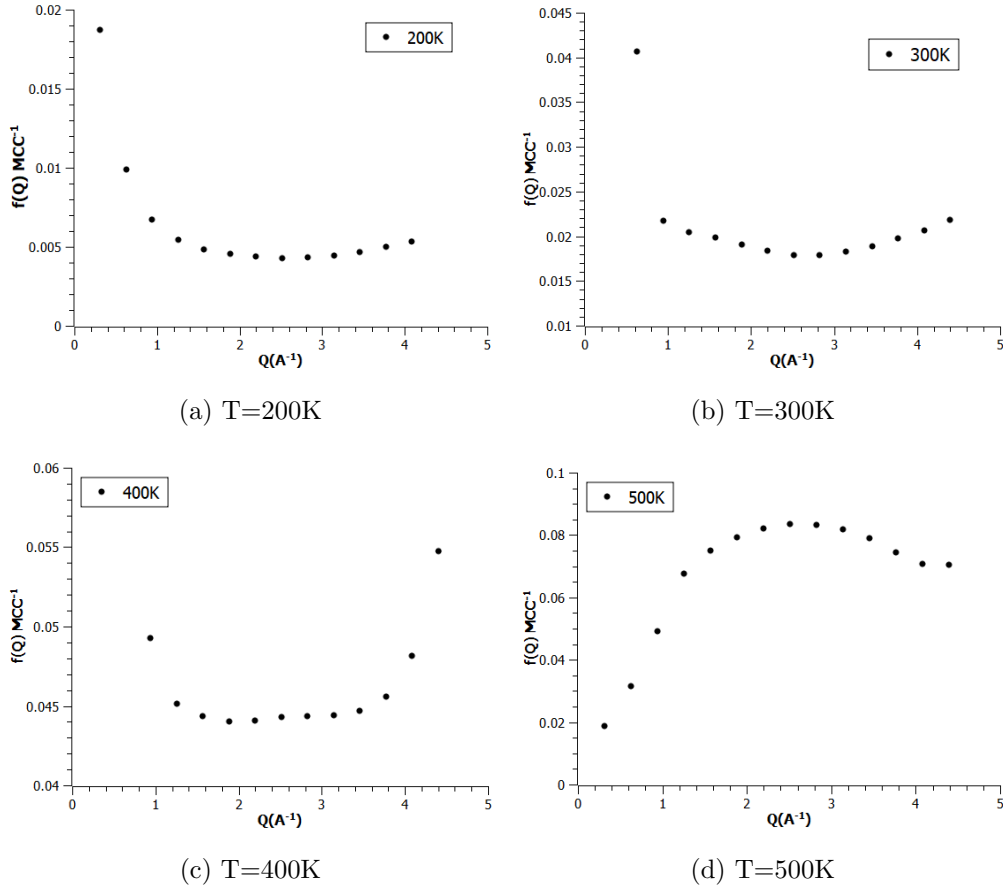
Figure 5.23: Short time scale half widths from a double exponential fit at 200K, 300K, 400K and 500K when concentration is C = 0.033.

β-Phase

In the results presented here the fitted parameters for each intermediate scattering function are passed to the Lebedev quadrature generated Q vectors for a given magnitude of Q. The resulting HWHM for a given magnitude of Q are then a sum of the directionally averaged widths of each of the contributing Q-vectors. Carrying this out on a Lebadev order of 25 results in 230 individual Q-vectors being used for each magnitude of Q. Due to the relatively simple nature of the PdH system in comparison to the C15

system in the previous chapter the calculations are relatively computationally inexpensive.

The effect of concentration with the inclusion of barrier heights is considered here in β-phase palladium hydride, concentration equal to 0.33, where nearly all the octahedral sites should be occupied. The widths of the slowly decaying intermediate scattering function reproduce the form of the Chudley Elliott model, Fig. 5.25 which is exact at low Q as would be expected with an increase in amplitude as the temperature is increased shown in figure 5.24.
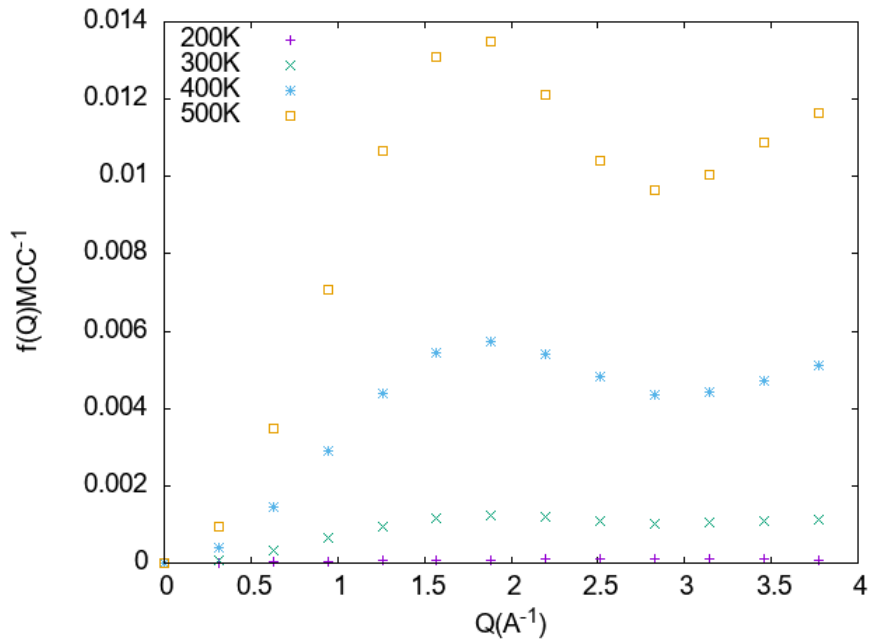
Figure 5.24: Polycrystalline widths at expected concentration of full octahedral ocupation (C=0.33).

From fitting the polycrystalline Chudley Elliott model (solid lines) in Fig. 5.25 the jump lengths can also be extracted from the long time scale. However as Q values increase above $3 \mathring{A}^{-1}$ the fit begins to diverge a small amount, this could be as a result of the localised component as at high Q the broadening becomes more sensitive to rapid motion.

163

(a) T=200K

(b) T=300K

(c) T=400K

(d) T=500K
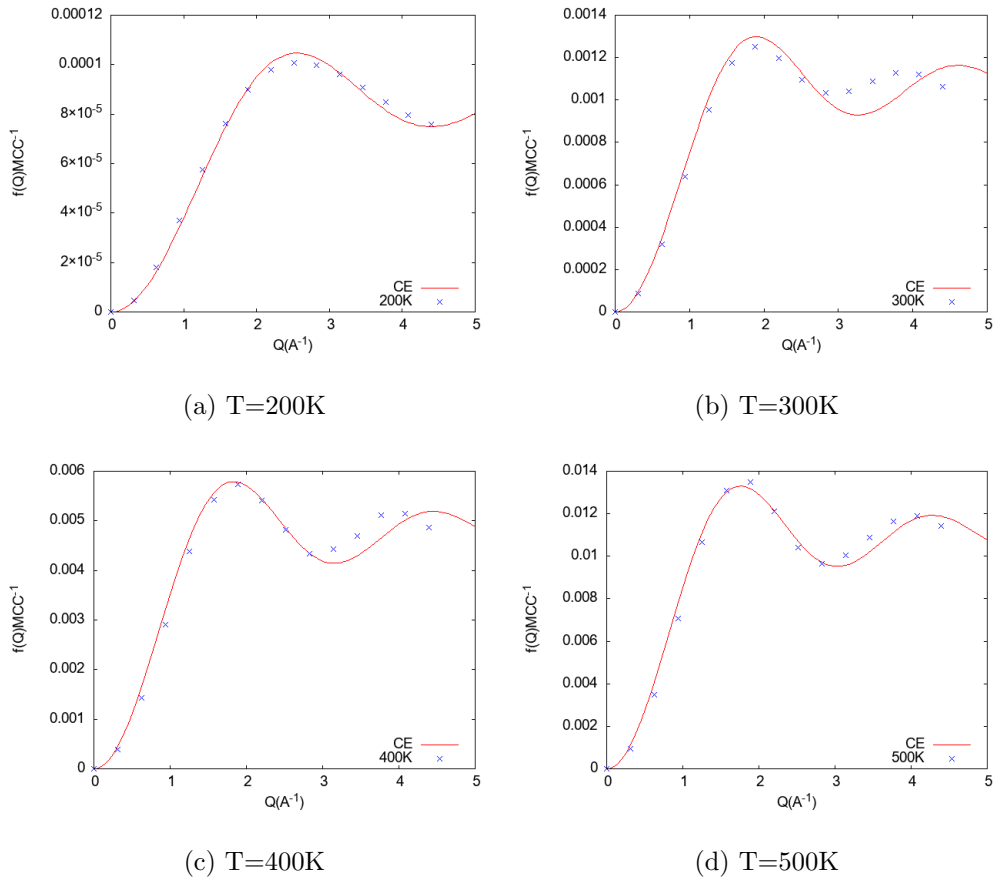
Figure 5.25: Chudley-Elliott fits to each individual broadening from directionally averaged half widths at 200K, 300K, 400K and 500K when concentration is C = 0.33.

It should be noted that the approach for calculating the polycrystalline widths used here, where the fitted values for $f(\mathbf{Q})$ are averaged, yields an accurate set of results compared to the width calculated by averaging the $I(\mathbf{Q},t)$ itself (Table 5.3) as demonstrated in the previous chapter for C15. For all temperatures as the Chudley Elliott model is in good agreement out to a higher Q value. This also gives a good estimate of the jump lengths at each temperature.

Temperature (K)	Jump length(Å) HWHM	Jump length(Å) Ave HWHM
200	1.67 ± 0.008	1.76 ± 0.019
300	1.76 ± 0.05	2.37 ± 0.06
400	1.75 ± 0.05	2.45 ± 0.05
500	1.97 ± 0.08	2.55 ± 0.04

Table 5.3: Comparison of jump lengths calculated from Chudley Elliott fits to data produced from both directionally averaged half widths $f(Q)$ and half widths produced from the directionally averaged $I(\mathbf{Q}, t)$ and the effect on their respective jump lengths.

Temperature(K)	Amplitude	l(Å) (MC)
200	8.60e-07	1.75875
250	0.00036	2.00989
275	0.00063	2.23670
300	0.00107	2.36756
325	0.00170	2.40356
350	0.00254	2.41337
375	0.00357	2.42622
400	0.00476	2.45003
425	0.00604	2.48068
450	0.00758	2.49820
475	0.00917	2.53013
500	0.01093	2.54946

Table 5.4: Fitted jump lengths from directionally averaged widths via the CE model with amplitudes when barrier heights are included, C=0.33

From the data in Table.(5.4) an Arrhenius plot can taken, Fig. 5.26b

(a)   (b)
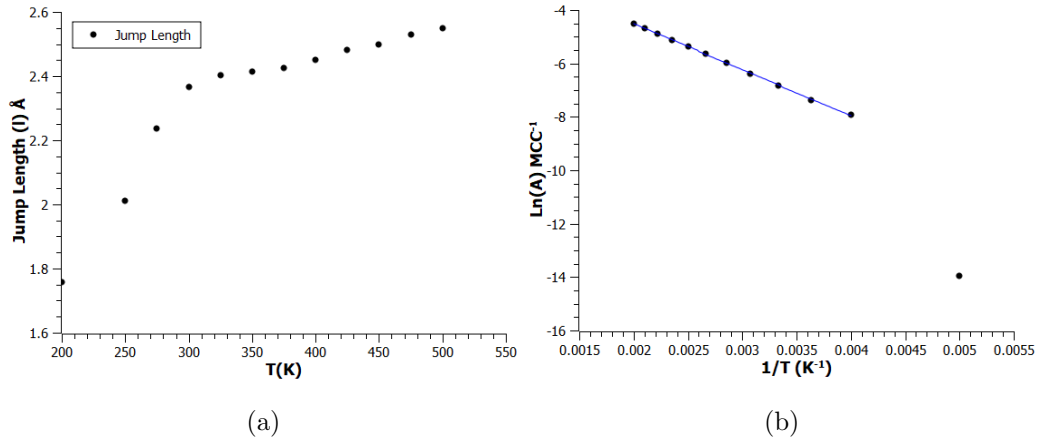
Figure 5.26: Extracted jump lengths from Chudley Elliott fits (Table.5.4) with an Arrhenius plot

Given the nearest neighbour distance between octahedral sites is $0.7071a$ where a is the lattice parameter. Giving a jump length of 2.8779Å given a suggested lattice parameter of 4.07Å from DFT calculations with full octahedral site occupation (Elsässer et al., 1991). The jump lengths extracted from the Long time scale intermediate scattering function calculated from the pair correlation function generated from Monte-Carlo simulations where only octahedral to tetrahedral jumps are allowed show a reduction in jump length from that of the suggested predicted jump length.
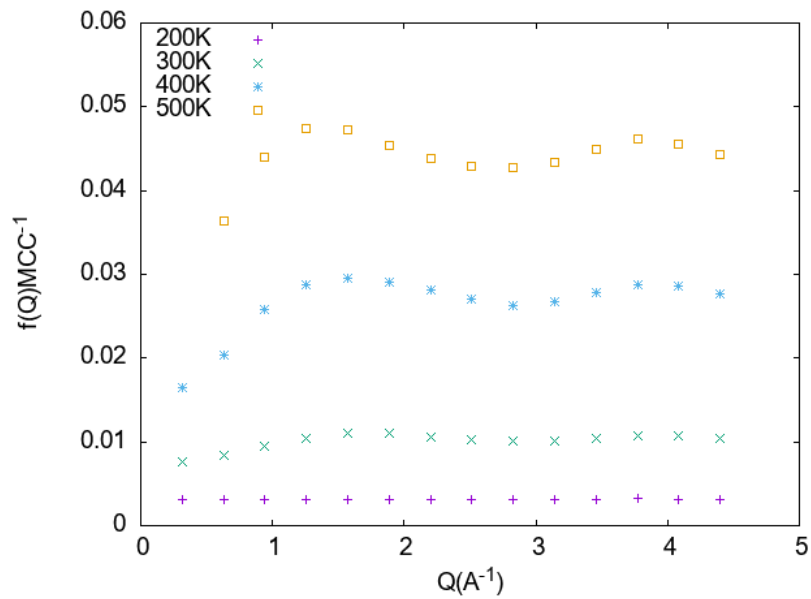
Figure 5.27: Directionally averaged decay constants from a double exponential fit over a range of temperatures.

The double exponential fitted to the rapidly decaying I(Q,t) over a short time scale compared to the time scale used to extract the CE model, shows evidence of there being motion. If there was purely O-O type motion one would expect to see the widths in Fig. 5.27 to go to Zero at low Q, these are shown on independent axis for each temperature in figure 5.36. This can be seen as evidence of an O-T-O jump mechanism.

(a) T=200K

(b) T=300K

(c) T=400K

(d) T=500K
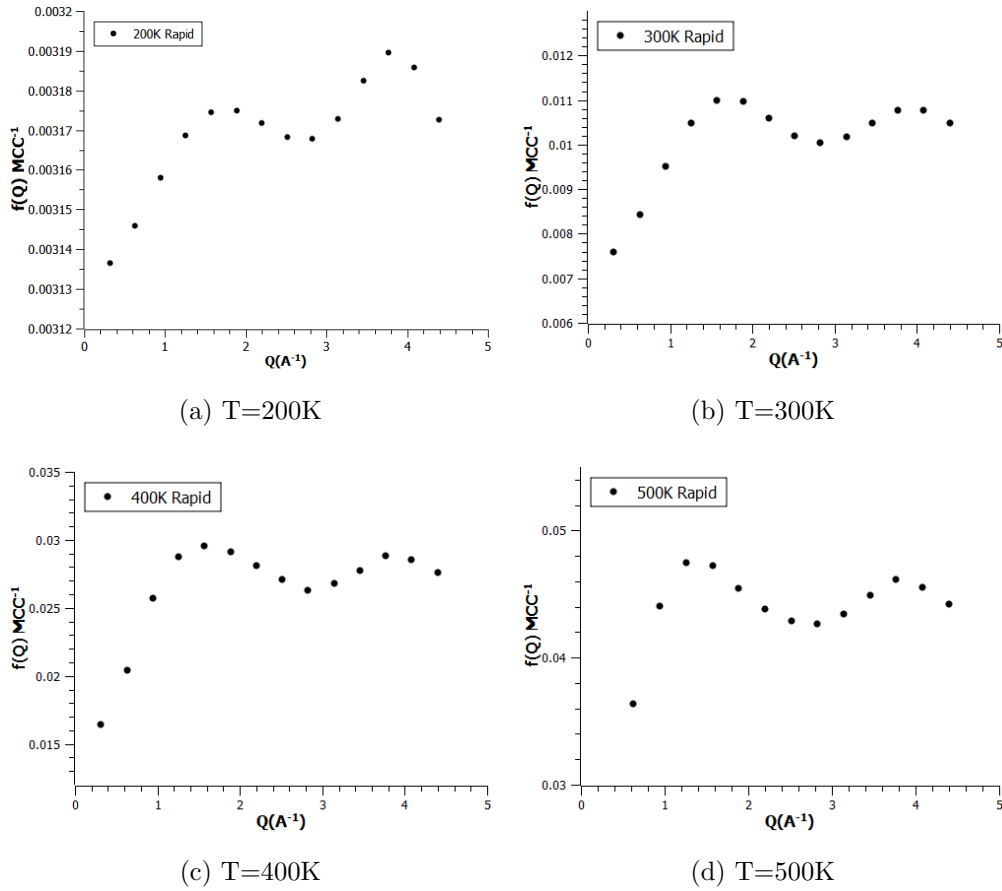
Figure 5.28: Short time scale directionally averaged half widths from a double ecponential fit at 200K, 300K, 400K and 500K when concentration is C = 0.33.

The plot of both the single fit and double fit exponentials on the short time scale at higher Q values demonstrates a divergence, Fig. 5.29 between the two suggesting that a double exponential is necessary to fully evaluate the Intermediate scattering function when both Octahedral and Tetrahedral sites are included in allowed jumps.
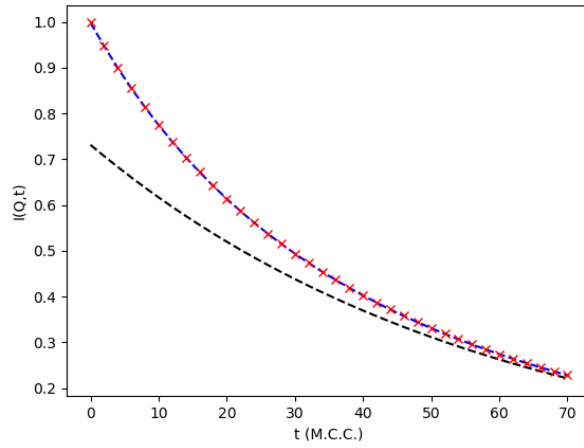
Figure 5.29: Short time scale $I(\mathbf{Q}, t)$ with single exponetial fit (dashed line) and Double exponential fit (dot-dash line) at Q=1.2Å, 500K.

If there is localised motion there should exist some elastic component in the intermediate scattering function in the short time scale, this is the elastic incoherent structure factor (EISF) Fig. 5.30.
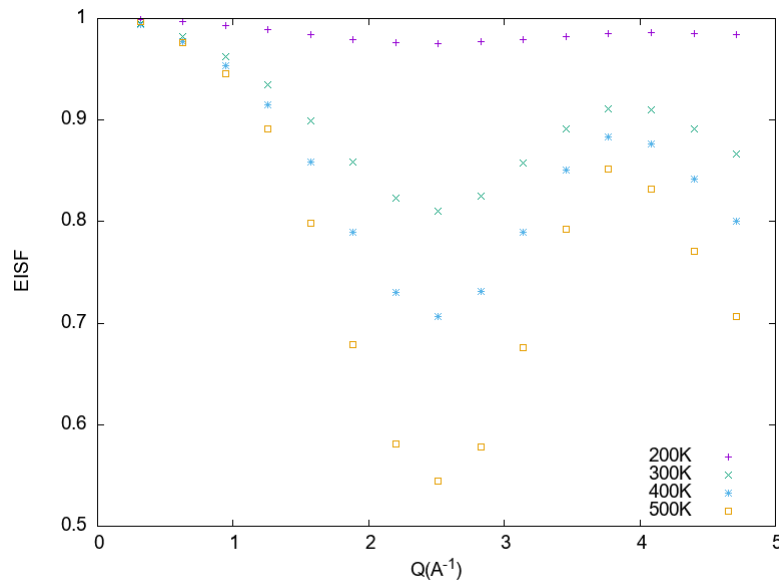
Figure 5.30: The Elastic Incoherent Structure Factor for 200K, 300K, 400K and 500K.

The fit to the Arrhenius plot in Fig.5.26b gives the activation energy $0.149eV$. This is in close agreement to the activation energy calculated for β-phase by Beg and Ross (1970) over a temperature range 293–473 K, $0.146eV$, however over similar temperature ranges Seymour et al. (1975) and Davis et al. (1976) reported activation energies of 0.229 and $0.228eV$ respectively.

This also agrees with work carried out by X.W. Zhou et al. (2018) who noted that at lower hydrogen concentrations there is just one diffusion barrier, shown by the linear behaviour of the Arrhenius plots, however at higher concentrations the barrier is no longer linear and becomes a continuous function meaning a single barrier activation energy could no longer being be determined which has yet to be displayed here as for beta-phase PdH with barrier heights included the Arrhenius plot still behaved in a linear fashion.

5.3.4 Including Site Energies

All the previous calculations have been carried out with both the octahedral and tetrahedral sites having no energy attributed to each of them respectively, we know this not to be the case however. In Palladium the tetrahedral site has a higher energy that the octahedral sites resulting in preferential octahedral occupation as reported in previous studies on the PdH systems. Here the octahedral site will be given a value of 0.0eV and all other sites will then be scaled relatively to that. From Hajime Kimizuka et al (2019) and Kimizuka Hajime et al (2018) the difference in energies between the O and T sites is given as 0.05eV therefore, the tetrahedral site here will hold an energy of 0.05 eV. Which is also of the same order of magnitude the delta E calculated by the Nudge Elastic Band DFT result presented in Fig. 6.14.

α-Phase

Beginning in the alpha phase as with barrier heights the polycrystalline widths have been calculated and extracted from the long time scale component of the intermediate scattering function and a Chudley-Elliott model was fitted to extract the amplitude and estimated jump lengths (Fig. 5.31),

(a) T=200K

(b) T=300K

(c) T=400K

(d) T=500K
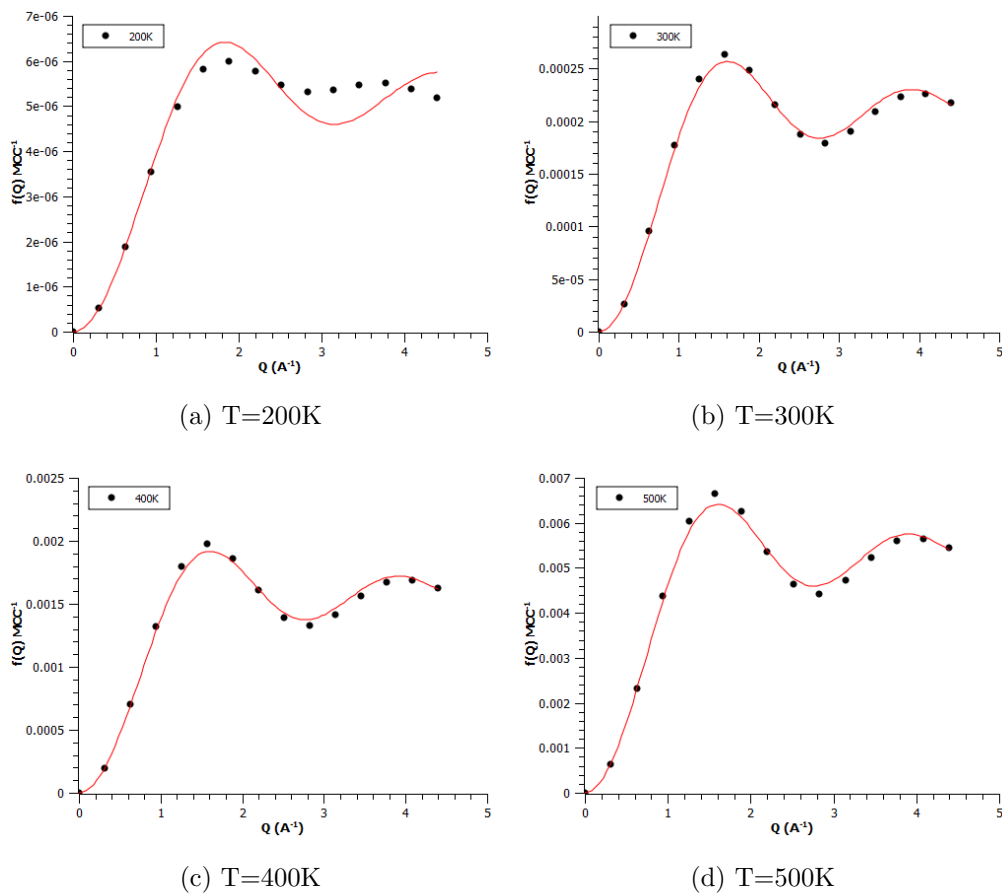
Figure 5.31: Chudley-Elliott fits to each individual broadening from directionally averaged half widths at 200K, 300K, 400K and 500K when concentration is C = 0.033. Site energies set to O=0.00eV and T = 0.05eV.

171

From the fitted CE model the jump lengths can be extracted along with the factor A from Eqn. 3.16 referred to as amplitude in the table below (Table. 5.7).

Temperature(K)	Amplitude	l(Å) (MC)
200	5.27e-06	2.4496
250	4.23e-05	2.7635
300	0.00021	2.79304
350	0.00067	2.77106
400	0.00158	2.78851
450	0.00309	2.76929
500	0.00527	2.78830

Table 5.5: Fitted jump lengths via the Chudley Elliott model with amplitudes when tetrahedral site energies and barrier heights are included in α-phase PdH.

Using these jump rates and amplitudes an Arrhenius plot can be produced which can give an in-site into the barrier in operation for the diffusing atom.

(a)   (b)
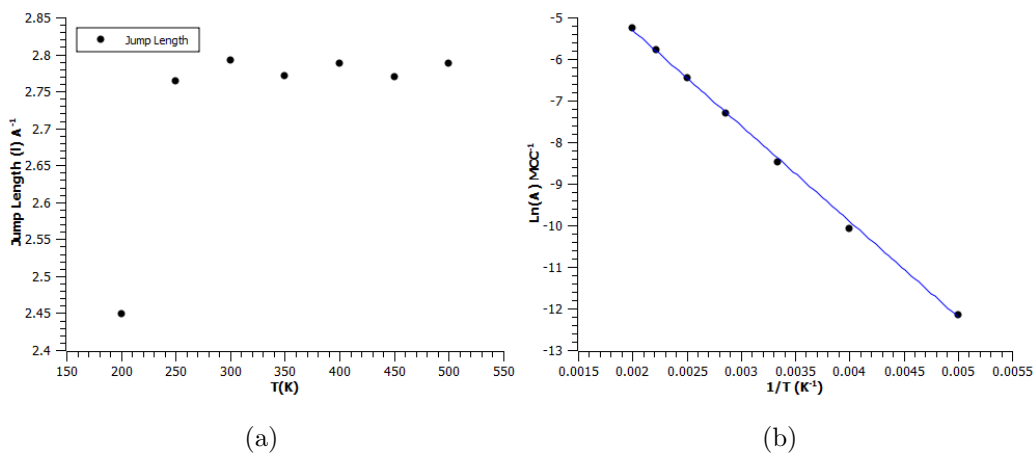
Figure 5.32: Extracted jump lengths from Chudley Elliott fits with an Arrhenius plot.

As the Arrhenius plot in Fig. 5.32 behaves linearly it could be expected that there is only the O-O jump barrier in operation. When looking at the Short time scale component of the intermediate scattering functions the widths extracted from the double exponential fit, Fig. 5.33, give some indications of a type of motion occurring on the shorter time scale while the Chudley Elliott type diffuse motion is still retrievable from the long time scale.

(a) T=200K

(b) T=300K

(c) T=400K

(d) T=500K
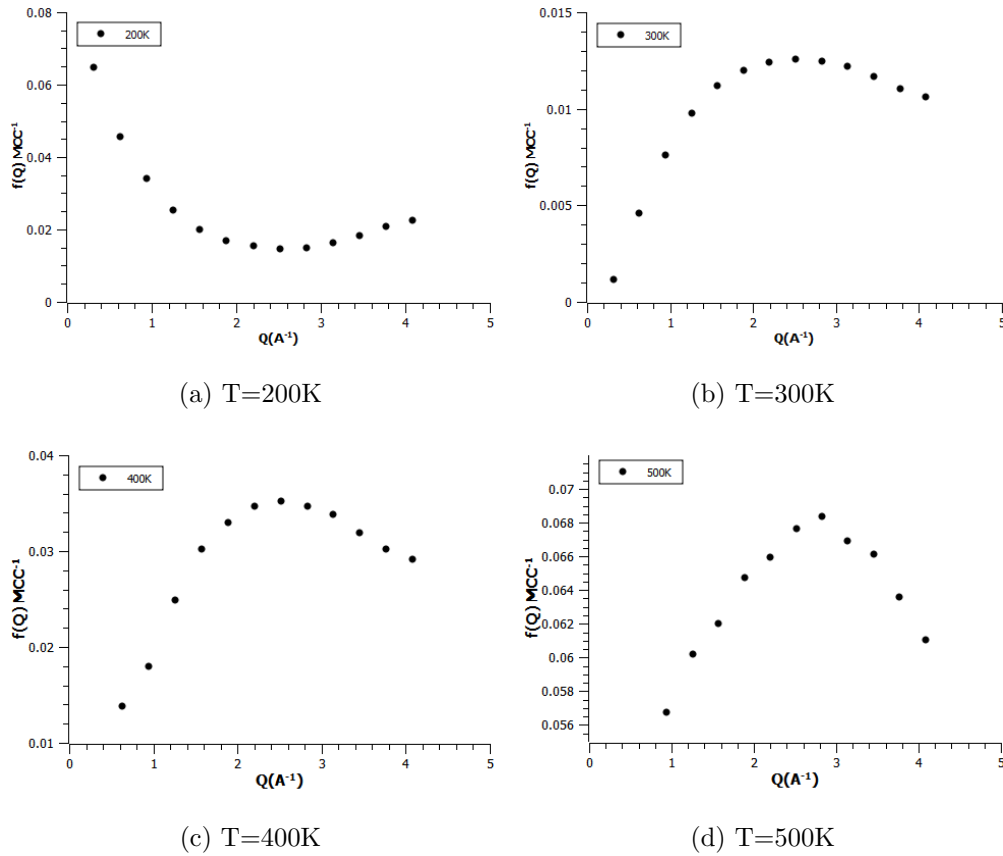
Figure 5.33: Short time scale directionally averaged half widths from a double exponential fit at 200K, 300K, 400K and 500K when concentration is C = 0.033. Site energies set to O=0.00eV and T = 0.05eV.

β-Phase

Two concentrations have been considered here, 1.0 and 0.7 when scalled in relation to the fraction of occupation of the octahedral sites these are 0.33 and 0.23 respectively. Beginning with the latter where there should still exist octahedral site vacancies, the extracted widths from the long time scale component agree well with the Chudley Elliot model, Fig. 5.34.

(a) T=200K

(b) T=300K

(c) T=400K

(d) T=500K
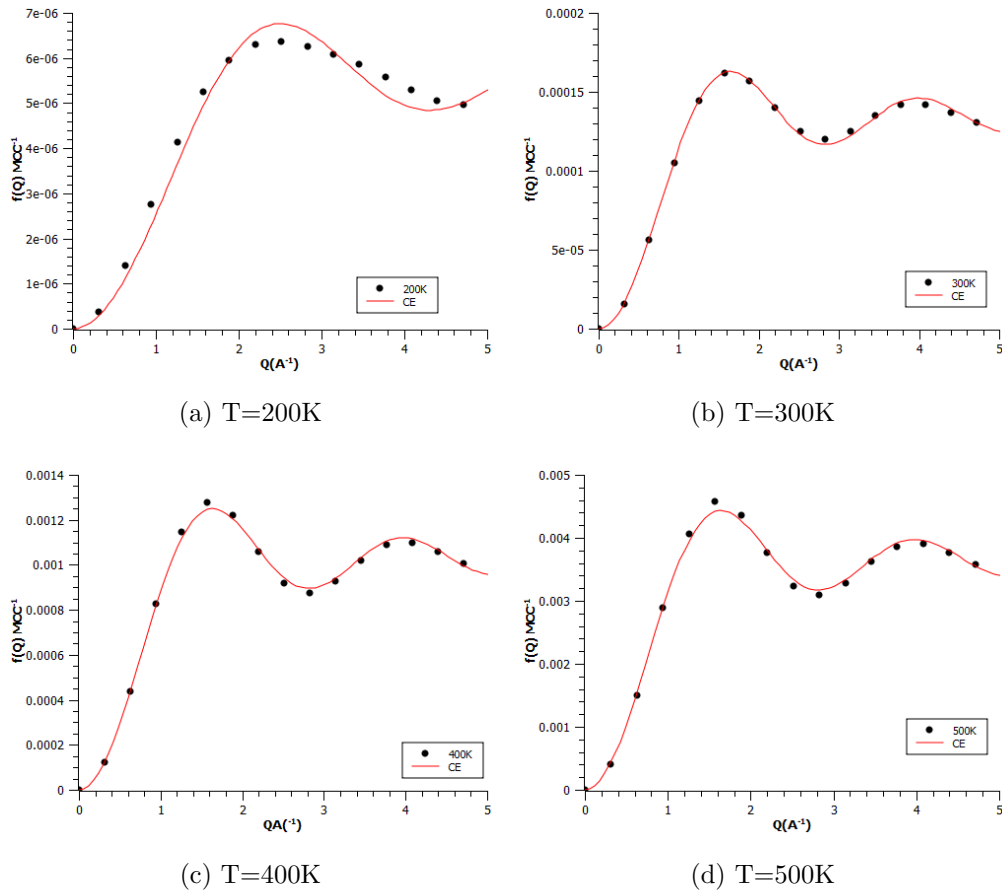
Figure 5.34: Chudley-Elliott fits to each individual broadening from directionally averaged half widths at 200K, 300K, 400K and 500K when concentration is C = 0.23. Site energies set to O=0.00eV and T = 0.05eV.

174

Temperature(K)	Amplitude	l(Å) (MC)
200	5.55e-06	1.79353
250	3.10e-05	2.65445
300	0.000134	2.73250
350	0.000419	2.74731
400	0.001026	2.74548
500	0.003641	2.73740

Table 5.6: Fitted jump lengths via the Chudley-Elliott model with amplitudes when tetrahedral site energies and barrier hights are included at C=0.23

(a)   (b)
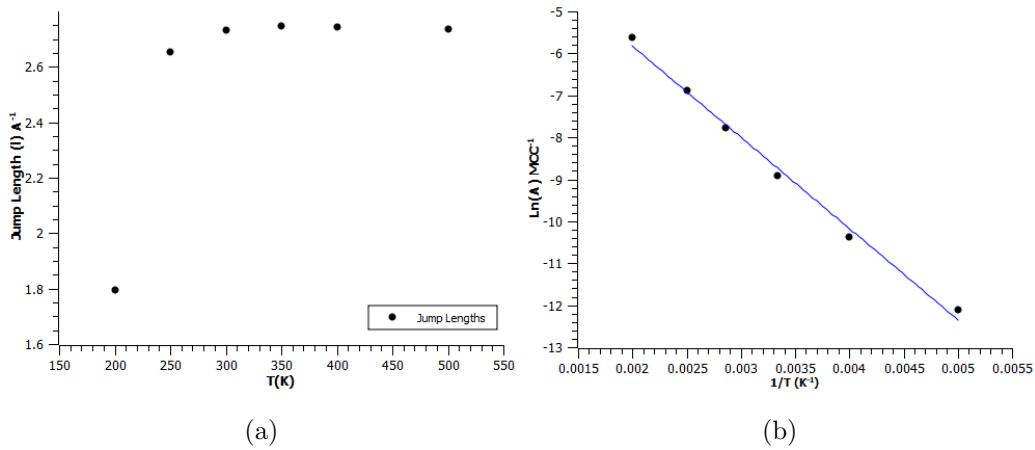
Figure 5.35: Extracted jump lengths from Chudley Elliott fits with an Arrhenius plot.

The fact that the Arrhenius plot in Fig. 5.35b appears to deviate from the linear nature seen when only one type of diffusion barrier is in operation indicates that as the hydrogen concentrations increase into the β-phase range that there is more than one type of diffusion mechanism being used by the diffusing hydrogen atoms.

(a) T=200K

(b) T=300K

(c) T=400K

(d) T=500K
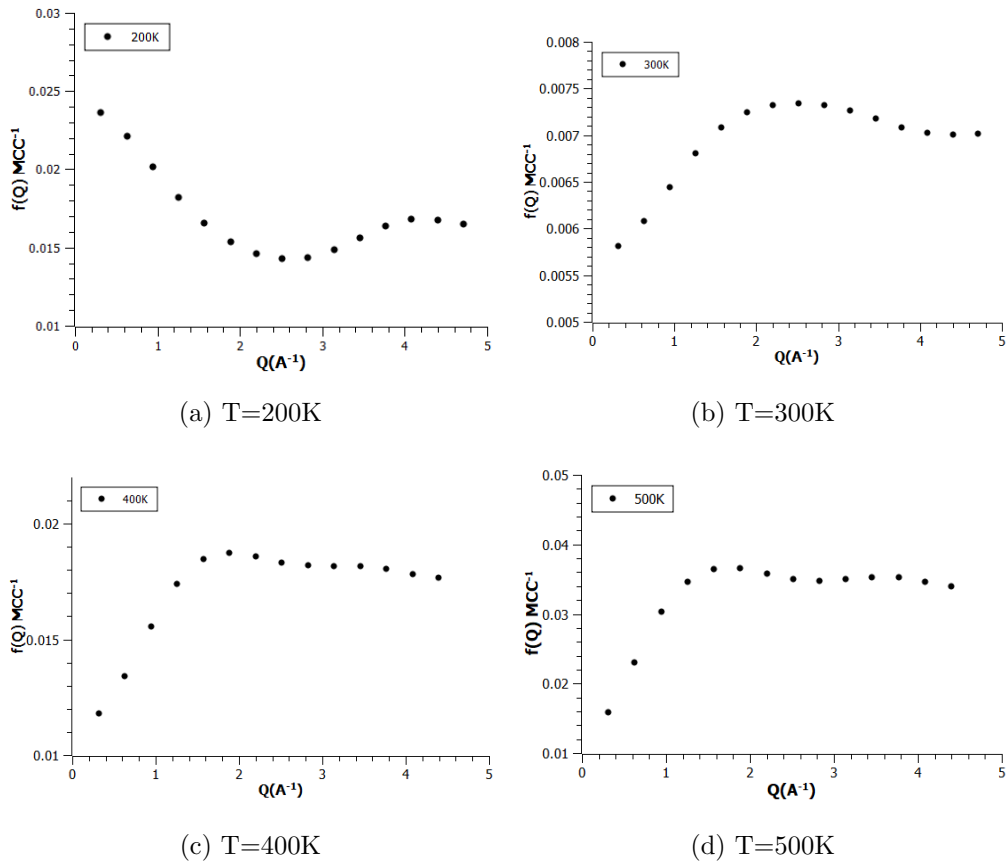
Figure 5.36: Short time scale directionally averaged half widths from a double exponential fit at 200K, 300K, 400K and 500K when concentration is C = 0.23. Site energies set to O=0.00eV and T = 0.05eV.

In Fig. 5.37 the hydrogen concentration is increased to 1.0, which is scaled such that all octahedral sites should be filled, despite this being unphysical in experiment terms.
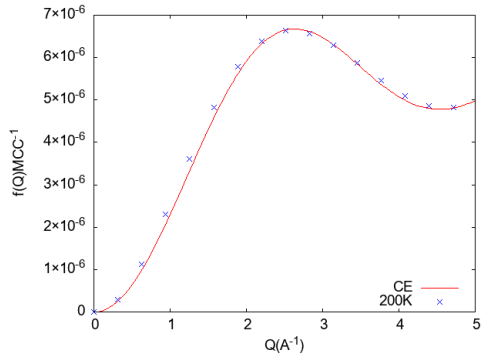
(a) T=200K
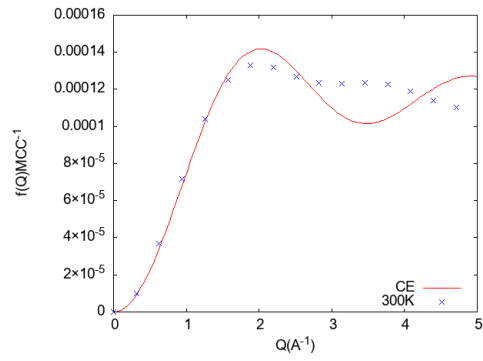
(b) T=300K
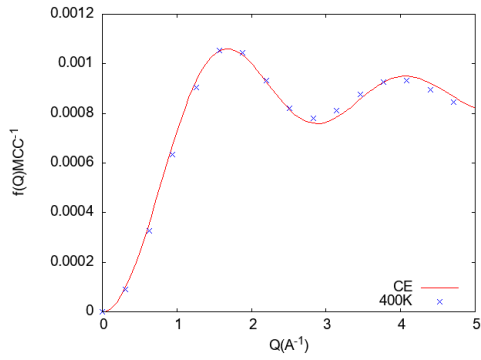
(c) T=400K
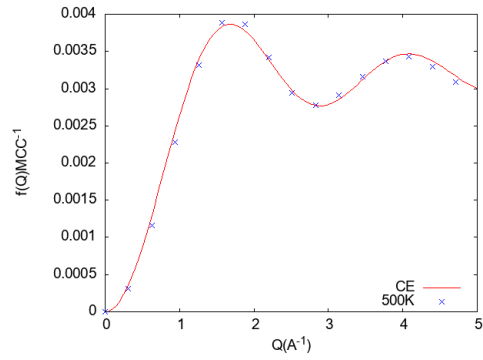
(d) T=500K

Figure 5.37: Chudley Elliott fits to each individual broadening from directionally averaged half widths at 200K, 300K, 400K and 500K when concentration is C = 0.33. Site energies set to O=0.00eV and T = 0.05eV.

The directionally averaged widths for the slowly decaying component on the long time scale are well represented by the Chudley Elliott polycrystalline model for diffusion with the inclusion of both barrier heights and the site energy of the tetrahedral sites, with the concentration equal to 0.33 equivalent to octahedral occupation.

Temperature(K)	Amplitude	l(Å) (MC)
200	5.48e-06	1.7407
250	2.97e-05	1.8440
275	6.17e-05	1.9751
300	0.00012	2.22131
325	0.00021	2.43749
350	0.00036	2.59236
375	0.00057	2.62188
400	0.00087	2.64044
425	0.00129	2.64160
450	0.00179	2.65209
475	0.00243	2.66343
500	0.00317	2.67412

Table 5.7: Fitted jump lengths via the Chudley-Elliott model with amplitudes when tetrahedral site energies and barrier heights are included

From these data an Arrhenius plot can be made again to find out the activation energy, Fig. 5.38b.
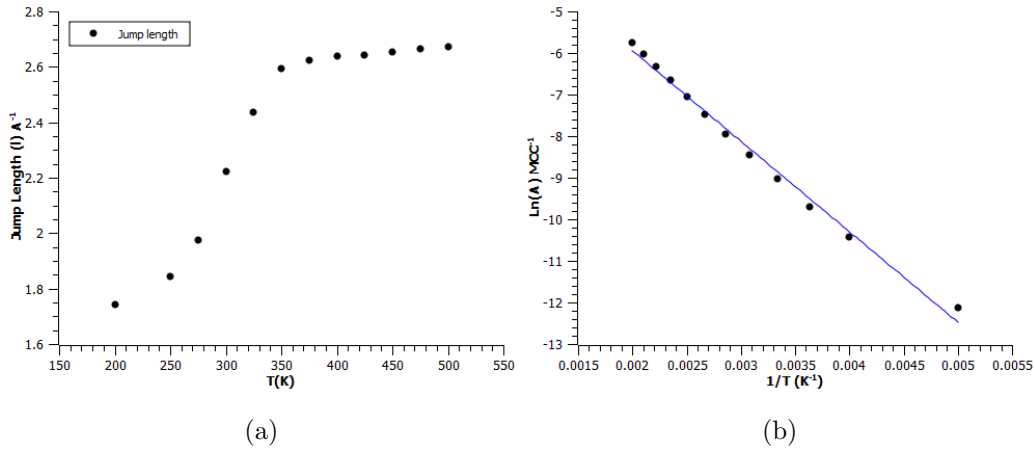
Figure 5.38: Extracted jump lengths from Chudley Elliott fits with an Arrhenius plot.

With the inclusion of a tetrahedral site energy at a concentration $c = 0.33$ it can be seen from Fig. 5.38b that the Arrhenius plot is no longer behaving linearly as would be expected if there was only one diffusion barrier available for the diffusing hydrogen atom. Because of this non linear behaviour it is not the case of simply extracting one activation energy as for alpha-phase concentrations. This then further supports the existence of multiple types of diffuse motion occurring via different path ways mainly the O-T-O mechanism.

The Rapidly decaying component extracted from the double exponential fit is shown in Fig. 5.36 as well supports the idea of a second type of diffuse motion occurring on a different time scale.
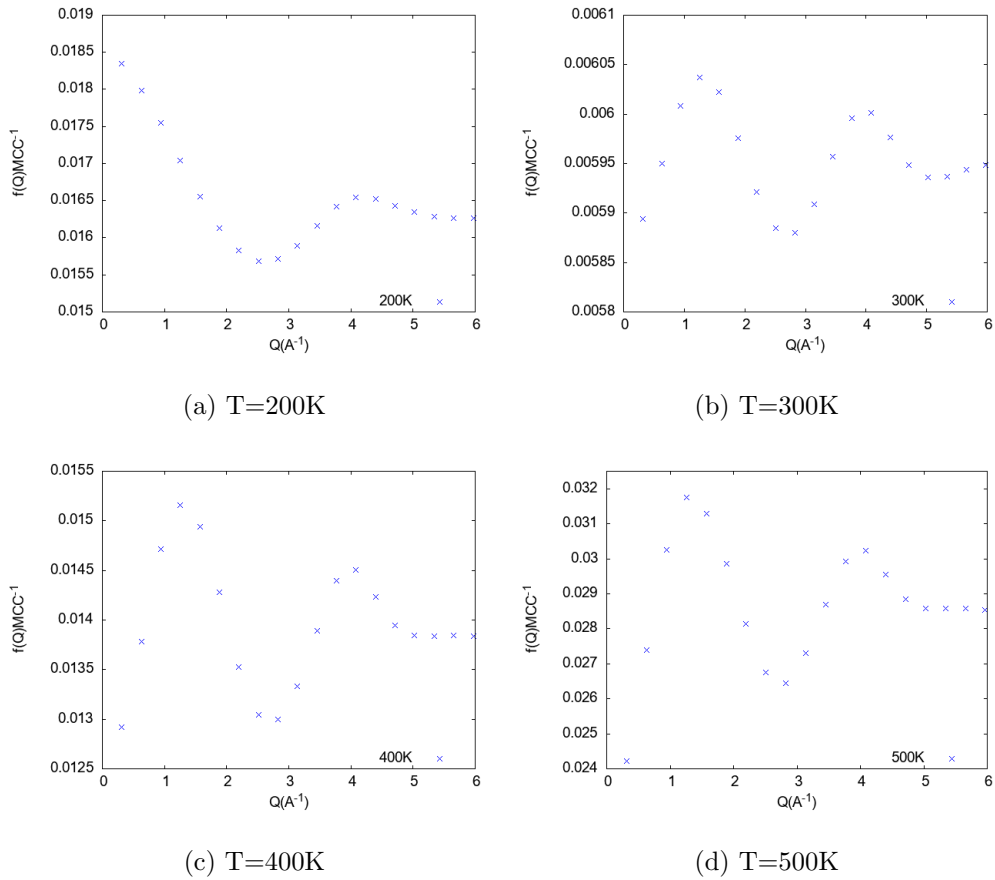
Figure 5.39: Short time scale directionally averaged half widths from a double exponential fit at 200K, 300K, 400K and 500K when concentration is C = 0.33. Site energies set to O=0.00eV and T = 0.05eV.

Widths indicative of localised motion occurring in the system can be seen at all four temperatures, these have been calculated using Monte-Carlo simulated pair-correlation functions using concentrations of 0.33 and 0.23 distributed over a lattice size 20x20x20 with a $g(r)$ radius = 5.0, tetrahedral site energy = 0.05 and barrier heights from DFT transition state searches and NEB calculations. The presence of a localised type of motion can also be seen when the EISF is examined for the inclusion of site energies, Fig. 5.42 and 5.43.
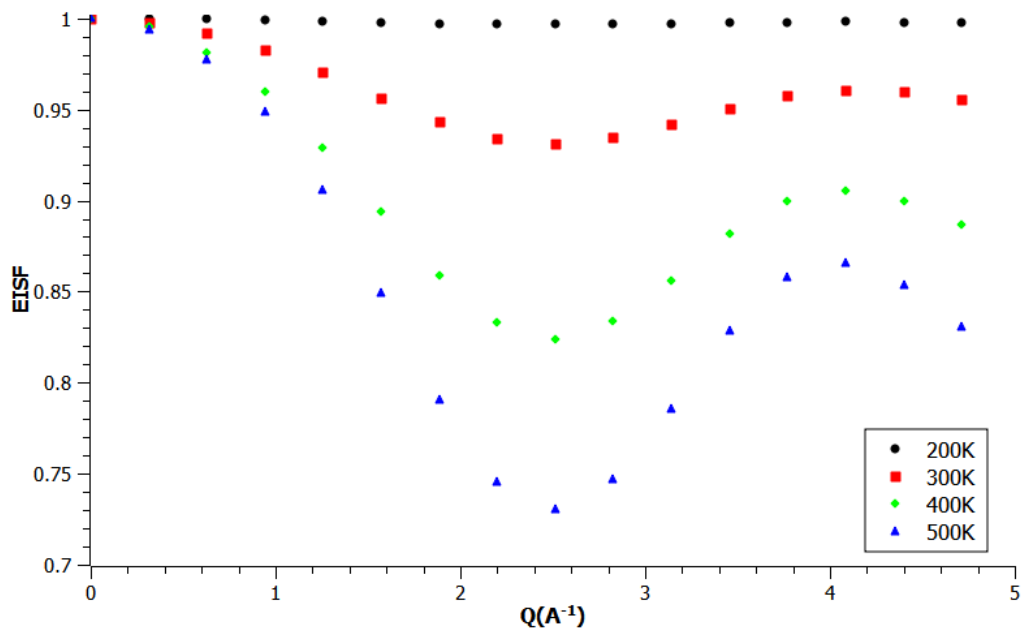
Figure 5.40: The Elastic Incoherent Structure Factor for 200K,300K and 400K with both barrier heights and site energies. c=0.23
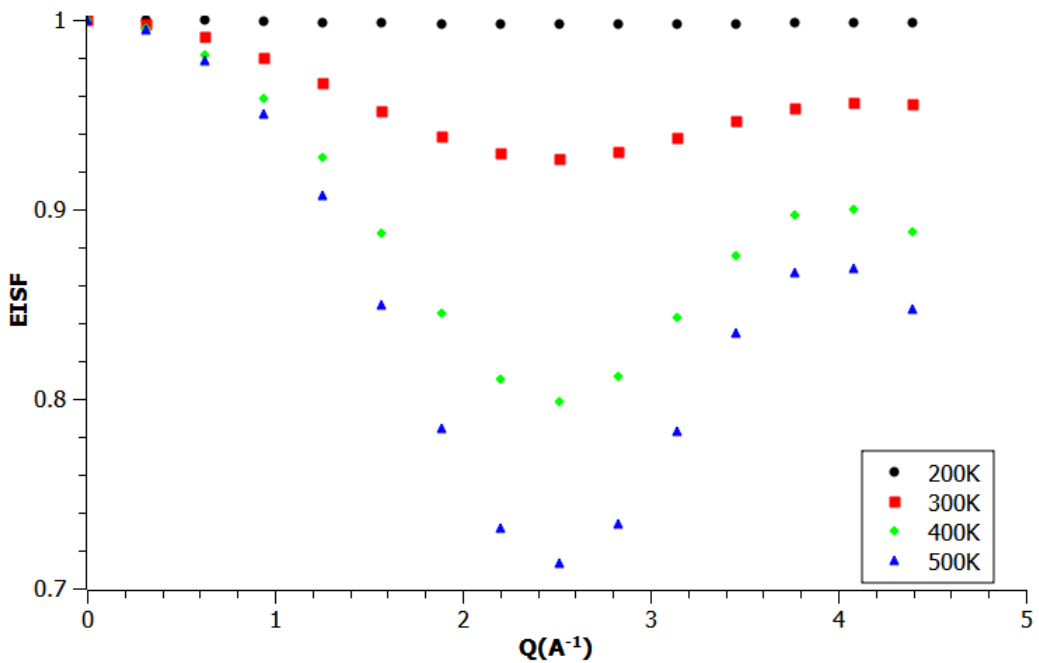
Figure 5.41: The Elastic Incoherent Structure Factor for 200K,300K and 400K with both barrier heights and site energies. c=0.33

The EISF's for both β-phase concentrations 0.7 and 1.0, shows resemblance to that of the form of two site Barnes model Fig.2.15. However, here the octerhedral and tetrahedral sites here are energetically in-equivalent. Knowing this it is possible to fit the 2 site model for energetically different sites using the following terms for A_0 and A_2 in Eqn.(2.63),

$$A_0(Q) = \frac{1}{1+\rho} \left[1 + \rho^2 + 2\rho j_0(Qd) \right] \tag{5.5}$$

$$A_1(Q) = \frac{2\rho}{1+\rho^2} \left[1 - j_0(Qd) \right] \tag{5.6}$$

where ρ if the ratio of attempt frequencies, $\rho = \tau_1/\tau_2$ (Bée, 1988), to the EISF data presented in figure 5.42 and 5.43 which can be seen to be in good agreement with the two site Barnes model.
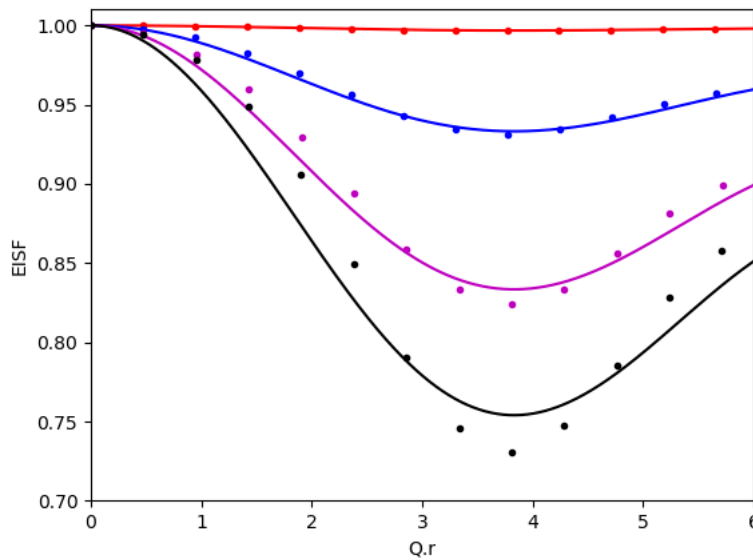
Figure 5.42: EISF for c=0.7 fitted with jump model between two sites with different transition rates.
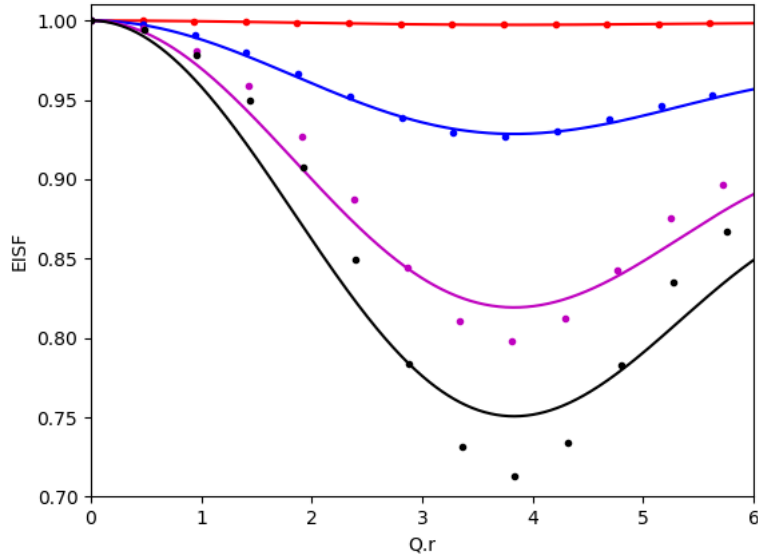
Figure 5.43: EISF for c=1.0 fitted with jump model between two sites with different transition rates.

These results presented here are significant as they display motion between the octahedral and tetrahedral sites as well as the recovery of the CE model for diffusion between octahedral and octahedral sites when there are more physically meaningful values used in the calculation of the pair-correlation function G(r,t), along with the EISF displaying behavior to that of diffusion among two energetically different sites. Interactions however, have yet to be included, this ideally would be in the form of an embedded atom potential, but is possible with the current code to include inter particle interactions via hard sphere blocking that was used in section 4.5.2 for the C15 test case.

The results from the double exponential fit over the shorter time scale in Fig. 5.33, 5.36 and 5.39 display some indication that there is not a strong Q dependence particularly at higher Q values. In some cases the widths appear

to decrease towards zero at low Q. However, in this rage the contribution from long range diffusion is likely to dominate, as low Q corresponds to large distances and is sensitive to long range motion. Here, the amplitudes of the quasi elastic contribution associated with localised motion tend to zero at low Q. The EISF Fig.5.42 and 5.43 provideds stronger evidance to suggest that there is some form of localised motion taking place. At the higher concentrations there is some evidence of Q dependence that could arise from Chudley-Elliott type behaviour. Attempts to parameterise the Chudley Elliott model did not result in any satisfactory fit.

Chapter 6

Concluding Remarks and Further Work

Results from Monte-Carlo simulations of PdH have been interpreted by following the example of localised motion seen in systems such as the C15 Laves phase system of ZrV_2H_x in which it is accepted that multiple types of motion are occurring both due to site blocking effects and the geometry of the system. The results presented here for PdH_x display behaviour indicative of different types of motion taking place, this can be seen as motion occurring on two distinct time scales: a long time scale Chudley-Elliott type motion and a short time scale more rapid localised motion. This localised motion becomes apparent when a double exponential is fitted to the shorter time scale, defined in terms of Monte-Carlo cycles, using the decay constant and amplitude from the fit of a reduced set of data points associated with the longer time scale. A significant part of these results occurs in regards to the motion occurring on the long time scale, as in the calculation of the pair correlation function there are only two allowed jumps octahedral to tetrahedral (O-T) and vice versa. As Chudley Elliott type motion would be expected for only the oc-

185

tahedral to octahedral jump type which in the Monte-Carlo calculations are not present. However when the widths from the single exponential fits of the long time scale $I(Q,t)$s are plotted a clear Chudley-Elliott type behavior can be seen, along with a behavior that is indicative of localised motion from the short time scale widths from the double exponential fit. Although a model has yet to be produced to characterise the decay constants from the short time scale like the Chudley Elliot model, there is a clear indication of a more localised type of motion occurring from these decay constants. This localised motion is believed to be as a result of rapid jumps between an octahedral site and any of its neighbouring tetrahedral sites with a low residency time or an immediate jump back to either the original octahedral site or a free neighbouring octahedral site, producing the typically seen O-O jump behavior but via a O-T-O jump mechanism. Jumps occurring via the O-T-O path have been previously suggested by Kofu et al (2020) and are schematically represented in Fig. 1.3, the two time scales suggested there were as a result of the diffusing atom being in its first excited and its ground state rather than localised jumps Fig. 1.6. This could be possible to model with slight modification to the current code however due to the introduction of another jump type, it would already be expected to produce jumps on multiple time scales. Here however, it is suggested that the motions are not mutually exclusive and are occurring along side each other such is supported by experimental QENS measurements schematically represented in figure 1.5 where the broad and narrow components can seen to be parts of the total lorentzian produced from the scattering. Primarily only the incoherent scattering function has been presented.

However, in the development of the methodology for calculating the widths the coherent broadening was considered and calculated for a face centered cubic lattice. The 'TOTAL' pair correlation function would be of interest to calculate going forward with the same parameters used in the results presented above.

6.0.1   Long Time Scale Component

The behavior of these calculated widths for PdH can be compared to those calculated experimentaly by QENS from previous works (Steel, 2018) and (Kofu et al., 2016) by using the Chudley Elliott model for a powder sample Eqn. 5.13. For this the the the residency times are required, these can be gained from the Arrhenius equation,

$$\tau = \tau_0 \exp\left(-E/k_B T\right) \tag{6.1}$$

Where E is the activation energy. If a Q value is selected for widths to be calculated at, they can be compared directly. Using the jump length $2.85\mathring{A}$ and $1.2\mathring{A}^{-1}$, the residency times from the ground state and activation energies of the ground state reported in Kofu and steel can be used at temperatures used for QENS experiments carried out by Steel *et al* widths can be calculated and compared between the two bodies of work in Table. 6.1 and Fig. 6.1,6.2.

Temperature(K)	$\Gamma_{kofu}(meV)$	$\Gamma_{Steel}(meV)$
230	0.0437	0.0252
360	0.1744	0.1073
300	0.7184	0.4714
340	2.1209	1.4625
433	12.1302	9.0597
453	16.0736	12.1606
468	19.5406	14.9164
483	23.4691	18.0660
498	27.8780	21.6297

Table 6.1: Comparison of widths calculated from data presented by Kofu et al (2020) and Steel (2018).
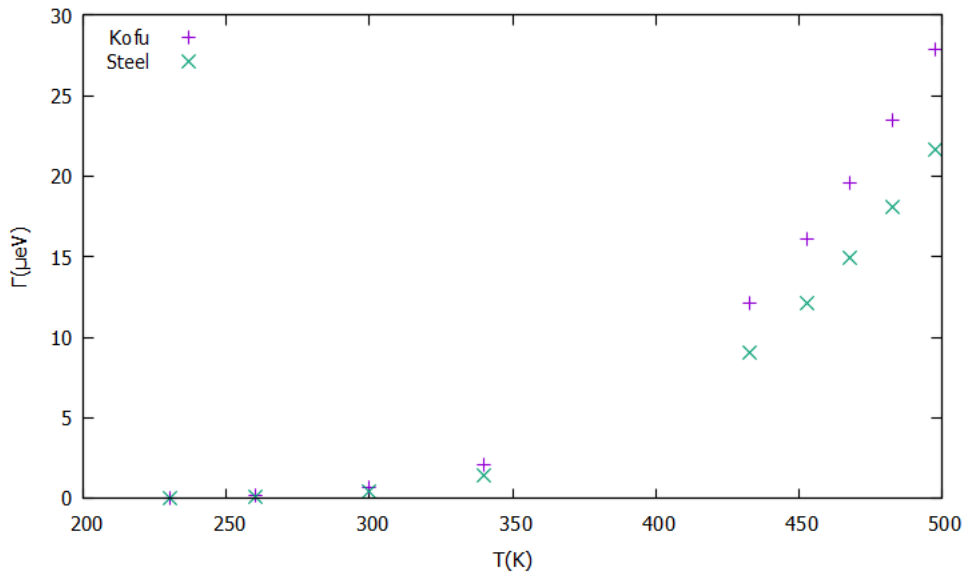
Figure 6.1: Widths from Table 6.1.
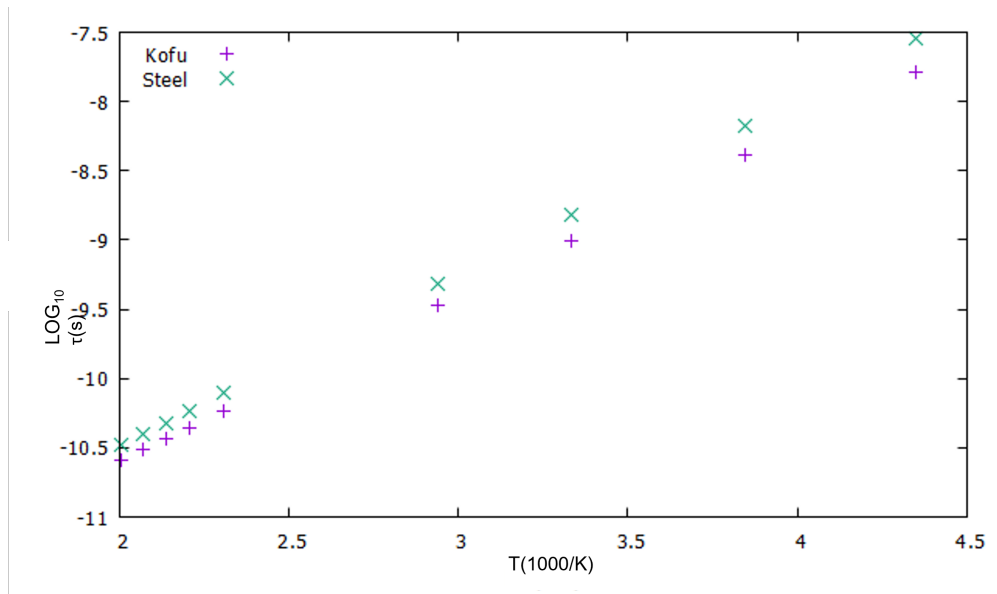
Figure 6.2: inverse temperature against against the log of residency time $(log(\tau))$.

These two sets of results show strong similarities to each other following the same pattern with an increase in half width half maximum as the temperature is increased. This feature of the data is also seen with the widths presented here for the Monte-Carlo simulations of PdH. The widths presented in the table above were calculated just using the residency time and the activation energies. Steel presented fitted results from Eqn.5.13 at higher end of the temperature range, if these values are used to calculate widths at again $Q = 1.2\mathring{A}^{-1}$ the simulated results and experimental results can be better compared.
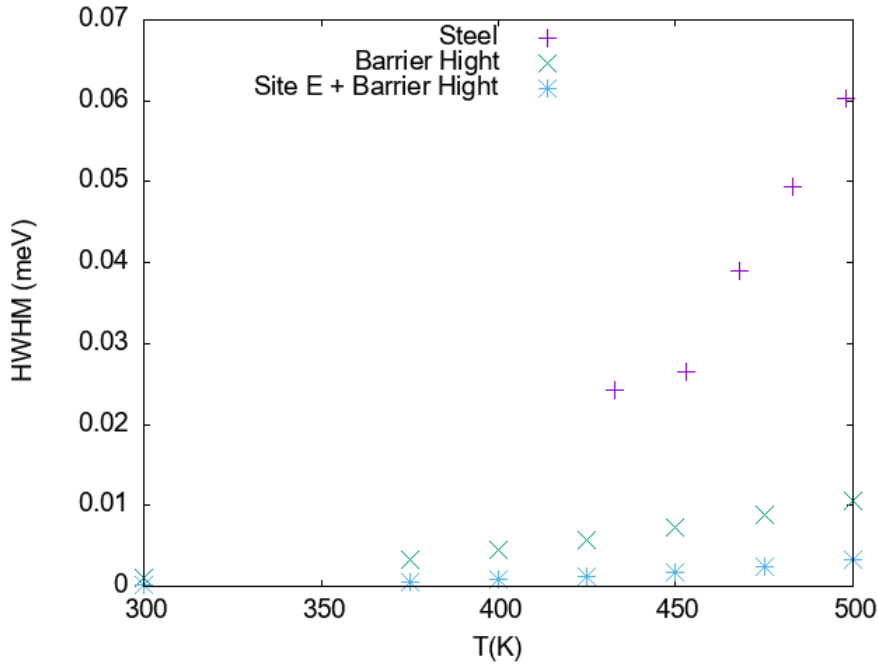
Figure 6.3: Comparison of widths calculated from (Steel, 2018) fitted parameters and Monte-Carlo simulated widths including barrier heights and barrier heights plus tetrahedral site energy

The widths calculated (Steel, 2018) although greater in magnitude show an increase in width as temperature increases, this same pattern can be seen in the simulated results from Monte-Carlo. This gives confidence that the narrow component of QENS broadening results behaves the same as the broadening of the motion of particles occurring on the long time scale calculated with MC.

6.0.2 Short Time Scale Component

The motion presented here occurring on the shorter time scale here supports previously findings presented by Steel (2018) where in the powder sample of PdH a broad component, Fig. 6.4 and 6.5, was identified presenting similar behaviour to that presented in results here,
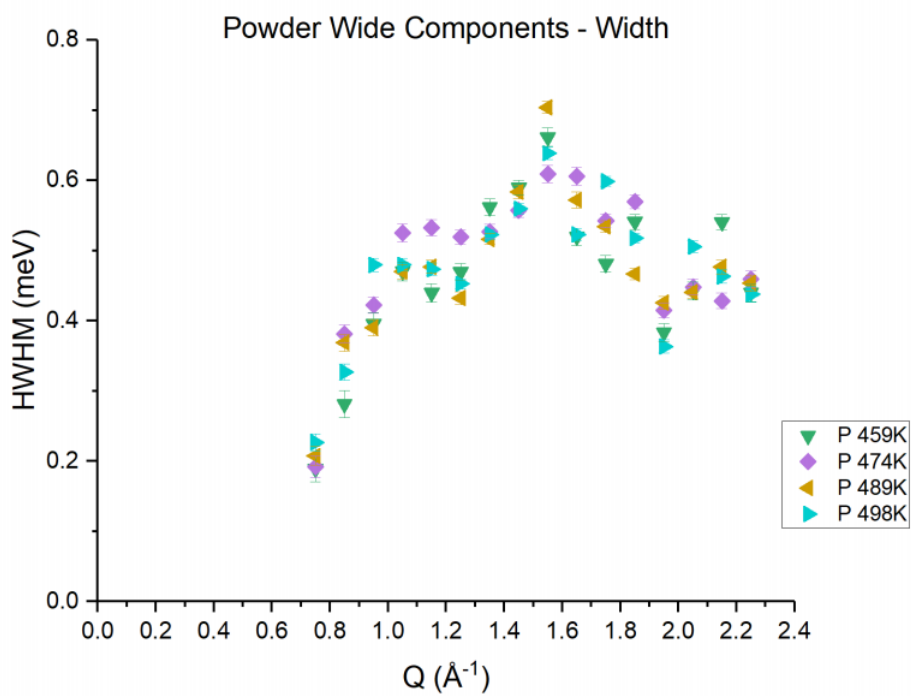
Figure 6.4: Broad component widths for high temperature range presented by Steel (2018)
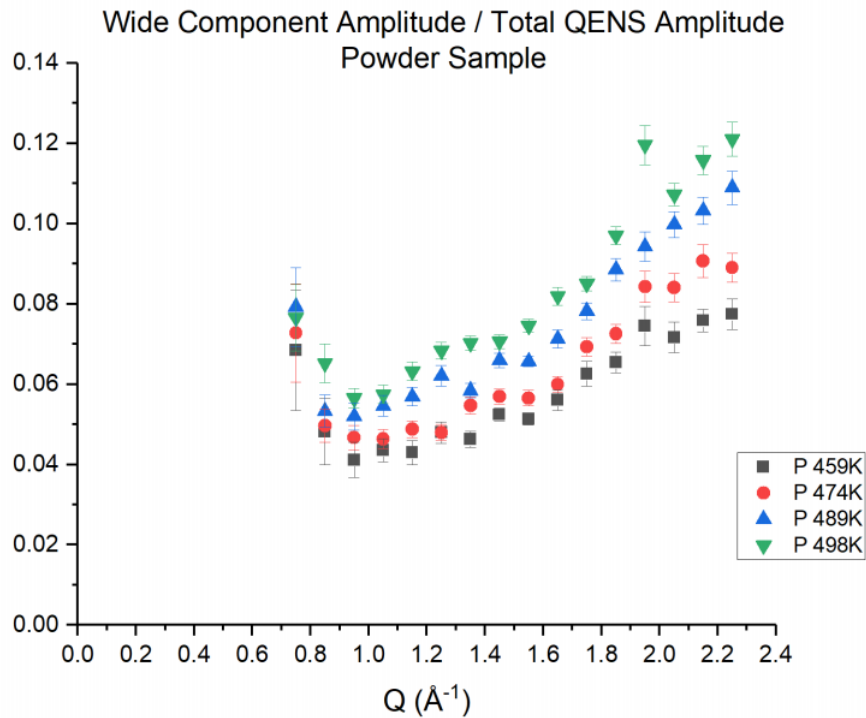
Figure 6.5: Broad component amplitudes as a fraction of the the total QENS for high temperature range presented by Steel (2018)

It was suggested that there is little discernible temperature dependence in the wide component, represented as the broad lorentzian (blue dot), Fig. 1.4 and Fig 1.5.

However, this motion becomes more apparent at higher temperatures, this could be seen as being analogous with the short time scale widths presented here as the amplitude of the fitted decay constants appears to increases with higher temperatures but appears relatively consistent ant low temperatures, Fig. 6.6, 6.7, 6.6
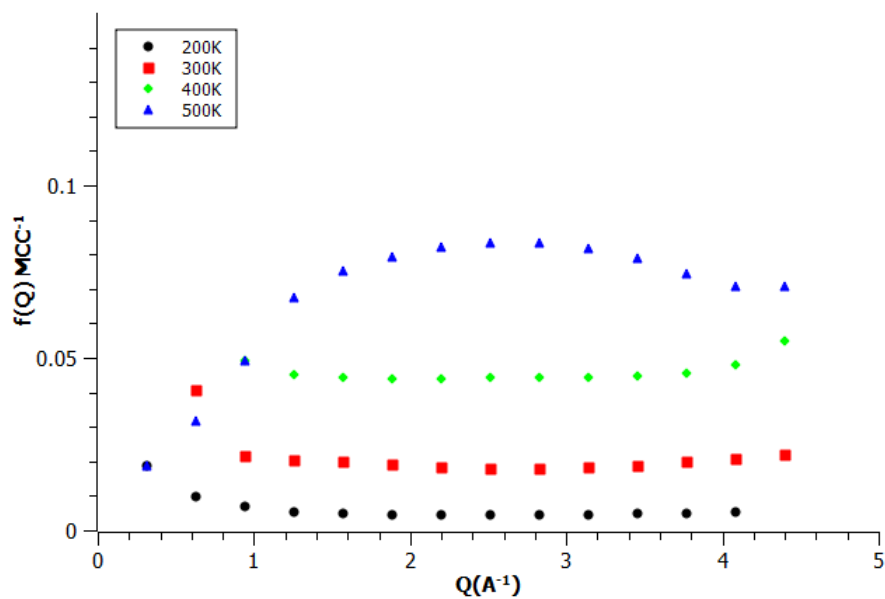
Figure 6.6: Directionally averaged decay constants from a double exponential fit over a range of temperatures for C=0.1
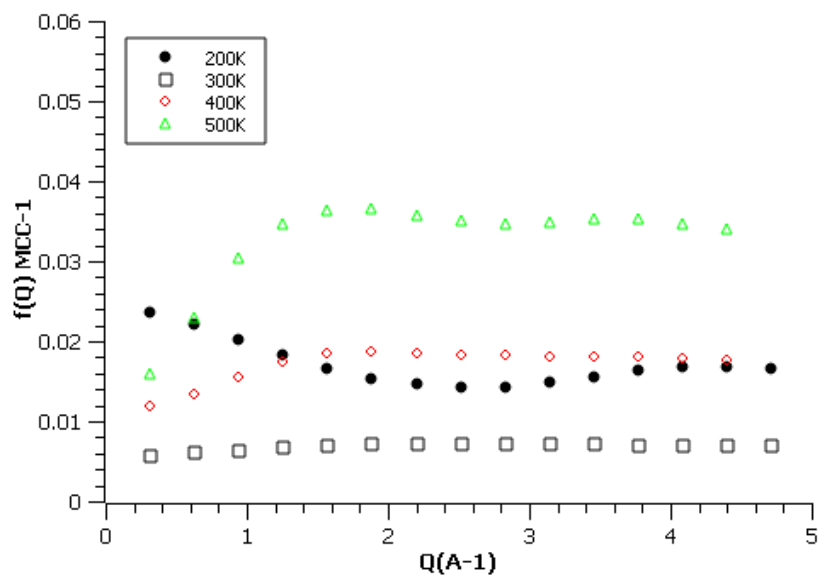
Figure 6.7: Directionally averaged decay constants from a double exponential fit over a range of temperatures for C=0.7
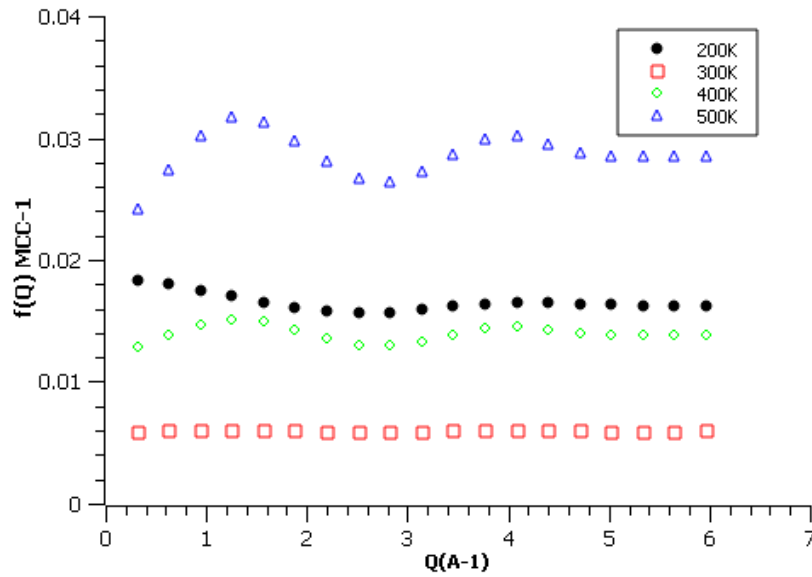
Figure 6.8: Directionally averaged decay constants from a double exponential fit over a range of temperatures for C=1.0

6.0.3 Site occupancy

It can be seen in the calculated jump lengths that as temperature increases there is also an initial increase in the jump lengths shown in Fig. 5.32, 5.35, 5.38. This apparent increase in jump lengths could be down to the average site occupancies Fig. 6.9 and Fig. 6.10 from which each of the Monte-Carlo simulations were started. These occupancies display an increase with temperature,

194
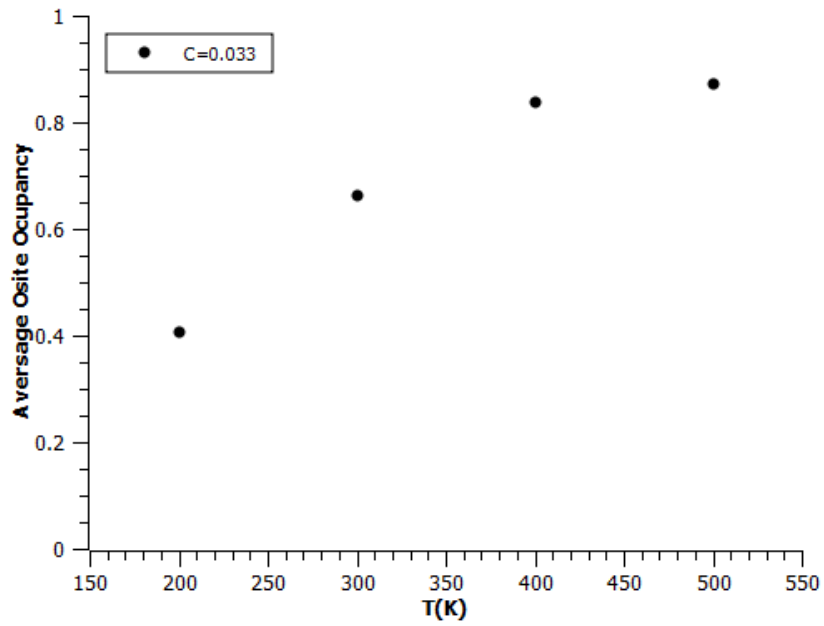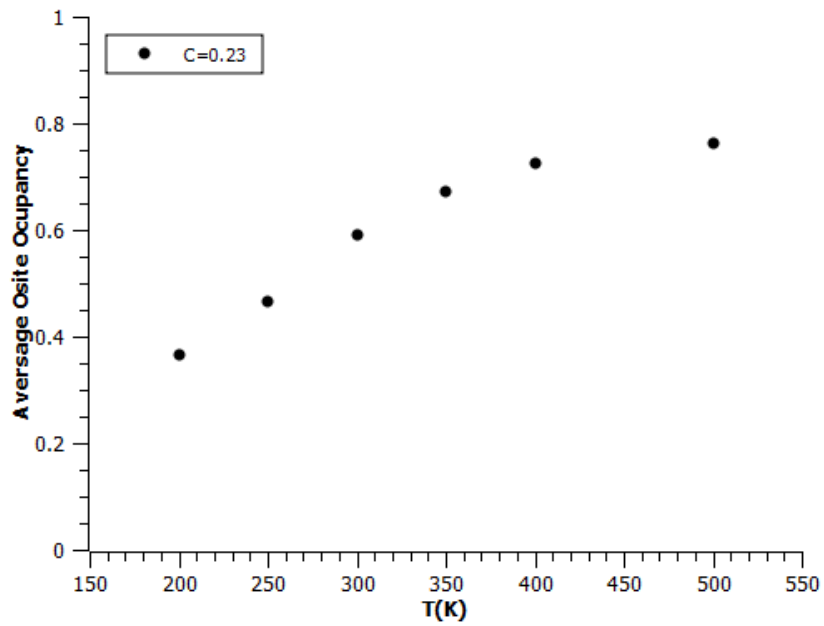
(a) C=0.033

(b) C=0.23

Figure 6.9: Average octahedral site occupancy with increasing temperature for concentrations C = 0.033,0.23. Site energies set to O =0.00eV and T = 0.05eV
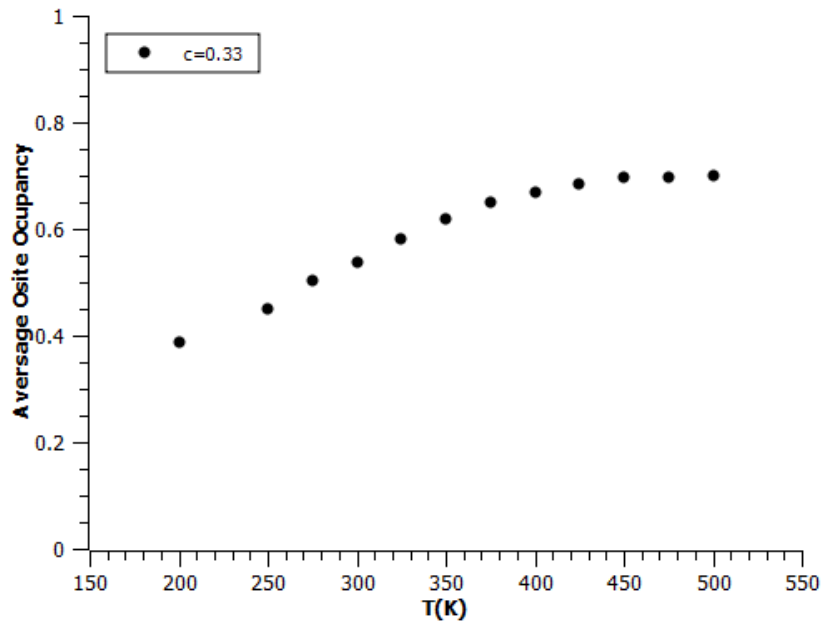
(a) C=0.33
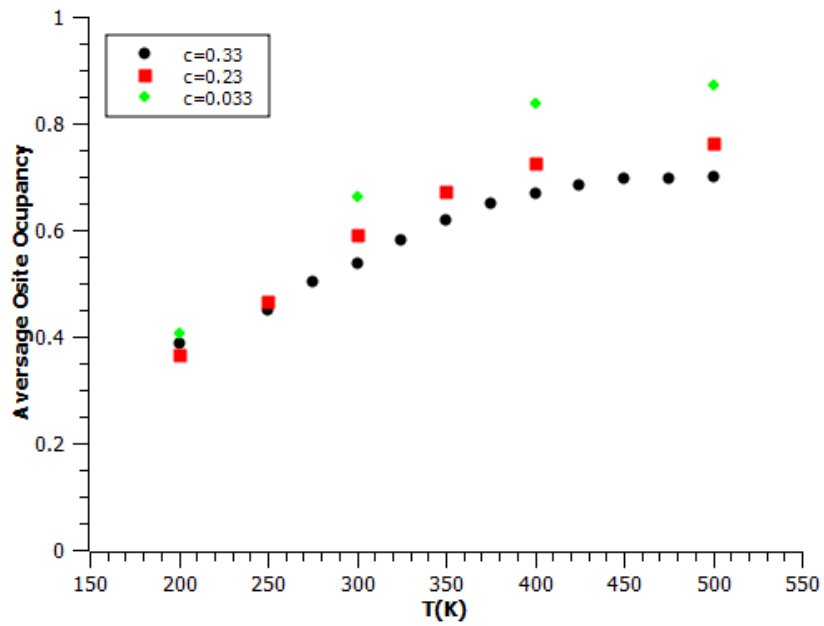
(b) Comparison of C

Figure 6.10: Average octahedral site occupancy with increasing temperature for concentrations C = 0.33 and a comparisons of C = 0.033,0.23 and 0.33. Site energies set to O=0.00eV and T = 0.05eV

When the individual burn in periods are considered for both α and β phase Palladium Hydride, Fig. 6.11, 6.12.
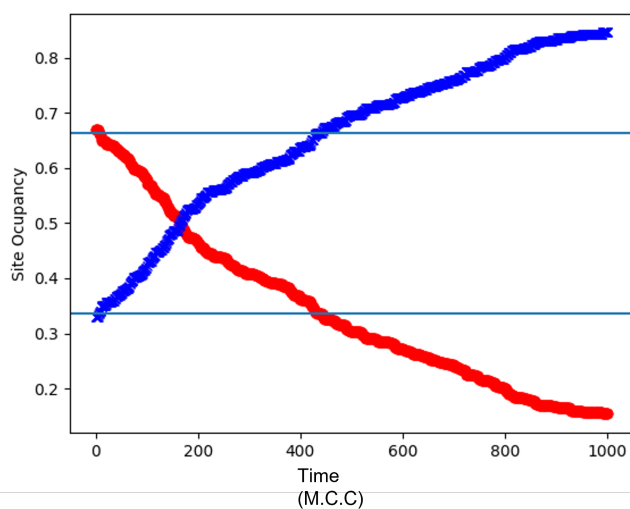
(a)
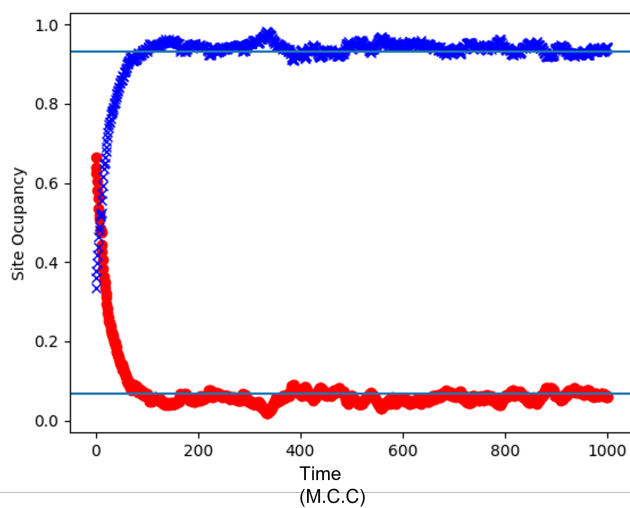
(b)

Figure 6.11: Examples of the 'Burn in' period over 1000 cycles for 200K and 400K at 0.1 concentration

197
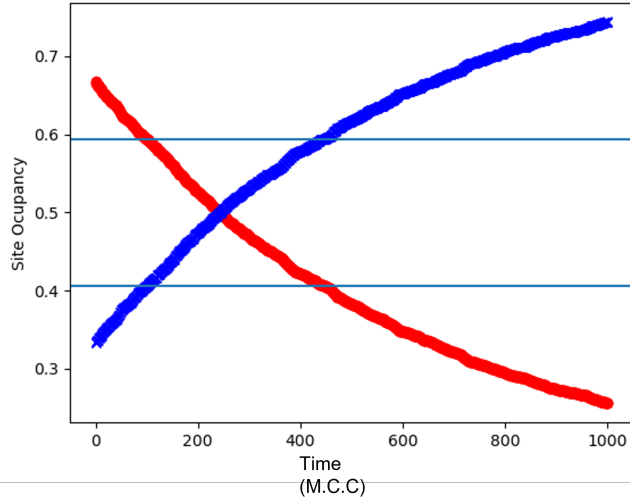
(a)
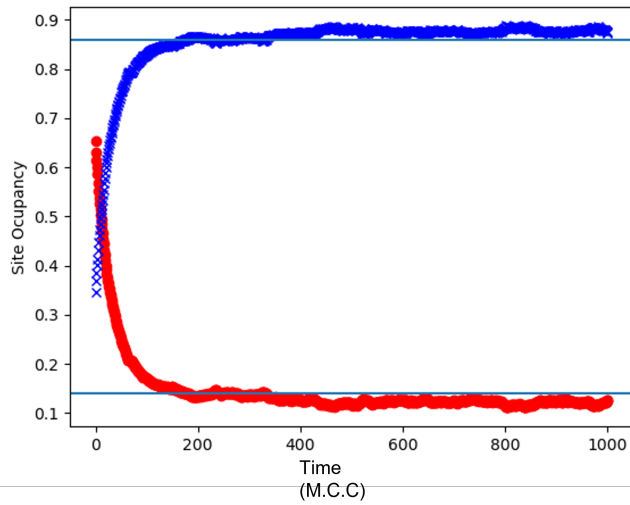
(b)

Figure 6.12: Examples of the 'Burn in' period over 1000 cycles for 200K and 400K at 0.7 concentration

It is clear that the system is not yet in a steady state at lower temperatures (200K) and appears to take a long time to approach a point where the atoms

198

are evenly distributed over available sites. More so at 200K the occupation initially is preferential to atoms in the tetrahedral site and a cross over occurs after a number of cycles and the octahedral sites begin to be preferentially occupied. It could be possible that there is some correlation between this cross over at the lower temperatures and the reduction in calculated jump lengths which could further be explored.

6.0.4 The Rowe Model

It was considered that due to the multiple basis created with the inclusion of tetrahedral sites that the Chudley Elliott model may not accurately describe the half width half maxima of the scattering function and instead the model produced by Rowe for Vanadium hydride would be better suited (Rowe et al., 1972), where an expression for the incoherent scattering function was given for a non-bravis lattice of energetically equivalent sites. Here the lattice is split up into m bases, with each basis having a different jump associated with it, where the probability of finding a particle on any of the m sub-latices at $\mathbf{r}$ for a given time becomes a weighted sum over all the sub-lattices (basis).

6.0.5 Particle Interactions

During the development of the methodology used to extract the widths associated with the more rapid motion multiple avenue's were explored but not fully pursued in regards to the parameters used in the calculation of the Pair-Correlation functions $G(\mathbf{r}, t)$. The natural extension of the work resented in the previous section would be to introduce hydrogen pair interactions in the form of an embedded atom potential (Zhou et al., 2008b) for hydrogen in palladium, Fig. 6.13
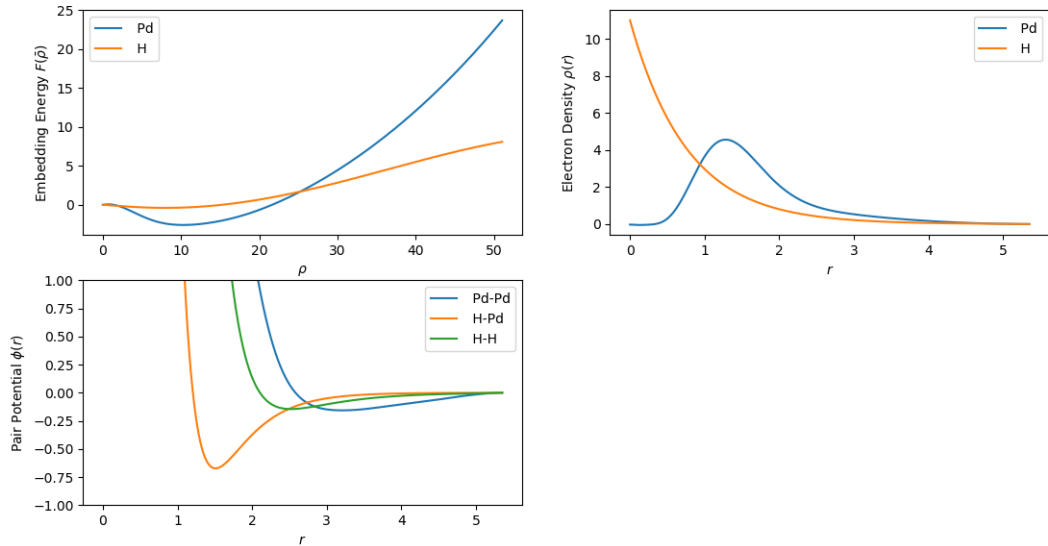
Figure 6.13: Example of the embedded atom potential for PdH. H-H, Pd-H and Pd-Pd potentials, calculated using ASE in Python and potentials from Zhou et al (2008a).

Another way of introducing hydrogen interactions into the PdH system is by hard sphere potentials which were tested on a simple cubic system and used in the C15 work in the previous chapter. In the simple cubic case a reduction in the amplitude of the calculated widths is seen from the non interacting to the interacting case, as well as a reduction in the jump lengths seen in ZrV_2H. For the case of the fcc lattice such as Palladium hydride, there are a number of points in reciprocal space where the maxima in $S(\mathbf{Q})$, the static structure factor, can occur depending on the relative strength of the inter-particle interactions over first and second nearest-neighbours; it is not immediately obvious how this will affect the spherically averaged forms. Before progressing to the case of the fcc lattice, simulations were run for a sc lattice, where there should by a single peak at $\mathbf{Q} = \frac{2\pi}{a} \left(\frac{1}{2}, \frac{1}{2}, \frac{1}{2} \right)$ in order to

200

test the methodology. This could be taken further and applied and refined for the fcc case as for the simple cubic case this was successfully was done for a range of reduced temperatures up to the transition temperature where as expected there was a large peak observed corresponding to the known location of a Bragg reflection from the ordered superstructure.

6.0.6 First principles calculations

Further work is needed to utilise the DFT calculator CASTEP with the Nudged Elastic Band model to be able to produce a more precise picture of the minimum energy pathway between sites in both the PdH and ZrV_2H system as a means of acquiring barrier heights and site data from first principles for use in the Monte-Carlo calculations. An attempt has been made using python to marry the two together with varying results (Fig. 6.14). The results of which for PdH showed dependence on which optimizer was used to optimise each image in the chain of configurations between the initial and final configuration, for which more work and a comparison is needed, as well as the determination of the thresholds required for the optimizer not to become trapped along the path when finding the saddle point. The phonons for both the octahedral and tetrahedral sites were calculated along with the phonons for the the possible saddle point found from the Nudged Elastic Band calculations, these have not yet been used but it was discussed that these can be used to calculate the zero point energies for each site respectively which would give activation energies for use in the calculation of the pair correlation function.

Similar calculations have been attempted in this work using a combination of Nudged Elastic Band calculations in partnership with DFT calculator CASTEP (Clark et al., 2005), to calculate a minimum energy path between

201

the octahedral and tetrahedral sites via a saddle point, Fig.6.14.
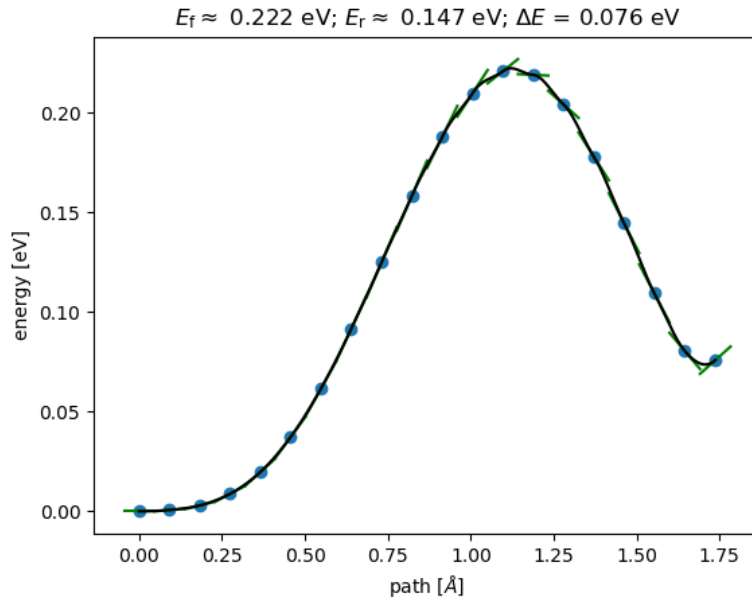
Figure 6.14: Miniumum Energy Pathway from a Nudge Elastic Band calculation

These calculations were carried out with a combination of both python and CASTEP using ASE (Atomic Simulation Environment) which is a set of Python tools and modules used for carrying out atomistic simulations (Larsen and Jørgen, 2017)

Appendix A

Example input files

A sample input file for both C15 and PdH Monte-Carlo runs are given below in sections such that is can be mapped onto the outline shown in Chapter 3 Section 3.2. For the C15 input file a hard sphere potential is included to model repulsive interactions, where as these were not included for the PdH Monte-Carlo simulations.

A.1 C15 ZrV_2H_x

```
'c15_070120_100.out'

7.44

400.0

1
0.0

'SHELLS'
3
0.2   10000
0.27 0.2
0.38 0.05

'FILLRAN'
0.0417
'CE'
500
'grt_070120_c15.dat'
'NODUMP'
```

Figure A.1: First section of an example input file ZrV_2H_x whose outline is shown in Fig. 3.4 for populating the lattice.

```
'GRT'
'c15GRt_070120_100.dat'
'FORMAT'
2.5

500
100
'DYNAMIC'

2
1 1 0.16 0.18 1.0 0.165
1 1 0.0 0.16 1.0 0.063

25
'SELF'
```

Figure A.2: Second section of an example input file ZrV_2H_x whose outline is shown in Fig. 3.5 for the parameters of the simulation of diffusion.

```
0.5        0.5        0.0
0.5        0.0        0.5
0.0        0.5        0.5
24
0.3125        0.3125        0.1250        1
0.1250        0.3125        0.3125        1
0.3125        0.1250        0.3125        1
0.0625        0.5625        0.3750        1
0.0625        0.3750        0.1875        1
0.8750        0.5625        0.1875        1
0.4375        0.9375        0.6250        1
0.6250        0.4375        0.9375        1
0.9375        0.6250        0.4375        1
0.6875        0.6875        0.8750        1
0.1875        0.8750        0.5625        1
0.3750        0.1875        0.0625        1
0.9375        0.8125        0.6250        1
0.6250        0.9375        0.8125        1
0.8125        0.6250        0.9375        1
0.5625        0.1875        0.8750        1
0.6875        0.8750        0.6875        1
0.3750        0.0625        0.5625        1
0.8125        0.4375        0.1250        1
0.1250        0.8125        0.4375        1
0.4375        0.1250        0.8125        1
0.1875        0.0625        0.3750        1
0.5625        0.3750        0.0625        1
0.8750        0.6875        0.6875        1
1.0        0.0        0.0
0.0        1.0        0.0
0.0        0.0        1.0
−10 −10 −10
```

Figure A.3: Final section of an example input file for ZrV_2H_x whose outline is shown in Fig. 3.3 for setting up the lattice.

A.2   Palladium Hydride

```
'PdH_200120_grt1.out'

4.0

400

2
0.0
0.05

'SHELLS'
0

'FILLRAN'
0.33
'CE'
100
'energy1s_grt0033.dat'
'NODUMP'
```

Figure A.4: First section of an example input file for PdH whose outline is shown in Fig. 3.4 for populating the lattice.

```
'GRT'
'grtPdH_1s_200120.dat'
'FORMAT'
5.0

250
2
'DYNAMIC'
2
1 2 0.0 0.6 1.0 0.16
2 1 0.0 0.6 1.0 0.11
35
'SELF'
```

Figure A.5: Second section of an example input file for PdH whose outline is shown in Fig. 3.5 for the parameters of the simulation of diffusion.

```
0.5     0.5     0.0
0.5     0.0     0.5
0.0     0.5     0.5
3
0.5     0.5     0.5     1
0.25    0.25    0.25    2
0.25    0.25    0.75    2
1.0     0.0     0.0
0.0     1.0     0.0
0.0     0.0     1.0
-20     -20     -20
```

Figure A.6: Final section of an example input file for PdH whose outline is shown in Fig. 3.3 for setting up the lattice.

Appendix B

Post Processing Python Scripts

On top of the FORTRAN code GRT outlined in chapter 3 a set of python scripts have been developed in order to effectively process the GRT results.

First of which is **grt2iqt.py** this carries out the first Fourier transform in space to generate the intermediate scattering function ($I(Q,t)$) for a given Q-vector (hkl). Also generates an output file containing data points of the calculates $I(Q,t)$.

Following this is **iqt2fq.py** which from the GRT output file carries out the the spatial Fourier transform generating $I(Q,t)$ to which a single exponential is fitted for the given Q vector and widths extracted. The process is repeated for a given interval along the chosen Q-vector i.e (0,0,0), (0.5,0.5,0.5) and (1,1,1) which would calculate 3 decay constants relating to the widths in the Quasi-elastic broadening. It should be noted that both theses scripts have Coherent and incoherent variants.

The above script was then modified to calculate the polycrystalline width **grt2fq poly.py**. This uses a Lebedev quadrature which requires a **Q** value from a range of **Q** vales to be passed to a quadpy.shphere.Lebedev function as well as a Lebedev order relating to the number of points to be used in the

spherical averaging.

```python
# List of q-values

q_start = 0.1
q_end = 2.1

n_step = 0.1

q = numpy.arange(q_start,q_end,n_step)

fq = []
for qval in q:
    val = quadpy.sphere.integrate(
        iqt_fit,
        [0.0, 0.0, 0.0], qval,
        quadpy.sphere.Lebedev(29)
            # Lebedev possible Orders:
            # {3,5,7,9,11,13,15,17,19,21,23,25,27,29,31,35,41,47,
            #  53,59,65,71,77, 83,89,95,101,107,113,119,125,131};
        )

    print(qval,val)

    fq.append(val/(4. * numpy.pi * qval * qval))

    out.write(str(qval) +'  '+ str(val/(4. * numpy.pi * qval * qval))+'\n')
out.close()
```

Figure B.1: Example of how the Quadpy Lebadev function is used in **grt2fq poly.py**

B.1 Multiple time scale scripts

GRT output from systems where there are multiple types of motion occurring requires a different set of post processing scripts.

grt2iqt 0.1.py to **grt2iqt 1.0.py** are a set of scripts that deals extracts the intermediate scattering functions and widths associated with two different time scales of GRT, requiring two different GRT output files for input files. **grt2iqt 1.0.py** carries out automated fitting of $I(Q,t)$ for both time scales for a range of given Q values. Produces output files of fitting parameters and plots of both time scales and one combined on the shorter time scale.

grt2iqt poly 0 1 4.py is structured the same as the above mentioned scripts however deals with the polycrystalline (spherically averaged) intermediate scattering function. This script however fits a single or double ex-

210

ponential to the averaged intermediate scattering function, which is a less accurate way of calculating the polycrystalline equivalent widths.

Improvements were made with a set of scripts where the fitted widths themselves are spherically averaged, **grt2fq poly 0 4 4tot.py** and **grt2fq poly 0 4 4tot shortT.py**. These were split into two separate scripts to be run in succession for ease of programming. **grt2fq poly 0 4 4tot shortT.py** uses the output files generated from **grt2fq poly 0 4 4tot.py** to calculated the short time scale widths.

The Elastic Incoherent Structure Factor was then calculated by using **grt2iqt poly 0 1 5.py** a modified version of the initial polycrystalline script.

Appendix C

Quasi-elastic Broadening from the Chudley-Elliott Model for an fcc Lattice

In this section, the expressions in Eqn. (2.56) and Eqns. (5.2, 5.3 and 5.4) are derived for the particular case of an fcc lattice.

The quasi-elastic broadening from the Chudley-Elliott Model is

$$f(\mathbf{Q}) = \frac{1}{n} \sum_{\mathbf{l}} 1 - e^{-i\mathbf{Q} \cdot \mathbf{l}} \tag{C.1}$$

where $\mathbf{l}$ are the set of vectors to the nearest neighbour sites in the fcc lattice.

A a general momentum transfer vector, $\mathbf{Q}$, can be written as

$$\mathbf{Q} = \frac{2\pi}{a}(Q_x, Q_y, Q_z) \tag{C.2}$$

For the jump vector $\mathbf{l}_1 = a(1/2, 1/2, 0)$, the dot product with $\mathbf{Q}$ is then

$$\mathbf{Q} \cdot \mathbf{l}_1 = \frac{a}{2}(1,1,0) \cdot \frac{2\pi}{a}(Q_x, Q_y, Q_z) = \pi Q_x + \pi Q_y \qquad \text{(C.3)}$$

The dot products for the 12 jump vectors are then

$$\mathbf{Q} \cdot \mathbf{l}_1 = \pi Q_x + \pi Q_y \qquad \text{(C.4)}$$

$$\mathbf{Q} \cdot \mathbf{l}_2 = -(\pi Q_x + \pi Q_y) \qquad \text{(C.5)}$$

$$\mathbf{Q} \cdot \mathbf{l}_3 = \pi Q_x - \pi Q_y \qquad \text{(C.6)}$$

$$\mathbf{Q} \cdot \mathbf{l}_4 = -(\pi Q_x + \pi Q_y) \qquad \text{(C.7)}$$

$$\mathbf{Q} \cdot \mathbf{l}_5 = \pi Q_x + \pi Q_z \qquad \text{(C.8)}$$

$$\mathbf{Q} \cdot \mathbf{l}_6 = -(\pi Q_x + \pi Q_z) \qquad \text{(C.9)}$$

$$\mathbf{Q} \cdot \mathbf{l}_7 = \pi Q_x - \pi Q_z \qquad \text{(C.10)}$$

$$\mathbf{Q} \cdot \mathbf{l}_8 = -(\pi Q_x - \pi Q_z) \qquad \text{(C.11)}$$

$$\mathbf{Q} \cdot \mathbf{l}_9 = \pi Q_y + \pi Q_z \qquad \text{(C.12)}$$

$$\mathbf{Q} \cdot \mathbf{l}_{10} = -(\pi Q_y + \pi Q_z) \qquad \text{(C.13)}$$

$$\mathbf{Q} \cdot \mathbf{l}_{11} = \pi Q_y - \pi Q_z \qquad \text{(C.14)}$$

$$\mathbf{Q} \cdot \mathbf{l}_{12} = -(\pi Q_y - \pi Q_z) \qquad \text{(C.15)}$$

Inserting into Eqn. C.2,

$$f(\mathbf{Q}) = \frac{1}{12}[12 - (2\cos(\pi Q_x + \pi Q_y) + 2\cos(\pi Q_x - \pi Q_y)$$
$$+ 2\cos(\pi Q_x + \pi Q_z) + 2\cos(\pi Q_x - \pi Q_y)$$
$$+ 2\cos(\pi Q_y + \pi Q_z) + 2\cos(\pi Q_y - \pi Q_z)] \quad \text{(C.16)}$$

$$f(\mathbf{Q}) = 1 - \frac{1}{3}(\cos(\pi Q_x)\cos(\pi Q_y)$$

$$+ \cos(\pi Q_x)\cos(\pi Q_z)$$

$$+ \cos(\pi Q_y)\cos(\pi Q_z)) \quad \text{(C.17)}$$

For the high symmetry directions, this expression can be simplified.

(100) direction

$$cos(\pi Q_y) = 1 \quad \text{(C.18)}$$

$$cos(\pi Q_z) = 1 \quad \text{(C.19)}$$

So that

$$f_{100}(\mathbf{Q}) = 1 - \frac{1}{3}(2\cos(\pi Q_x) + 1) \quad \text{(C.20)}$$

(110) direction

$$cos(\pi Q_y) = cos(\pi Q_x) \quad \text{(C.21)}$$

$$cos(\pi Q_z) = 1 \quad \text{(C.22)}$$

so that

$$f_{110}(\mathbf{Q}) = 1 - \frac{1}{3}(\cos^2(\pi Q_x) + \cos(\pi Q_x)) \quad \text{(C.23)}$$

(111) direction

$$cos(\pi Q_y) = cos(\pi Q_x) \tag{C.24}$$

$$cos(\pi Q_z) = cos(\pi Q_x) \tag{C.25}$$

so that

$$f_{111}(\mathbf{Q}) = 1 - \cos^2(\pi Q_x) \tag{C.26}$$

References

quadpy. URL `https://pypi.org/project/quadpy/`.

H. Akiba, M. Kofu, H. Kobayashi, H. Kitagawa, K. Ikeda, T. Otomo, and O. Yamamuro. Nanometer-size effect on hydrogen sites in palladium lattice. *Journal of the American Chemical Society*, 138(32):10238–10243, 2016.

H. Barlag, L. Opara, and H. Züchner. Hydrogen diffusion in palladium based fcc alloys. *Journal of alloys and compounds*, 330:434–437, 2002.

J. D. Barnes. Inelastic neutron scattering study of the "rotator" phase transition in n-nonadecane. *The Journal of Chemical Physics*, 58(12):5193–5201, 1973.

M. Bée. *Quasielastic neutron scattering*. Adam Hilger, 1988.

M. Beg and D. Ross. The quasielastic scattering of cold neutrons from the beta phase of palladium hydride (and hydrogen diffusion). *Journal of Physics C: Solid State Physics*, 3(12):2487, 1970.

G. Bernardo, T. Araújo, T. da Silva Lopes, J. Sousa, and A. Mendes. Recent advances in membrane technologies for hydrogen purification. *International Journal of Hydrogen Energy*, 45(12):7313 – 7338, 2020. ISSN

0360-3199. doi: https://doi.org/10.1016/j.ijhydene.2019.06.162. Hydrogen separation/purification via membrane technology.

B. Bhatia and D. S. Sholl. Quantitative assessment of hydrogen diffusion by activated hopping and quantum tunneling in ordered intermetallics. *Physical Review B*, 72(22):224302, 2005.

F. Botter, J. Gowman, J. Hemmerich, B. Hircq, R. Lässer, D. Leger, S. Tistchenko, and M. Tschudin. The gas chromatographic isotope separation system for the jet active gas handling plant. *Fusion Technology*, 14 (2P2A):562–566, 1988.

R. Bowman Jr, E. Venturini, B. Craft, A. Attalla, and D. Sullenger. Electronic structure of zirconium hydride: A proton nmr study. *Physical Review B*, 27(3):1474, 1983.

D. P. Broom. *Hydrogen Storage Materials: The Characterisation of Their Storage Properties*. Green Energy and Technology. 2011. ISBN 9780857292216.

D. Bull. Static and dynamic correlation in lattice gas systems : an application to the intermetallic hydride ZrV_2H_x. September 2001. URL `http://usir.salford.ac.uk/id/eprint/61030/`.

D. Bull and D. Ross. Monte carlo simulation of hydrogen diffusion in c15 laves phase intermetallic compounds. *Journal of Alloys and Compounds*, 293-295:296 – 299, 1999a. ISSN 0925-8388. doi: https://doi.org/10.1016/S0925-8388(99)00319-9.

D. Bull and D. Ross. Monte carlo simulation of hydrogen diffusion in c15 laves phase intermetallic compounds. *Journal of alloys and compounds*, 293:296–299, 1999b.

217

D. Bull and D. Ross. Monte carlo simulation of quasi-elastic neutron scattering from lattice gas systems. *Physica B: Condensed Matter*, 301(1):54 – 58, 2001. ISSN 0921-4526. doi: https://doi.org/10.1016/S0921-4526(01)00511-7. Proceedings of the Fifth International Workshop on Quasi-Elastic Neutron Scattering.

D. Bull, D. Broom, and D. Ross. Monte carlo simulation of quasielastic neutron scattering from localised and long-range hydrogen motion in c15 laves phase intermetallic compounds. *Chemical Physics*, 292(2):153 – 160, 2003. ISSN 0301-0104. doi: https://doi.org/10.1016/S0301-0104(03)00155-1. Quasielastic Neutron Scattering of Structural Dynamics in Condensed Matter.

S. Campbell, M. Kemali, D. Ross, D. Bull, J. Fernandez, and M. Johnson. Quasi-elastic neutron scattering study of the hydrogen diffusion in the c15 laves structure, $TiCr_1$. *Journal of alloys and compounds*, 293:351–355, 1999.

R. Caputo and A. Alavi. Where do the H atoms reside in PdH_x systems? *Molecular Physics*, 101(11):1781–1787, 2003.

C. Chudley and R. Elliott. Neutron scattering from a liquid on a jump diffusion model. *Proceedings of the Physical Society*, 77(2):353, 1961.

S. J. Clark, M. D. Segall, C. J. Pickard, P. J. Hasnip, M. J. Probert, K. Refson, and M. Payne. First principles methods using CASTEP. *Z. Kristall.*, 220:567–570, 2005.

D. A. Cornell and E. Seymour. Nuclear magnetic resonance study of hydrogen diffusion in palladium and palladium-cerium alloys. *Journal of the Less Common Metals*, 39(1):43–54, 1975.

P. Davis, E. Seymour, D. Zamir, W. D. Williams, and R. Cotts. Nuclear magnetic resonance study of hydrogen diffusion in palladium-silver alloys. *Journal of the Less Common Metals*, 49:159–168, 1976.

W. Davis. Diffusion of gases through metals. i. diffusion of hydrogen through palladium. Technical report, Knolls Atomic Power Lab., 1954.

F. Demmel. Quasielastic neutron scattering, 2013. URL `https://www.isis.stfc.ac.uk/Pages/quasi-elastic-neutron-scattering13583.pdf`.

J.-J. Didisheim, K. Yvon, D. Shaltiel, P. Fischer, P. Bujard, and E. Walker. The distribution of the deuterium atoms in the deuterated cubic laves-phase zrv2d4· 5. *Solid State Communications*, 32(11):1087–1090, 1979.

J.-J. Didisheim, K. Yvon, P. Fischer, and D. Shaltiel. The deuterium site occupation in zrv2dx as a function of the deuterium concentration. *Journal of the Less Common Metals*, 73(2):355–362, 1980.

M. Dornheim. *Thermodynamics of Metal Hydrides: Tailoring Reaction Enthalpies of Hydrogen Storage Materials*. Thermodynamics - Interaction Studies - Solids, Liquids and Gases, Juan Carlos Moreno-Pirajan, IntechOpen, Available from, 2011. doi: 10.5772/21662.

A. Einstein. Über die von der molekularkinetischen theorie der wärme geforderte bewegung von in ruhenden flüssigkeiten suspendierten teilchen. *Annalen der physik*, 4, 1905.

C. Elsässer, M. Fähnle, K. Ho, and C. T. Chan. Ab initio pseudopotential calculations of total energies and forces for hydrogen in palladium. *Physica B: Condensed Matter*, 172(1-2):217–224, 1991.

D. A. Fick. V. on liquid diffusion. *The London, Edinburgh, and Dublin Philosophical Magazine and Journal of Science*, 10(63):30–39, 1855. doi: 10.1080/14786445508641925.

P. Fischer, F. Fauth, A. Skripov, A. Podlesnyak, L. Padurets, A. Shilov, and B. Ouladdiaf. Neutron diffraction study of deuterium ordering in c15 type $TaV_2D_x(x > 1)$ in the temperature range of 1.5–295 k. *Journal of alloys and compounds*, 253:282–285, 1997.

T. B. Flanagan and W. Oates. The palladium-hydrogen system. *Annual Review of Materials Science*, 21(1):269–304, 1991.

S. Fukada, K. Fuchinou, and M. Nishikawa. Hydrogen isotope separation by displacement chromatography with palladium. *Journal of nuclear science and technology*, 32(6):556–564, 1995.

Y. Fukai. *The metal-hydrogen system : basic bulk properties*. Springer series in materials science ; v. 21. Springer, Berlin ; New York, 2nd rev. and updated ed. edition, 2005. ISBN 9783540004943.

M. Gillan. A simulation model for hydrogen in palladium. i. single-particle dynamics. *Journal of Physics C: Solid State Physics*, 19(31):6169, 1986.

W. Gissler and H. Rother. Theory of the quasielastic neutron scattering by hydrogen in bcc metals applying a random flight method. *Physica*, 50(3): 380–390, 1970.

F. Giustino. *Materials modelling using density functional theory: properties and predictions*. Oxford University Press, 2014.

M. Glugla, I. R. Cristescu, I. Cristescu, and D. Demange. Hydrogen isotope separation by permeation through palladium membranes. *Jour-*

nal of Nuclear Materials, 355(1):47–53, 2006a. ISSN 0022-3115. doi: https://doi.org/10.1016/j.jnucmat.2006.04.003.

M. Glugla, D. Murdoch, A. Antipenkov, S. Beloglazov, I. Cristescu, I.-R. Cristescu, C. Day, R. Laesser, and A. Mack. Iter fuel cycle r and d: Consequences for the design. *Fusion Engineering and Design*, 81(1):733–744, 2006b. ISSN 0920-3796. doi: https://doi.org/10.1016/j.fusengdes.2005.07.038. Proceedings of the Seventh International Symposium on Fusion Nuclear Technology.

T. Graham. Xviii. on the absorption and dialytic separation of gases by colloid septa. *Philosophical transactions of the Royal Society of London*, (156):399–439, 1866.

O. Hatlevik, S. K. Gade, M. K. Keeling, P. M. Thoen, A. Davidson, and J. D. Way. Palladium and palladium alloy membranes for hydrogen separation and production: History, fabrication strategies, and current performance. *Separation and Purification Technology*, 73(1):59 – 64, 2010. ISSN 1383-5866. doi: https://doi.org/10.1016/j.seppur.2009.10.020. Inorganic Membrane-ICIM10.

R. Hempelmann, D. Richter, O. Hartmann, E. Karlsson, and R. Wäppling. The positive muon in the intermetallic hydride ZrV_2H_x: A muon tracer study supplemented by differential thermoanalysis, neutron vibrational spectroscopy, and quasielastic neutron scattering. *The Journal of chemical physics*, 90(3):1935–1949, 1989.

J. Hu. Amorphous materials. *MIT OpenCourseWare*, 2015. URL https://ocw.mit.edu/courses/ materials-science-and-engineering/ 3-071-amorphous-materials-fall-2015/.

S. W. Kelly and C. A. Sholl. Theory and monte carlo calculation of the tracer correlation factor. *Journal of Physics C: Solid State Physics*, 20(32):5293, 1987. URL `http://stacks.iop.org/0022-3719/20/i=32/a=015`.

M. Kemali, J. Totolici, D. Ross, and I. Morrison. Inelastic neutron scattering measurements and ab initio calculations of hydrogen in single-crystal palladium. *Physical review letters*, 84(7):1531, 2000.

H. Kimizuka and S. Ogata. First-principles path-integral molecular dynamics study of diffusion process of hydrogen in face-centered cubic metals. In *APS March Meeting Abstracts*, volume 2016, pages G1–362, 2016.

H. Kimizuka, S. Ogata, and M. Shiga. Mechanism of fast lattice diffusion of hydrogen in palladium: Interplay of quantum fluctuations and lattice strain. *Physical Review B*, 97(1):014102, 2018.

H. Kimizuka, S. Ogata, and M. Shiga. Unraveling anomalous isotope effect on hydrogen diffusivities in fcc metals from first principles including nuclear quantum effects. *Physical Review B*, 100(2):024104, 2019.

M. Kofu and O. Yamamuro. Dynamics of atomic hydrogen in palladium probed by neutron spectroscopy. *Journal of the Physical Society of Japan*, 89(5):051002, 2020.

M. Kofu, N. Hashimoto, H. Akiba, H. Kobayashi, H. Kitagawa, M. Tyagi, A. Faraone, J. R. Copley, W. Lohstroh, and O. Yamamuro. Hydrogen diffusion in bulk and nanocrystalline palladium: A quasielastic neutron scattering study. *Physical Review B*, 94(6):064303, 2016.

H. Krimmel, L. Schimmele, C. Elsasser, and M. Fahnle. Self-trapped hydrogen states in metals determined from quantum mechanical calculations

using potentials based on ab initio data: I. hydrogen isotopes in pd. *Journal of Physics: Condensed Matter*, 6(38):7679, 1994.

K.Y.Lee. *Statistical Thermodynamics of Hydrogen Absorption by Alloys*. PhD thesis, Department of Mechanical Engeneering, University of Newcastle, Australia, 01 1993.

P. Langevin. *On the theory of Brownian motion.* 1908.

H. Larsen and J. Jørgen. The atomic simulation environment—a python library for working with atoms. *Journal of Physics: Condensed Matter*, 29(27):273002, jun 2017. doi: 10.1088/1361-648x/aa680e. URL https://doi.org/10.1088/1361-648x/aa680e.

V. Lebedev. Values of the nodes and weights of ninth to seventeenth order gauss-markov quadrature formulae invariant under the octahedron group with inversion. *USSR Computational Mathematics and Mathematical Physics*, 15(1):44–51, 1975.

F. Lewis. The palladium-hydrogen system. *Platinum Metals Review*, 11(3): 99–99, 1967.

F. Lewis. The palladium-hydrogen system. *Platinum Metals Review*, 26(2): 70–78, 1982.

F. Lewis. Hydrogen in palladium and palladium alloys. *International Journal of Hydrogen Energy*, 21(6):461 – 464, 1996. ISSN 0360-3199. doi: https://doi.org/10.1016/0360-3199(95)00126-3.

Y. Li and G. Wahnström. Molecular-dynamics simulation of hydrogen diffusion in palladium. *Physical Review B*, 46(22):14528, 1992.

Y. Liao. Practical electron microscopy and database. *An Online Book*, 2006.

F. Manchester, A. San-Martin, and J. Pitre. The H-Pd (hydrogen-palladium) system. *Journal of phase equilibria*, 15(1):62–83, 1994.

A. A. Markov. *Wahrscheinlichkeits-rechnung*. Ripol Classic, 1912.

N. Metropolis. Monte carlo method. *From Cardinals to Chaos: Reflection on the Life and Legacy of Stanis law Ulam*, page 125, 1989.

N. Metropolis, A. W. Rosenbluth, M. N. Rosenbluth, A. H. Teller, and E. Teller. Equation of state calculations by fast computing machines. *The journal of chemical physics*, 21(6):1087–1092, 1953.

S. F. Parker and P. Collier. Applications of neutron scattering in catalysis. *Johnson Matthey Technol. Rev*, 60(2):132–144, 2016.

R. Pynn. Neutron scattering—a non-destructive microscope for seeing inside matter. In *Neutron applications in earth, energy and environmental sciences*, pages 15–36. Springer, 2009.

D. Ross and D. Wilson. The use of monte carlo calculations in the prediction of quasi-elastic neutron scattering from atoms diffusing in periodic lattices. In *Neutron inelastic scattering 1977*. 1978.

J. Rowe, J. Rush, L. De Graaf, and G. Ferguson. Neutron quasielastic scattering study of hydrogen diffusion in a single crystal of palladium. *Physical Review Letters*, 29(18):1250, 1972.

E. Salomons. On the lattice gas description of hydrogen in palladium: a molecular dynamics study. *Journal of Physics: Condensed Matter*, 2(4): 845, 1990.

L. Schlapbach and A. Züttel. Hydrogen-storage materials for mobile applications. In *Materials For Sustainable Energy: A Collection of Peer-Reviewed Research and Review Articles from Nature Publishing Group*, pages 265–270. World Scientific, 2011.

C. Schönfeld, R. Schätzler, and R. Hempelmann. Diffusion of hydrogen in ZrV_2H_x. *Berichte der Bunsengesellschaft für physikalische Chemie*, 93 (11):1326–1330, 1989.

E. Seymour, R. Cotts, and W. D. Williams. Nmr measurement of hydrogen diffusion in β-palladium hydride. *Physical Review Letters*, 35(3):165, 1975.

D. Shaltiel. Hydride properties of AB_2 laves-phase compounds. *Journal of the Less Common Metals*, 73(2):329–338, 1980.

J. Shinar, D. Davidov, and D. Shaltiel. Proton nmr study of diffusion in continuous, nonstoichiometric metal-hydrogen systems: HfV_2H_x and ZrV_2H_x. *Physical Review B*, 30(11):6331, 1984.

J. Simons and T. B. Flanagan. Diffusion of hydrogen in the α-phase of the palladium-hydrogen system. *The Journal of Physical Chemistry*, 69(10): 3581–3587, 1965.

S. Sinha and D. Ross. Self-consistent density response function method for dynamics of light interstitials in crystals. *Physica B+ C*, 149(1-3):51–56, 1988.

K. Sköld and G. Nelin. Neutron study of the diffusion of hydrogen in palladium. *Solid State Communications*, 4(6):303–306, 1966.

K. Sköld and G. Nelin. Diffusion of hydrogen in the α-phase of Pd-H stud-

ied by small energy transfer neutron scattering. *Journal of Physics and Chemistry of Solids*, 28(12):2369–2380, 1967.

A. Skripov, S. Rychkova, M. Y. Belyaev, and A. Stepanov. Nuclear magnetic resonance study of diffusion and localised motion of H(D) atoms in $TaV_2H_x(D_x)$. *Journal of Physics: Condensed Matter*, 2(34):7195, 1990.

A. Skripov, M. Y. Belyaev, S. Rychkova, and A. Stepanov. Nuclear magnetic resonance study of hydrogen diffusion in $HfV_2H_x(D_x)$ and $ZrV_2H_x(D_x)$: effects of phase transitions and isotope substitution. *Journal of Physics: Condensed Matter*, 3(33):6277, 1991.

A. Skripov, M. Pionke, O. Randl, and R. Hempelmann. Quasielastic neutron scattering study of hydrogen motion in c14-and c15-type $ZrCr_2H_x$. *Journal of Physics: Condensed Matter*, 11(6):1489, 1999.

A. Skripov, J. Cook, T. Udovic, and V. Kozhanov. Quasielastic neutron scattering study of hydrogen motion in c 15- type $HfMo_2H_{0.26}$. *Physical Review B*, 62(21):14099, 2000.

A. V. Skripov, J. C. Cook, C. Karmonik, and R. Hempelmann. Localized motion of hydrogen in c15-type : a quasielastic neutron scattering study. *Journal of Physics: Condensed Matter*, 8(23):L319–L324, jun 1996. doi: 10.1088/0953-8984/8/23/001.

M. Smoluchowski. The kinetic theory of brownian molecular motion and suspensions. *Ann. Phys*, 21:756–780, 1906.

G. L. G. L. Squires. *Introduction to the theory of thermal neutron scattering.* Dover Publications, Mineola, NY, 1996 - 1978. ISBN 048669447X.

S. Steel. *Study of the properties of hydrogen and deuterium in beta phase palladium hydride and deuteride.* PhD thesis, University of Salford, May 2018. URL `http://usir.salford.ac.uk/id/eprint/46767/`.

A. Stepanov, A. Skripov, and M. Y. Belyaev. Nuclear magnetic resonance study of the electronic structure of $HfV_2H_x(D_x)$ and $ZrV_2H_x(D_x)$. *Zeitschrift für Physikalische Chemie*, 163(2):603–608, 1989.

R. Thetford. *Theory of defect interactions in metals.* PhD thesis, University of Oxford, 1989.

L. Van Hove. Correlations in space and time and born approximation scattering in sy stems of interacting particles. *Physical Review*, 95(1):249, 1954.

J. Van Vucht, F. Kuijpers, and H. Bruning. Reversible room-temperature absorption of large quantities of hydrogen by intermetallic compounds. *Philips Res. Rep. 25: 133-40 (Apr 1970).*, 1970.

E. Wimmer, W. Wolf, J. Sticht, P. Saxe, C. B. Geller, R. Najafabadi, and G. A. Young. Temperature-dependent diffusion coefficients from ab initio computations: Hydrogen, deuterium, and tritium in nickel. *Physical Review B*, 77(13):134305, 2008.

W. H. Wollaston. Xxii. on the discovery of palladium; with observations on other substances found with plantina. *Philosophical Transactions of the Royal Society of London*, (95):316–330, 1805.

J. Worsham Jr, M. Wilkinson, and C. Shull. Neutron-diffraction observations on the palladium-hydrogen and palladium-deuterium systems. *Journal of Physics and Chemistry of Solids*, 3(3-4):303–310, 1957.

227

S. Yun and S. Ted Oyama. Correlations in palladium membranes for hydrogen separation: A review. *Journal of Membrane Science*, 375(1):28 – 45, 2011. ISSN 0376-7388. doi: https://doi.org/10.1016/j.memsci.2011.03.057.

X. Zhou, J. Zimmerman, B. Wong, and J. Hoyt. An embedded-atom method interatomic potential for pd–h alloys. *Journal of Materials Research*, 23 (3):704–718, 2008a. doi: 10.1557/JMR.2008.0090.

X. Zhou, J. A. Zimmerman, B. M. Wong, and J. J. Hoyt. An embedded-atom method interatomic potential for pd–h alloys. *Journal of Materials Research*, 23(3):704–718, 2008b.

X. Zhou, T. W. Heo, B. C. Wood, V. Stavila, S. Kang, and M. D. Allendorf. Temperature-and concentration-dependent hydrogen diffusivity in palladium from statistically-averaged molecular dynamics simulations. *Scripta Materialia*, 149:103–107, 2018.